Université de Montréal

Dispositifs optoélectroniques à base de semi-conducteurs organiques en couches minces

par
Pierre-Louis Marc Brunner

Département de Chimie
Faculté des arts et des sciences

Thèse présentée à la Faculté des études supérieures et postdoctorales

en vue de l'obtention du grade de
Philosophiae doctor (Ph.D.) en chimie

Août 2015

Université de Montréal
Faculté des études supérieures et postdoctorales

Cette thèse intitulée :

Dispositifs optoélectroniques à base de semi-conducteurs organiques en couches minces

présentée par :

Pierre-Louis Marc Brunner

a été évaluée par un jury composé des personnes suivantes :

Professeure Antonella Badia	Présidente-Rapporteuse
Professeur James D. Wuest	Directeur de recherche
Professeur Mickael Dollé	Membre du jury
Professeur Mario Leclerc	Examinateur externe
Professeur David London	Représentant de la Doyenne de la FAS

Résumé

Les petites molécules de type p à bandes interdites étroites sont de plus en plus perçues comme des remplaçantes possibles aux polymères semi-conducteurs actuellement utilisés conjointement avec des dérivés de fullerènes de type n, dans les cellules photovoltaïques organiques (OPV). Par contre, ces petites molécules tendent à cristalliser facilement lors de leur application en couches minces et forment difficilement des films homogènes appropriés. Des dispositifs OPV de type hétérojonction de masse ont été réalisés en ajoutant différentes espèces de polymères semi-conducteurs ou isolants, agissant comme matrices permettant de rectifier les inhomogénéités des films actifs et d'augmenter les performances des cellules photovoltaïques. Des polymères aux masses molaires spécifiques ont été synthétisés par réaction de Wittig en contrôlant précisément les ratios molaires des monomères et de la base utilisée. L'effet de la variation des masses molaires en fonction des morphologies de films minces obtenus et des performances des diodes organiques électroluminescentes reliées, a également été étudié. La microscopie électronique en transmission (MET) ou à balayage (MEB) a été employée en complément de la microscopie à force atomique (AFM) pour suivre l'évolution de la morphologie des films organiques minces. Une nouvelle méthode rapide de préparation des films pour l'imagerie MET sur substrats de silicium est également présentée et comparée à d'autres méthodes d'extraction. Motivé par le prix élevé et la rareté des métaux utilisés dans les substrats d'oxyde d'indium dopé à l'étain (ITO), le développement d'une nouvelle méthode de recyclage eco-responsable des substrats utilisés dans ces études est également présenté.

Mots-clés : Cellules solaires organiques, photovoltaïque, diodes organiques électroluminescentes, matériaux à bande interdite étroite, petite molécule de type push-pull, morphologie des films minces, matrices polymériques, goussets polymériques, masse molaire des polymères, polymères électroluminescents, réglage d'émission, rendements quantiques, recyclage, oxyde d'indium dopé à l'étain (ITO), microscopie à transmission électronique, rayon ionique focalisé, gaufre de silicium, substrats de NaCl, gabarit organique, patron nanométrique

Abstract

Small p-type low band-gap semi-conducting molecules are rapidly gaining notoriety as potential replacements for conjugated polymers used in organic photovoltaic devices (OPV) along with n-type fullerene derivatives. As these active compounds often tend to crystallize upon coating, homogeneous, smooth thin-film formation is usually not trivial to obtain. We have devised bulk heterojunction OPVs in which various species of semi-conducting polymers or readily available insulating polymers are used as third-component matrices in order to rectify film inhomogeneity and enhance device performances. Polymers of specific molecular weights (MW) were also synthesised via a controlled Wittig type polymerization process by efficiently controlling the monomer and base ratios, and the effects of the MW variation were correlated with the thin-film morphologies and the resulting electroluminescence performances. In order to follow the evolution of the morphologies and the molecular arrangements, scanning and transmission electronic microscopy (SEM and TEM, respectively) was used, together with atomic force microscopy (AFM), and a new technique was introduced for preparing thin-film samples for imaging based on Si-wafer coating. Motivated by the increasing price of indium and the high cost of ITO-coated substrates, we have also examined ways to recover and recycle the tin-doped indium oxide (ITO) substrates used in these studies via environmentally benign methods.

Keywords : organic solar cells, photovoltaics, organic light-emitting diodes, low bandgap materials, push-pull small molecules, thin film morphologies, polymer matrices, polymer pockets, polymer molar mass, electroluminescent polymers, emission tuning, quantum yield, recycling, tin-doped indium oxide (ITO), transmission electron microscopy, focused ion beam, silicon wafer, NaCl substrates, organic templates, nano-patterning

Table des matières

Liste des tableaux

Liste des figures

Liste des schémas

Liste des vidéos

Liste des équations

Liste des sigles

CIE : Commission Internationale de l'Éclairage

NREL: National Renewable Energy Laboratory

Liste des abréviations

Å	: Ångström
A	: ampères
Ac	: acétyle
AFM	: atomic force microscopy
aq	: aqueux
Ar	: aryl
atm	: atmosphère
Bu	: butyle
br	: *broad*
^{o}C	: degré Celsius
calcd	: *calculated*
cat	: catalytique
Cd	: candela
cm	: centimètre
conc	: concentré
Δ	: reflux
δ	: déplacement chimique
d	: doublet (en RMN)
DAPI	: 4',6-diamidino-2-phénylindole
dd	: doublet de doublet (en RMN)
DMF	: N,N-diméthylformamide
DMSO	: diméthyl sulfoxyde
E	: énergie
Eg	: énergie de la bande interdite (gap)
EDXS	: energy-dispersive X-ray spectroscopy
EET	: electronic energy transfer
elec	: electronique

Et	: éthyle
ETL	: electron transport layer
eV	: electron volt
F-DTS	: 7,7′-[4,4-bis(2-ethylhexyl)-4*H*-silolo[3,2-*b*:4,5-*b*′]dithiophene-2,6-diyl]bis[6-fluoro-4-(5′-hexyl-[2,2′-bithiophen]-5-yl)benzo[*c*][1,2,5]thiadiazole]
FF	: facteur de forme
FIB	: focused ion beam
FRET	: Förster resonance energy transfer
FWHM	: full width at half maximum
g	: gramme
GPC	: gel permeation chromatography
h	: heure
HMDS	: hexamethyldisiloxane
HOMO	: highest occupied molecular orbital
HTL	: hole transport layer
Hz	: hertz
IR	: infrarouge
I	: courant
I_D	: courant de diode
I_{SH}	: courant shunt
I_T	: courant de travail
ITO	: indium tin oxide
J	: constante de couplage
Jsc	: courant de court-circuit
kcal	: kilocalorie
kDa	: kilo dalton
kV	: kilovolt
kWh	: kilowatt heure
L	: litre
L	: luminance

Lm : lumens

LS : light scattering

LUMO : lowest unocuppied molecular orbital

M : molaire

m : mètre

m : multiplet (en RMN)

mA : milliampère

mbar : millibar

Me : méthyle

MEB : microscopie électronique à balayage

MET : microscopie électronique à transmission

mg : milligramme

MHz : mégahertz

min : minute

mL : millilitre

mm : millimètre

mmole : millimole

mol : mole

mp : melting point

M_n : masse molaire moyenne en nombre

M_w : masse molaire moyenne en masse

n : négatif (type-n)

N : normal

N : Newton

nm : nanomètre

OLED : organic light-emitting diode

OPV : organic photovoltaic

OTFT : organic thin-film transistor

ORTEP : Oak Ridge thermal ellipsoid program

ox : oxidation

p : positif (type-p)

P	: puissance
P3HT	: poly(3-hexylthiophène-2,5-diyl)
PCBM	: [6,6]-phényl-C_{61}-butanoate de méthyle
PCDTBT	: poly[N-9'-heptadécanyl-2,7-carbazole-alt-5,5-(4,7-di-2-thiényl-2',1',3'-benzothiadiazole]
PCE	: power conversion efficiency
PDI	: indice de polydispersité
PDMS	: polydiméthylsiloxane
PEDOT	: poly(3,4-éthylènedioxythiophène)
PFO-MEH-PPV	: poly[(9,9-dioctyl-2,7-divinylène-fluorènylène)-alt-co-(2-méthoxy-5-(2-éthylhexyloxy)-1,4-phénylène)]
PEG	: polyéthylène glycol
Ph	: phényle
PLED	: polymer light-emitting diode
PMMA	: poly(méthacrylate de méthyle)
ppm	: partie par million
PPV	: poly(phénylène vinylène)
PS	: polystyrène
PSS	: polystyrene standard
PSS	: poly(styrènesulfonate) de sodium
PVC	: poly(chlorure de vinyle)
red	: reduction
RMN	: résonance magnétique nucléaire
Rs	: résistance en série
Rsh	: résistance de shunt
RMS	: root mean square
RPM	: revolutions per minute
RQY	: relative quantum yield
s	: singulet (en RMN)
s	: seconde
SEI	: secondary electron imaging

SEM	: scanning electronic microscopy
SHE	: standard hydrogen electrode
SM	: spectre de masse
Tg	: transition vitreuse
TGA	: thermogravimetric analysis
THF	: tétrahydrofurane
TV	: télévision
μL	: microlitre
μm	: micromètre, micron
UV	: ultraviolet
US	: United States
V	: volt
Voc	: voltage en circuit ouvert
W	: watt
w/w	: weight by weight
WOLED	: white organic light-emitting diode

À mes deux guignols ; Maya et Edgar, et ma douce femme Karla

"Did you see in the morning light
I really talked, yes I did, to God's early dawning light
And I was privileged to be as I am to this day
To be with you."

- Jon Anderson and Evangelos Odysseas Papathanassiou

Remerciements

Si la réalisation d'une thèse de doctorat permet d'enrichir les connaissances, d'en acquérir de nouvelles, de modifier les façons de faire et d'élargir les champs de pensées, c'est également l'opportunité de rencontrer des gens intéressants et stimulants, avec qui il fait bon vivre, discuter et travailler. À ces personnes, je veux dire merci.

Merci tout d'abord à mon superviseur, Professeur James Wuest, qui a su sortir des sentiers battus pour s'engouffrer dans une aventure moins commune mais ô combien excitante. Sa vision large et juste de la science et du monde, son audace et sa curiosité en ont fait un des plus grands dans son domaine. Que se soit pour partager un bon moment, une découverte ou un bon verre de vin, Jim est toujours de bonne compagnie. Merci.

Merci également aux différents professeurs qui ont mis leur temps à disposition pour faire en sorte que je puisse grandir scientifiquement. J'aimerais remercier particulièrement Dr. André Beauchamp, Dr. Robert Prud'homme et Dr. Garry Hanan qui ont pris le temps de préparer et évaluer mon examen pré-doctoral. J'aimerais aussi remercier Dre. Clara Santato et Dr. Fabio Cicoira pour leur aide technique, matériel et moral. Pour leur excellents cours et conseils, je remercie également Dre. Suzanne Giasson, Dr. Michel Lafleur et Dr. Richard Martel. Et finalement, merci à mon comité de thèse pour avoir bien voulu prendre le temps d'évaluer ce travail. Merci.

J'aimerais aussi remercier les membres du groupe Wuest pour leur aide et support durant toutes ces années. J'ajouterais une mention toute particulière à mes collègues et amis Daniel, Minh, Alice et Marc-André qui ont participé à la réalisation d'une partie de ce travail. Merci également à Richard Beal, Alex Mann et Kirk Tierney qui furent des acteurs importants dans la réalisation des nouvelles infrastructures permettant la création d'un laboratoire propice au montage de cellules photovoltaïques et leur caractérisation. Ce n'est pas facile quand on part de rien, et leur aide fut particulièrement appréciée. J'aimerais également saluer mon cher ami François Raymond qui a su me tendre la main plus d'une fois, et avec qui j'ai toujours trouvé un malin plaisir à discuter, que ce soit de science, de politique, ou du Général Boulanger. Il y a aussi ceux avec qui nous avons laissé la puck et le bon temps rouler; Nick,

Pierre-Marc, Chewy. Après toutes ces années, je me demande encore pourquoi la division sportive de Honda s'appellerait Mazda Speed, et qui est l'acteur qui jouait John Wayne? Merci.

Si les défis furent parfois titanesques dans l'entreprise d'une vie aux multiples facettes, je dois lever *mes* chapeaux à mon fidèle partenaire d'affaires et ami Dominic Laliberté, qui su dire oui au moment opportun, lorsque l'aventure commença. Et quelle aventure! Merci.

N'ayant pas tous les équipements nécessaires durant la genèse du projet, je voudrais remercier les gens de l'IMS de l'Université de Bordeaux de bien avoir voulu m'accueillir plus d'une fois dans leurs laboratoires. Merci particulièrement à Guillaume Wantz, Lionel Hirsch et Pascal Tardif. On groque? Aller, groquons! Merci.

Je ne dois surtout pas oublier les membres scientifiques et agents de recherches qui ont su converger leurs efforts vers ce travail en m'aidant à comprendre certains phénomènes à travers l'analyse de résultats. Je remercie spécialement Patricia Moraille, Sylvain Essiembre et Pierre Ménard-Tremblay pour leur aide précieuse. Merci.

Je veux également remercier certains membres du personnel qui m'ont spécialement appuyé d'une manière ou d'une autre durant mon séjour à l'Université de Montréal : Christian, Saverio, Claude, Joël et Francine. Merci.

Si la partie expérimentale de la recherche se passe principalement entre les quatre murs d'un laboratoire, le processus intellectuel en passe les frontières. J'aimerais donc remercier mes amis qui ont contribués au processus de cogitation en m'aidant à résoudre, parfois sans s'en rendre compte, certains problèmes techniques : Jean-Sébastien Mailloux, Carl Leblanc, Eric Demers. Merci.

Pour terminer, j'aimerais remercier ma famille et mes parents qui, avec leurs encouragements et leurs appuis inconditionnels, m'ont permis de passer à travers cette aventure en un seul morceau. Je vous en dois une… Merci.

"Great spirits have always encountered violent opposition from mediocre minds."

- Albert Einstein

Notes

Pour simplifier l'insertion des articles et faciliter la lecture de cette thèse, l'auteur a fait les modifications suivantes :

- La numérotation des molécules dans les articles n'a pas été modifiée dû au nombre restreint de molécules impliquées, et reste donc confinée par chapitre.
- Toutes les informations des articles, incluant les parties expérimentales supplémentaires invoquées, sont préservées dans un même chapitre pour maintenir la cohérence des papiers présentés.
- Les numéros des figures, tableaux, équations, et schémas ont été redéfinis dans une suite logique à travers la thèse en ajoutant le numéro de chapitre ou de section en préfixe.
- Les références dans les articles et les parties expérimentales supplémentaires sont placées à la fin de chaque chapitre et demeurent indépendantes du chapitre dans lequel l'article est inséré.

La liste suivante démontre les contributions personnelles de Pierre-Louis Brunner et des co-auteurs pour les articles présentés dans cette thèse :

- Toutes les synthèses ainsi que les cristallisations des molécules de l'article 1 furent effectuées par Daniel Beaudoin et Alice Heskia.
- Tous les calculs de TD-DFT de l'article 1 furent effectués par Marc-André Dubois.
- Toutes les structures cristallographiques de l'article 1 ont été résolues par le Dr Thierry Maris.
- L'article 1 a été écrit par Pierre-Louis Brunner avec la participation de Daniel Beaudoin, et corrigé par le professeur James D. Wuest et par les co-auteurs respectifs.
- L'article 2 a été écrit par Pierre-Louis Brunner et corrigé par le professeur James D. Wuest.

- L’article 3 a été écrit par Pierre-Louis Brunner et corrigé par le professeur James D. Wuest assisté de la professeure Clara Santato, et par les co-auteurs respectifs.
- Toutes les synthèses de l’article 3 ont été effectuées par le Dr. Dominic Laliberté et Solaris Chem Inc.
- L’article 4 a été écrit par Pierre-Louis Brunner et Jean-Philippe Masse, et corrigé par les professeurs Gilles L’Espérance et James D. Wuest.
- L’article 5 a été écrit par le Dr. Minh Trung Dang et Pierre-Louis Brunner et corrigé par le professeur James D. Wuest.

Chapitre 1

Introduction

"My eyes are constantly wide open to the extraordinary fact of… existence of life and how this breathtakingly powerful process… has managed to take the very simple facts of physics and chemistry and build them up to redwood trees and humans."

- Richard Dawkins

1.1 Énergie dans le monde

Plusieurs grandes révolutions ont changé la face du monde au cours des années. Beaucoup d'entre nous ont récemment vécu la révolution informatique, qui a su transformer notre monde analogique en monde numérique, ou la révolution des télécommunications, qui a changé notre perception même des distances entre nous. Nous serons encore plus nombreux à redéfinir nos modes de vie face aux défis énergétiques qui nous font déjà face. Les deux crises pétrolières de 1973 et 1981 ont permis à plusieurs de réaliser la fragilité de l'économie globale reposant sur les énergies fossiles non renouvelables et disponibles en quantités limitées pour une demande de plus en plus croissante. En effet, selon les projections de croissance de la population humaine sur terre d'ici les trente prochaines années, 1,4 milliards d'individus se rajouteront au berceau de population actuel[1] avant d'atteindre les 10 milliards d'individus en 2100.[2]

Les sources fossiles comblent actuellement 85% de nos besoins en énergie[1, 3] avec plus de 90 millions de barils de pétrole consommés à chaque jour dans le monde. Avec des réserves connues de 1700 milliards de barils disponibles, il est prévisible que la fin du pétrole comme combustible ce situe à moins de 50 ans. Le maintien d'un prix relativement bas du pétrole (Brent ou West Texas Intermediate autour de 40 $US/baril présentement) promet une détérioration accélérée des réserves, une forte hausse du prix dans un avenir proche, et procure un faux sentiment de continuité à longs termes. Pour ce qui est du charbon, les réserves actuelles, au taux de consommation actuel, nous permettrons son exploitation pour les 200 prochaines années. Par contre, les impacts environnementaux d'une exploitation à grande échelle du charbon pourraient gravement altérer la qualité de vie de la population.[4]

La demande en énergie d'ici 2040 sera en augmentation de 50% à moins d'altérer grandement nos habitudes de consommation et d'exploiter des sources d'énergie alternatives.[1] Un récent rapport du Département de l'Énergie aux É.-U. estime que plus de 12% de l'énergie consommée est dû à l'éclairage résidentiel et commercial.[5] La recherche de dispositifs, de sources lumineuses ou d'appareils peu énergivores permettra de limiter l'augmentation de nos

besoins énergétiques. Couplés au développement de l'exploitation des sources d'énergie renouvelables, ils constitueront une part intégrale d'une stratégie globale pour éviter d'autres crises énergétiques.

1.2 Énergie solaire

La source d'énergie la plus abondante disponible sur terre est le soleil. La fusion continue de près de 600 millions de tonnes d'hydrogène par seconde (dont la transformation de 4 millions de tonnes d'hydrogène par seconde en énergie) lui confère une constance solaire de 1000 Wm^{-2} mesurée en surface de la Terre.[6] La transformation d'une fraction de cette immense réserve d'énergie lumineuse en énergie électrique permettrait de suffire largement aux besoins énergétiques mondiaux actuels et futurs de manière propre et saine.

1.2.1 Effet photovoltaïque

L'effet photovoltaïque fut initialement observé par le français Antoine Becquerel et présenté à l'Académie des Sciences en 1839 par son fils Alexandre-Edmond Becquerel dans le Comptes Rendus Hebdomadaires des Séances de l'Académie des Sciences.[7] Il observa la production d'un courant électrique lorsque deux plaques de platine ou d'or d'une cellule électrolytique furent exposées aux rayons solaires. En 1905, Albert Einstein expliqua l'effet photoélectrique en proposant l'idée de *quanta* énergétiques où l'énergie lumineuse est alors transférée par paquets entiers à un électron par absorption.[8] Lorsque l'effet a lieu à l'intérieur d'un dispositif permettant la collecte de ces électrons excités (et des trous à l'état fondamental générés par leur absence) à l'aide d'électrodes, un courant pouvant produire un travail est alors généré, donnant naissance à un effet photovoltaïque (Figure 1.1). Einstein fut le récipiendaire du prix Nobel de Physique en 1923 pour sa théorie sur l'effet photoélectrique.

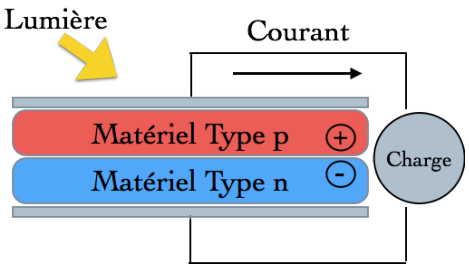

Figure 1.1. Schéma d'une cellule à effet photovoltaïque à jonction p-n simple, composée de deux matériaux semi-conducteurs de type p et n entre deux électrodes.

1.2.2 Bref historique des cellules photovoltaïques

En 1876, les premières ancêtres des cellules photovoltaïques modernes firent leur apparition, grâce aux travaux des pionniers William G. Adams et Richard E. Day sur des architectures impliquant la disposition de sélénium entre deux plaques de platine. En 1894, Charles Fritts prépara la première cellule solide moderne en appliquant une fine couche d'or sur une gaufre de sélénium.[9] Il faudra attendre les années 50 pour que les recherches de Gerald Pearson, Daryl Chapin et Calvin Fuller, travaillant tous aux Bell Laboratories, proposent les premières cellules photovoltaïques utilisant une jonction p-n à base de silicium dopé au bore avec des rendements élevés, pour l'époque, de 4%.[10] Ces recherches en photovoltaïque furent accélérées durant les années subséquentes, surtout pour leurs applications dans la conquête de l'espace comme source énergétique pour les satellites.

Le développement du domaine des semi-conducteurs organiques par Heeger, MacDiarmid et Shirakawa, qui ont trouvé que le dopage du polyacétylène par l'iode le rendent conducteur,[11] a permis aux trois chercheurs d'obtenir le prix Nobel de Chimie de 2000 pour la découverte et le développement de polymères conducteurs.[12-14] Les premiers dispositifs photovoltaïques basés sur de tels matériaux organiques furent par la suite réalisés par Tang et Van Slyke à partir de 1986 lorsqu'une cellule bicouche formée de phthalocyanine de cuivre recouverte d'un dérivé de pérylène produisit un rendement de 0.95%.[15-16]

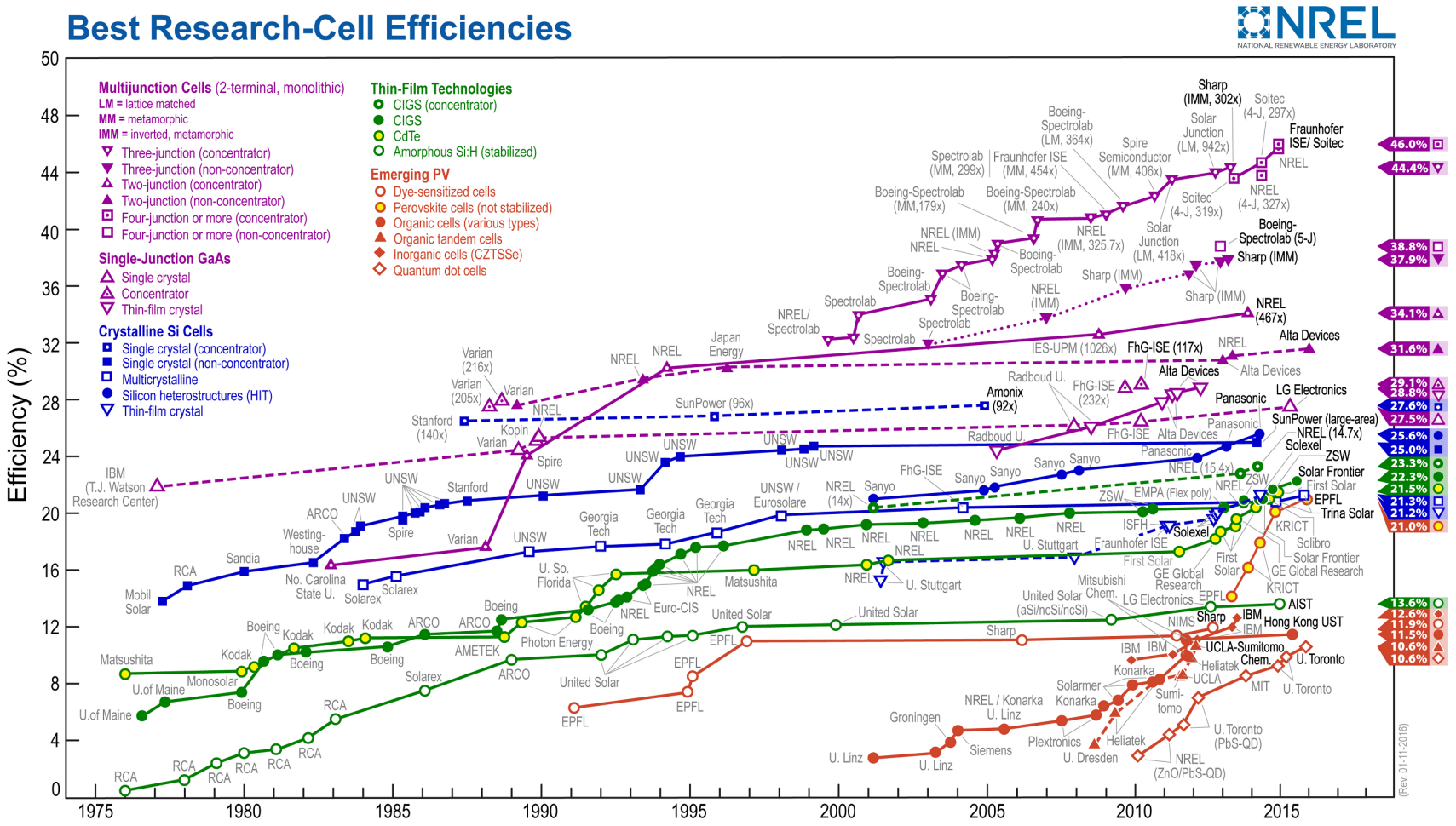

Figure 1.2. Graphique des meilleures cellules photovoltaïques et leurs rendements par technologies recensées par le National Renewable Energy Laboratory (NREL) entre 1975 et 2016.[17]

Le National Renewable Energy Laboratory (NREL), situé à Golden au Colorado, publie depuis plusieurs années un graphique montrant l'évolution dans le temps des différentes technologies reliées au développement de cellules et de panneaux solaires et leurs efficacités (Figure 1.2). On peut y constater que le domaine du photovoltaïque organique a rapidement gagné en popularité avec des rendements actuels de plus de 13% rapporté par Heliatek[18] dans une course à la commercialisation de dispositifs photovoltaïques qui sont peu couteux, flexibles et légers à base de petites molécules ou de polymères π-conjugués organiques.

1.2.3 Principe de fonctionnement des cellules photovoltaïques

Le soleil est la principale source énergétique permettant aux cellules photovoltaïques de générer de l'énergie électrique utile. Il est donc important de discuter de la chaine réactionnelle engendrée par l'exposition des dispositifs aux photons solaires (ou provenant d'autres sources lumineuses). Il faut également établir que seuls les photons ayant la quantité d'énergie transférable, tel que décrit par Einstein en 1905, correspondante à l'énergie de la bande interdite du matériau ou des matériaux utilisés dans la couche active des cellules, auront un impact direct sur les rendements des dispositifs. Le spectre d'absorption des matériaux doit le plus possible correspondre au spectre solaire d'émission (Figure 1.3). La Figure 1.3 représente les spectres solaires tels que mesurés à la surface de l'atmosphère terrestre (extraterrestre) et à la surface de la Terre en prenant en considération un angle d'incidence du rayonnement de 37° par rapport au sol (plan incliné). Le spectre calculé prend en considération les paramètres atmosphériques tels que définis par le 1976 U. S. atmosphere standards, notamment un filtre 1.5 AM (Air Mass), ou 1.5 fois l'épaisseur de l'atmosphère, une turbidité de l'air à 500 nm de 0.084, une colonne de vapeur d'eau de 1.42 cm et une colonne d'ozone de 0.34 cm.[17, 19-20]

Les travaux de Alan J. Heeger, Alan G. MacDiarmid et Hideki Shirakawa ont permis le passage d'une époque où seulement les matériaux inorganiques étaient considérés

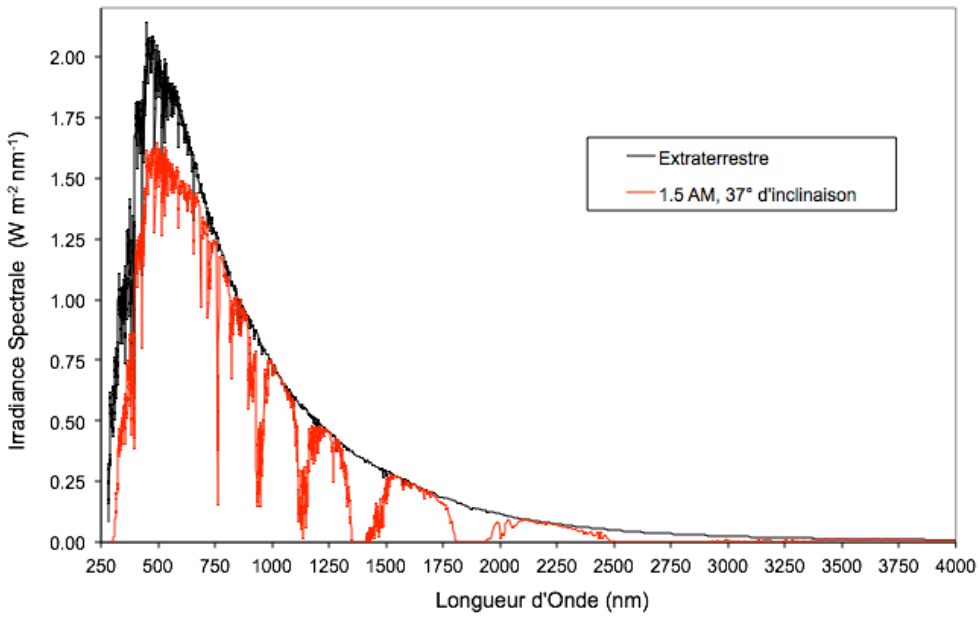

Figure 1.3. Émission radiative du spectre solaire extraterrestre et à la surface calculée à partir d'un standard 1.5 AM et un angle d'inclinaison de l'irradiation de 37° par rapport au sol. Graphique généré à partir des données brutes mises à disposition par NREL.[17]

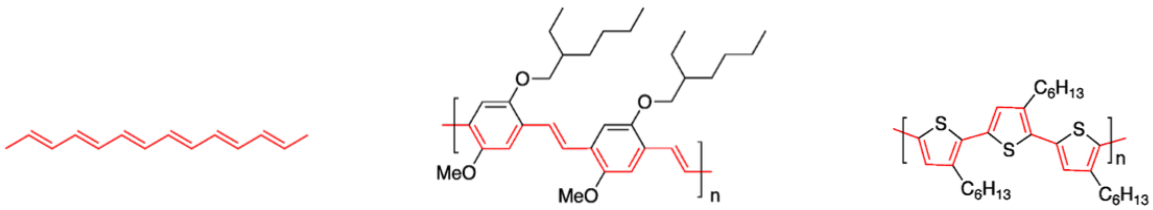

a b c

Figure 1.4. Systèmes π-conjugués représentatifs, avec la conjugaison principale montrée en rouge. (a) Polyacétylène. (b) Poly[2-méthoxy-5-(2-éthylhexyloxy)-1,4-phénylènevinylène] (MEH-PPV). (c) Poly(3-hexylthiophène-2,5-diyl) (P3HT).

comme composantes potentielles pour réaliser des dispositifs photovoltaïques, vers une nouvelle aire de l'électronique organique utilisant des matériaux π-conjugués (Figure 1.4). Ces matériaux moléculaires sont constitués d'une alternance de liens carbone-carbone simples (σ) et multiples (π), leur donnant un squelette conjugué dû à la délocalisation des électrons π par le recouvrement des orbitales p à travers les liens σ. La structure simple étant vue comme un dimère de carbones, une dégénérescence de la bande π est créée, formant ainsi une bande π et une bande π* par le principe d'instabilité de Peierls.[21] La bande π accommodera les deux électrons π à l'état fondamental, laissant vide la bande de plus haute énergie π*. Ces deux bandes seront référées respectivement aux niveaux énergétiques HOMO (highest- occupied molecular orbital), ou bande de valence, et LUMO (lowest unoccupied molecular orbital), ou bande de conduction. La différence énergétique de ces deux orbitales moléculaires définit l'énergie de la bande interdite (E_g) pour un matériau moléculaire π-conjugué (Équation 1.1).

$$E_g = E_\pi - E_{\pi^*} = E_{HOMO} - E_{LUMO} \qquad \text{Équation 1.1}$$

L'absorption des photons correspondant à l'énergie caractéristique (E_g) permettra en premier lieu la génération d'électrons excités qui seront promus dans la bande conductrice π* de plus haute énergie. Les photons de plus basses énergies pourront passer à travers le matériel alors que les photons de plus hautes énergies seront absorbés, mais leur énergie supérieure à E_g sera dissipée sous forme de chaleur (phonons). La séquence d'évènements qui s'en suit est illustrée par la Figure 1.5. L'irradiation de la couche active constituée d'un matériau donneur (type p) et d'un matériau accepteur (type n) à travers l'anode transparente permet donc la génération d'excitons, une quasi-particule constituée d'un électron et d'un trou fortement liés par forces de Coulomb. Ces excitons diffuseront par la suite à travers la couche active et, à la rencontre de la jonction p-n des deux matériaux actifs, une séparation de charge se produira permettant la génération d'un électron et d'un trou libres qui diffuseront par percolation ou dériveront à travers le champ électrique du dispositif vers la cathode et l'anode. Il est également possible qu'un exciton, ayant un temps de vie limité ne lui permettant généralement pas une diffusion de plus de 20 nm environ, n'ait pas le temps de rejoindre la jonction p-n avant que l'électron et le trou le constituant se recombinent et dissipent l'énergie emmagasinée

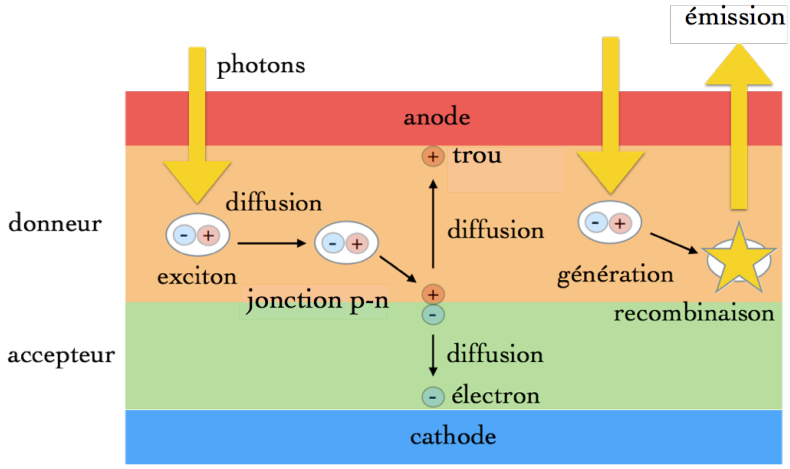

Figure 1.5. Génération, diffusion et séparation des charges à la jonction p-n de la couche active d'une cellule photovoltaïque organique bicouche.

par l'émission d'un photon.[22-23] Les rendements des cellules photovoltaïques sont directement reliés à la capacité des matériaux de la couche active à générer des excitons, séparer les charges et permettre la diffusion/dérive efficace des différentes espèces.

Fondamentalement, il est impératif de comprendre qu'un compromis doit être fait entre la capacité d'absorption de la couche active et sa capacité à permettre une diffusion efficace des excitons ou de capter les charges générées selon l'architecture choisie. Si l'utilisation d'une couche active plus épaisse résulte en une plus grande absorption des photons incidents et un nombre supérieur d'excitons générés, les distances de diffusion à travers la couche active seront également plus importantes, ce qui favorisera les évènements de recombinaison et limitera l'efficacité du système. La génération de charges, lors de la rencontre des excitons avec une jonction p-n, et la collections des charges aux électrodes seront pour leur part favorisées par des films plus minces.

1.2.4 Architecture des cellules photovoltaïques

Les premiers dispositifs solaires à base de matériaux organiques furent réalisés de manière séquentielle en adoptant une architecture de type sandwich où les couches furent disposées les unes sur les autres entre deux électrodes.[15] La jonction du matériau de type p est recouverte du matériau de type n, formant ainsi la jonction p-n simple permettant la séparation et la collection des charges générées (Figure 1.5). Par contre, les distances que doivent parcourir les excitons dans une telle configuration encouragent grandement la recombinaison de charges, ce qui résulte en des dispositifs peu performants. Pour parer à cet inconvénient, Heeger et ses collègues proposèrent de mélanger les deux matériaux de types p et n, multipliant ainsi la surface disponible de jonction p-n permettant une séparation de charges plus efficace en limitant la distance de diffusion requise par l'exciton pour rencontrer une telle

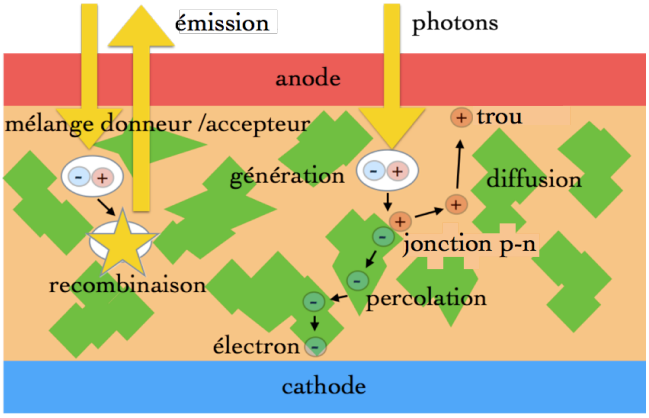

Figure 1.6. Architecture d'une cellule photovoltaïque organique de type hétérojonction de masse, où le donneur et l'accepteur sont mélangés.

jonction (Figure 1.6).[24] Le principe fut baptisé 'bulk heterojunction', ou hétérojonction de masse, et ouvrit la porte au développement rapide de cellules beaucoup plus performantes.[25-26] Par contre, les bicouches offrent de meilleures diffusions de charges vers leurs électrodes respectives une fois que les charges sont séparées. L'architecture à hétérojonction de masse

doit être constituée de matériaux permettant une percolation de charge efficace à travers le film actif.[27] En variant les proportions donneur-accepteur pour un couple donné et en contrôlant la morphologie du film et son épaisseur, il est possible de maximiser les rendements de ces cellules photovoltaïques. Le rendement maximum pour un système donneur-accepteur sera obtenu en ajustant le nombre de jonctions p-n par rapport au nombre d'entités permettant une percolation de charge efficace. La présence de zones cristallines de plus hautes mobilités de chacun des deux matériaux (p et n) favorise le transport des charges, au détriment du nombre d'interfaces p-n disponibles.

1.2.5 Conception de molécules π-conjuguées

La conception de molécules π-conjugués organiques pour leur application en cellules solaires, demande une attention particulière à certains facteurs primordiaux. Premièrement, il est important de concevoir des molécules, de faibles masses ou polymériques, qui pourront absorber le plus largement possible le rayonnement solaire jusqu'à l'infrarouge proche tel que discuté plus tôt. Ainsi, l'apport en énergie au système par l'absorption de photons en sera maximisé. Pour ce faire, l'énergie de la bande interdite (E_g) doit être minimisée en ajustant les niveaux HOMO et LUMO par un choix judicieux des unités ou monomères organiques qui forment le composé.[28-32] Le niveau d'énergie de l'orbitale $LUMO_{donneur}$ par rapport au niveau du vide, est importante puisque celle-ci déterminera, en tenant compte également de l'énergie de liaison de l'exciton formé,[31, 33] la propension à un électron excité d'être transféré, durant la séparation de charges, vers la LUMO d'un accepteur à la jonction p-n. L'ampleur du voltage a circuit ouvert (V_{oc}) que la cellule pourra potentiellement développer correspond directement à l'écart entre la LUMO de l'accepteur et la HOMO du donneur[31, 34] tel que décrit par l'Équation 1.2, où *e* représente la charge élémentaire, et C une constante (0.3-0.4 eV) correspondant à l'énergie de liaison d'un exciton.

$$V_{oc} \propto 1/e\,(E_{LUMO\ accepteur} - E_{HOMO\ donneur}) - C \qquad \text{Équation 1.2}$$

Les dérivés [6,6]-phényl-C_{61}-butanoate de méthyle ($PC_{61}BM$) ou [6,6]-phényl-C_{71}-butanoate de méthyle ($PC_{71}BM$) sont largement utilisés comme accepteurs efficaces pour réaliser des cellules solaires ayant une architecture de type hétérojonction de masse.[35-37] Ces dérivés de fullerène possèdent une LUMO autour de -4.0 à -4.3 eV par rapport au vide.[38] La position de la HOMO du matériel donneur devra donc être suffisamment profonde pour permettre une amplitude du V_{oc} maximale tout en gardant un E_g adéquat de 1.2 à 1.9 eV[31] correspondant à la zone d'émission privilégiée du spectre solaire. Pour espérer une durabilité des dispositifs en présence des éléments environnementaux comme l'eau et l'air, une profondeur de la HOMO d'au moins -5.2 eV est souhaitable pour assurer une certaine stabilité des matérieaux actifs.[39] La HOMO du donneur devrait donc idéalement se trouver à un niveau d'énergie profond entre -5.2 et -5.5 eV par rapport au vide.[29]

Une fois les charges générées et séparées, le matériel doit également permettre la mobilité des porteurs de charges libres vers les électrodes. Une conception planaire des molécules favorisant un empilement moléculaire proche contribuera à une bonne mobilité des charges à travers le matériel.[40] Par contre, une trop grande propension des matériaux à cristalliser est à proscrire puisqu'une séparation de phases donneur-accepteur trop importante diminuera, entre autre, le nombre de jonctions p-n à l'intérieur de l'hétérojonction de masse (Figure 1.6) et l'efficacité du système à créer des porteurs de charges libres. L'étendue de la conjugaison π étant favorisée par une planéité des molécules de faibles masses ou polymériques, il est donc favorable de limité l'empilement moléculaire en ajoutant des chaines moléculaires adjacentes plus ou moins encombrantes ou fonctionalisées[41-42] plutôt que d'induire des torsions ou des plis à même le squelette moléculaire. Ces chaines fonctionnelles permettront également d'assurer une certaine solubilité aux matériaux permettant leur mise en forme en films minces par des procédés utilisant des formulations à base de solvants comme l'enduction centrifuge, l'impression à jet d'encre ou la sérigraphie.

1.2.6 Paramètres de caractérisation des cellules photovoltaïques

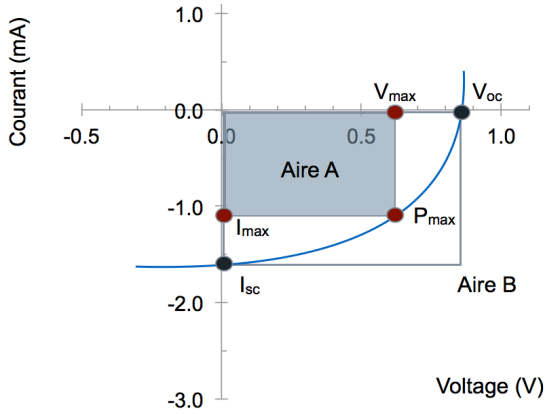

Figure 1.7. Courbe I-V typique obtenue lors de l'illumination d'une cellule photovoltaïque et les principaux paramètres obtenus : Voltage de circuit ouvert (V_{oc}), courant de court-circuit (I_{sc}), puissance maximale (P_{max}), voltage maximal (V_{max}) et courant maximal (I_{max}).

La caractérisation des cellules photovoltaïques se fait généralement à l'aide d'un simulateur solaire permettant de reproduire le spectre solaire dans des conditions contrôlées. Le simulateur solaire est généralement calibré à l'aide d'une cellule de référence certifiée, à une puissance de sortie d'un (1) soleil, c'est-à-dire, 100 $mWcm^{-2}$. Pendant l'illumination contrôlée du dispositif, un balayage du voltage à partir d'une source est effectué et le courant mesuré pour obtenir une courbe de caractérisation I-V (Figure 1.7). Lorsque le voltage est nul, le courant mesuré est égal au courant de court-circuit (I_{sc}). Au voltage correspondant au circuit ouvert (V_{oc}), le courant mesuré est nul. La recherche du carré le plus grand possible au dessus de la courbe (Aire A) permet d'identifier I_{max} et V_{max}. Cette aire comparée à l'aire définie par les paramètres mesurés I_{sc} et V_{oc} (Aire B) donne le paramètre du facteur de forme (FF) (Équation 1.3).

$$FF = \frac{I_{max} \times V_{max}}{I_{sc} \times V_{oc}} \qquad \text{Équation 1.3}$$

Une fois ces paramètres déterminés, le pourcentage d'efficacité à convertir la lumière incidente en électricité (PCE) peut être calculé à partir de l'équation 1.4 en utilisant la puissance lumineuse (P_L) fournie par le simulateur solaire (généralement 100 $mWcm^{-2}$) et la densité de courant mesurée (J_{sc} en $mAcm^{-2}$).

$$\eta = PCE = \frac{P_{sortie}}{P_L} = \frac{\mathbf{J_{sc}} \times V_{oc} \times FF}{P_L} \times 100 \qquad \text{Équation 1.4}$$

Une cellule photovoltaïque peut être représentée par un circuit électrique équivalent, tel que proposé à la Figure 1.8. La génération de charges dérivant à travers la jonction p-n crée un champ électrique qui lui-même crée l'équivalent d'une diode par laquelle un courant de dérive (I_D) est généré, à l'inverse, et contre balançant de la diffusion des électrons et des trous. La cellule n'étant pas une diode parfaite, une résistance de type shunt (R_{SH}) représentant les fuites de courant, ou court-circuit, entre les deux électrodes à travers la couche active, est ajoutée en parallèle. Cette résistance devrait idéalement être infinie. Une seconde résistance en série (R_s) permet de prendre en compte les résistances des contacts métalliques et des pertes ohmiques dans le film. Cette résistance devrait idéalement être nulle (0 ohms). Le courant de sortie disponible pour la charge sera donc égal au total du courant produit par la cellule solaire (I_L) amputé du courant passant par la diode (I_D) et par le courant passant par la résistance shunt (I_{SH}) (Équation 1.5).

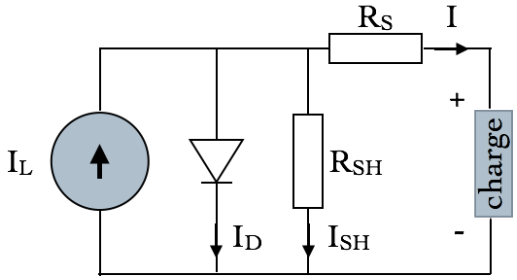

Figure 1.8. Équivalent schématique d'un circuit électrique représentant une cellule photovoltaïque : Courant de sortie (I), courant de travail photogénéré (I_T), courant de diode parfaite équivalente (I_D), courant shunt (I_{SH}), résistance shunt (R_{SH}) et résistance en série (R_S).

$$I = I_L - I_D - I_{SH} \qquad \text{Équation 1.5}$$

Une augmentation de la résistance en série provoquera premièrement une diminution du facteur de forme (FF) et de la puissance maximale (P_{max}), puis une chute du courant de court-circuit (I_{sc}) pour des valeurs plus élevées. Une diminution de la résistance shunt provoque également une diminution du FF, en plus d'une diminution du V_{oc}.

1.3 Diodes organiques émettrices de lumière (OLEDs)

Comme les cellules photovoltaïques organiques décrites auparavant, les diodes organiques sont constituées de composés semi-conducteurs organiques π-conjugués (Figure 1.4) qui, une fois mis en forme en couches minces entre deux électrodes, peuvent émettre de la lumière par électroluminescence. Par contre, la couche active pourra être constituée d'un seul matériau puisque dans ce cas-ci, les électrons seront transmis au dispositif qui transformera l'énergie électrique en énergie lumineuse par l'émission de photons. Il faut se rappeler que les cellules photovoltaïques sont représentées par un circuit équivalent à une diode (Figure 1.8). Ces diodes organiques peuvent donc être perçues, de manière large, comme étant des cellules photovoltaïques fonctionnant à l'envers, où la recombinaison efficace des charges induites par une source électrique externe sera cette fois-ci souhaitée. Par contre, la conception des molécules π-conjuguées utilisées en OLED dépendra directement de la couleur d'émission recherchée, celle-ci étant déterminé par l'énergie de la bande interdite (E_g) tel que défini par l'Équation 1.1.

1.3.1 Premières diodes organiques

Les premiers travaux sur l'électroluminescence à base de films polymère ont été publiés en 1981 par Partridge qui utilisa du polycarbazole contenant du pentachlorure d'antimoine.[43] La première diode organique, basée sur le tris(8-hydroxyquinolinato)aluminium

(Alq3), a été rapportée par Tang et Van Slyke en 1987 alors qu'ils travaillaient chez Eastman Kodak.[16] Par la suite, Burroughes et ses collaborateurs des laboratoires Cavendish présentèrent une diode fabriquée à partir de poly(p-phenylène vinylène) (PPV) en film mince de l'ordre de 100 nm d'épaisseur.[44]

Bien que plusieurs recherches furent dirigées vers l'amélioration du transport des électrons et des trous à travers la couche active par l'ajout de couches favorisant leur transport respectif,[45-47] le gros de la recherche s'est concentré sur l'amélioration et la modification des matériaux de la couche émissive.[48-49]

1.3.2 Principe de fonctionnement

Généralement, une diode organique simple sera constituée d'un matériel semi-conducteur organique juxtaposé entre deux électrodes permettant l'injection de charges. Une électrode transparente est alors utilisée pour permettre la sortie des photons émis. Lorsqu'un courant est appliqué à travers le dispositif, des électrons sont alors injectés dans la LUMO du semi-conducteur organique à partir de la cathode et des trous, résultants du retrait d'électrons à l'anode, sont injectés dans la HOMO. Par la suite, les électrons et les trous diffusent vers l'électrode de collection ou les uns vers les autres sous l'influence du potentiel appliqué et de leur interaction mutuelle par forces de Coulomb, pour former des excitons, une paire électron-trou fortement liée (Figure 1.9). La relaxation de l'électron accompagnée d'une émission d'un photon peut alors survenir lors de sa recombinaison avec le trou de la HOMO.

Si pour les cellules photovoltaïques il est nécessaire d'utiliser des composés ayant une absorption maximisée du spectre solaire et une bande interdite plutôt étroite, pour les diodes organiques il est primordial de contrôler précisément la largeur de E_g. C'est en effet la largeur de la bande interdite qui dicte l'énergie qui sera dispersée lors de la relaxation des électrons présents à l'état excité (HOMO) vers l'état fondamental (LUMO). Cette dispersion énergétique se traduit entre autre par l'émission de photons ayant une longueur d'onde

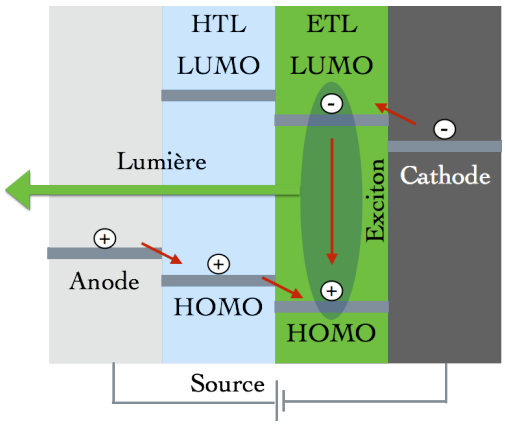

Figure 1.9. Représentation des mouvements des électrons et des trous injectés, à travers les niveaux énergétiques d'une diode organique composée d'une couche transporteur de trous (HTL) et d'une couche transporteur d'électrons (ETL) entre deux électrodes.

correspondante à cette énergie. Il est donc possible pour le chimiste de varier les substituants présents sur un squelette π-conjugués en ajoutant des groupements électro-donneurs ou électro-accepteurs pour en modifier la bande interdite résultante. Par exemple, l'ajout de groupements électro-donneurs de type alkoxy sur le polymère PPV utilisé par Burroughes et al. (Figure 1.3b) fera passer le λ_{max} d'émission du polymère de 566 nm[44] à 587 nm et la couleur d'émission du jaune-vert au orange.[50] L'ajout de chaines alkyles permet également de rendre le polymère plus soluble dans les solvants organiques, ce qui donne l'opportunité de les inclure dans des formulations propres à l'imprimerie et facilite grandement leur mise en forme en films minces. La présence de groupements encombrants permettant de tordre le squelette π-conjugué hors du plan de recouvrement orbitalaire fera également élargir E_g pour donner des émissions à des longueurs d'ondes plus basses. Finalement, la compétition des mécanismes de relaxation de l'électron à travers les dégénérescences des orbitales π* dictera finement les pertes énergétiques non radiatives possibles, résultant en des émissions de photons possédant des énergies plus faibles et des longueurs d'onde d'émission affligées d'un déplacement bathochrome.

1.4 Avantages et inconvénients de l'utilisation de matériaux organiques pour la réalisation de dispositifs électroniques

Que ce soit pour la réalisation de cellules photovoltaïques, de diodes électroluminescentes ou des transistors, l'utilisation de matériaux organiques procure certains bénéfices non négligeables. Comme ces dispositifs sont constitués de films organiques très minces de l'ordre de 100-300 nm, il est possible de les mettre en forme sur des substrats flexibles qui permettent de réaliser, par exemple, des écrans ou des panneaux solaires enroulables,[51-52] portables et ultralégers par rapport aux dispositifs équivalents basés sur des matériaux inorganiques. La possibilité de les imprimer à partir de solutions à température de la pièce par des techniques de hauts débits, comme par exemple l'impression à jet d'encre, la sérigraphie ou le procédé 'roll-to-roll', permettra de fabriquer de larges surfaces actives à bas couts, autant en termes énergétiques que des matériaux.[53-55] Les cellules photovoltaïques organiques permettent également de meilleurs rendements en éclairage faible ou lorsque exposées à un rayonnement à larges angles d'incidence. Par contre, leurs plus faibles rendements (Figure 1.2) et leur durabilité limitent présentement leur déploiement commercial. Il est certain que ces dispositifs participeront de plus en plus activement dans le futur au développement durable de notre société.

1.5 Objectifs de cette thèse

Premièrement, un laboratoire permettant de réaliser des dispositifs électroniques à base de semi-conducteurs organiques et de faire leur caractérisation devait être monté de toute pièce à l'Université de Montréal. Les détails sur l'instrumentation, le design sur mesure des différentes composantes et le montage du laboratoire se retrouvent à l'Annexe 1. Par la suite, la réalisation de dispositifs simples à base de matériaux connus devait permettre de valider les procédés impliqués dans le dépôt de couches, dans la manufacture des dispositifs et dans leur caractérisation. L'apprentissage des différentes techniques et leur maitrise devait permettre avant toute chose de pouvoir obtenir des résultats valides et reproductibles.

Plusieurs nouveaux matériaux font leur apparition sur la scène de l'électronique organique chaque année et les petites molécules remplaçant les traditionnels polymères utilisés depuis déjà plusieurs années semblent promettre certains avantages face à leurs homologues. Un des objectifs de ce travail est de concevoir une nouvelle gamme de petites molécules organiques π-conjuguées de type p (donneur) semi-conducteurs, à partir de certains concepts connus dans la littérature, puis de les étudier à l'intérieur de couches actives dans des cellules photovoltaïques.

Si plusieurs paramètres entrent en ligne de compte pour l'optimisation des rendements provenant de matériaux donnés, il est important de savoir comment ceux-ci se comportent les uns par rapport aux autres dans des conditions données. La compréhension du rôle des agencements moléculaires et la proposition de stratégies permettant un certain contrôle des morphologies de ces films minces actifs basés sur de nouveaux matériaux à bandes interdites étroites sont parmi les objectifs principaux de ce travail. Les caractérisations adaptées à ces systèmes et matériaux dans leurs différentes formes sont également explorées, complétant ainsi les buts principaux de ces recherches en matière de matériaux.

L'industrie et les recherches actuelles en électronique organique reposent beaucoup sur des matériaux inorganiques qui peuvent être rares et dispendieux tel l'indium et l'étain (700 $US et 15 US$ par kilo respectivement, sur le marché actuel), qui entre dans la composition des électrodes transparentes. Les dispositifs présentés dans cette thèse ont tous été réalisés sur des substrats de verre recouverts d'une électrode d'oxydes d'indium et d'étain (ITO). Un des sous-objectifs de ce travail est donc d'explorer des solutions de recyclage de ces substrats pour permettre de limiter les couts de la recherche et offrir une véritable solution eco-viable en matière de dispositifs électroniques.

Ce travail se concentre donc sur les matériaux composant la couche active de cellules photovoltaïques organiques ou de diodes électroluminescentes organiques plutôt que sur l'optimisation de l'architecture des dispositifs. Les rendements sont donc mis en valeur

relativement aux résultats globaux et n'impliquent pas nécessairement des valeurs maximales pour un matériau donné.

Chapitre 2

Molécules à bandes interdites étroites utilisées dans les cellules photovoltaïques à base de matrices polymères

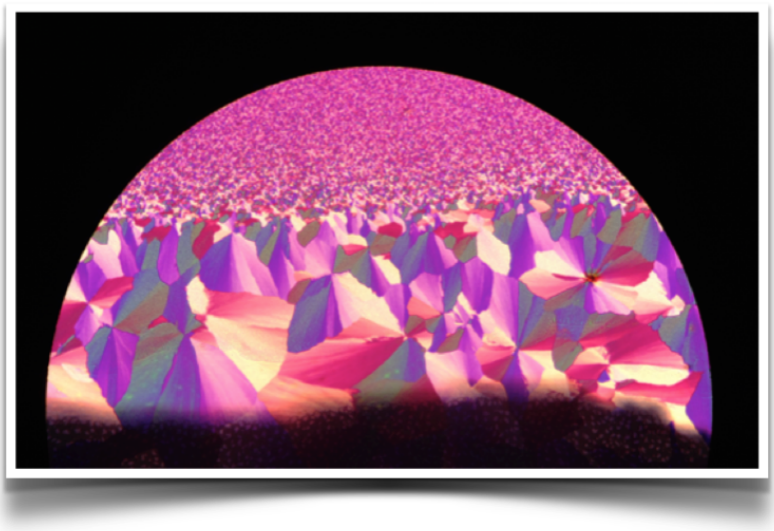

« Ls D0° » – Cristaux du $IF(BTC)_2$ sous lumière polarisée

2.1 Introduction Article 1

Les cellules photovoltaïques organiques sont généralement composées de polymères semi-conducteurs en couches minces, mais l'utilisation de petites molécules organiques π-conjuguées à bandes interdites étroites comme donneurs a récemment suscité un engouement certain pour remplacer les polymères.[56-57] En effet, ces petites molécules sont généralement plus faciles à reproduire d'un lot à l'autre puisqu'elles ont des structures bien déterminées. Ceci élimine ainsi certaines variables importantes pour la mise en forme régulière de ces matériaux en films minces, tel les limites de solubilité et la viscosité des solutions résultantes. Une gamme particulière de petites molécules, possédant à la fois un groupement électro-donneur et un groupement électro-attracteur en configuration "push-pull" et généralement fortement π-conjuguées, ont récemment faites leur apparition.[36, 58-59] Un design planaire favorisant le recouvrement des orbitales π et une conjugaison maximisée procurera un spectre d'absorption pouvant englober le plus possible le spectre solaire et favoriser de hauts rendements par une génération soutenue de charges. Ces molécules sont couplées à un matériau de type n à l'intérieur d'une couche active, pour ainsi créer une ou des jonctions p-n lorsque utilisées dans une architecture de type hétérojonction de masse.[35-37] Les dérivés de fullerènes C_{60} ou C_{70}, particulièrement les dérivés [6,6]-phényl-C_{61}-butanoate de méthyle ($PC_{61}BM$) ou [6,6]-phényl-C_{71}-butanoate de méthyle ($PC_{71}BM$) sont souvent utilisés comme accepteurs[37] de part leur forte propension à accepter des électrons. Leur géométrie est composée de cycles à cinq et six carbones, hybridés sp2. Par contre, la délocalisation des électrons à travers la structure est limitée et les fullerènes sont généralement définis comme des alcènes électro-déficients.[60]

Si les petites molécules font promesses de régularité structurelle, il n'en va pas de même pour leur applicabilité en films minces.[61] La production de petites cellules photovoltaïques en laboratoire par évaporation thermique n'est pas toujours simple et ne permet pas de couvrir de vaste surfaces, limitant l'avenir de l'évaporation pour déposer ces molécules au niveau commercial. Des matériaux pouvant être mis en forme à partir de

solutions sont favorisés pour pouvoir les appliquer grâce à des techniques de hauts débits comme la sérigraphie et la technique “Roll-to-Roll”.

Ce chapitre présente les concepts et les synthèses de deux nouvelles molécules de type “push-pull” à bandes interdites étroites basées sur les groupements attracteurs dicyanovinyles et les groupements donneurs indénofluorène ou indénobithiophène. Leurs mises en forme en films minces assistées par des matrices polymériques sont explorées pour tenter de rectifier leur manque de propension à former des films homogènes. Pour ce faire, le p3HT-RR (poly(3-hexylthiophène-2,5-diyl, régio-régulier)[62] et le PCDTBT (poly[[9-(1-octylnonyl)-9*H*-carbazole-2,7-diyl]-2,5-thiophènediyl-2,1,3-benzothiadiazole-4,7-diyl-2,5-thiophènediyl])[63], deux polymères semi-conducteurs reconnus pour leurs aptitudes en cellules photovoltaïques, seront utilisés pour leur capacités à transporter des charges et former des films continus et homogènes.[64-65]

2.2 Article 1

Low-Bandgap Push-Pull Molecules in Polymer Matrices for Use in Thin-Film Organic Photovoltaic Devices

Pierre-Louis M. Brunner, Daniel Beaudoin, Alice Heskia, Thierry Maris, Marc-André Dubois et James D. Wuest

Solar Energy Materials and Solar Cells, **2016**, soumis pour publication.

2.2.1 Keywords

Keywords: organic solar cells, low bandgap materials, push-pull small molecules, thin film morphologies, polymer matrices

2.2.2 Abstract

Conjugated polymers are widely used in current thin-film organic photovoltaic devices to absorb light and serve as electron donors or acceptors, but small molecular analogues are attractive substitutes because they have fully defined structures, can be purified rigorously, and are typically more soluble and volatile. However, producing active films composed primarily of small molecules remains challenging. We have devised bulk heterojunction solar cells in which poly(3-hexylthiophene-2,5-diyl) (P3HT) and poly[[9-(1-octylnonyl)-9*H*-carbazole-2,7-diyl]-2,5-thiophenediyl-2,1,3-benzothiadiazole-4,7-diyl-2,5-thiophenediyl] (PCDTBT) are used as matrices to yield films containing low-bandgap push-pull molecules as electron donors and [6,6]-phenyl-C_{61}-butyric acid methyl ester ($PC_{61}BM$) or [6,6]-phenyl-C_{71}-butyric acid methyl ester ($PC_{71}BM$) as electron acceptors. Compared with reference devices, increases in power-conversion efficiencies (PCE) up to 30.4% were measured, due mainly to higher values of short-circuit current density (J_{sc}), fill factor (FF), and open-circuit voltage (V_{oc}).

2.2.3 Introduction

With sustained global economic growth and a swelling world population, the international consumption of energy is projected to rise over 50% by 2040, reaching the equivalent of nearly 150 billion barrels of crude oil per annum.[1]

Meeting this projected need will require increased reliance on solar energy reaching the earth. The production of photocurrent from sunlight, first observed by Becquerel in 1839,[2] allows solar energy to be collected and converted into a useful form. However, energy derived from current photovoltaic devices remains more expensive than energy derived from fossil fuels, which meet more than 80% of our current need for power.[1] A worldwide effort to devise cheap, efficient, lightweight, and flexible sources of solar power has begun to focus on devices composed of thin layers of molecular materials, first reported by Tang in 1986.[3] These organic photovoltaic devices (OPVs) are evolving rapidly, and large-scale commercialization is becoming economically feasible. Notably, the benchmark of 10% in power-conversion efficiency (PCE) has been surpassed, and the latest record of 13.2% has been reached by Heliatek.[4]

Conjugated polymers are widely used in current thin-film OPVs to absorb light and serve as electron donors or acceptors, but small molecular analogues are attractive substitutes because they have fully defined structures, can be purified rigorously, and are typically more soluble and volatile.[5-9] Of particular interest in the development of small-molecule components are so-called "push-pull" compounds, which have conjugated structures consisting of π-bridged electron-donating and electron-accepting moieties (D-π-A). Such compounds exhibit intramolecular charge transfer (ICT),[10-12] and their absorption spectra can be broadened and shifted to match the solar spectrum.[7, 8, 13] As a result, push-pull compounds have been widely employed in thin-film OPVs with bulk heterojunction (BHJ) architectures,[14-18] using derivatives of fullerenes as the electron acceptors.[8]

Single molecules have well-defined structures and are monodisperse; moreover, they offer better batch-to-batch consistency than polymers, are typically easier to purify, and allow for the rapid creation of larger libraries of finely tuned derivatives. However, processing small molecules to create thin films for use in organic electronics can be challenging.[19] Small molecules can sometimes be deposited in thin films by solvent-free low-throughput methods such as thermal evaporation. This technique may be acceptable for manufacturing small displays, but the coverage of larger areas requires blading, roll-to-roll printing, offset printing, or other techniques, and solution-processable compounds are needed.

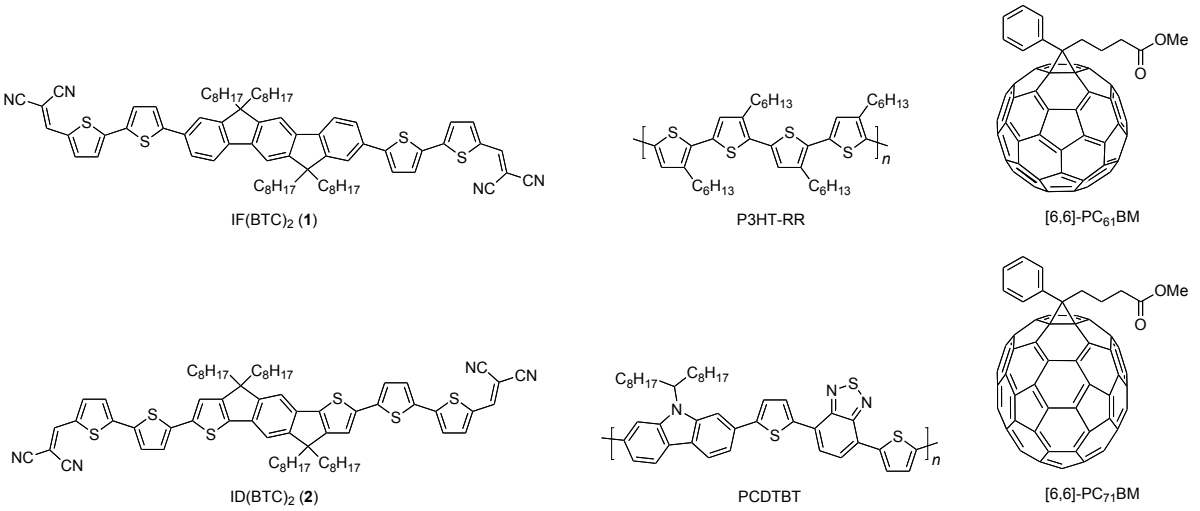

Figure 2.1. Structures of $IF(BTC)_2$ (1) and $ID(BTC)_2$ (2), as well as other key materials used in OPVs. C_6H_{13} and C_8H_{17} denote straight alkyl chains in all figures and schemes.

The present work examines OPVs that incorporate novel D-π-A "push-pull" compounds $IF(BTC)_2$ (**1**) and $ID(BTC)_2$ (**2**), in which dicyanovinyl groups serve as electron-withdrawing moieties, and indeno[1,2-*b*]fluorene or *s*-indaceno[1,2-*b*:5,6-*b*']dithiophene units linked to bithiophenes act as electron-donating components (Figure 2.1). Both compounds are highly soluble in various solvents, but their ability to form stable uniform thin films is mediocre. For this reason, they were added to known semiconducting polymers in various

ratios in attempts to make matrices more suitable for producing thin films. Regioregular (RR) poly(3-hexylthiophene-2,5-diyl) (P3HT) and poly[[9-(1-octylnonyl)-9*H*-carbazole-2,7-diyl]-2,5-thiophenediyl-2,1,3-benzothiadiazole-4,7-diyl-2,5-thiophenediyl] (PCDTBT) were used as active matrices known for their ability to transport charges as thin films (Figure 2.1).[20,21] To our knowledge, these polymers have not previously been used in OPVs in conjunction with small active molecules, although P3HT has been used with small molecular additives in transistors to increase the mobility of thin films.[21]

2.2.4 Material and Methods

2.2.4.1 Active materials

$IF(BTC)_2$ (**1**) and $ID(BTC)_2$ (**2**) were synthesized by the routes shown in Scheme 1. P3HT, PCDTBT, $PC_{61}BM$, and $PC_{71}BM$ were provided by Solaris Chem Inc. and used as received. 2,2'-(6,6,12,12-Tetraoctyl-6,12-dihydroindeno[1,2-*b*]fluorene-2,8-diyl)bis(4,4,5,5-tetramethyl-1,3,2-dioxaborolane) (**3**)[22], 4,9-dihydro-*s*-indaceno[1,2-*b*:5,6-*b*']dithiophene[23], and 5-bromo-2,2'-bithiophene[24] were prepared according to reported procedures. The detailed synthesis of $IF(BTC)_2$ (**1**) and $ID(BTC)_2$ (**2**) are provided in the supporting information section.

2.2.4.2 Cyclic voltammetry

Cyclic voltammetry (CV) was carried out using a BASi C3 cell stand with a glassy carbon working electrode, an Ag/Ag^+ ($AgNO_3$) reference electrode, and a platinum counter electrode. Tetrabutylammonium hexafluorophosphate (99.0%, Aldrich), recrystallized from deionized water and vacuum dried, was used as the supporting salt. Analytes were dissolved in THF (30 mg mL^{-1}), coated on the carbon glassy working electrode by dipping, and allowed to dry for 5 min under N_2. Scans were taken at the rate of 25 mVs^{-1} using ferrocene as the internal reference. The standard reduction potential of ferrocene ($E^o_{Fc+/Fc}$ = 0.64 V vs the

standard hydrogen electrode (SHE))[25] was measured at +0.09 V versus an Ag/Ag^+ reference electrode ($E^o_{Ag/Ag+}$ = 0.23 V vs SHE)[26] with a SHE absolute potential, $E^o_{(H+/H2)}$ ^{H_2O} (abs) = 4.44 ± 0.02 eV),[27] using a glassy carbon working electrode. The HOMO and LUMO energy levels were calculated from the oxidation and reduction onset values of the first scan.[28] For both compounds **1** and **2**, film decomposition was observed after each scan.

2.2.4.3 Calculations using time-dependent density functional theory (TD-DFT)

GAUSSIAN 03 was used to fully optimize the geometries of compounds **1** and **2** at the DFT level of theory, employing the hybrid functional PBE0[29] and a 6-311G basis set. The optimized geometries then allowed the absorption spectra to be calculated by TD-DFT, using the hybrid PBE0 functional with a 6-311++G** basis set. The PBE0 functional was chosen for its established applicability to calculations of excited states.[30]

2.2.4.4 Crystallographic studies

Data for structural analyses were collected using a Bruker-X8 Microstar diffractometer equipped with an FR591 rotating anode generating Cu Kα radiation. Crystals of compound **1** (grown from 2-methoxyethanol) were studied at 100 K, and crystals of analogue **2** (grown from ethanol) were studied at 150 K. Determinations of initial unit-cell lattice parameters were performed with the *APEX2* suite of software, and final lattice parameters and integrated intensities were calculated after data integration using the *APEX2* and *SAINT* software.[31] A multiscan absorption correction was applied using *SADABS*.[32] Structures were solved and refined using the SHELX suite of software (Version 2013)[33] within the graphical user interface of *OLEX2*.[34]

CCDC 1023521 and 1023522 contain the supplementary crystallographic data for this paper. These data can be obtained free of charge from The Cambridge Crystallographic Data Centre via www.ccdc.cam.ac.uk/data_request/cif.

2.2.4.5 Fabrication, characterization, and testing of OPVs

Bulk heterojunction OPVs were fabricated using a glass/ITO/PEDOT:PSS/polymer:SM:PCBM/Al architecture. Custom-made ITO substrates (20 × 18 mm^2, with a standard resistivity of 20 Ω per square) were purchased from Colorado Concept Coatings LLC. Current density-voltage (J-V) measurements were carrie`d out using a computer-controlled Keithley Model 236 Source-Measure Unit. The source of light was a 150 W Oriel solar simulator using a xenon arc lamp with an AM 1.5 filter. The incident optical power at the height of the sample was assessed at 100 $mWcm^{-2}$ with the aid of a monocrystalline Si photovoltaic reference cell provided by PV Measurements Inc. and calibrated by the National Renewable Energy Laboratory. To avoid overestimations, the photovoltaic performance of cross-bar circular-island cells was determined using a circular shadow mask with an aperture corresponding to the active area of the devices (12.6 mm^2).[35-36] Statistical analyses of data are based on measurements using eight different devices.

OPVs were fabricated in the following way. ITO-coated glass substrates were cleaned by sequential 15 min ultrasonic treatments in deionized water, acetone, and isopropanol, followed by exposure in a UV-ozone cleaner for 15 min. Aqueous dispersions of PEDOT:PSS (Clevios PH 1000, Heraeus) were filtered through a 0.45 μm Teflon membrane and spin coated at 4000 rpm for 90 s on the cleaned ITO-coated glass substrates. The resulting films were baked at 110 °C for 20 min in air. A film thickness of 30 ± 4 nm was measured by profilometry, using a Dektak 3030ST stylus profilometer. Solutions of the components of the active layer in 1,2-dichlorobenzene were prepared under N_2 in a glove box by gentle stirring at 40 °C on a hot plate for at least 2 h. The resulting solutions were spin coated on top of the underlying PEDOT:PSS layer at 1000 rpm for 90 s, with acceleration to the final speed achieved over 10 seconds. The thicknesses of the active layers were determined using atomic force microscopy (AFM). Cathodes (100 nm) were then applied by thermal evaporation of Al (99.999% pure pellets from Kurt J. Lesker Company) onto the active layer under reduced pressure (10^{-6} mbar) through a shadow mask at a rate of 1-2 Å s^{-1}. All thicknesses and deposition rates were determined using a quartz crystal thickness monitor. The circular active

cell area was determined to be 12.6 mm^2. Post-fabrication thermal treatments were conducted under N_2 in a glove box equipped with a hotplate, using various temperatures and times of annealing.

2.2.4.6 Imaging

AFM images were acquired in air at room temperature using a Digital Instruments EnviroScope (Santa Barbara, CA) and a Nanoscope IIIa controller (Veeco/Bruker). Imaging with intermittent contact ("tapping mode") was performed at a scan rate of 1 Hz using etched Si cantilevers (ACTA, Applied NanoStructures, Inc.) with a resonant frequency of around 300 kHz, a spring constant of approximately 42 N m^{-1}, and a tip radius of <10 nm. All AFM images were acquired with a medium tip oscillation damping (20-30%).

Transmission electron microscopy (TEM) was carried out using a JEOL JEM-2100F microscope operated at 200 kV for bright-field imaging of samples. Detached samples of thin films were prepared by a new method,[37] in which materials are deposited by spin coating on various polished surfaces. Subsequent thermal annealing was done in the way used to process completed OPVs. Detached films were floated off the underlying solid surface and allowed to settle on a standard 100 mesh Cu grid, which was dried prior to imaging. Further annealing experiments could be carried out directly on the Cu grid.

2.2.5 Results and Discussion

2.2.5.1 Syntheses of small molecules 1 and 2

$IF(BTC)_2$ (**1**) was prepared from 2,2'-(6,6,12,12-tetraoctyl-6,12-dihydroindeno[1,2-*b*]fluorene-2,8-diyl)bis(4,4,5,5-tetramethyl-1,3,2-dioxaborolane) (**3**)[22] by the route set out in Scheme 2.1a. Suzuki coupling with 5-bromo-2,2'-bithiophene,[24] followed by Vilsmeier-Haack formylation and condensation with malononitrile, provided the desired compound in 39%

overall yield as a red solid. Analogue ID(BTC)$_2$ (**2**) was synthesized in 31% overall yield as a purple solid by the related route summarized in Scheme 2.1b, starting from 4,9-dihydro-4,4,9,9-tetraoctyl-*s*-indaceno[1,2-*b*:5,6-*b*′]-dithiophene (**7**).

Scheme 2.1. Synthesis of small molecules 1 (a) and 2 (b). C_8H_{17} denotes straight alkyl chains.

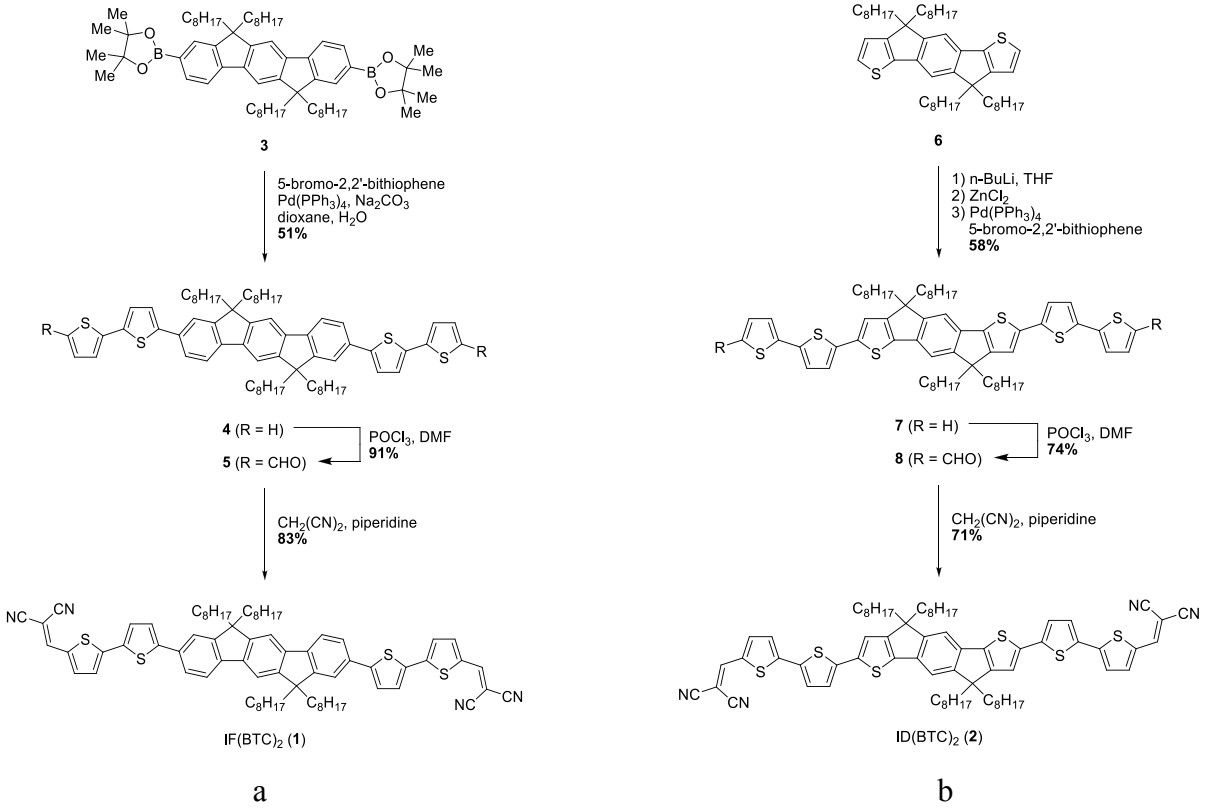

2.2.5.2 Properties of small molecules 1 and 2

The conjugated push-pull design of small molecules **1** and **2** provided compounds with relatively low molecular weights and low bandgaps, as determined by cyclic voltammetry[28] and UV-vis spectroscopy (Table 1). The compounds were determined to have electronic bandgaps (E^{elec}_g) of 2.64 and 2.42 eV, respectively, by cyclic voltammetry. Their HOMO and

Table 2.1. Electronic properties of **1** and **2**.

SM	E^{ox} [V][a)]	E^{red} [V][b)]	HOMO [eV][c)]	LUMO [eV][d)]	E^{elec}_g [eV][e)]	E^{opt}_g [eV][f)]	E^{est}_g [eV][g)]	E^{cal}_g [eV][h)]	F [A.U.][i)]
1	+0.52	-2.13	-5.28	-2.63	2.64	2.05	2.45	2.58	2.08
2	+0.42	-2.00	-5.18	-2.76	2.42	1.77	2.17	2.33	1.93

[a, b] Determined by cyclic voltammetry using films on glassy carbon electrodes,[24] with redox potentials vs Ag/Ag^+ measured in MeCN containing NBu_4PF_6; [c] HOMO calculated as $E_{HOMO} = -(E^{ox} + 4.76)$ eV; [d] LUMO calculated as $E_{LUMO} = -(E^{red} + 4.76)$ eV; [e] Electronic bandgap (E_{LUMO} - E_{HOMO}); [f] Optical bandgap, as determined using UV-Vis-NIR absorption of films (Figure 6); [g] Electronic bandgap estimated from the optical bandgap and excitonic binding energy (E^{opt}_g + 0.40) eV[38-39]; [h] Bandgap calculated by TD-DFT, using the hybrid PBE0 functional with a 6-311++G** basis set; [I] Oscillator strength (F)

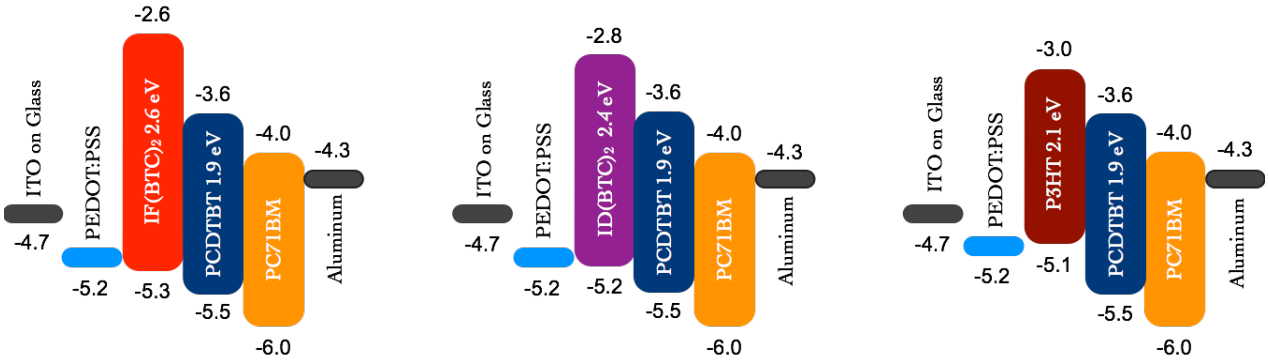

ITO/PEDOT:PSS/(**1**):PCDTBT/$PC_{71}BM$/Al — a

ITO/PEDOT:PSS/(**2**):PCDTBT/$PC_{71}BM$/Al — b

ITO/PEDOT:PSS/P3HT:PCDTBT/$PC_{71}BM$/Al — c

Figure 2.2. Representation of the relative positions of the HOMOs and LUMOs of components of the proposed OPVs, as well as the sequence of layers that defines the architecture of devices containing (a) $IF(BTC)_2$ (**1**), (b) $ID(BTC)_2$ (**2**), and (c) P3HT. ITO is indium tin oxide, and PEDOT:PSS is poly(3,4-ethylenedioxythiophene): poly(styrenesulfonate).

LUMO energy levels were found to lie in a range suitable for efficient operation of photovoltaic devices containing PCBMs and the polymer matrices, assuming an excitonic binding energy of 0.4 eV (Figure 2.2).[40-41] Deep HOMO energy levels were measured,

assuring high values of V_{oc} ($HOMO_{donor}$ – $LUMO_{acceptor}$). Because the measured optical bandgap (E^{opt}_{g}) reflects the difference in energy of the excitonic levels S^0 and S^1, an excitonic binding energy of 0.4 eV was added.[38, 42] Values of the estimated bandgap, E^{est}_{g}, were thereby determined from E^{opt}_{g} to be 2.45 eV and 2.17 eV for small molecules **1** and **2**, respectively. In addition, calculations using time-dependent density functional theory (TD-DFT), based on the hybrid PBE0 functional with a 6-311++G** basis set, were carried out to determine the HOMO and LUMO energy levels of analogues in which the octyl chains are replaced by methyl groups. The calculated bandgaps (E^{cal}_{g}), which were determined to be 2.58 eV and 2.33 eV for analogues of compounds **1** and **2**, respectively, are in acceptable agreement with the experimental values derived from cyclic voltammetry and spectroscopy. As expected, the TD-DFT calculations indicate that for both compounds **1** and **2**, the HOMO and LUMO are concentrated on the central donor unit and on the terminal acceptor unit, respectively (Figure 2.3).

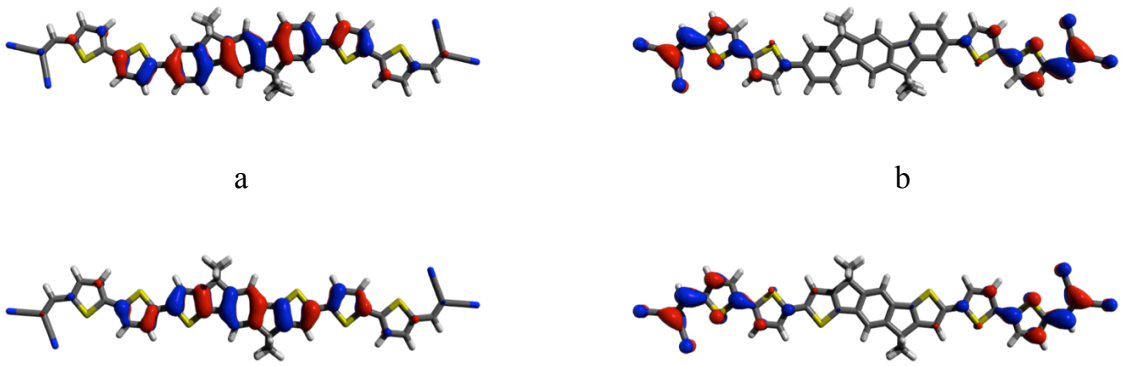

Figure 2.3. Molecular orbitals determined by TD-DFT calculations (PBE0/6-311++G**). (a) HOMO for model of $IF(BTC)_2$ (1). (b) LUMO for model of compound 1. (c) HOMO for model of $ID(BTC)_2$ (2). (d) LUMO for model of compound 2.

X-ray crystallographic studies can provide invaluable information about the molecular structure and organization of the components of OPVs, but such analyses are not routinely carried out, particularly when the components have complex structures with multiple long alkyl groups to enhance solubility. We were able to crystallize small molecules **1** and **2** from

2-methoxyethanol and ethanol, respectively, and their structures were resolved (Figure 2.4). As planned, the thiophene-substituted indacenodithiophene core of compound **2** is flatter and more highly conjugated than the corresponding indenofluorene core of compound **1**. Of particular note are the angles between the aromatic rings at the junctions between the 2,2'-bithiophene units and the rigid fused central aromatic cores, which lie in the range 15.21-30.02° in compound **1**, whereas the value is only 6.35° in analogue **2**. The conformational differences seen in the crystalline state presumably reflect preferences in solution as well, thereby leading to increased conjugation in compound **2** and a smaller bandgap.

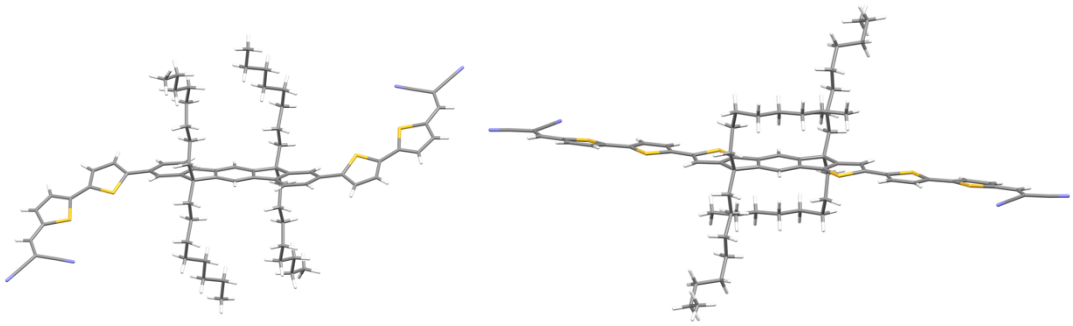

a b

Figure 2.4. Representations of molecular structures determined by X-ray diffraction. (a) $IF(BTC)_2$ (1) as crystallized from 2-methoxyethanol. (b) $ID(BTC)_2$ (2) as crystallized from ethanol. In both images, atoms of carbon are shown in gray, atoms of hydrogen in white, and atoms of sulfur in yellow. The unit cell of compound 1 includes two slightly different conformations, and only one is shown.

The flattened extended geometries of the cores, together with specific intermolecular interactions, help determine the overall molecular organization. In particular, the geometries favor packing in sheets, with interdigitated octyl chains and parallel cores held together in part by π-stacking (Figure 2.5). Such stacking creates an opportunity for extended intermolecular electronic interactions in the solid state, as well as in molecular aggregates in solution. In both structures, adjacent sheets are joined by short CH···NC interactions. In the case of compound **1**, the length of these interactions lies in the range 2.373-2.412 Å, whereas in the case of analogue **2** the value is 2.594 Å.

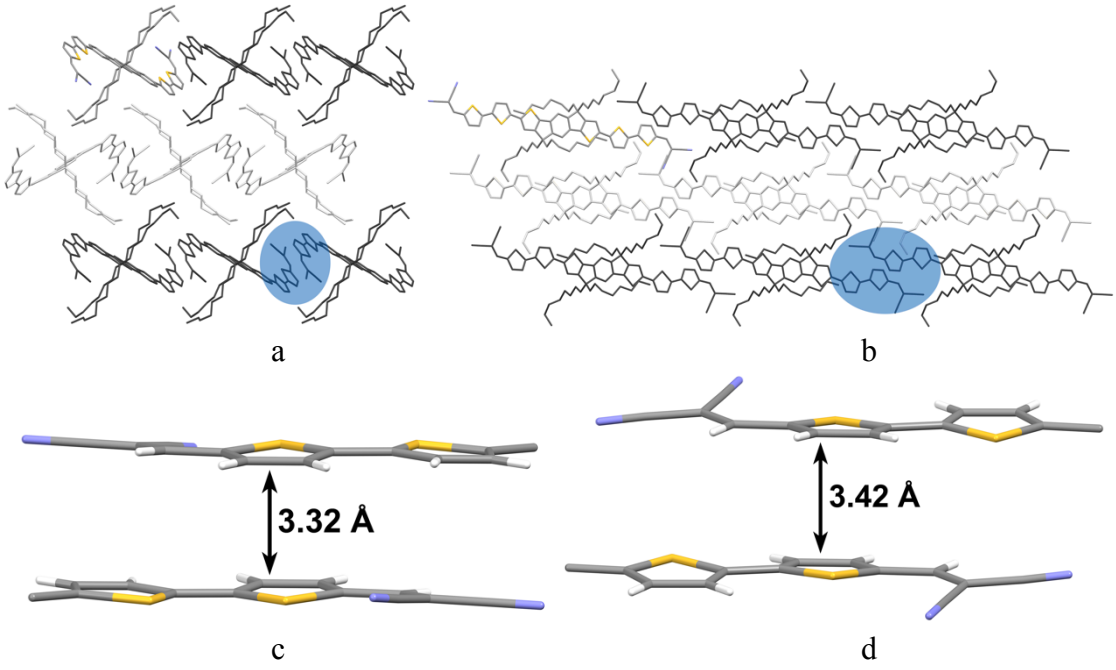

Figure 2.5. Representations of the sheet structures of 1 and 2, as determined by using X-ray diffraction to analyze crystals grown from 2-methoxyethanol and ethanol, respectively. In Figure 2.5a and 2.5b, adjacent π-stacked ribbons are highlighted in dark and light gray, and atoms of hydrogen are omitted for clarity. (a) View along the *a* axis showing a top view of a sheet composed of 1 and underscoring (in blue) π-stacking within ribbons in a single sheet. (b) Detailed view of π-stacking in the structure of 1. (c) View along the *b* axis illustrating a top view of a sheet composed of 2 and highlighting (in blue) π-stacking within ribbons in a single sheet. (d) Detailed representation of π-stacking in 2.

Both small molecular compounds proved to be visibly solvatochromic, as shown by UV-Vis-NIR spectra in various solvents,[28] and both are soluble in solvents with varying degrees of polarity, ranging from hexane and cyclohexane (with dielectric constants of about 2) to simple alcohols and acetone (with dielectric constants of approximately 20).[39] Intramolecular charge transfer between the push-pull units was facilitated in polar solvents, leading to red shifts in absorbance as previously observed in conjugated 2-aminobithiophenes.[43] These distinctive properties of wide solubility and solvatochromism may

allow compounds **1** and **2** to be formulated as versatile inks in combination with various other components.

UV-Vis-NIR spectra of films of small molecules **1** and **2** on glass displayed absorption maxima at 515 nm and 588 nm, respectively (Figure 2.6). Again, the distinct bathochromic shift in the case of **2** (73 nm) presumably results in part from its flattened conformation. In addition, Figure 2.6 provides images of films of compounds **1** and **2** in reflection and transmittance modes. As in typical metallic and semiconducting materials with valence electron plasmas,[44] shiny metallic lusters can be observed for both compound **1** (golden luster) and analogue **2** (copper luster). This characteristic appearance can be rationalized by noting that the distinctive lusters of metallic gold and copper arise from interband transitions at 539 nm and 590 nm, respectively,[45] which are very close to the transitions of compounds **1** and **2**.

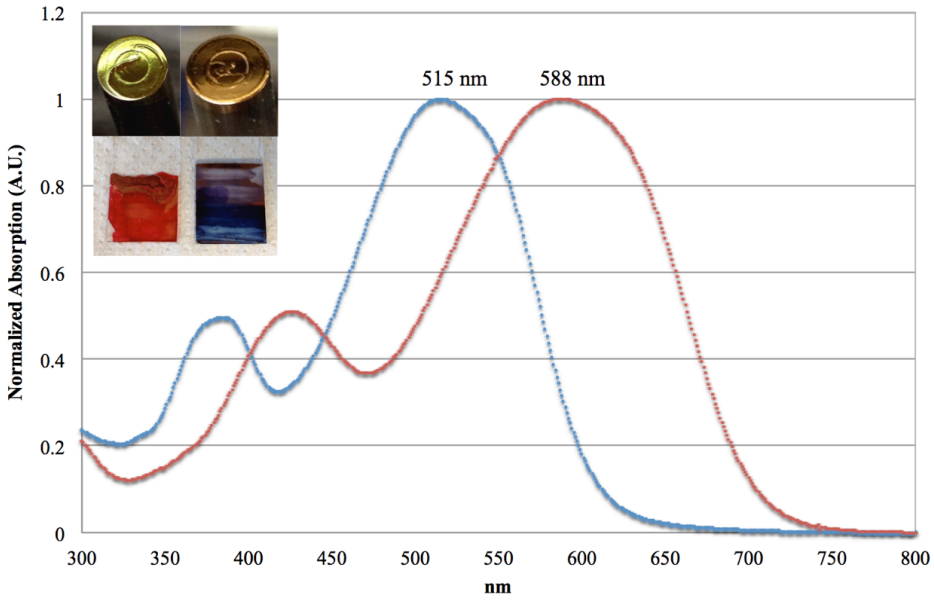

Figure 2.6. UV-Vis-NIR absorption spectra of films of 1 (blue) and 2 (red), deposited on glass by evaporation from solutions in THF. The inserted images show the films in reflection mode (upper pair) and transmittance mode (lower pair), with 1 on the left and 2 on the right.

2.2.6 Photovoltaic Devices

Both small molecules **1** and **2** were tested as the active electron donors and main light-harvesting components in OPVs containing $PC_{61}BM$ and $PC_{71}BM$ as the electron acceptors.[46] The devices featured a standard architecture (glass/ITO/PEDOT:PSS/SM:PCBM/Al, where SM = small molecule) and were fabricated using conventional methods. The power-conversion efficiency (PCE) of the devices was studied as a function of the SM/PCBM ratio, the thickness of the film, and the temperature and time of annealing. The results are reported in Table 2.2. The highest values of PCE obtained for devices containing compounds **1** and **2** were 0.06% and 1.40%, respectively, using $PC_{71}BM$ as the electron acceptor. The optimal values of PCE were attained using SM:fullerene ratios of 1:1 by weight, with no annealing and with film thicknesses of 120±10 nm in both cases. These cells displayed open-circuit voltages (V_{oc}) that were lower than expected and relatively low fill factors (FF). The short-circuit current densities (J_{sc}) measured for devices containing compound **2** were similar to those of standard all-polymer reference cells containing P3HT:$PC_{61}BM$, but the values of J_{sc} were very low in the case of compound **1**. Together, these data suggest that films composed of SM:PCBM are of poor quality, with high series resistance (R_s) and low shunt resistance (R_{sh}), leading to inefficient cells with low values of FF, as observed in other devices in which small molecules are primary components of the active layers.[47]

To improve the quality of the films and achieve higher values of PCE, we blended small molecules **1** and **2** with $PC_{71}BM$ in a matrix of P3HT (M_w: 60 kDa, polydispersity index (PDI) 1.5). The ratio of mixed donor to acceptor ($PC_{71}BM$) was maintained at 1:1 by weight, and the ratio P3HT:SM was varied from 0:1 to 1:0. The thickness of the films was kept constant by adjusting the overall concentration of the components dissolved in 1,2-dichlorobenzene. This required increasing the concentration of SM and $PC_{71}BM$ when lowering the amount of P3HT. Because devices containing 1:1 P3HT:$PC_{71}BM$ were used as a benchmark for assessing the performance of modified cells containing SM, standard post-fabrication annealing was carried out at 150 °C for 20 min. The resulting values of V_{oc}, J_{sc}, FF, and PCE are summarized in Table 2.2. When fabricated without annealing, devices containing

Table 2.2. Performance of OPVs incorporating active layers containing various amounts of **1** or **2** in P3HT or PCDTBT, with $PC_{61}BM$ or $PC_{71}BM$ as electron acceptors. Unless indicated otherwise, the devices are unannealed.

SM	Polymer	Acceptor	SM (%)	V_{oc} (mV)	J_{sc} (mA/cm^2)	FF (%)	PCE_{max} (%)	PCE Gain (%)	Film RMS (nm) [c),d)]
-	P3HT	$PC_{61}BM$	0	584	8.04	54.8	2.58[a), b)]	-	-
-	P3HT	$PC_{71}BM$	0	640	8.31	56.9	3.03[a)]	-	-
-	PCDTBT	$PC_{61}BM$	0	827	6.80	47.8	2.92	-	-
-	PCDTBT	$PC_{71}BM$	0	845	8.85	50.8	3.49	-	0.83
1	-	$PC_{61}BM$	100	478	0.45	28.1	0.05	-	-
1	-	$PC_{71}BM$	100	360	0.61	24.7	0.06	-	1.78
1	P3HT	$PC_{61}BM$	10	629	7.02	58.1	2.57[a)]	-	-
1	P3HT	$PC_{71}BM$	50	528	1.69	32.1	0.28	-	-
1	P3HT	$PC_{71}BM$	50	604	3.37	41.2	0.84[a)]	-	-
1	PCDTBT	$PC_{61}BM$	25	834	6.72	52.5	3.04	4.1	-
1	PCDTBT	$PC_{61}BM$	50	848	6.81	54.0	3.18	8.9	-
1	PCDTBT	$PC_{71}BM$	25	861	9.15	50.2	3.83	9.7	-
1	PCDTBT	$PC_{71}BM$	50	867	9.68	52.0	4.27	22.3	1.39
2	-	$PC_{61}BM$	100	780	3.93	33.0	1.01	-	-
2	-	$PC_{71}BM$	100	583	7.87	30.4	1.40	-	4.34
2	P3HT	$PC_{71}BM$	50	409	2.56	33.8	0.36	-	-
2	P3HT	$PC_{71}BM$	50	473	4.59	24.2	0.53[a)]	-	-
2	PCDTBT	$PC_{61}BM$	25	818	6.57	52.9	2.97	1.7	-
2	PCDTBT	$PC_{61}BM$	50	849	6.97	53.0	3.13	7.2	-
2	PCDTBT	$PC_{71}BM$	25	854	9.02	49.0	3.61	3.4	-
2	PCDTBT	$PC_{71}BM$	50	867	9.97	52.0	4.55	30.4	1.93

a) With post-fabrication thermal annealing at 150 °C for 20 min under Nitrogen. **b)** Reference with glass/ITO/PEDOT:PSS/P3HT:$PC_{71}BM$/Al architecture, used to validate the complete process of fabrication and testing; **c)** Root-mean-squared roughness, as measured by AFM (analysed on a representative 3 μm x 3 μm area), **d)** See the supporting information.

P3HT were inefficient, with PCE values of 0.28% and 0.36% for compounds **1** and **2**, respectively. Annealing raised the PCE values to 0.84% and 0.53%, respectively, mainly through an increase in J_{sc} and FF resulting from greater phase separation, as well as from higher R_{sh} (shunt resistance)/lower R_s (serial resistance) within the films, as generally observed in P3HT:PCBM systems.[48] In the case of compound **1**, the increase in PCE caused by adding P3HT is particularly high (from 0.06% to 0.84%). It is noteworthy that devices using only small molecule **2** as the electron donor still performed better (1.40%) than those containing annealed blends of compound **2** with P3HT (0.53%). This suggests that high-temperature annealing may induce excessive separation of phases and facilitates crystallization of the small molecular components, leading to low values of FF and poor performance.

To avoid the need for annealing to optimize performance, analogous devices were fabricated using matrices of PCDTBT with a similar molecular weight (M_w: 80 kDa, PDI 2.1), because layers of PCDTBT:PCBM are known to perform well when deposited near room temperature, without needing post-fabrication thermal annealing.[49] $PC_{61}BM$ and $PC_{71}BM$ were used as the electron acceptors in a constant SM:PCBM ratio of 1:4 by weight. The resulting values of V_{oc}, J_{sc}, FF, and PCE are presented graphically in Figure 2.7 as a function of the amount of added SM, and quantitative data for all devices are compiled in Table 2.2. The gradual addition of small molecules **1** and **2** to PCDTBT maintained high values of V_{oc} and increased both J_{sc} and FF, resulting in substantial gains in PCE of up to 30.4% relative to the performance of devices containing the polymer and PCBM alone. Similarly, the performance of cells incorporating compound **1** increased from 0.06% to 3.80% by adding 25% PCDTBT by weight.

Imaging by AFM established that the addition of polymer smooths films of both compounds **1** and **2**, with root-mean-square (RMS) roughness reduced from 1.78 nm to 1.39 nm in the case of compound 1 and from 4.34 nm to 1.93 nm in the case of analogue **2**.[28] Optical micrographs under polarized light demonstrate that both small molecules form inhomogeneous films displaying birefringence even at room temperature before annealing,[28] which suggests a high propensity to crystallize during deposition in thin films. This tendency

may facilitate the gross separation of phases, especially when annealing is carried out at high temperature, as in the case of devices containing P3HT.

By employing an innovative new method to separate thin films from an underlying solid support,[37] we were able to use transmission electron microscopy (TEM) to image thin films containing 1:1 blends (by weight) of PCDTBT with $IF(BTC)_2$ (**1**) or $ID(BTC)_2$ (**2**). These images reveal 10-20 nm domains spread evenly across the films (Figure 2.8), suggesting that the small-molecule components undergo phase separation even at room temperature to form nanodomains within matrices of PCDTBT. These self-assembled

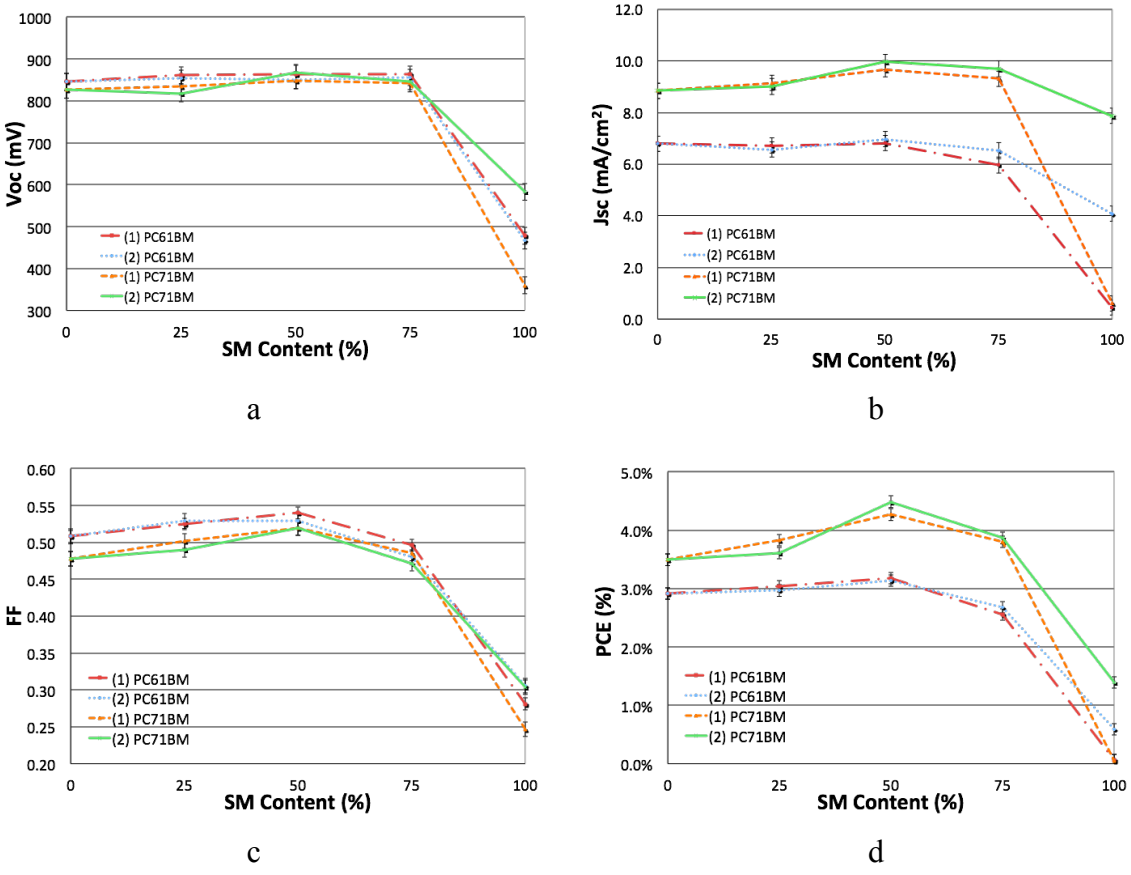

Figure 2.7. Performance of OPVs incorporating unannealed active layers containing various amounts of small-molecule compounds 1 or 2 in PCDTBT, with $PC_{61}BM$ or $PC_{71}BM$ as electron acceptors. (a) V_{oc}. (b) J_{sc}. (c) FF. (d) PCE. In all graphs, parameters are plotted as a function of the percentage by weight of the small-molecule additive, relative to PCDTBT.

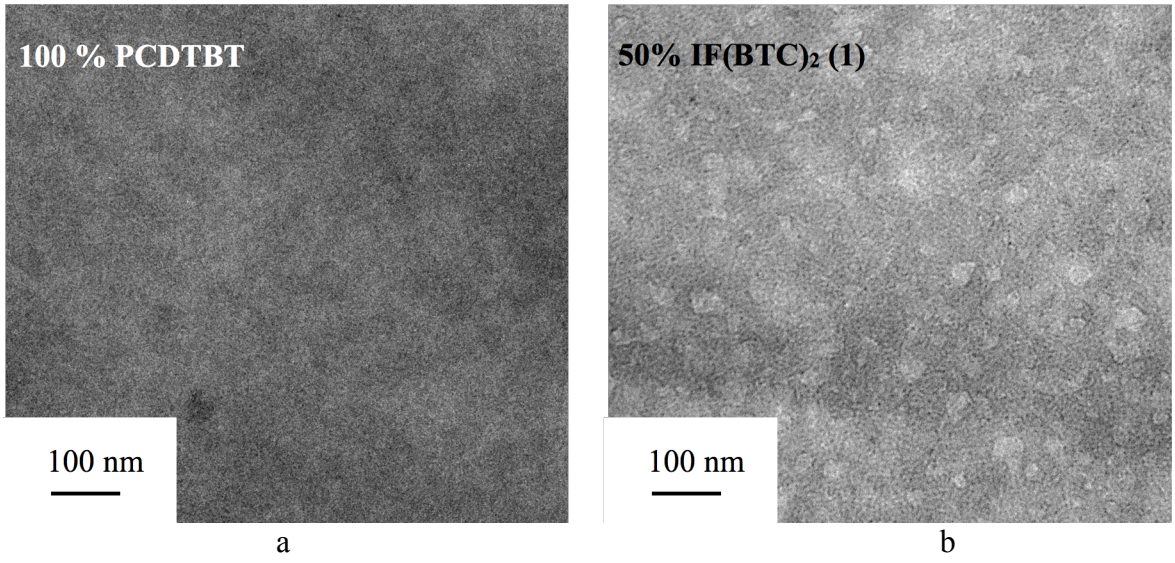

Figure 2.8. TEM images of separated thin films. (a) Film containing only PCDTBT. (b) Film composed of 1:1 PCDTBT:(1) (by weight).

nanodomains may facilitate efficient separation and percolation of charges within the active layer by allowing short-lived excitons to reach a suitable donor/acceptor (D/A) interface by diffusion, thereby limiting the recombination of charges and losses of efficiency.[50-52] It is noteworthy that the polymer appears to inhibit more extensive phase separation of the small molecules, and bulk crystallization and the formation of rough films are avoided, as shown by AFM.

In principle, the gain in PCE achieved by adding small molecules **1** and **2** to active layers containing PCDTBT and PCBM could simply result from improved harvesting of light caused by complementarity in the absorption regimes of the additives and PCDTBT. possibility, we replaced the small molecules with P3HT, which has an absorption spectrum and HOMO/LUMO levels similar to those of compound **2**, but is not expected to permit facile diffusion and phase separation within the blend. OPVs were prepared using a standard architecture (glass/ITO/PEDOT:PSS/P3HT:PCDTBT:$PC_{71}BM$/Al), with a total polymer:$PC_{71}BM$ ratio of 1:3 by weight and P3HT:PCDTBT ratios ranging from 0:1 to 1:0. Post-fabrication thermal treatments varied from no annealing to annealing at 165 °C for 20 min in order to assay the effect of conditions shown to be best suited for the two polymeric

components when used alone; in particular, optimization of devices containing PCDTBT requires no annealing, whereas those incorporating P3HT require post-fabrication annealing at 150-175 °C for best performance.

The results of these trials are summarized in Table 2.3. Devices containing PCDTBT with no P3HT showed stable performance (3.50% PCE) up to at least 100 °C, with decreased efficiency (2.35% PCE) at higher annealing temperatures, when $PC_{71}BM$ presumably undergoes further phase separation to form larger domains. Adding P3HT to PCDTBT lowers the PCE in all cases toward the maximum value attained by devices containing P3HT alone under the same conditions (high donor:acceptor ratio). As a result, improved harvesting of light alone cannot account for the improved performance of devices containing compounds **1** or **2**. Under the conditions studied, the small molecules can diffuse within the blend, unlike their macromolecular substitute P3HT, and they can crystallize to create nanodomains well distributed throughout the polymer matrix, as shown by TEM. Added P3HT cannot form these nanodomains, presumably because it is embedded in the overall matrix, thereby inhibiting its diffusion and phase separation.

Table 2.3. Values of PCE (in %) as a function of the percentage of P3HT (in weight %) blended in 1:3 mixtures of PCDTBT:$PC_{71}BM$ after annealing at various temperatures for 20 min.

Annealing temperature [°C]	25	65	100	135	165
P3HT added [%]					
0	3.48	3.50	3.48	3.16	2.35
25	2.06	1.95	1.93	1.74	1.71
50	1.22	1.15	1.16	1.27	1.48
75	0.65	0.63	0.66	0.91	1.70
100	0.63	0.65	0.72	0.97	1.50

Similarly enhanced performances have been observed when oligomers of low molecular weight are added to polymer blends.[53-54] For example, organic thin-film transistors with high mobilities have been fabricated by co-depositing small molecules that form crystals and thereby bridge large polymeric domains of P3HT.[21] In this case, the formation of interpenetrating nanoscale networks of donors and acceptors appears to be a prerequisite for high efficiency.

Incorporating compounds **1** and **2** in matrices of P3HT did not lead to devices of improved performance, but it is noteworthy that P3HT:PCBM-based devices could accommodate up to 10% of these small-molecule additives without loss of efficiency (see Table 2.2). Optimization of P3HT:PCBM-based devices requires post-fabrication annealing, under conditions that allow high levels of added small molecules to cause disruptive phase separation and reduced performance. Nevertheless, our results show that significant fractions of polymeric components can be replaced by small-molecule additives without loss of efficiency. This observation points the way to the rational use of other small molecules as additives in polymer-based thin-film devices. As we have shown, such additives can be designed to have suitable optoelectronic properties for incorporation in OPVs, and their rates of diffusion and crystallization are inherently higher than those of polymeric components. This can give rise, as in the present study, to the creation of ordered nanodomains and an increased density of productive heterojunctions. Our results are an important step toward reaching the goal of making efficient hybrid devices in which polymeric components are used primarily for their film-forming abilities, and small molecules play a major role in the absorbance of light, separation of charge, and electronic transport.

2.2.7 Conclusions

Two new "push-pull" compounds, $IF(BTC)_2$ (**1**) and $ID(BTC)_2$ (**2**), have been prepared for use in thin-film OPVs, in part to test whether conventional polymeric components can be replaced to a significant extent by small well-defined molecules. Both new compounds feature extended conjugation, have optoelectronic properties suitable for inclusion in OPVs, and are

readily soluble in a wide range of solvents. However, their tendency to crystallize is high, making them inherently unsuitable for the formation of homogeneous thin films, and leading to OPVs of low efficiency. Nevertheless, these compounds can be used as components in highly efficient devices when they are incorporated in matrices of semiconducting polymers. In particular, blends of compounds **1** or **2** with PCDTBT, including $PC_{61}BM$ or $PC_{71}BM$ as the electron acceptors, yielded OPVs with values of PCE significantly higher than those achieved in analogous devices containing only PCDTBT. This increase apparently arises from the presence of 10-20 nm domains of the small molecules dispersed within the polymer matrix, allowing for more efficient excitonic splitting at donor/acceptor interfaces and better overall spatial separation of charge. Similarly, the addition of 25% PCDTBT to compound **1** increased the value of PCE from 0.06% to 3.80%. OPVs with the highest efficiencies did not need annealing, which simplifies fabrication. The OPVs we describe can be considered to be prototypes of efficient hybrid devices in which polymeric components promote the formation of suitable films, and small molecules are actively involved in absorbing light, separating charges, and transporting electrons.

2.2.8 Acknowledgments

The authors are grateful to the Natural Sciences and Engineering Research Council of Canada, the Ministère de l'Éducation du Québec, the Canada Foundation for Innovation, the Canada Research Chairs Program, NanoQuébec, and the Université de Montréal for financial support. The authors acknowledge with gratitude the fruitful advice of Patricia Moraille (Laboratoire de caractérisation des matériaux, Département de chimie, Université de Montréal), Jean-Philippe Masse (Centre de Caractérisation Microscopique des Matériaux $(CM)^2$, École Polytechnique de Montréal), Dr. Minh Trung Dang (Département de chimie, Université de Montréal), and Dr. Dominic Laliberté (Solaris Chem Inc., Montréal).

2.2.9 Supplemental Information

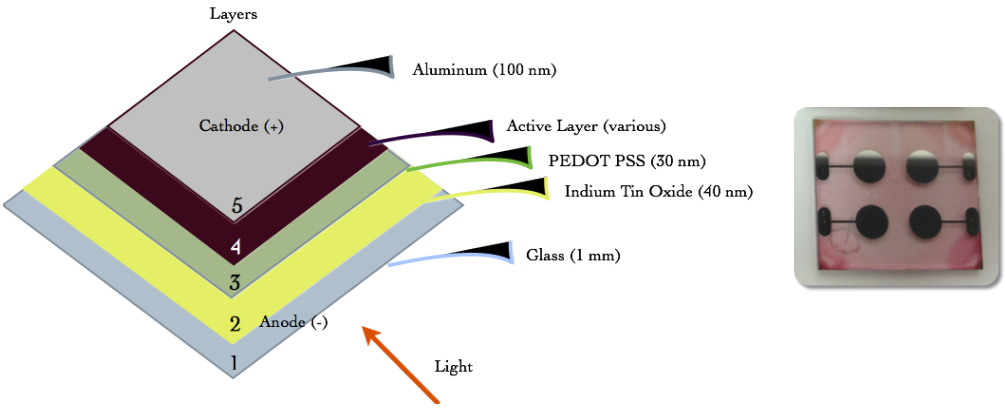

a b

Figure S2.1. (a) Schematic showing the architecture of OPVs. (b) Photograph of four-cell substrate with circular aluminum electrodes.

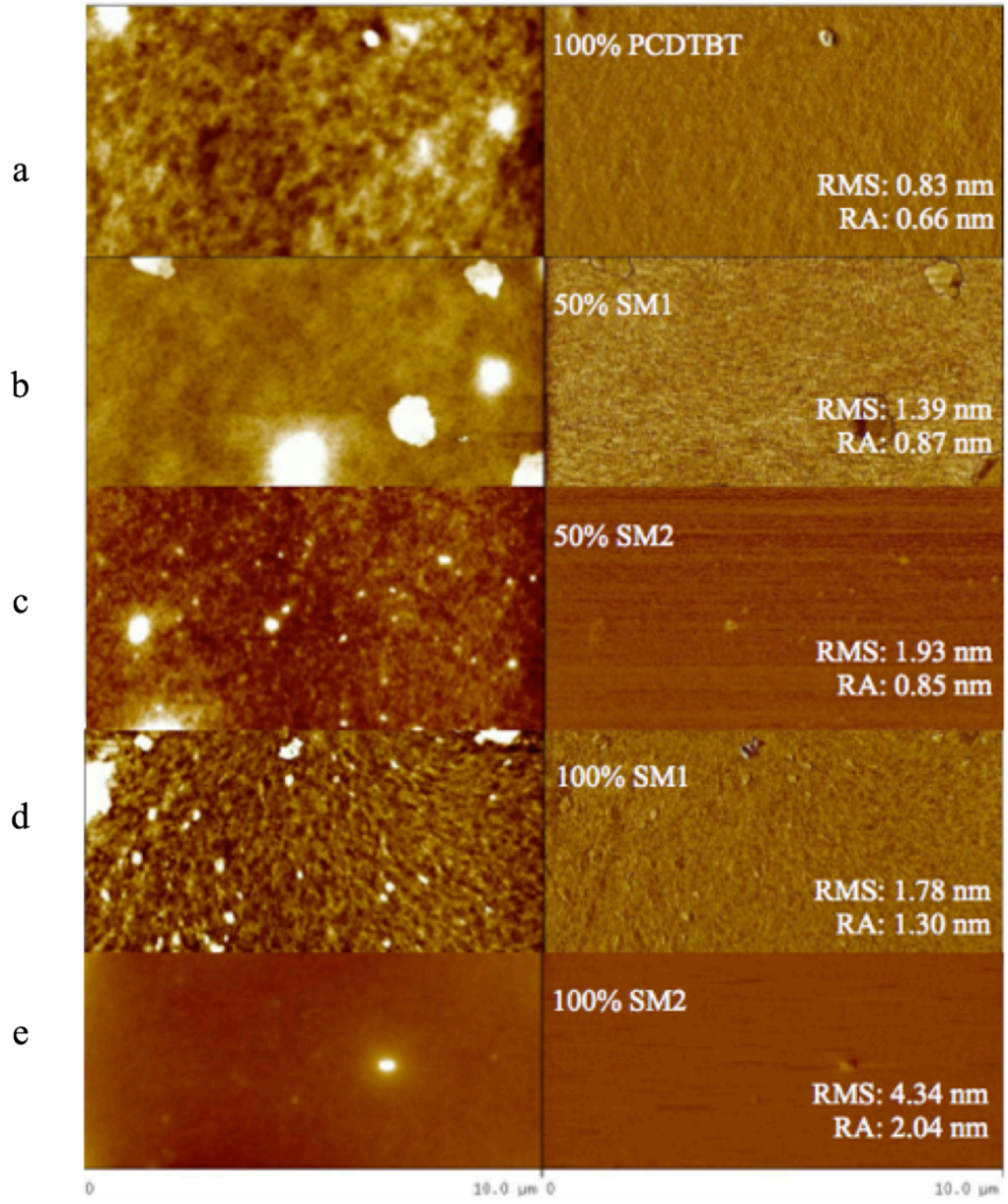

Figure S2.2. AFM images (left) and contrast (right) of thin films. (a) PCDTBT. (b) 1:1 (by weight) PCDTBT:SM1. (c) 1:1 (by weight) PCDTBT:SM2. (d) SM1. (e) SM2.

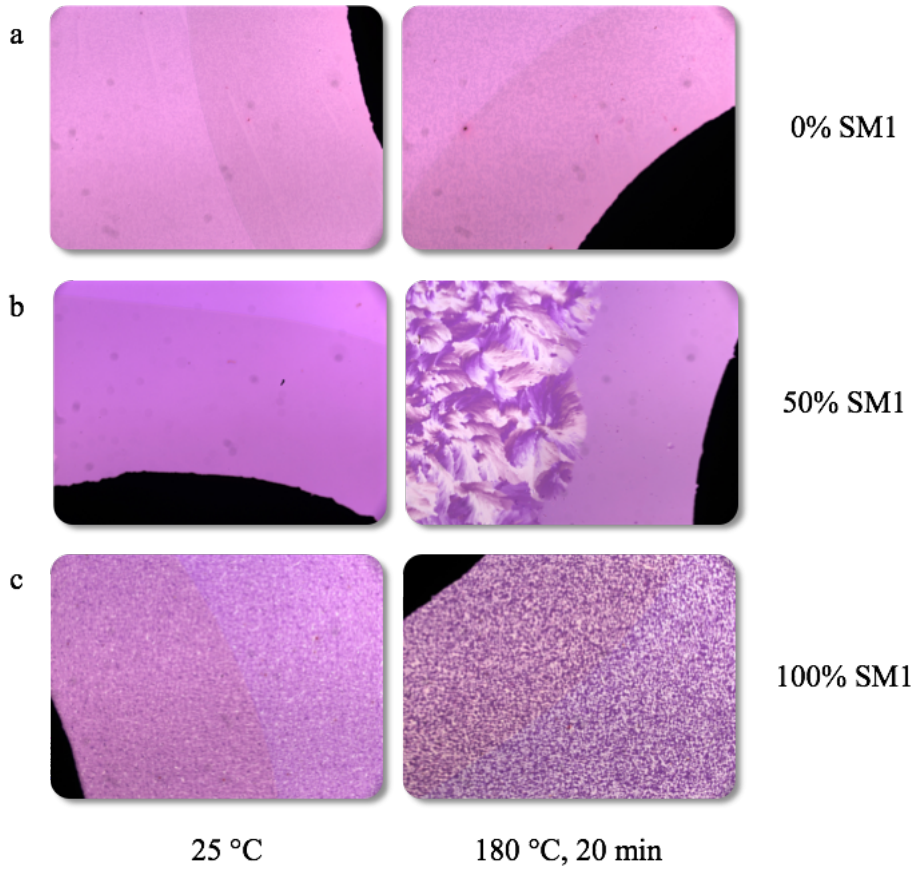

Figure S2.3. Optical micrographs (50X) showing thin films of SM1:P3HT in various proportions together with $PC_{61}BM$, before annealing (25 °C) and after annealing (180 °C). (a) P3HT alone. (b) 1:1 (by weight) SM1:P3HT. (c) SM1 alone.

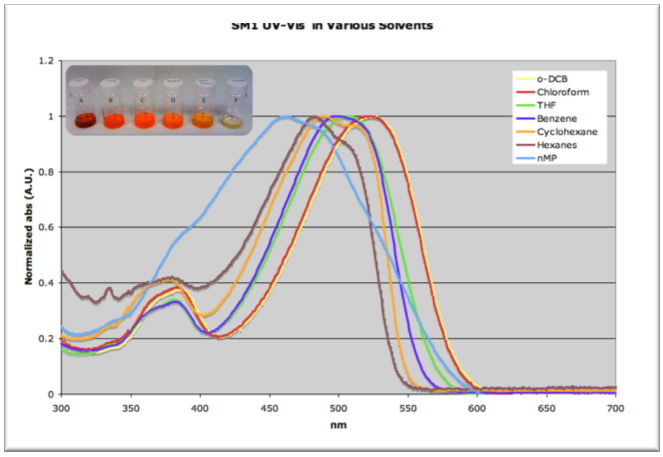

Figure S2.4. UV-Vis spectra of solutions of SM1 in various solvents to demonstrate solvatochromism. (a) *N*-Methylpyrrolidone. (b) Chloroform. (c) Tetrahydrofuran. (d) Benzene. (e) Cyclohexane. (f) Hexane.

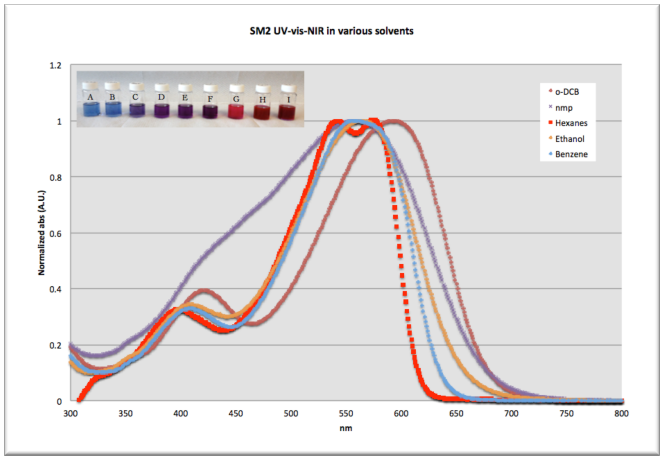

Figure S2.5. UV-Vis spectra of solutions of SM2 in various solvents to demonstrate solvatochromism. (a) 1,2-Dichlorobenzene. (b) Chloroform. (c) *N*-Methylpyrrolidone. (d) Tetrahydrofuran. (e) Ethanol. (f) Acetone. (g) Hexane. (h) Cyclohexane. (i) Benzene.

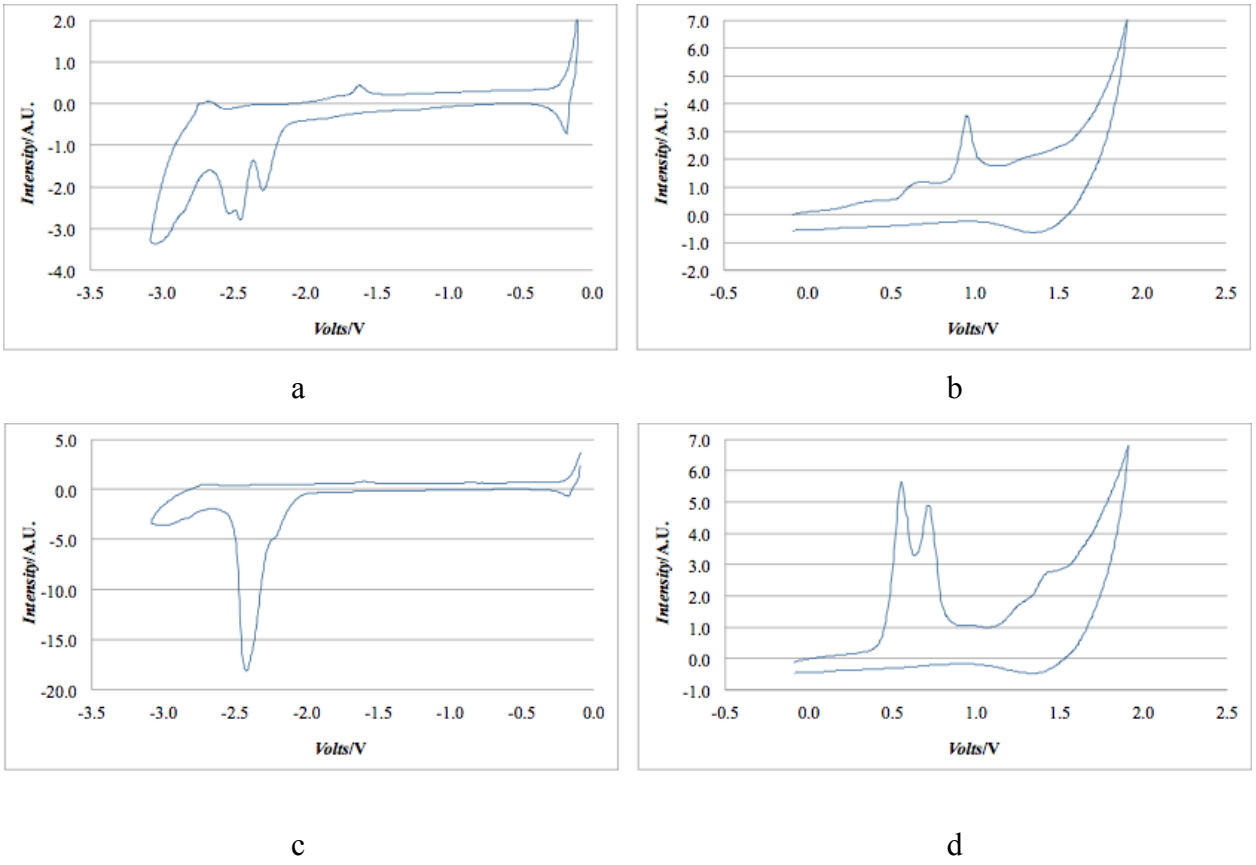

Figure S2.6. Cyclic voltammograms vs Fc/Fc+ (centered at 0 V) of: a) and b) film of $IF(BTC)_2$ (**1**); c) and d) film of $ID(BTC)_2$ (**2**). Films coated on glassy carbon working electrodes, using a Ag/Ag^+ reference electrode ($[AgNO_3]$ = 0.01 M) and a platinum wire as counter electrode. Measured in MeCN containing NBu_4PF_6 ($[NBu_4PF_6]$ = 0.1M) at a scan rate of 25 mVs^{-1}.

2.2.9.1 Synthesis and characterization: Generalities

Unless otherwise stated, commercially available reagents were used without further purification. Tetrahydrofuran, 1,4-dioxane, and dichloromethane were prepared in anhydrous oxygen-free form by passage through columns packed with activated alumina and supported copper catalyst (Glass Contour, Irvine, CA). Unless otherwise stated, reactions were carried

out under an atmosphere of dry N_2 with rigid exclusion of moisture, using standard techniques for manipulating air-sensitive compounds.

Analytical thin-layer chromatography was performed using silica gel precoated on glass slides. Developed chromatograms were visualized by exposure to UV or iodine vapor. Flash column chromatography was carried out using 230-400 mesh silica. Melting points were recorded with a Barnstead Electrothermal Digital IA9200 apparatus and are uncorrected. Infrared spectra were obtained by using a Nicolet 6700 FTIR spectrophotometer equipped with a Spectratech Foundations ATR probe. ^{1}H and ^{13}C NMR spectra were recorded on a Bruker Avance 400 spectrometer (400 MHz for ^{1}H NMR spectra and 100 MHz for ^{13}C NMR spectra). Chemical shifts in ^{1}H NMR spectra are reported in parts per million from tetramethylsilane, with the solvent resonance used as an internal standard. Data are presented in the following order: chemical shift, multiplicity (s = singlet, d = doublet, t = triplet, q = quartet, qn = quintet, sx = sextet, h = heptet, o = octet, m = multiplet, and br = broad), integration, and coupling constant in Hz. Chemical shifts for ^{13}C NMR spectra are reported in parts per million from tetramethylsilane, using the central peak of the solvent resonance as the internal standard. All ^{13}C NMR spectra were obtained with complete proton decoupling. High-resolution mass measurements were made with an Agilent Technologies TOF LC/MS spectrometer operated in positive mode by either atmospheric pressure chemical ionization (APCI), atmospheric pressure photoionization (APPI), or electrospray ionization (ESI). Elemental analyses were performed either on a Fisons Instruments EA1108 analyzer or on a Costech ECS 4010 instrument. UV-Vis measurements were done using a Cary 500 spectrophotometer.

2.2.9.2 Synthesis

5,5''-(6,6,12,12-Tetraoctyl-6,12-dihydroindeno[1,2-b]fluorene-2,8-diyl)di-2'',2'''-bithiophene (**4**). A mixture of 2,2'-(6,6,12,12-tetraoctyl-6,12-dihydroindeno[1,2-*b*]fluorene-2,8-diyl)bis(4,4,5,5-tetramethyl-1,3,2-dioxaborolane) (**3**; 600 mg, 0.628 mmol), 5-bromo-2,2'-bithiophene (339 mg, 1.38 mmol), $Pd(PPh_3)_4$ (36.3 mg, 0.0314 mmol), and sodium carbonate

(666 mg, 6.28 mmol) in 1,4-dioxane (6.3 mL) and water (3.2 mL) was sparged with N_2 for 20 min. The mixture was then stirred at 80 °C for 15 h and cooled to room temperature. The resulting mixture was diluted with water and extracted with Et_2O. The combined organic extracts were washed with brine and dried over $MgSO_4$. Volatiles were removed by evaporation under reduced pressure to yield a yellow solid. Further purification by flash chromatography (5/95 to 30/70 CH_2Cl_2/hexane) yielded compound **4** as a bright yellow powder (330 mg, 0.320 mmol, 51%): mp 105-106 °C; ^{1}H NMR (400 MHz, $CDCl_3$) δ 7.75 (d, 2H, ^3J = 7.9 Hz), 7.65-7.59 (m, 4H), 7.56 (d, 2H, ^4J = 1.2 Hz), 7.31 (d, 2H, ^3J = 3.7 Hz), 7.25-7.21 (m, 4H), 7.19 (d, 2H, ^3J = 3.7 Hz), 7.05 (dd, 2H, ^3J = 3.8 Hz, 4.8 Hz), 2.12-1.99 (m, 8H), 1.21-0.97 (m, 40H), 0.78 (t, 12H, ^3J = 6.8 Hz), 0.74-0.63 (m, 8H); ^{13}C NMR (100 MHz, $CDCl_3$) δ 151.9, 150.4, 144.1, 141.1, 140.2, 137.6, 136.2, 132.5, 127.8, 124.6, 124.4, 124.2, 123.5, 123.3, 119.9, 119.8, 113.9, 54.9, 40.6, 31.7, 30.0, 29.7, 29.2, 23.7, 22.6, 14.0; FTIR (ATR) 2923, 2852, 1494, 1463, 1375, 1323, 882, 838, 822, 795, 720, 687 cm^{-1}; HRMS (APPI) calcd for $C_{68}H_{86}S_4$ + H^+ *m/z* 1031.56851, found 1031.56517. Anal. calcd for $C_{68}H_{86}S_4$: C, 79.17; H, 8.40; S, 12.43. Found: C, 79.11; H, 8.49; S, 12.12.

5',5'''-(6,6,12,12-Tetraoctyl-6,12-dihydroindeno[1,2-b]fluorene-2,8-diyl)bis([2'',2'''-bithiophene]-5-carbaldehyde) (**5**). A solution of compound **4** (460 mg, 0.446 mmol) in 1,2-dichloroethane (4.5 mL) was cooled to 0 °C and treated dropwise with a solution of Vilsmeier reagent, freshly prepared by adding $POCl_3$ (207 mg, 1.35 mmol) dropwise to DMF (0.5 mL) at 0 °C. The dark red solution was heated to reflux and stirred for 7.5 h. The resulting mixture was cooled to room temperature and poured into an aqueous solution of NaOAc (2 M, 20 mL). After being stirred for a few hours, the mixture was extracted with CH_2Cl_2, and the combined organic extracts were dried over $MgSO_4$. Volatiles were removed by evaporation under reduced pressure to yield an orange solid. Further purification by flash chromatography (15/85 to 100/0 CH_2Cl_2/hexane) yielded compound **5** as an orange powder (447 mg, 0.411 mmol, 91%): mp 155-156 °C; ^{1}H NMR (400 MHz, $CDCl_3$) δ 9.88 (s, 2H), 7.76 (d, 2H, ^3J = 7.9 Hz), 7.70 (d, 2H, ^3J = 4.0 Hz), 7.65-7.62 (m, 4H), 7.57 (d, 2H, ^4J = 1.2 Hz), 7.39 (d, 2H, ^3J = 3.8 Hz), 7.36 (d, 2H, ^3J = 3.8 Hz), 7.30 (d, 2H, ^3J = 3.9 Hz), 2.12-1.99 (m, 8H), 1.21-0.97 (m, 40H), 0.77 (t, 12H, ^3J = 6.8 Hz), 0.74-0.63 (m, 8H); ^{13}C NMR (100 MHz, $CDCl_3$) δ 182.4, 152.1, 150.6, 147.3, 147.2, 141.8, 141.4, 140.2, 137.4, 134.6, 131.9, 127.2, 124.7, 123.9,

123.8, 120.1, 120.0, 114.1, 54.9, 40.6, 31.8, 29.9, 29.2, 29.1, 23.7, 22.6, 14.0; FTIR (ATR) 2955, 2921, 2850, 1660, 1458, 1431, 1383, 1325, 1226, 1213, 1158, 1047, 879, 831,823, 794, 755, 721, 662, 474 cm^{-1}; HRMS (APPI) calcd for $C_{70}H_{86}O_2S_4 + H^+$ *m/z* 1087.55834, found 1087.55754. Anal. calcd for $C_{70}H_{86}O_2S_4$: C, 77.30; H, 7.97; S, 11.79. Found: C, 77.06; H, 8.09; S, 11.58.

2,2'-((5',5'''-(6,6,12,12-Tetraoctyl-6,12-dihydroindeno[1,2-*b*]fluorene-2,8-diyl)bis([2'',2'''-bithiophene]-5'',5'-diyl))bis(methanylylidene))dimalononitrile (IF(BTC)$_2$) (1). A solution of compound **5** (360 mg, 0.327 mmol) and malononitrile (59.0 mg, 0.893 mmol) in CH_2Cl_2 (10 mL) was treated dropwise with piperidine (3 drops). The dark solution was stirred at room temperature for 2.5 h. Volatiles were removed by evaporation under reduced pressure to yield a red solid. Further purification by flash chromatography (75/25 to 100/0 CH_2Cl_2/hexane) yielded IF(BTC)$_2$ (**1**) as a bright red powder (320 mg, 0.270 mmol, 83%): mp 218-219 °C; ^{1}H NMR (400 MHz, $CDCl_3$) δ 7.80-7.76 (m, 4H), 7.67-7.63 (m, 6H), 7.56 (d, 2H, ^4J = 1.2 Hz), 7.47 (d, 2H, ^3J = 3.9 Hz), 7.40 (d, 2H, ^3J = 3.9 Hz), 7.32 (d, 2H, ^3J = 4.1 Hz), 2.13-2.03 (m, 8H), 1.18-1.02 (m, 40H), 0.77 (t, 12H, ^3J = 6.8 Hz), 0.73-0.63 (m, 8H); ^{13}C NMR (100 MHz, $CDCl_3$) δ 152.2, 150.7, 150.0, 149.6, 148.6, 142.2, 140.3, 140.2, 133.7, 133.2, 131.6, 128.4, 124.8, 124.3, 124.1, 120.2, 120.0, 114.3, 114.2, 113.5, 75.7, 55.0, 40.6, 31.8, 29.9, 29.2, 29.1, 23.7, 22.6, 14.0; FTIR (ATR) 2923, 2849, 2219, 1574, 1534, 1453, 1424, 1361, 1325, 1055, 936, 878, 799, 720, 605, 434 cm^{-1}; HRMS (ESI) calcd for $C_{76}H_{86}N_4S_4^-$ *m/z* 1182.57408, found 1182.57155. Anal. calcd for $C_{76}H_{86}N_4S_4$: N, 4.73; C, 77.11; H, 7.32; S, 10.83. Found: N, 4.67; C, 77.01; H, 7.47; S, 10.51.

4,4,9,9-Tetraoctyl-4,9-dihydro-*s*-indaceno[1,2-*b*:5,6-*b*']dithiophene (**6**). To a solution of 4,9-dihydro-*s*-indaceno[1,2-*b*:5,6-*b*']dithiophene (1.73 g, 6.50 mmol) and 1-bromooctane (7.53 g, 40.0 mmol) in DMSO (65 mL) was added potassium hydroxide (2.92 g, 52.0 mmol). The dark suspension was stirred in the dark at room temperature for 48 h. Second portions of 1-bromooctane (3.77 g, 20.0 mmol) and potassium hydroxide (1.46 g, 26.0 mmol) were then added. After the mixture was stirred further for 72 h at room temperature, water (65 mL) was added. The mixture was extracted with Et_2O, and the combined organic extracts were thoroughly washed with water and dried over $MgSO_4$. Volatiles were removed by evaporation

under reduced pressure to yield a yellow solid. Further purification by flash chromatography (hexane) yielded compound **6** as a pale yellow powder (3.14 g, 4.39 mmol, 68%): mp 54-55°C; ^{1}H NMR (400 MHz, $CDCl_3$) δ 7.27 (s, 2H), 7.25 (d, 2H, ^{3}J = 4.8 Hz), 6.96 (d, 2H, ^{3}J = 4.8 Hz), 2.09-1.76 (m, 8H), 1.30-1.00 (m, 40H), 0.92-0.70 (m, 20H); ^{13}C NMR (100 MHz, $CDCl_3$) δ 155.1, 153.2, 141.6, 135.5, 126.1, 121.7, 113.1, 53.6, 39.1, 31.8, 30.0, 29.3, 29.2, 24.2, 22.6, 14.0; FTIR (ATR) 2952, 2923, 2849, 1464, 1374, 1329, 1082, 877, 823, 806, 722, 664, 542 cm^{-1}; HRMS (APCI) calcd for $C_{48}H_{74}S_2$ + H^+ *m/z* 715.53047, found 715.52837. Anal. calcd for $C_{48}H_{75}S_2$: C, 80.61; H, 10.43; S, 8.97. Found: C, 80.61; H, 10.55; S, 8.82.

2,7-Di([2,2'-bithiophen]-5-yl)-4,4,9,9-tetraoctyl-4,9-dihydro-*s*-indaceno[1,2-*b*:5,6-*b*']dithiophene (**7**). A solution of compound **6** (2.50 g, 3.50 mmol) in THF (50 mL) was cooled to 0 °C and treated dropwise with a solution of butyllithium (3.10 mL, 2.50 M in hexane, 7.75 mmol). The pale yellow solution was warmed to room temperature and stirred for 2 h. After the mixture was cooled to 0 °C, anhydrous zinc chloride (1.06 g, 7.75 mmol) was added in one portion. The resulting suspension was warmed to room temperature and stirred for 1 h. 5-Bromo-2,2'-bithiophene (2.06 g, 8.40 mmol) and $Pd(PPh_3)_4$ (202 mg, 0.175 mmol) were then added in succession. The resulting bright yellow solution was finally heated to 50 °C and stirred for 2 h. After the mixture was cooled to 0 °C, 1 M aqueous HCl (25 mL) was added. The mixture was extracted with Et_2O, and the combined organic extracts were washed with brine and dried over $MgSO_4$. Volatiles were removed by evaporation under reduced pressure to yield a red solid. Further purification by flash chromatography (hexane) yielded compound **7** as a bright red powder (2.12 g, 2.03 mmol, 58%) [Note: This product was contaminated with <5% of monocoupled product, which could be removed in the subsequent step]: ^{1}H NMR (400 MHz, $CDCl_3$) δ 7.25-7.21 (m, 4H), 7.19 (dd, 2H, ^{3}J = 3.6 Hz, ^{4}J = 0.8 Hz), 7.14-7.09 (m, 4H), 7.06 (s, 2H), 7.04 (dd, 2H, ^{3}J = 5.1 Hz, 3.6 Hz) 2.10-1.80 (m, 8H), 1.34-1.02 (m, 40H), 1.02-0.76 (m, 20H); ^{13}C NMR (100 MHz, $CDCl_3$) δ 153.5, 149.8, 149.2, 142.5, 141.9, 140.3, 135.7, 133.2, 132.8, 128.3, 124.0, 119.5, 114.4, 113.6, 113.3, 54.2, 39.0, 31.8, 30.0, 29.3, 29.2, 24.2, 22.6, 14.1; FTIR (ATR) 3066, 2952, 2921, 2950, 1780, 1738, 1525, 1502, 1456, 1422, 1376, 1331, 1244, 1160, 1134, 1051, 870, 826, 789, 721, 687 cm^{-1}; HRMS (APCI) calcd for $C_{64}H_{82}S_6$ + H^+ *m/z* 1043.48135, found 1043.47957.

5',5'''-(4,4,9,9-Tetraoctyl-4,9-dihydro-*s*-indaceno[1,2-*b*:5,6-*b*']dithiophene-2,7-diyl)bis([2,2'-bithiophene]-5-carbaldehyde) (**8**). A solution of compound **7** (1.88 g, 1.80 mmol) in 1,2-dichloroethane (20 mL) was cooled to 0 °C and treated dropwise with a solution of Vilsmeier reagent, freshly prepared by adding $POCl_3$ (828 mg, 5.40 mmol) dropwise to DMF (2 mL) at 0 °C. The dark red solution was heated to 60 °C and stirred for 14 h. The resulting mixture was cooled to room temperature and poured over ice-cold water (40 mL). The mixture was extracted with CH_2Cl_2, and the combined organic extracts were thoroughly washed with water and dried over $MgSO_4$. Volatiles were removed by evaporation under reduced pressure to yield a dark red solid. Further purification by flash chromatography (65/35 CH_2Cl_2/hexane) yielded compound **8** as a dark red powder (1.46 g, 1.33 mmol, 74%): mp 106-107 °C; ^{1}H NMR (400 MHz, $CDCl_3$) δ 9.87 (s, 2H), 7.69 (d, 2H, ^3J = 4.0 Hz), 7.30 (d, 2H, ^3J = 3.8 Hz), 7.26-7.24 (m, 4H), 7.14 (d, 2H, ^3J = 3.8 Hz), 7.12 (s, 2H), 2.08-1.82 (m, 8H), 1.34-1.03 (m, 40H), 1.02-0.74 (m, 20H); ^{13}C NMR (100 MHz, $CDCl_3$) δ 182.4, 156.2, 153.3, 147.0, 141.8, 141.4, 140.4, 137.8, 137.4, 135.7, 133.7, 127.0, 123.8, 123.7, 119.0, 113.2, 54.2, 39.0, 31.8, 30.0, 29.3, 29.2, 24.2, 22.6, 14.0; FTIR (ATR) 2918, 2847, 2362, 2336, 1663, 1460, 1438, 1417, 1378, 1221, 1136, 1048, 873, 834, 791, 751, 665 cm^{-1}; HRMS (APCI) calcd for $C_{66}H_{83}O_2S_6 + H^+$ *m/z* 1099.47118, found 1099.46853. Anal. calcd for $C_{66}H_{82}O_2S_6$: C, 72.08; H, 7.52; S, 17.49. Found: C, 72.17; H, 7.69; S, 17.56.

2,2'-((5',5'''-(4,4,9,9-Tetraoctyl-4,9-dihydro-*s*-indaceno[1,2-*b*:5,6-*b*']dithiophene-2,7-diyl)bis([2,2'-bithiophene]-5',5-diyl))bis(methanylylidene))dimalononitrile (ID(BTC)$_2$) (2). A solution of compound **8** (1.10 g, 1.00 mmol) and malononitrile (198 mg, 3.00 mmol) in chloroform (25 mL) was treated dropwise with piperidine (3 drops). The dark solution was stirred at room temperature for 14 h, and water (10 mL) was added. The resulting mixture was extracted with CH_2Cl_2, and the combined organic extracts were thoroughly washed with water and dried over Na_2SO_4. Volatiles were removed by evaporation under reduced pressure to yield a black solid. Further purification by flash chromatography (65/35 CH_2Cl_2/hexane) yielded ID(BTC)$_2$ (**2**) as a dark purple powder (852 mg, 0.712 mmol, 71%): mp 133-134 °C; ^{1}H NMR (400 MHz, $CDCl_3$) δ 7.75 (s, 2H), 7.64 (d, 2H, ^3J = 4.0 Hz), 7.38 (d, 2H, ^3J = 3.8 Hz), 7.30-7.22 (m, 6H), 7.15 (s, 2H), 2.08-1.83 (m, 8H), 1.30-1.03 (m, 40H), 1.00-0.71 (m, 20H); ^{13}C NMR (100 MHz, $CDCl_3$) δ 156.4, 153.5, 149.8, 149.2, 147.0, 142.5, 141.9, 140.3,

137.6, 135.7, 133.2, 132.8, 128.3, 124.1, 119.5, 114.4, 113.6, 113.3, 75.6, 54.2, 39.0, 31.8, 30.0, 29.3, 29.2, 24.2, 22.6, 14.1; FTIR (ATR) 2917, 2847, 2361, 2336, 2219, 1569, 1515, 1489, 1456, 1434, 1409, 1355, 1334, 1278, 1260, 1136, 1055, 874, 831, 798, 721, 607 cm^{-1}; HRMS (APCI) calcd for $C_{72}H_{82}N_4S_6 + H^+$ *m/z* 1195.49365, found 1195.49029. Anal. calcd for $C_{72}H_{83}N_4S_6$: C, 72.31; H, 6.91; N, 4.69; S, 16.09. Found: C, 72.25; H, 7.45; N, 4.38; S, 15.30.

2.2.9.3 GPC analysis of the polymer matrices

Samples of P3HT and PCDTBT were characterized by gel permeation chromatography (GPC) according to the following protocol. The polymers were dissolved in THF (2 mg mL^{-1}), and the solutions were filtered through a 0.45 μ membrane. GPC analyses were carried out using a Waters 1525 binary pump system, a Waters 717 Plus autosampler, and a Waters 2414 refractive index detector. The flow was set at 1 mL/min and was passed through a Waters column heater at 35 °C and then into a Waters Styragel pre-column (50 mm × 7.8 mm) and a series of three Phenomenex columns: a Phenogel 500 Å (300 mm × 7.8 mm), a Phenogel 10^4 Å (300 mm × 7.8 mm), and a Phenogel 10^5 Å (300 mm × 7.8 mm). Analyte (100 μL) was injected after two hours of system equilibration. Nine narrow polystyrene standards in three THF solutions were used to plot a calibration curve and allow calculation of the number-average molar mass (M_n), the weight-average molar mass (M_w), and the polydispersity (PDI) of analytes, using the Waters software system Breeze.

2.2.10 References

[1] Conti, J. J.; Holtberg, P. D.; Beamon, J. A.; Napolitano, S. A.; Schaal, M. A.; Turnure, J. T.; Westfall, L. D. International Energy Outlook 2013. *U. S. Energy Information Administration* **2013**.

[2] Becquerel, A. E. Memoire sur les effets electriques produit sous l'influence des rayons solaires. *C. R. Acad. Sci.* **1839,** *9*, 561-567.

[3] Tang, C. W. Two-layer organic photovoltaic cell. *Appl. Phys. Lett.* **1986,** *48* (2), 183-185.

[4] Heliatek. Heliatek sets new Organic Photovoltaic world record efficiency of 13.2%. http://www.heliatek.com/en/press/press-releases/details/heliatek-sets-new-organic-photovoltaic-world-record-efficiency-of-13-2 (accessed February 2016).

[5] Kim, J.; Cho, N.; Ko, H. M.; Kim, C.; Lee, J. K.; Ko, J. Push-pull organic semiconductors comprising of bis-dimethylfluorenyl amino benzo[b]thiophene donor and various acceptors for solution processed small molecule organic solar cells. *Sol. Energ. Mat. Sol. Cells* **2012,** *102*, 159–166.

[6] Ko, H. M.; Choi, H.; Paek, S.; Kim, K.; Song, K.; Lee, J. K.; Ko, J. Molecular engineering of push-pull chromophore for efficient bulkheterojunction morphology in solution processed small molecule organic photovoltaics. *J. Mater. Chem.* **2011,** *21*, 7248-7253.

[7] Liu, Y.; Chen, C.-C.; Hong, Z.; Gao, J.; Yang, Y. M.; Zhou, H.; Dou, L.; Li, G.; Yang, Y. Solution-processed small-molecule solar cells: breaking the 10% power conversion efficiency. *Sci. Rep.* **2013,** *3* (3356), 1-8.

[8] Mikroyannidis, J. A.; Tsagkournos, D. V.; Sharma, S. S.; Vijay, Y. K.; Sharma, G. D. Low band gap conjugated small molecules containing benzobisthiadiazole and thienothiadiazole central units: synthesis and application for bulk heterojunction solar cells. *J. Mater. Chem.* **2011,** *21*, 4679-4688.

[9] Zhang, L.; Pei, K.; Zhao, H.; Wu, S.; Wang, Y.; Gao, J. Rational design of novel A-A-D-A-A type electron donors for small molecule organic solar cells. *Chem. Phys. Lett.* **2012,** *543*, 199–204.

[10] Kaura, N.; Singh, M.; Pathak, D.; Wagner, T.; Nunzi, J. M. Organic materials for photovoltaic applications: Review and mechanism. *Synth. Met.* **2014,** *190*, 20-26.

[11] Pauszek, R. F.; Kodali, G.; Caldwell, S. T.; Fitzpatrick, B.; Zainalabdeen, N. Y.; Cooke, G.; Rotello, V. M.; Stanley, R. J. Excited State Charge Redistribution and Dynamics in the Donor-π-Acceptor Flavin Derivative ABFL. *J. Phys. Chem. B* **2012,** *117* (49), 15684–15694.

[12] Yan, L.; Chen, X.; He, Q.; Wang, Y.; Wang, X.; Guo, Q.; Bai, F.; Xia, A.; Aumiler, D.; Vdović, S. Localized Emitting State and Energy Transfer Properties of

Quadrupolar Chromophores and (Multi)Branched Derivatives. *J. Phys. Chem. A* **2012,** *116* (34), 8693–8705.

[13] Liua, Y.; Du, X.; Xiao, Z.; Cao, J.; Tan, S.; Zuo, Q.; Ding, L. Solution processable low bandgap small molecule donors with naphthalene end-groups for organic solar cells. *Synth. Met.* **2012,** *162*, 1665–1671.

[14] Lin, Y.; Lia, Y.; Zhan, X. Small molecule semiconductors for high-efficiency organic photovoltaics. *Chem. Soc. Rev.* **2012,** *41*, 4245–4272.

[15] Liu, H. Q.; Xiang, L. H. Recent progress of bulk heterojunction solar cells based on small-molecular donors. *Chin. Sci. Bull.* **2013,** *58*, 2677-2685.

[16] Roncali, J.; Leriche, P.; Blanchard, P. Molecular Materials for Organic Photovoltaics: Small is Beautiful. *Adv. Mater.* **2014,** *26*, 3821–3838.

[17] Walker, B.; Kim, C.; Nguyen, T.-Q. Small Molecule Solution-Processed Bulk Heterojunction Solar Cells. *Chem. Mater.* **2011,** *23* (3), 470–482.

[18] Yu, G.; Gao, J.; Hummelen, J. C.; Wudl, F.; Heeger, A. J. Polymer Photovoltaic Cells: Enhanced Efficiencies via a Network of Internal Donor-Acceptor Heterojunctions. *Science* **1995,** *270* (5243), 1789-1791.

[19] Cheng, Y.-J.; Yang, S.-H.; Hsu, C.-S. Synthesis of Conjugated Polymers for Organic Solar Cell Applications. *Chem. Rev.* **2009,** *109*, 5868–5923.

[20] Lee, H. K. H.; Chan, K. K. H.; So, S. K. Charge transport studies of polymeric photovoltaic thin films with an electron blocking and trapping layer. *Org. Photon. V* **2012,** *8435*, 84351U.

[21] Orgiu, E.; Masillamani, A. M.; Vogel, J.-O.; Treossi, E.; Kiersnowski, A.; Kastler, M.; Pisula, W.; Dotz, F.; Palermo, V.; Samorí, P. Enhanced mobility in P3HT-based OTFTs upon blending with a phenylene–thiophene–thiophene–phenylene small molecule. *Chem. Commun.* **2012,** *48*, 1562–1564.

[22] Kim, J.; Kim, S. H.; Jung, I. H.; Jeong, E.; Xia, Y.; Cho, S.; Hwang, I.-W.; Lee, K.; Suh, H.; Shim, H.-K.; Woo, H. Y. Synthesis and characterization of indeno[1,2-b]fluorene-based low bandgap copolymers for photovoltaic cells. *J. Mater. Chem.* **2010,** *20* (8), 1577-1586.

[23] Zhang, W.; Smith, J.; Watkins, S. E.; Gysel, R.; McGehee, M.; Salleo, A.; Kirkpatrick, J.; Ashraf, S.; Anthopoulos, T.; Heeney, M.; McCulloch, I. Indacenodithiophene

Semiconducting Polymers for High-Performance, Air-Stable Transistors. *J. Am. Chem. Soc.* **2010,** *132* (33), 11437–11439.

[24] Wu, R.; Schumm, J. S.; Pearson, D. L.; Tour, J. M. Convergent Synthetic Routes to Orthogonally Fused Conjugated Oligomers Directed toward Molecular Scale Electronic Device Applications. *J. Org. Chem.* **1996,** *61* (20), 6906–6921.

[25] Connelly, N. G.; Geiger, W. E. Chemical Redox Agents for Organometallic Chemistry. *Chem. Rev.* **1996,** *96*, 877-910.

[26] Bates, R. G.; MacAskill, J. B. Standard Potential of the Silver-Silver Chloride Electrode. *Pure Appl. Chem.* **1978,** *50*, 1701-1706.

[27] Trasatti, S. The absolute electrode potential: An explanatory note. *Pure Appl. Chem.* **1986,** *58* (7), 955-966.

[28] *See the supporting information for details.*

[29] Adamo, C.; Barone, V. Toward reliable density functional methods without adjustable parameters : The PBE0 model. *J. Chem. Phys* **1999,** *110*, 6158.

[30] Jacquemin, D.; Perpete, E. A.; Scuseria, G. E. TD-DFT performance for the visible absorption spectra of organic dyes : Conventional versus long-range hybrids. *J. Chem. Theory Comput.* **2008,** *4* (1), 123–135.

[31] *APEX2 and SAINT*, 7.68A; Bruker AXS Inc.: Madison, WI 53719-1173, **2009**.

[32] Sheldrick, G. M. *SADABS*, 2008/1; Bruker AXS Inc.: Madison, WI 53719-1173, **2008**.

[33] Sheldrick, G. M. *Acta Crystallogr. Sect. A* **2008,** *A64*, 112.

[34] Dolomanov, O. V.; Bourhis, L. J.; Gildea, R. J.; Howard, J. A. K.; Puschmann, H. OLEX2: A complete structure solution, refinement and analysis program. *J. Appl. Cryst.* **2009,** *42*, 339-341.

[35] Cravino, A.; Schilinsky, P.; Brabec, C. J. Characterization of organic solar cells: The importance of device layout. *Adv. Funct. Mater.* **2007,** *17* (18), 3906-3910.

[36] Kim, M.-S.; Kang, M.-G.; Guo, L. J.; Kim, J. Choice of electrode geometry for accurate measurement of organic photovoltaic cell performance. *Appl. Phys. Lett.* **2008,** *92* (13), 133301-133303.

[37] Brunner, P.-L. M.; Masse, J.-P.; L'Espérance, G.; Wuest, J. D. Imaging Layers in Thin-Film Molecular Devices by Transmission Electron Microscopy, Using Milling by Focused Ion Beams and Deposition on NaCl and Si. **2015**, submitted for publication.

[38] Knupfer, M. Exciton binding energies in organic semiconductors. *Appl. Phys. A Mater. Sci. Process.* **2003,** *77* (5), 623-626.

[39] Maryett, A. A.; Smith, E. R. Table of Dielectric Constants of Pure Liquids. Commerce, U. S. D. o., Ed. National Bureau of Standards: Washington D.C., 1951; Vol. 514.

[40] Koster, L. J. A.; Smits, E. C. P.; Mihailetchi, V. D.; Blom, P. W. M. Device model for the operation of polymer/fullerene bulk heterojunction solar cells. *Phys. Rev. B* **2005,** *72*, 085205.

[41] Scharber, M. C.; Móhlbacher, D.; Koppe, M.; Denk, P.; Waldauf, C.; Heeger, A. J.; Brabec, C. J. Design Rules for Donors in Bulk-Heterojunction Solar Cells - Towards 10% Energy-Conversion Efficiency. *Adv. Mater.* **2006,** *18* (6), 789-794.

[42] Deibel, C.; Mack, D.; Gorenflot, J.; Schöll, A.; Krause, S.; Reinert, F.; Rauh, D.; Dyakonov, V. Energetics of excited states in the conjugated polymer poly(3-hexylthiophene). *Phys. Rev. B* **2010,** *81*.

[43] Bolduc, A.; Dong, Y.; Guerin, A.; Skene, W. G. Solvatochromic investigation of highly fluorescent 2-aminobithiophene derivatives. *Phys. Chem. Chem. Phys.* **2012,** *14*, 6946–6956.

[44] Heeger, A. J. Nobel Lecture: Semiconducting and metallic polymers: The fourth generation of polymeric materials. *Rev. Mod. Phys.* **2001,** *73* (3), 681-701.

[45] West, P. R.; Ishii, S.; Naik, G. V.; Emani, N. K.; Shalaev, V. M.; Boltasseva, A. Searching for better plasmonic materials. *Laser Photon. Rev.* **2010,** *4* (6), 795–808.

[46] Sariciftci, N. S.; Smilowitz, L.; Heeger, A. J.; Wudl, F. Photoinduced Electron Transfer from a Conducting Polymer to Buckminsterfullerene. *Science* **1992,** *258*, 1474.

[47] Williams, G.; Aziz, H. Implications of the device structure on the photo-stability of organic solar cells. *Sol. Energ. Mat. Sol. Cells* **2014,** *128*, 320-329.

[48] Verploegen, E.; Mondal, R.; Bettinger, C. J.; Sok, S.; Toney, M. F.; Bao, Z. Effects of Thermal Annealing Upon the Morphology of Polymer–Fullerene Blends. *Adv. Funct. Mater.* **2010,** *20*, 3519–3529.

[49] Park, S. H.; Roy, A.; Beaupré, S.; Cho, S.; Coates, N.; Moon, J. S.; Moses, D.; Leclerc, M.; Lee, K.; Heeger, A. J. Bulk heterojunction solar cells with internal quantum efficiency approaching 100%. *Nature Photon.* **2009,** *3* (5), 297-302.

[50] Friend, R. H.; Denton, G. J.; Halls, J. J. M.; Harrison, N. T.; Holmes, A. B.; Köhler, A.; Lux, A.; Moratti, S. C.; Pichler, K.; Tessler, N.; Towns, K. Electronic Processes of Conjugated Polymers in Semiconductor Device Structures. *Synth. Met.* **1997,** *84* (1-3), 463-470.

[51] Haugeneder, A.; Neges, M.; Kallinger, C.; Spirkl, W.; Lemmer, U.; Feldmann, J.; Scherf, U.; Harth, E.; Gügel, A.; Müllen, K. Exciton diffusion and dissociation in conjugated polymer/fullerene blends and heterostructures. *Phys. Rev. B* **1999,** *59* (23), 15346.

[52] Shaw, P. E.; Ruseckas, A.; Samuel, D. W. Exciton Diffusion Measurements in Poly(3-hexylthiophene). *Adv. Mater.* **2008,** *20* (18), 3516-3520.

[53] Lim, E.; Lee, S.; Lee, K. K. Improved photovoltaic performance of P3HT:PCBM cells by addition of a low band-gap oligomer. *Chem. Commun.* **2011,** *47*, 914–916.

[54] Ma, W.; Kim, J. Y.; Lee, K.; Heeger, A. J. Effect of the molecular weight of poly(3-hexylthiophene) on the morphology and performance of polymer bulk heterojunction solar cells. *Macromol. Rapid Commun.* **2007,** *28* (17), 1776-1780.

Chapitre 3

Cellules photovoltaïques en films minces à base de petites molécules à bandes interdites étroites dispersées dans des matrices polymériques passives

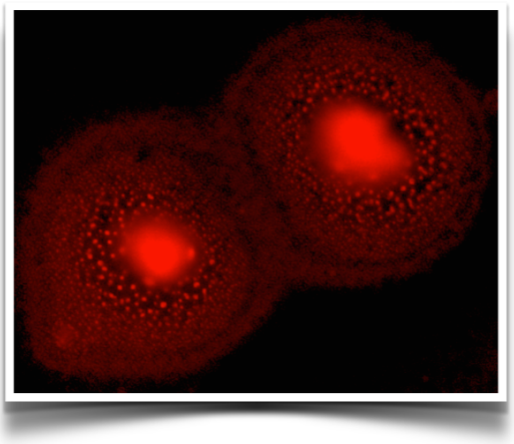

« Rider on the Storm », Cristaux fluorescents

3.1 Introduction article 2

Pour faire suite à la publication présentée au chapitre 2, cette étude reprend les concepts proposés en modifiant le type de matrice polymère utilisée. Le premier postulat voulait qu'une matrice polymère semi-conductrice doive participer activement en terme de transport de charges à travers le film mince. Leur utilisation a non seulement permis de former des films homogènes à partir de petites molécules ayant plutôt une propension à cristalliser, mais a aussi permis d'augmenter les rendements globaux des cellules photovoltaïques à base de ces polymères.

Pour ce chapitre, une approche similaire est présentée. Par contre, les polymères servant à rectifier l'inhomogénéité des films à base de petites molécules sont maintenant non-conducteurs (isolants). Bien que l'utilisation de ce type de polymère comme matrice électroniquement passive semble contre intuitive, certains d'entre eux, notamment le polystyrène (PS) et le polyméthylméthacrylate (PMMA), ont été étudiés conjointement avec certains semi-conducteurs polymériques dans le passé. Ils ont été utilisés en cellules photovoltaïques à base de polymères comme stabilisateurs de la morphologie,[66-68] greffés à des polymères semi-conducteurs pour former des copolymères blocs,[69] ou comme matrices pour étudier par spectroscopie certains semi-conducteurs.[70-71]

Le polystyrène, le polyméthylméthacrylate, le polychlorure de vinyle (PVC), le polyéthylène glycol (PEG) et le poly(diméthylsiloxane) (PDMS) sont des polymères abondant, peu couteux, et qui entres dans la composition d'une grande variété d'objets communs. Ils ont été sélectionnés pour cette étude comme matrices passives potentielles pour la rectification des films minces du composé ID(BTC)$_2$ présenté plus tôt, ou du 7,7′-[4,4-bis(2-éthylhexyl)-4*H*-silolo[3,2-*b*:4,5-*b*′]dithiophène-2,6-diyl]bis[6-fluoro-4-(5′-héxyl-[2,2′-bithiophèn]-5-yl)benzo [*c*]-[1,2,5]thiadiazole] (F-DTS), une molécule disponible commercialement, donnant de bons rendements en cellules photovoltaïques et servant de banc de comparaison.[72] La morphologie des films peut par la suite être étudiée par différentes méthodes de microscopie, dont la

microscopie à force atomique (AFM) et la microscopie électronique à transmission ou a balayage (MET, MEB).

3.2 Article 2

Thin-Film Photovoltaic Devices Incorporating Low-Bandgap Push-Pull Molecules Dispersed in Passive Polymeric Matrices

Pierre-Louis M. Brunner et James D. Wuest

Journal of Polymer Science Part B: Polymer Physics, **2016**, accepté pour publication.

3.2.1 Keywords

Keywords: Organic photovoltaic devices (OPVs), low-bandgap push-pull small molecules, thin films, nanomorphologies, polymer matrices

3.2.2 Abstract

Active layers in thin-film organic photovoltaic devices (OPVs) typically contain light-absorbing polymers that serve as electron donors, mixed with appropriate electron acceptors. In principle, the polymeric components can be advantageously replaced by small molecules with suitable band gaps, which have precisely defined structures and can be synthesized and purified by methods that provide uniform samples. However, such materials often undergo rapid separation of phases and crystallization, so the formation of long-lived thin films that are smooth, homogeneous, flexible, and transparent is not trivial. We have now found that effective active layers in thin-film OPVs can be made by dispersing mixtures of low-bandgap push-pull small molecules as electron donors and [6,6]-phenyl-C_{71}-butyric acid methyl ester ($PC_{71}BM$) as electron acceptor in matrices of optoelectronically passive conventional polymers, including polystyrene, poly(methylmethacrylate), poly(vinylchloride), poly(ethylene glycol), and poly(dimethylsiloxane). By varying the identity of the matrix, its molecular weight, the loading of active components, and the conditions of annealing, we produced efficient OPVs from components that would otherwise have undergone phase separation and crystallization, leading to poor performance. Layers containing up to 35% of passive polymers were found to be effective and could be fabricated at room temperature by simple processes. To probe the role of the polymers as dispersants, morphologies of composite films were examined by AFM and electron microscopy.

3.2.3 Introduction

Fossil fuels provide more than 85% of power currently used, and nearly 100 million barrels of crude oil are consumed daily.[1-2] Fossil fuels will eventually be depleted, and their use damages the environment, making it increasingly urgent to develop alternative sources of energy derived renewably from the sun. Photovoltaic devices, which convert light directly into electricity, have emerged as a prominent source of renewable energy. The best devices of this type are highly efficient, but they remain expensive and tend to be laden with toxic ingredients, particularly heavy elements. An important long-range objective is to produce effective carbon-based analogues that are composed of materials derived from renewable sources and can be fabricated cheaply on a large scale by simple methods such as roll-to-roll printing. A key step in this direction was taken in 1986 by Tang, who reported effective organic photovoltaic devices (OPVs) based on molecular components.[3] Research and development in this area have continued to evolve rapidly, and current OPVs offer the advantages of increasingly high performance, flexibility, light weight, and low cost, making them attractive alternatives to conventional photovoltaic cells based primarily on inorganic materials.[4]

Active layers in typical OPVs contain light-absorbing polymers that serve as electron donors, mixed with suitable electron acceptors. Promising replacements for the polymeric components are small molecules with extended π-conjugation and suitably low band gaps. These replacements are attractive in part because small molecules have precisely defined structures and can be synthesized and purified by methods that provide uniform samples.[5-9] However, such materials often undergo rapid separation of phases and crystallization, so the formation of long-lived thin films that remain smooth, homogeneous, flexible, and transparent is not trivial.[10] We recently reported a new family of small-molecule semiconductors with conjugated π-bridged electron-donating and electron-accepting moieties, which can be described as "push-pull" compounds.[11] Such compounds can absorb broadly across the solar spectrum,[7-8, 12] engage in intramolecular charge-transfer interactions,[13-15] and are increasingly employed as blends with fullerene derivatives in the active layers of thin-film OPVs with bulk

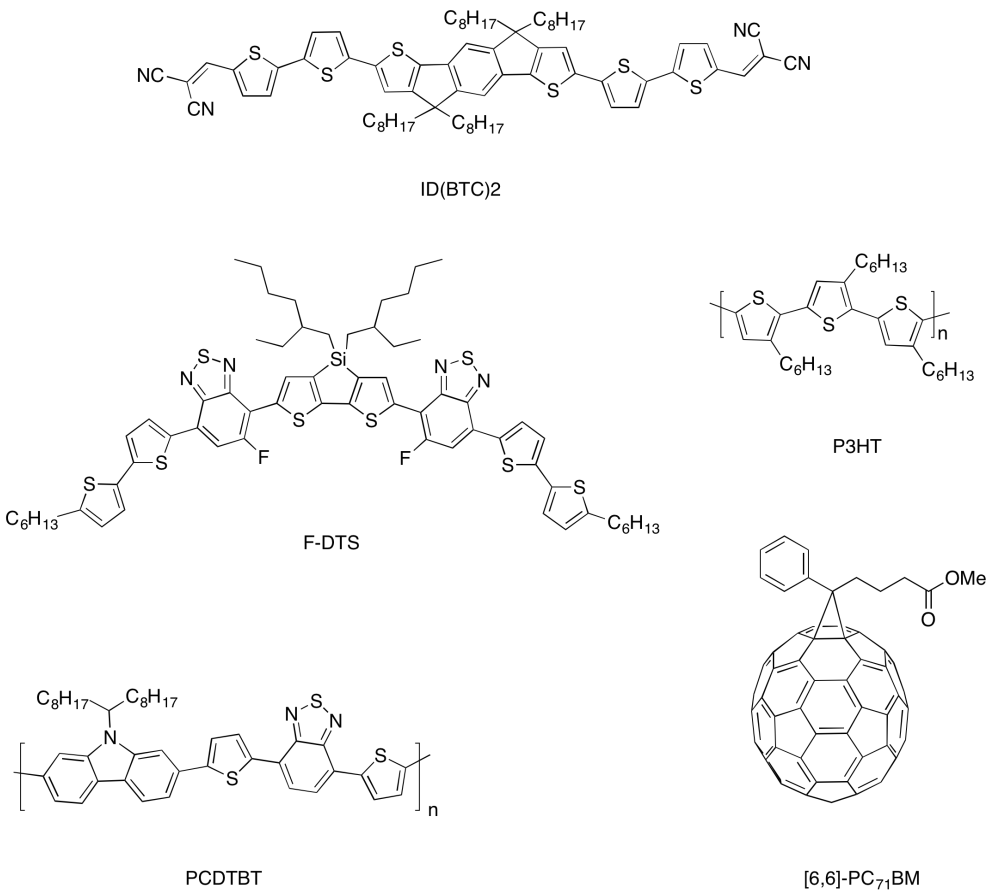

Figure 3.1. Structures of $ID(BTC)_2$ (1), F-DTS, P3HT, PCDTBT, and $PC_{71}BM$. In these structures, C_6H_{13} and C_8H_{17} denote straight alkyl chains.

heterojunction (BHJ) architectures.[16-20] Eventual industrial-scale production of large OPV panels will require high-throughput methods of production such as roll-to-roll printing or offset printing, so effective small-molecule semiconductors that can be formulated as inks and deposited at room temperature to yield uniform films will need to be devised.

The present work examines OPVs incorporating representative push-pull small molecules that show attractive optoelectronic features but cannot readily be deposited as suitable thin films. Examples include push-pull compound $ID(BTC)_2$ (Figure 3.1),[11] in which dicyanovinyl groups serve as electron-withdrawing moieties, and s-indaceno[1,2-*b*:5,6-

b′]dithiophene units linked to bithiophenes act as electron-donating components. In addition, OPVs containing 7,7′-[4,4-bis(2-ethylhexyl)-4*H*-silolo[3,2-*b*:4,5-*b*′]dithiophene-2,6-diyl]bis[6-fluoro-4-(5′-hexyl-[2,2′-bithiophen]-5-yl)benzo[*c*][1,2,5]thiadiazole], a commercially available small push-pull molecule known as F-DTS (Figure 3.1),[21] were studied for comparison. Although $ID(BTC)_2$ and F-DTS are both highly soluble, they crystallize easily when pure and do not readily yield uniform films suitable for use in OPVs. Processes of hot coating, in which both the solutions and the substrates are kept at elevated temperatures during deposition, can help suppress or retard crystallization, but such methods do not provide a general solution to the problem of making continuous thin films composed of small molecules.

As part of previous efforts to inhibit crystallization, we presented the concept of dispersing small active molecules in semiconducting polymers such as regioregular poly(3-hexylthiophene-2,5-diyl) (P3HT) and poly[[9-(1-octylnonyl)-9*H*-carbazole-2,7-diyl]-2,5-thiophenediyl-2,1,3-benzothiadiazole-4,7-diyl-2,5-thiophenediyl] (PCDTBT), which are also shown in Figure 3.1.[11] Surprisingly, we have now found that polymers known to behave as insulators can also serve as matrices. Specifically, polystyrene (PS), poly(methylmethacrylate) (PMMA), poly(vinylchloride) (PVC), poly(ethylene glycol) (PEG), and poly(dimethylsiloxane) (PDMS) can all be used to disperse small active molecular components in the form of homogeneous thin films. To our knowledge, such matrices have not previously been used in this way, although other applications of insulating polymers in thin-film devices have been reported. For example, PS has been incorporated in block copolymers with P3HT (PS-*b*-P3HT) to create compatibilizers for use in OPVs,[22] and low concentrations of PMMA have been added to solar cells containing P3HT and nanorods of TiO_2.[23] In addition, PS has served as a matrix for photoinduced oligomerization of fullerene derivatives to enhance the morphological stability of conventional polymer-fullerene OPVs,[24] and PS has also been blended with P3HT and fullerene derivatives to favor productive molecular self-organization in OPVs.[25] Moreover, a recent paper has reported that the photoluminescence of poly[2-methoxy-5-(2-ethylhexyloxy)-1,4-phenylenevinylene] (MEH-PPV) is enhanced when the compound is blended in thin films with PS.[26] Passive polymeric matrices have also been used in the optical detection and spectroscopy of single molecules.[27] Nevertheless, the use of

passive polymeric matrices to disperse active small molecules and inhibit their crystallization remains little explored in the area of thin-film devices.

3.2.4 Results and Discussion

3.2.4.1 Materials

$ID(BTC)_2$ was synthesized as a purple solid by the reported method,[11] and F-DTS, P3HT, PCDTBT, and $PC_{71}BM$ were provided by Solaris Chem Inc. and used as received. Samples of PS were purchased from Tosoh, samples of PDMS and PMMA from American Polymer Standards Corporation, and samples of PVC and PEG from Sigma-Aldrich. All passive polymeric matrices were used as received.

3.2.4.2 Properties of materials

Relevant electronic properties of $ID(BTC)_2$, F-DTS, and $PC_{71}BM$ are summarized in Table 3.1. $ID(BTC)_2$ is a low-bandgap compound with HOMO and LUMO levels of -5.18 eV and -2.76 eV, respectively, so its electronic properties make it suitable for use in OPVs containing $PC_{71}BM$ as electron acceptor (Figure 3.2a), assuming an excitonic binding energy

Table 3.1. Relevant electronic properties of $ID(BTC)_2$, F-DTS, and $PC_{71}BM$.

	E^{ox} [V]	E^{red} [V]	HOMO [eV]	LUMO [eV]	E^{elec}_g [eV]
$ID(BTC)_2$	+0.42[a]	-2.00[a]	-5.18[b]	-2.76[c]	2.42[d]
F-DTS			-5.12[e]	-3.34[e]	1.78[e]
$PC_{71}BM$			-6.0[f]	-4.0[f]	2.0[f]

[a]Determined by cyclic voltammetry using films on glassy carbon electrodes,[24] with redox potentials vs Ag/Ag^+ measured in solutions of NBu_4PF_6 in MeCN; [b]HOMO calculated as $E_{HOMO} = -(E^{ox} + 4.76)$ eV; [c]LUMO calculated as $E_{LUMO} = -(E^{red} + 4.76)$ eV; [d]Electronic bandgap ($E_{LUMO} - E_{HOMO}$); [e]Reported value[21]; [f]Reported value[28]

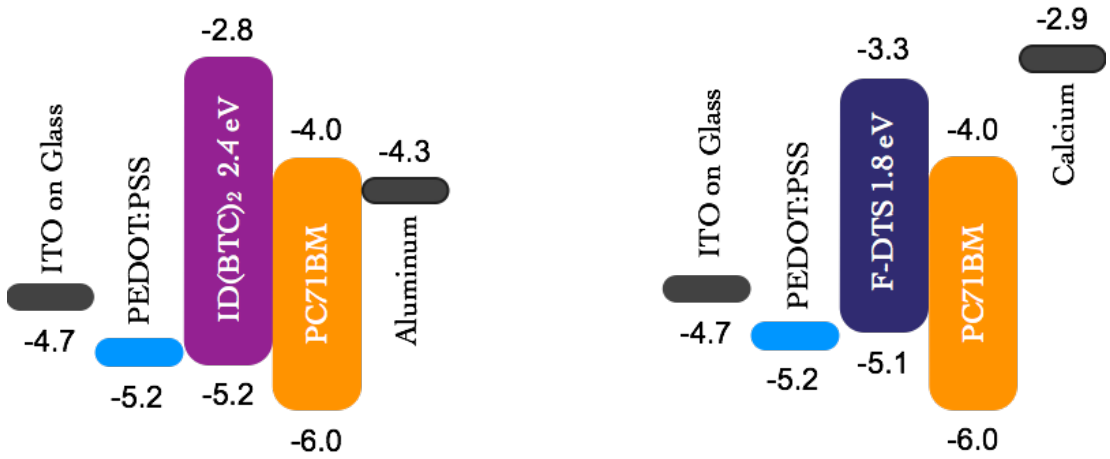

ITO/PEDOT:PSS/ID(BTC)$_2$:PC$_{71}$BM/Al

a

ITO/PEDOT:PSS/F-DTS:PC$_{71}$BM/Ca

b

Figure 3.2. Representation of the relative positions of the HOMOs and LUMOs of components of OPVs, as well as the sequence of layers that defines the architecture of the devices. (a) Devices containing ID(BTC)$_2$. (b) Devices containing F-DTS.[21] In both cases, ITO is used to abbreviate indium tin oxide, and PEDOT:PSS signifies poly(3,4-ethylenedioxythiophene):poly(styrenesulfonate).

of 0.4 eV.[29-30] F-DTS is also suitable (Figure 3.2b), based on reported HOMO and LUMO levels of -5.12 eV and -3.34 eV, respectively,[21] giving a bandgap lower than that of ID(BTC)$_2$. High values of V_{oc} are expected in OPVs containing ID(BTC)$_2$ or F-DTS, as determined by the large differences $HOMO_{donor}$ - $LUMO_{PC71BM}$ arising from the low HOMO energy levels of both electron donors.

Polymers used as passive matrices were selected from among commonly available materials widely used as standards for gel-permeation chromatography because of their low dispersity and well-characterized molecular weights (M_W and M_N). The molecular weights, polydispersity indices (PDI), and glass-transition temperatures (T_g) for the selected polymers are presented in Table 3.2.

Table 3.2. Physical properties of selected polymer matrices.[a]

	M_w	M_n	PDI	T_g (°C)
PS10	1.02×10^4	1.00×10^4	1.02	92
PS100	9.64×10^4	9.55×10^4	1.01	98
PS1000	1.09×10^6	1.00×10^6	1.08	102
PMMA10	1.20×10^4	1.06×10^4	1.13	105
PMMA100	9.04×10^4	8.85×10^4	1.02	105
PMMA1000	1.00×10^6	9.30×10^5	1.08	115[31]
PDMS150	1.48×10^5	1.11×10^5	1.33	150[32]
PEG150	1.49×10^5	1.31×10^5	1.11	-67
PVC80	8.00×10^4	4.70×10^4	1.70	80[33]

[a]Values provided by the supplier unless indicated otherwise

3.2.4.3. Photovoltaic devices

Small molecules $ID(BTC)_2$ and F-DTS were both tested individually, without a polymeric matrix, as the active electron donors and main light-harvesting components in OPVs containing $PC_{71}BM$ as the electron acceptor. The devices featured a standard architecture (glass/ITO/PEDOT:PSS/SM:$PC_{71}BM$/metal, where SM = small molecule and metal = Ca or Al) and were fabricated using conventional methods. In particular, the components of the active layers were deposited by spin coating at 25 °C, using solutions in 1,2-dichlorobenzene. The power conversion efficiency (PCE) of the devices was assessed as a function of SM:$PC_{71}BM$ ratios, film thicknesses,[11, 21] and conditions of annealing (Table 3.3). The highest value of PCE obtained for matrix-free devices containing $ID(BTC)_2$ as the active donor was 1.40%, obtained with $PC_{71}BM$ as the electron acceptor, an $ID(BTC)_2$:fullerene ratio of 1:1 by weight, no annealing, and a film thickness of 120 ± 10 nm. The resulting cells showed a modest open-circuit voltage (V_{oc} = 583 mV), which was lower than expected based on the difference between the HOMO of $PC_{71}BM$ (-4.0 eV) and the HOMO of $ID(BTC)_2$

Table 3.3. Performance of OPVs based on active layers with $ID(BTC)_2$:$PC_{71}BM$ or F-DTS:$PC_{71}BM$ dispersed in passive polymer matrices, along with other data added for comparison. Unless indicated otherwise, devices were annealed for 10 min.

SM	Polymer Matrix	Matrix M_w (kDa)	Matrix Content (%)	Annealing Temp. (°C)[e]	V_{oc} (mV)	J_{sc} (mA/cm^2)	FF (%)	PCE_{max} (%)
$ID(BTC)_2$	-	-	0	-	583	7.87	30.4	1.40
$ID(BTC)_2$	-	-	0	-	680	6.72	30.0	1.37[b,c]
$ID(BTC)_2$	-	-	0	65	771	6.28	28.0	1.35
$ID(BTC)_2$	PS10	10	35	65	684	7.04	31.1	1.50
$ID(BTC)_2$	PS100	96	15	65	768	7.12	29.0	1.59
$ID(BTC)_2$	PS1000	1090	25	65	707	5.66	27.3	1.09
$ID(BTC)_2$	PMMA10	12	25	65	808	3.34	26.0	0.70
$ID(BTC)_2$	PMMA100	90	25	65	734	3.72	27.0	0.74
$ID(BTC)_2$	PMMA1000	1000	25	65	753	3.53	24.0	0.64
$ID(BTC)_2$	PEG150	149	25	65	809	7.14	29.0	1.68
$ID(BTC)_2$	PVC80	80	25	65	550	6.45	30.7	1.09
$ID(BTC)_2$	PVC80	80	25	165	890	6.82	49.6	3.01
$ID(BTC)_2$	PVC80	80	25	225	748	5.02	27.5	1.03
$ID(BTC)_2$	PDMS150	148	25	-	624	0.38	21.0	0.05
$ID(BTC)_2$	PCDTBT	80	25	-	846	9.70	47.1	3.87[a]
F-DTS	-	-	0	135	667	1.95	37.5	0.49
F-DTS	-	-	0	65	815	7.51	31.2	1.91[b,c]
F-DTS	-	-	0	135	682	11.31	52.0	4.01[b,c]
F-DTS	PS100	96	15	65	763	10.97	51.5	4.32[b,c]
F-DTS	PS100	96	15	135	738	11.19	49.7	4.11[b,c]
F-DTS	PS100	96	25	65	772	10.47	52.0	4.13[b,c]
F-DTS	PS100	96	25	135	726	8.62	36.1	2.26[b,c]
F-DTS	PVC80	80	15	65	755	11.85	50.4	4.50[b,c]
F-DTS	PVC80	80	15	135	705	10.73	37.7	2.86[b,c]
F-DTS	PVC80	80	25	65	701	2.76	34.6	0.67[b,c]
F-DTS	PVC80	80	25	135	827	8.23	28.4	1.94[b,c]
F-DTS	PVC80	80	25	65	719	3.29	31.8	0.75
F-DTS	PVC80	80	25	135	758	7.19	36.0	1.95
P3HT	-	-	0	150[f]	615	8.05	51.9	2.56[d]
P3HT	PS100	96	15	150[f]	587	7.72	55.7	2.53[d]
PCDTBT	-	-	0	-	866	10.26	51.7	4.59[d]
PCDTBT	PS100	96	15	-	825	9.71	47.2	3.78[d]
PCDTBT	PS100	96	15	65	825	9.74	46.2	3.71[d]

[a]Using PCDTBT polymer matrix as previously reported[11]
[b]Annealing of film at 65 °C for 10 min before depositing the electrode
[c]Spin coating carried out at 80 °C (solution and substrate)
[d]Reference using a standard semiconducting polymer as donor
[e]Post-production annealing of complete device for 10 min except where indicated otherwise
[f]Annealing for 20 min

(-5.18 eV) as the Voc is proportional to the difference between the aceptor's $LUMO_{PC71BM}$ and the donor's HOMO $_{ID(BTC)2}$.[34] The short-circuit current density (J_{sc}) was high (7.87 mA/cm^2), but the fill factor (FF) was only 30.4%. For matrix-free devices containing F-DTS and $PC_{71}BM$, the highest value of PCE was only 0.49% when spin coating was carried out at 25 °C. In both series of matrix-free devices, the low values of PCE can be attributed to films of poor quality, as observed in other cases in which small molecules are primary components of the active layers.[35] Films deposited from solutions at 25 °C revealed a strong tendency for the components to crystallize, as demonstrated by higher roughness in images obtained by atomic force microscopy (AFM) and by the direct observation of birefringent crystals using optical microscopy under polarized light.[36] Hot spin coating, carried out by keeping substrates for deposition (glass/ITO/PEDOT:PSS) and solutions of the active components at 80-90 °C under N_2, was examined because encouraging results have been reported for F-DTS using this technique,[21] but the method did not prove to be effective for $ID(BTC)_2$.

To improve the quality of films and attain higher values of PCE, we decided to disperse small-molecule components in various passive matrices listed in Table 3.2. The ratios of donor to acceptor ($PC_{71}BM$) were 1:1 by weight for $ID(BTC)_2$ and 3:2 by weight for F-DTS. The amounts of passive matrix lay in the range 0-50% of the total weight of the active layers, and the film thicknesses were kept constant at approximately 120 nm by adjusting concentrations in 1,2-dichlorobenzene (for $ID(BTC)_2$) or chlorobenzene (for F-DTS).

In the case of $ID(BTC)_2$, PS10 (M_W = 10 kDa), PS100 (M_W = 100 kDa), and PS1000 (M_W = 1000 kDa) were used as matrices for the active components. The performance of the resulting OPVs was found to be highly dependent on M_W and on the amount of matrix (Figure 3.3). For PS100, PCE was higher (1.59%) than the one measured for unannealed matrix-free reference cells (1.40%), despite dilution of the active components. The improved performance can be attributed to an increased value of FF when the matrix was used, whereas V_{oc} and J_{sc} (750 mV and 7.0 mA/cm^2, respectively) remained similar to values observed in matrix-free reference cells. Incorporating PS10 also gave a higher value of PCE (1.54%), even when the passive matrix was present at the level of 35% w/w. Increasing the amount of matrix steadily raised FF, thereby counterbalancing potentially adverse effects on morphology related to the

ability of $ID(BTC)_2$ (acting as electron donor) and $PC_{71}BM$ (acting as electron acceptor) to undergo a proper degree of phase separation and attain an optimal molecular organization. In this optimal organization, efficient separation of charges and subsequent percolation can occur within the active layer because short-lived excitons are able to survive long enough to reach a suitable donor/acceptor interface.[37-39]

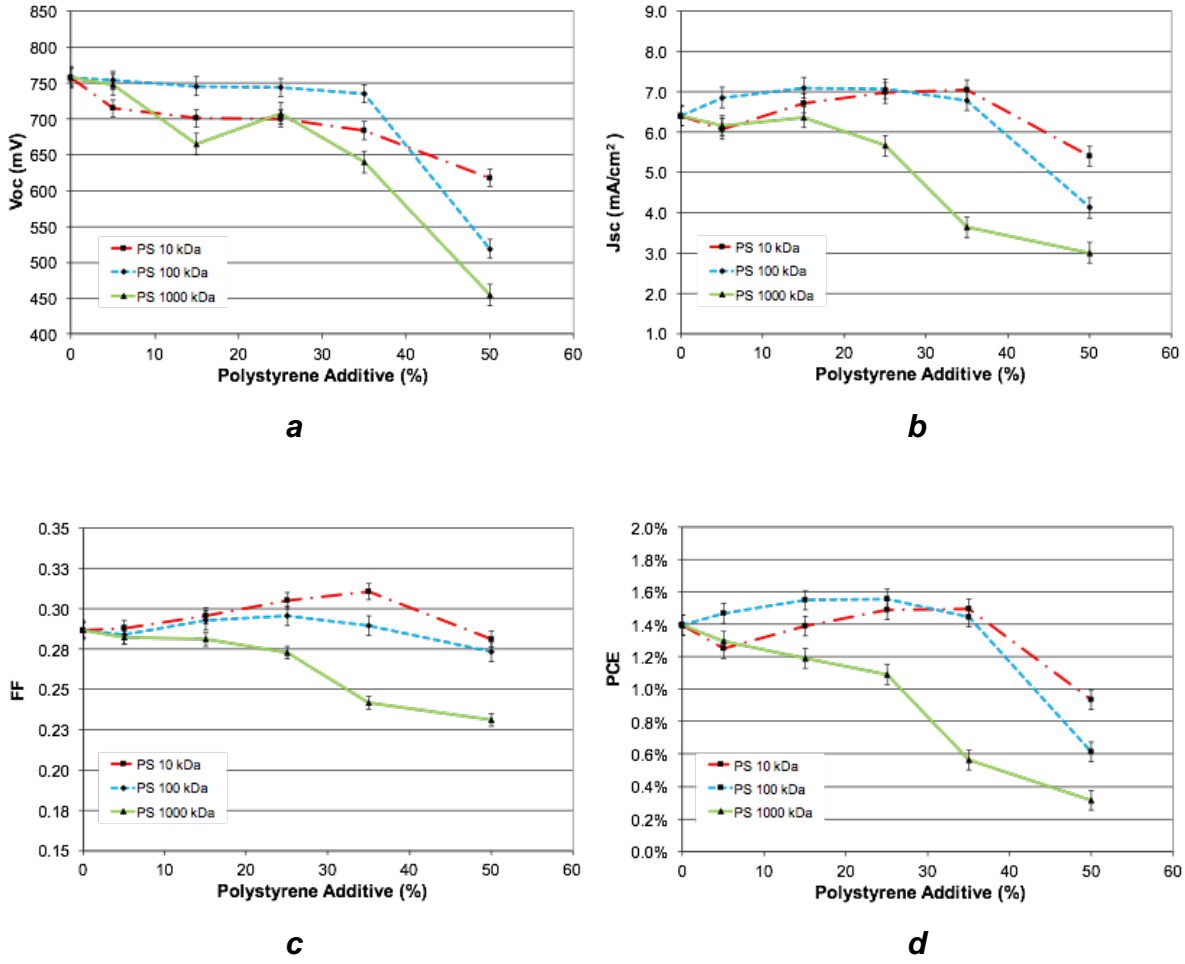

Figure 3.3. Performance of OPVs incorporating unannealed active layers containing $ID(BTC)_2$ as the electron donor and $PC_{71}BM$ as the electron acceptor, with PS of different molecular weights (10 kDa, 100 kDa, and 1000 kDa) added in varying amounts as a passive matrix. (a) V_{oc}. (b) J_{sc}. (c) FF. (d) PCE. In all graphs, parameters are plotted as a function of the percentage by weight of the passive matrix as a component of the entire active layer.

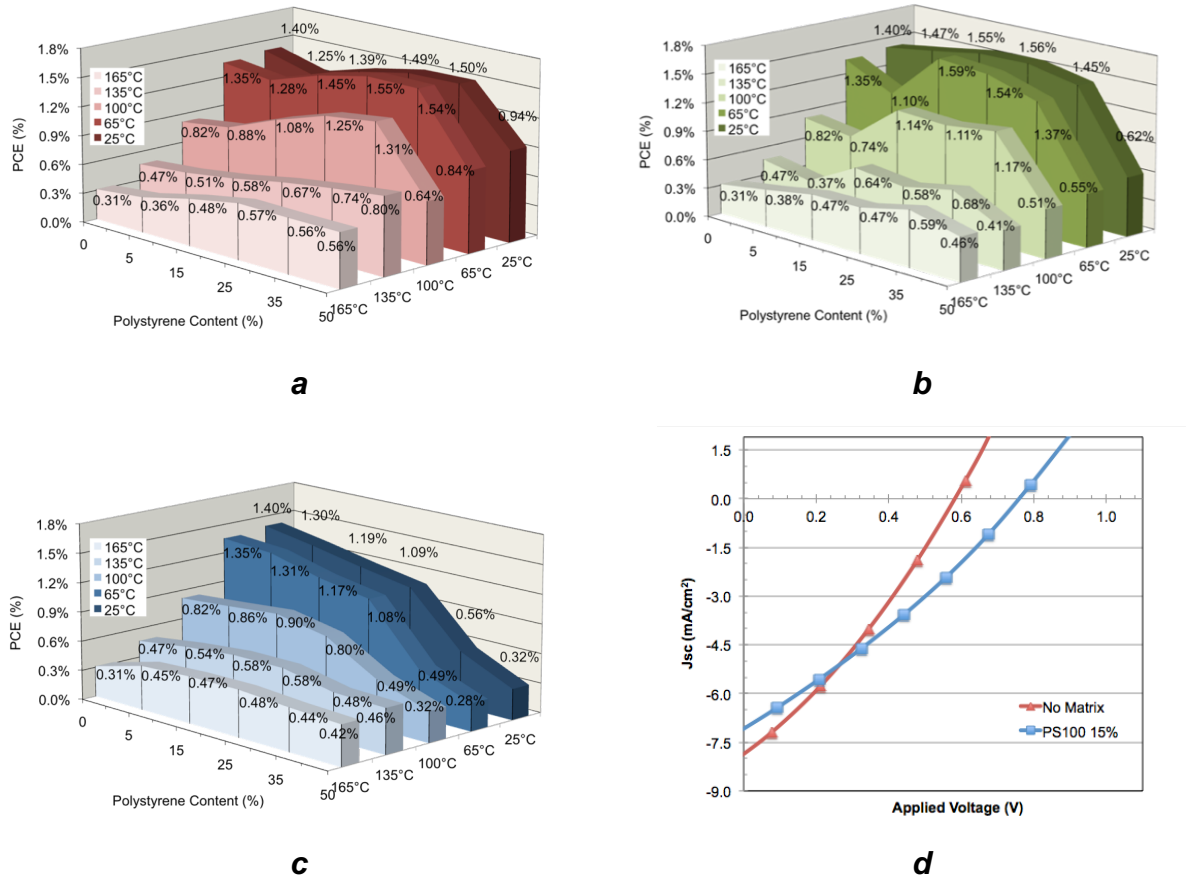

Figure 3.4. Performance of OPVs with active layers containing ID(BTC)$_2$:PC$_{71}$BM annealed at temperatures in the range 25-165 °C, as a function of the weight percentage of added PS with different values of M_W. (a) PS10. (b) PS100. (c) PS1000. (d) J-V curve showing the performance of a reference cell with no added PS matrix and the performance of an analogue with an active layer containing 15% PS100, after annealing at 65 °C.

In the case of F-DTS, "cold" spin coating at 25 °C gave poor results, because PS matrices could not prevent crystallization effectively until over 50% of polymer had been added.[36] At this level of added matrix, we believe that the bulk of the thin film is no longer able to transport charges toward the electrodes because the active components are too highly dispersed, and charge percolation is inefficient.

Annealing OPVs at elevated temperatures for short periods frequently allows the active components to undergo a degree of phase separation and achieve effective nanomorphologies, thereby increasing performance.[40-41] As a result, $ID(BTC)_2$ and $PC_{71}BM$ were combined with PS10, PS100, or PS1000 as passive matrices, and the resulting films were briefly annealed (10 min) at temperatures in the range 25-165 °C (Figure 3.4). Annealing films containing PS10 and PS100 at 65 °C yielded devices with slightly higher values of PCE (1.55% and 1.59%, respectively) than those of unannealed references, whereas annealed cells containing active layers with no matrix or a matrix of PS1000 performed less well. In all cases, performance decreased when films were annealed at temperatures above 65 °C.

All key data related to the addition of passive matrices, annealing, and the performance of OPVs are collected in Table 3.3. Together, this information suggests that high-temperature annealing may induce excessive phase separation and facilitate crystallization of the small molecular components, leading to low values of FF and poor performance. It is noteworthy that OPVs with 35% PS10 by weight showed enhanced thermal stability and maintained a PCE value of 1.31% after being heated at 100 °C, whereas reference cells without matrix showed a decreased PCE value of 0.82% when subjected to the same conditions. This suggests that matrices can offer two potential advantages as components of the active layers in devices incorporating small molecules: (1) Matrices can help forestall an undesirable degree of phase separation or crystallization of small molecules, and (2) they can also inhibit subsequent alteration of effective molecular organization, once it has been created.

To probe the effects of dispersing active components in matrices of PS, layers containing $ID(BTC)_2$:$PC_{71}BM$ were imaged by AFM, and the results are presented in Figure 3.5. Thin films without PS were the roughest, with a root-mean-square (RMS) value of 4.34 nm. In addition, large birefringent particles indicative of crystallization could be observed by optical microscopy under polarized light.[36] Dispersal in PS (15% by weight) resulted in smoother films, with RMS values of 0.66 nm, 1.44 nm, and 0.85 nm for PS10, PS100, and PS1000, respectively. Furthermore, features observed in the AFM images suggest that the matrix alters the nanomorphology of the films. The samples are nearly flat, so the phase-shift

signal reflects local differences in viscoelastic properties.[42] In the case of PS10, changes in contrast are easily visible in the phase image, but they are more diffuse and subtle than those seen in the case of PS100, where well-dispersed discotic features appeared and grew upon annealing at 165 °C for 10 min (Figure 3.6). Similar images have been noted when mixtures of P3HT:$PC_{61}BM$ are dispersed in matrices of PS.[25] The discotic features show a very narrow range of sizes, with an average of about 600 nm. In the case of PS1000, segregation of materials was also observed as diffuse patches, although they were not as well defined as in the case of PS100.

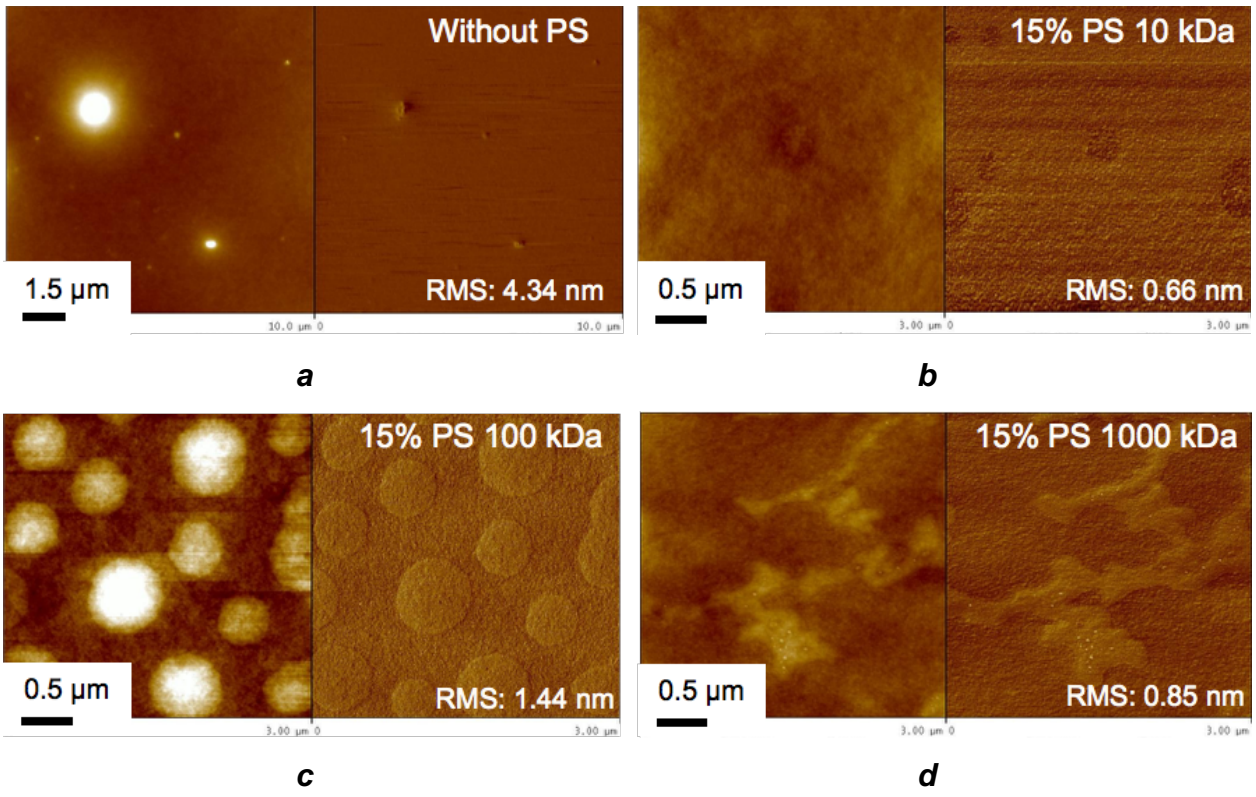

Figure 3.5. Pairs of AFM images of thin films containing $ID(BTC)_2$:$PC_{71}BM$, with topography on the left side of the pairs and phase imaging on the right. (a) No added PS. (b) 15% PS10 by weight. (c) 15% PS100 by weight. (d) 15% PS1000 by weight. The films were annealed at 165 °C for 10 min. The images are 3 × 3 μm^2 in all cases, except for the image in Figure 3.5a, which is 10 × 10 μm^2 in size.

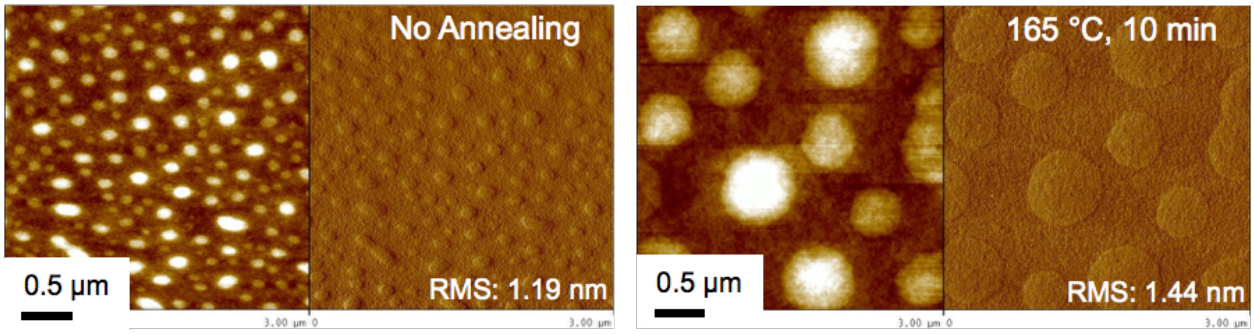

Figure 3.6. Pairs of AFM images of thin films containing ID(BTC)$_2$:PC$_{71}$BM in a matrix of PS100 (15% by weight), with topography on the left side of the pairs and phase imaging on the right. (a) Film without annealing. (b) Film annealed at 165 °C for 10 min. The images are 3 × 3 µm^2 in size.

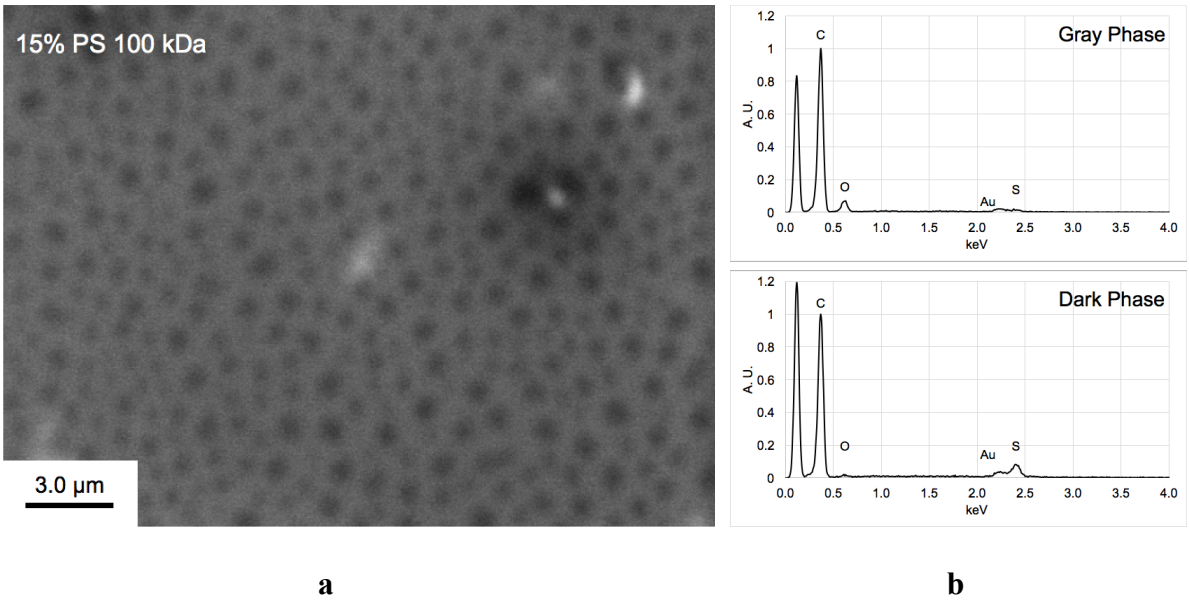

Figure 3.7. (a) SEM image of a thin film of ID(BTC)$_2$ and PC$_{71}$BM containing 15% PS100 by weight, after annealing at 165 °C. (b) Analyses of the dark discotic phase and surrounding light gray phase by EDXS (normalized data).

Scanning electron microscopy (SEM) was used to examine the characteristic discotic features of films of ID(BTC)$_2$ and PC$_{71}$BM containing 15% PS100 (Figure 3.7), and the images again reveal a pattern of disks (Figure 3.7a). Because only ID(BTC)$_2$ contains sulfur and only PC$_{71}$BM contains oxygen, their distribution in the film can be assessed by using energy-dispersive X-ray spectroscopy (EDXS) to measure S/C and O/C ratios in the dark disks versus the surrounding light gray phase (Figure 3.7b). The EDXS data clearly reveal that the dark disks are enriched in ID(BTC)$_2$, and the surrounding phase is enriched in PC$_{71}$BM.

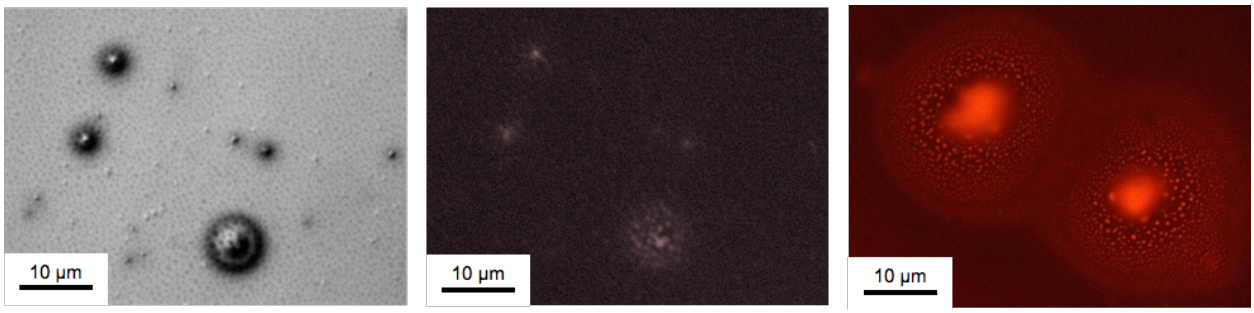

a **b** **c**

Figure 3.8. Fluorescence micrographs of thin films of ID(BTC)$_2$:PC$_{71}$BM containing 15% PS100, after annealing at 165 °C. (a) Large (2-8 µm) crystallites of PC$_{71}$BM appearing as prominent dark regions against a background of more finely structured film (imaged with no filter and light source off). (b) Fluorescence of the region shown in Figure 8a, now under illumination (imaged using a Zeiss DAPI filter). (c) Fluorescence from large (6-10 µm) crystals of ID(BTC)$_2$ under illumination (imaged using a Zeiss DAPI filter).

Annealed thin films of ID(BTC)$_2$ and PC$_{71}$BM containing 15% PS100 were also imaged by fluorescence microscopy to help identify the composition of the phases (Figure 3.8). The finely structured light gray background of the image in Figure 3.8a reveals discotic features roughly 600 nm in size, which are similar in size and shape to the features imaged by AFM (Figure 3.6b) and SEM (Figure 3.7a). In addition, large spherulites (2-8 µm) of crystallizing PC$_{71}$BM are also visible as prominent dark features. Large crystals of ID(BTC)$_2$

also appeared in the films, and their bright photoluminescence allowed them to be identified by fluorescence microscopy (Figure 3.8c). The large crystals were found to be surrounded by many smaller photoluminescent particles within a halo of radius 15 μm. This phenomenon may reflect scavenging of $ID(BTC)_2$ from the surrounding medium in the course of nucleation and growth of crystallites. Fullerenes are known to quench fluorescence by photoinduced electron transfer from the excited state of conducting polymers, leading to local suppression of emission in mixed phases where both components are present.[43, 44] Depleted levels of $PC_{71}BM$ in the immediate vicinity of crystallizing $ID(BTC)_2$ can thereby account for enhanced emission.

Other insulating polymers were added at a level of 25% by weight as potential passive matrices for $ID(BTC)_2$ and F-DTS. Table 3.3 summarizes the performance of OPVs containing PEG150 (M_W = 150 kDa), PVC80 (M_W = 80 kDa), PDMS150 (M_W = 150 kDa), PMMA10 (M_W = 10 kDa), PMMA100 (M_W = 100 kDa), and PMMA1000 (M_W = 1000 kDa). In addition, the films were annealed at temperatures in the range 25-225 °C and imaged by AFM and SEM to trace the evolution of their structures (Figure 3.9). Although most of the matrices gave films with diffuse features or no phase separation visible by optical microscopy, 25% PEG150 gave rise to a marked discotic arrangement (Figure 3.9b), as also found for 15% PS100 incorporating either $ID(BTC)_2$ or F-DTS. The disks were found to be uniform in size (approximately 500 nm) and to be evenly dispersed. Pure films of polymers were also annealed at these temperatures and imaged to confirm that the observed discotic nanostructure is a feature of the active layers, not merely the polymeric matrix itself.[36] Slight differences were observed in the discotic structure of annealed films containing 15% PS100 (Figure 3.6) and 25% PS100 (Figure 3.8a), but the value of PCE was about 1.6% in both cases.

Unlike the disks resulting from dispersal in 15% PS100 (Figure 3.6), those observed in films containing 25% PEG150 did not grow during annealing but rather appeared to become spherical and extend from the surface, increasing the RMS roughness to over 35 nm. Imaging by SEM (Figure 3.10) revealed that growing crystalline masses of $ID(BTC)_2$ or $PC_{71}BM$ appear to be drawing additional molecules from the surroundings, creating halos

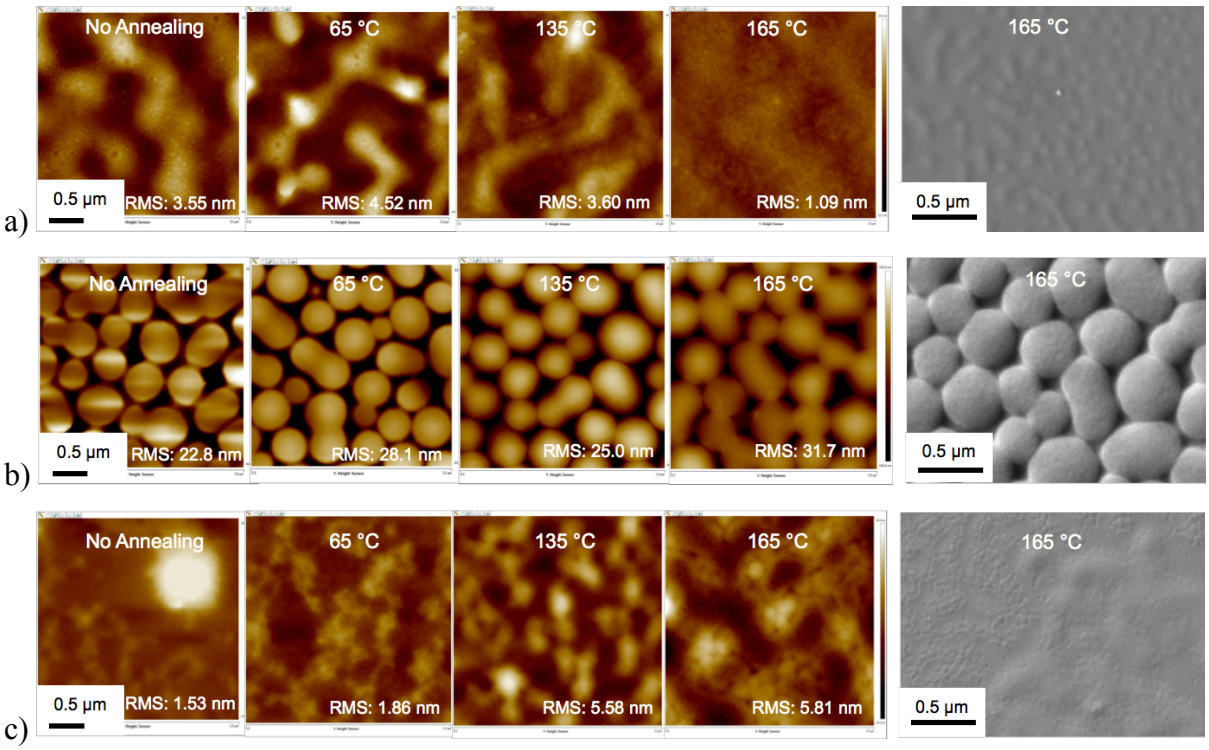

Figure 3.9. AFM images (colored) and SEM images (grayscale) of thin films containing $ID(BTC)_2$:$PC_{71}BM$ dispersed in matrices of PS, PEG, and PVC, recorded before and after annealing at various temperatures. (a) 25% PS100. (b) 25% PEG150. (c) 25% PVC80. The AFM images are 3×3 µm in size.

corresponding to zones of depletion. For both small molecules $ID(BTC)_2$ and F-DTS, optical micrographs under polarized light show small crystals that appear to diminish in size and be subsumed by larger growing crystals, as observed previously by fluorescence microscopy (Figure 3.8). This phenomenon was not observed by optical microscopy for crystals of $PC_{71}BM$ (although fluorescence varied in the surrounding area because of depletion), thereby providing a reliable method to distinguish crystals of $PC_{71}BM$ from those of other components. We believe that the characteristic discotic domains are rich in polymer and also contain high concentrations of $ID(BTC)_2$ or F-DTS, and the surrounding areas have an

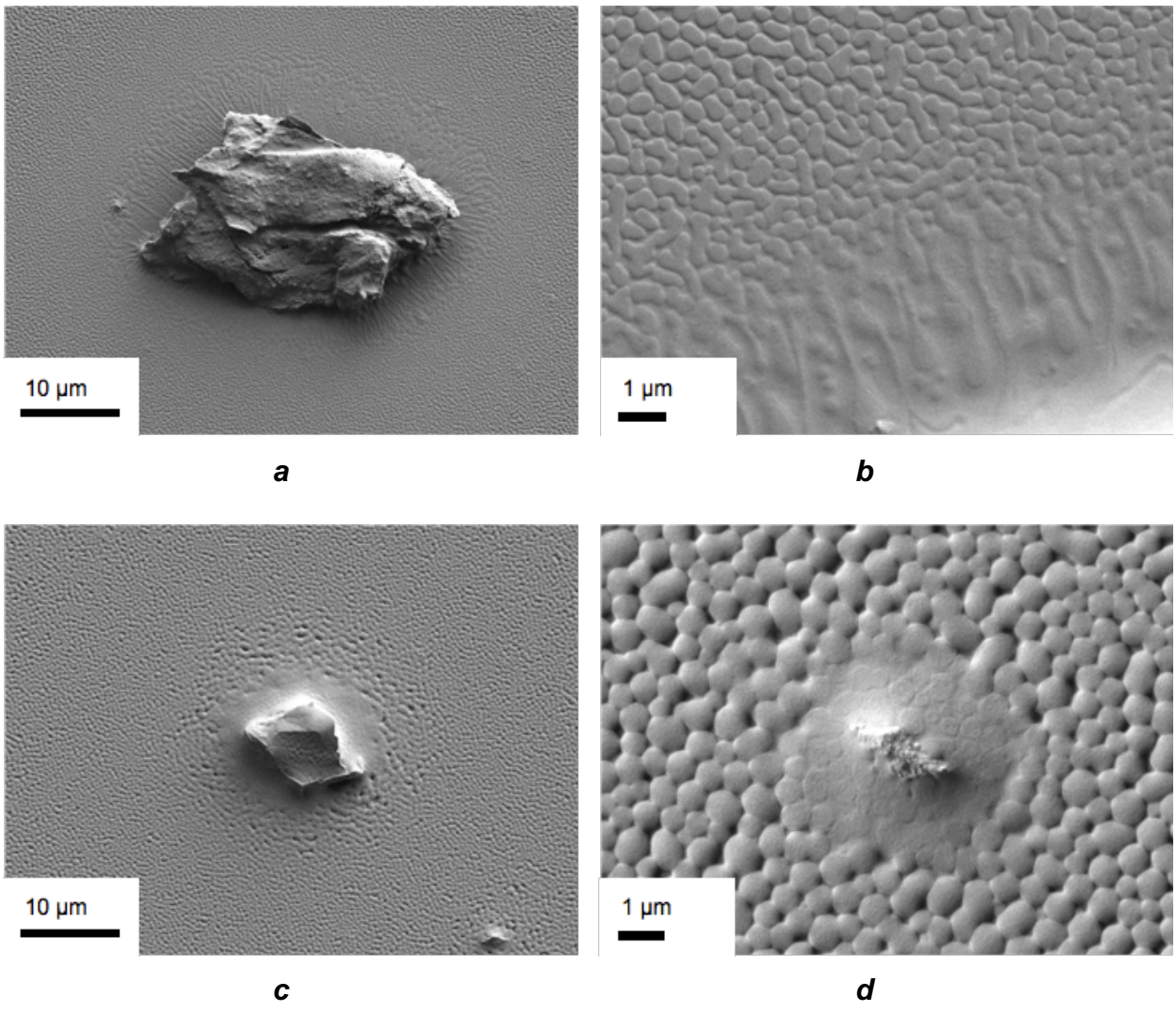

Figure 3.10. SEM images of thin films of $ID(BTC)_2$:$PC_{71}BM$ containing 25% PEG150 by weight, after annealing at 165 °C. (a) Crystalline mass of $ID(BTC)_2$. (b) Enlarged view of the discotic organization of the film surrounding the crystalline mass in Figure 3.10a. (c) Crystalline mass of $PC_{71}BM$. (d) Enlarged view of the discotic organization of the film surrounding an emerging crystalline mass of $PC_{71}BM$.

abundance of $PC_{71}BM$, as established by EDXS (Figure 3.7b). Similar features were not detected in films of pure polymer annealed at any temperatures, so the observed discotic morphology requires blending of the polymer with other components of the active layer.[36] Discotic domains enriched in $ID(BTC)_2$ or F-DTS can change shape and become elongated,

flatter, or more diffuse as they are depleted by the scavenging effect of growing crystals. In particular, growing depleted zones around crystals of the small-molecule components was observed both by SEM (Figure 3.10b) and by fluorescence microscopy (Figure 3.8c). When crystals of $PC_{71}BM$ grow in the films, the surrounding regions are again depleted, but in this case material is now scavenged from non-discoidal domains, leaving the disks intact in size and shape around growing crystals, as shown in Figure 3.10d. However, the disks become more closely spaced as $PC_{71}BM$ is drawn toward growing crystals, both in films containing PEG150 and PS100.[36] Fully intact discoidal domains containing either $ID(BTC)_2$ or F-DTS were found in close proximity to crystallites of $PC_{71}BM$, as revealed by optical microscopy under polarized light and by fluorescence microscopy (Figure 3.8).

3.2.4.3.1 Results using other matrices

Matrices of PDMS yielded OPVs with very poor performance (PCE = 0.05%) and gave very rough films, suggesting that PDMS does not inhibit crystallization effectively. Films containing PMMA of any value of M_W gave poorer cells (PCE = 0.64%-0.70%) than those fabricated from films without matrices. It is possible that PMMA has an affinity for $PC_{71}BM$ through weak interactions involving carboxymethyl groups, thereby disfavoring phase separation and preventing the formation of bulk heterojunctions. Indeed, optical microscopy and fluorescence microscopy established that adding up to 50% PMMA did not prevent crystallization of $ID(BTC)_2$ or F-DTS, but no crystals of $PC_{71}BM$ were detected. Instead of making distinctive disks, PDMS and PMMA yielded more diffuse patterns of interconnected plates.[36]

Films with either $ID(BTC)_2$ or F-DTS in PVC80 required annealing at much higher temperatures to produce effective devices. After annealing at 165 °C, devices containing $ID(BTC)_2$ exhibited a value of PCE in excess of 3.0%, mainly by increasing V_{oc} (890 mV) and FF (49.6%). Such devices also displayed high thermal stability, with PCE = 1.03% even after annealing at 225 °C. Increasing the temperature of annealing generally results first in increased roughness of films, as components diffuse to form larger features. Decreased

roughness can then observed at still higher temperatures, when the matrices are no longer able to retain the small molecular components, which diffuse and converge to form phase-separated crystalline domains, as revealed by optical microscopy.[36] The matrices are thereby purified and can form films that are smooth, except in the vicinity of crystallites.

Films created by spin coating F-DTS and $PC_{71}BM$ at 25 °C without a polymeric matrix yielded ineffective OPVs (PCE = 0.49% PCE), but hot spin coating at 80-90 °C boosted the value of PCE to 4.01%. Hot spin coating and rapid evaporation appear to inhibit the crystallization of F-DTS and lead to the creation of uniform films. Adding PS100 to the mixtures used for hot spin coating resulted in even better devices, with PCE = 4.32% (15% PS100) and 4.13% (25% PS100) when lower temperatures of subsequent annealing were used (65 °C). Replacing PS100 by PVC80 resulted in PCE = 4.50% (15% PVC80) and 0.67% (25% PVC80) after annealing at 65 °C, suggesting that a high proportion of PVC80 disfavors proper phase separation. Both hot and cold spin coating of mixtures of F-DTS, $PC_{71}BM$, and 25% PVC80, followed by annealing of the films at 135 °C, gave similar results, with values of PCE of about 2.0% in both cases. AFM images revealed that films produced by either hot or cold spin coating had similar morphologies and roughness (Figure 3.11). It is noteworthy that the incorporation of PVC80 increased PCE by 12% (from 4.01% to 4.50%) and allowed annealing to be carried out at a lower temperature.

The AFM images in Figure 3.11 reveal that major changes in nanomorphology occur during thermal annealing. Increased smoothness arising in the range 65-135 °C appears to reflect T_g of PVC80 (80 °C). At 165 °C, crystallites become visible, and overall roughness begins to rise. As the temperature of annealing is further increased, even larger crystals are formed, leaving a depleted thin film in intervening spaces, which shows lower roughness locally.

Table 3.3 also includes comparative tests that show how adding PS100 (15% by weight) alters the performance of classic polymer-based OPVs containing P3HT (1:1 with $PC_{71}BM$) or PCDTBT (1:3 with $PC_{71}BM$). In the case of P3HT, adding small amounts of

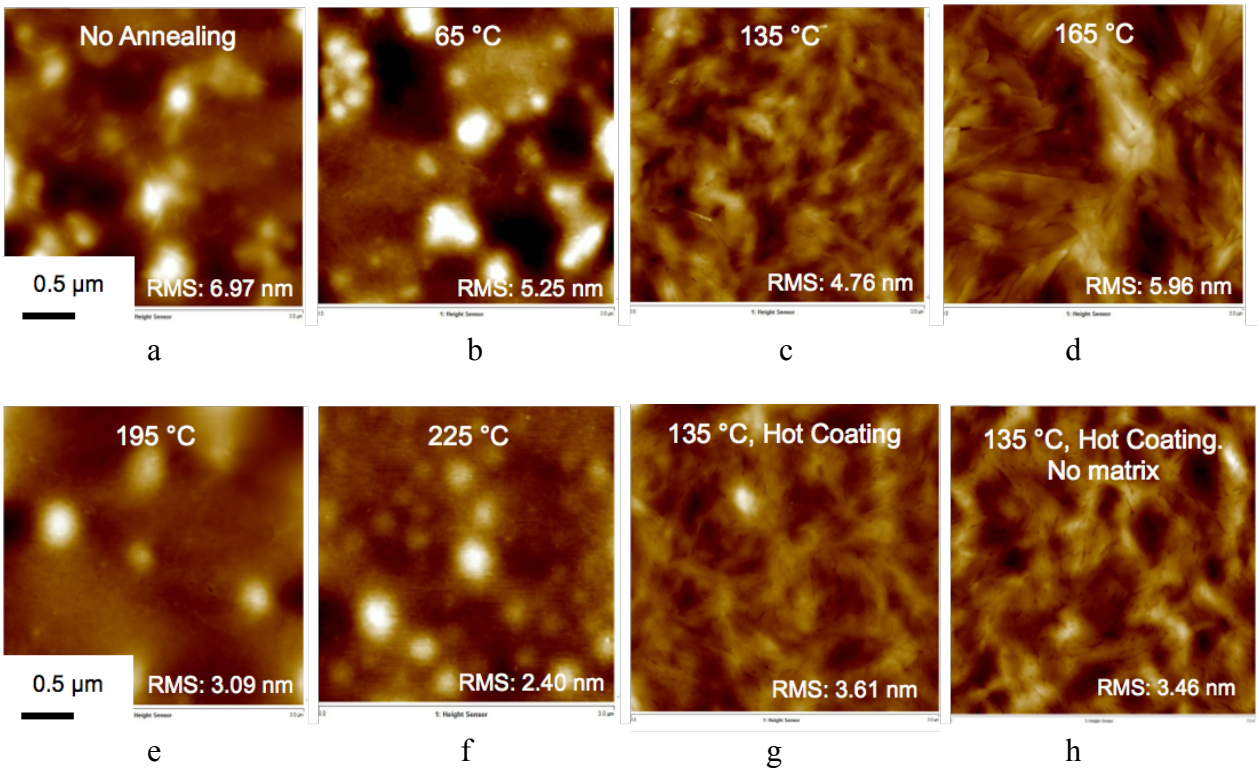

Figure 3.11. AFM images of thin films of F-DTS:$PC_{71}BM$ blended with 25% of PVC 80 kDa, as a function of the annealing temperature from 25 to 225 °C. (a) 25 °C. (b) 65 °C. (c) 135 °C. (d) 165 °C. (e) 195 °C. (f) 225 °C. (g-h) Using hot coating of the solutions. (g) 25% PVC 80 kDa. (h) No matrix added. All samples annealed for 10 minutes.

PS100 did not affect performance, even after annealing at the high temperatures generally required for active layers of P3HT:$PC_{71}BM$. PCDTBT was tested without annealing and with annealing at relatively low temperatures, because the performance of active layers of PCDTBT:$PC_{71}BM$ is normally highest under these conditions.[45] We found that PCE dropped from 4.59% to about 3.75% after the addition of only 15% PS100, suggesting that the additive reduces the density of productive heterojunctions. In the cases of P3HT and PCDTBT, added polymeric matrices are not needed to produce effective thin films; however, dilution of costly components with cheap polymers may be advantageous, whenever it can be done without significant loss of performance.

3.2.5 Conclusions

The high tendency of small molecules to crystallize makes them inherently unsuitable for producing uniform thin films, so their direct use in OPVs and other devices is problematic. We have found that blending optoelectronically active small molecules with passive polymeric matrices makes it possible to modulate the rates of diffusion, phase separation, and crystallization. By proper selection of the polymeric matrix, its molecular weight, and other variables including the amount of matrix added, conditions used to deposit the active layer, and the temperature of annealing, it is possible to produce effective OPVs from components that would not otherwise yield suitable thin films. In addition, typical active components are much more expensive than passive polymeric matrices of the type we have used, so the ability to dilute active films with inexpensive fillers is of substantial commercial interest, especially when performance is maintained or even enhanced. Furthermore, the addition of passive matrices can make OPVs more resistant to thermal degradation, as exemplified by the sustained performance of devices containing $ID(BTC)_2$ after annealing at 225 °C. Finally, it is possible that passive matrices can act as barriers that inhibit the diffusion of O_2, water, or other agents, thereby minimizing chemical degradation of sensitive active components. Our results will thereby help lead to the creation of efficient hybrid OPVs in which low-bandgap small molecules serve to absorb light, separate charges, and transport charges to electrodes, and passive film-forming polymeric components are used to fine-tune morphology, increase performances, minimize cost, and lengthen lifetime.

3.2.6 Experimental Section

3.2.6.1 Active materials

$ID(BTC)_2$ was synthesized as previously described.[11] F-DTS, PCDTBT and $PC_{71}BM$ were provided by Solaris Chem Inc. and used as received. PS was purchased from Tosoh,

PVC was purchase from Sigma Aldrich, and PMMA, PEG, and PDMS were purchased from American Standards and used as received.

3.2.6.2 Fabrication, characterization, and testing of OPVs

Unless stated otherwise, thin-film OPVs were fabricated using a standard architecture defined as follows: glass/ITO/PEDOT:PSS/SM:$PC_{71}BM$:matrix/Ca/Al, where SM designates a small molecular component and matrix refers to a passive polymeric component. Custom-made ITO substrates (20 × 18 mm^2, with a standard resistivity of 20 Ω $square^{-1}$) were purchased from Colorado Concept Coatings LLC. Current density-voltage (J-V) measurements were carried out using a computer-controlled Keithley Model 236 Source-Measure Unit. The source of light was a 150 W Oriel solar simulator using a xenon arc lamp with an AM 1.5 filter. The incident optical power at the height of the sample was assessed at 100 mW/cm^2 with the aid of a monocrystalline Si photovoltaic reference cell provided by PV Measurements Inc. and calibrated by the National Renewable Energy Laboratory (NREL). To avoid overestimations, the photovoltaic performance of cross-bar circular-island cells was determined using a circular shadow mask with an aperture corresponding to the active area of the devices (12.6 mm^2).[46-47]

OPVs were fabricated in the following way. ITO-coated glass substrates were cleaned by sequential 15 min ultrasonic treatments in deionized water, acetone, and isopropanol, followed by exposure in a UV-ozone cleaner for 15 min. Aqueous dispersions of PEDOT:PSS (Clevios PH 1000, Heraeus) were filtered through a 0.45 μm Teflon membrane and spin coated at 4000 rpm for 90 s on the cleaned ITO-coated glass substrates. The resulting films were baked at 110 °C for 20 min in air. A film thickness of 30 ± 4 nm was measured by profilometry, using a Dektak 3030ST stylus profilometer. Solutions of the components of the active layer in 1,2-dichlorobenzene (for $ID(BTC)_2$) or chlorobenzene (for F-DTS) were prepared under N_2 in a glove box by gentle stirring at 40 °C on a hotplate for at least 2 h. The resulting solutions were spin coated on top of the underlying PEDOT:PSS layer at 1000 rpm for 90 s, with acceleration to the final speed achieved over 10 sec. In the case of F-DTS, the

substrates and solutions were heated at 80-90 °C on a hotplate in a glove box, then spin coating was carried out at 1750 rpm for 1 min. The thicknesses of the active layers were determined using atomic force microscopy (AFM). Cathodes (100 nm) were then applied by thermal evaporation of either Al (99.999% pure pellets from Kurt J. Lesker Company) or Ca (Sigma Aldrich) onto the active layer under reduced pressure (10^{-6} mbar) through a shadow mask at a rate of 1-2 Å s^{-1}. The Ca cathodes were covered by Al from a second deposition. All thicknesses and deposition rates were determined using a quartz crystal thickness monitor. The circular area of the active cell was determined to be 12.6 mm^2. Thermal treatments were conducted under N_2 in a glove box equipped with a hotplate, using various temperatures and times of annealing.

3.2.6.3 Imaging

AFM images were acquired in air at 25 °C using a Digital Instruments EnviroScope (Santa Barbara, California) and a Nanoscope IIIa controller (Veeco/Bruker). Imaging with intermittent contact ("tapping mode") was performed at a scan rate of 1 Hz using etched Si cantilevers (ACTA, Applied NanoStructures, Inc.) with a resonant frequency of about 300 kHz, a spring constant of approximately 42 N m^{-1}, and a tip radius of <10 nm. All AFM images were acquired with medium damping of tip oscillation (20-30%).

Transmission electron microscopy (TEM) was carried out using a JEOL JEM-2100F microscope operated at 200 kV for bright-field imaging of samples. Detached samples of thin films were prepared by an innovative method,[48] in which materials are deposited by spin coating on various polished surfaces. Subsequent thermal annealing was done in the way used to process completed OPVs. Detached films were floated off the underlying solid surface and allowed to settle on films of carbon (100-mesh ultrathin carbon or holey carbon), which were dried prior to imaging. Further annealing experiments could be carried out by heating the carbon films mounted on Cu grids.

Scanning electronic microscopy (SEM) was performed with a JEOL JSM-7600F field-emission instrument using backscattered electrons. Thin films were covered with a layer of gold (about 10 nm) before imaging. EDXS measurements were made at 10 kV.

3.2.6.4 Fluorescence microscopy

Fluorescence optical microscopy was done using a Carl Zeiss LSM 510/AxioImager.M1 confocal microscope equipped with a Zeiss AxioCam MRm camera and an X-Cite 120 fluorescence illuminator. The system used either (1) a Zeiss filter set 02 (DAPI) with G 365 excitation, FT 495 beam splitter, and LP 420 emission or (2) a Zeiss filter set 43HE (Cy3) with G 550 excitation, FT 570 beam splitter, and BP 605 emission. Images were recorded with an LD EC Epiplan-Neofluar 100x/0.75 HD DIC M27 objective with a working distance of 4.0 mm.

3.2.7 Acknowledgments

The authors are grateful to the Natural Sciences and Engineering Research Council of Canada, the Ministère de l'Éducation du Québec, the Canada Foundation for Innovation, the Canada Research Chairs Program, NanoQuébec, and the Université de Montréal for financial support. The authors acknowledge with gratitude the fruitful advice of Patricia Moraille (Laboratoire de caractérisation des matériaux, Département de chimie, Université de Montréal), Jean-Philippe Masse (Centre de caractérisation microscopique des matériaux $(CM)^2$, École Polytechnique de Montréal), Antoine Leblanc-Hotte (École Polytechnique de Montréal), Dr. Daniel Beaudoin (Université de Montréal), and Dr. Dominic Laliberté (Solaris Chem Inc., Montréal).

3.2.8 Supplemental Information

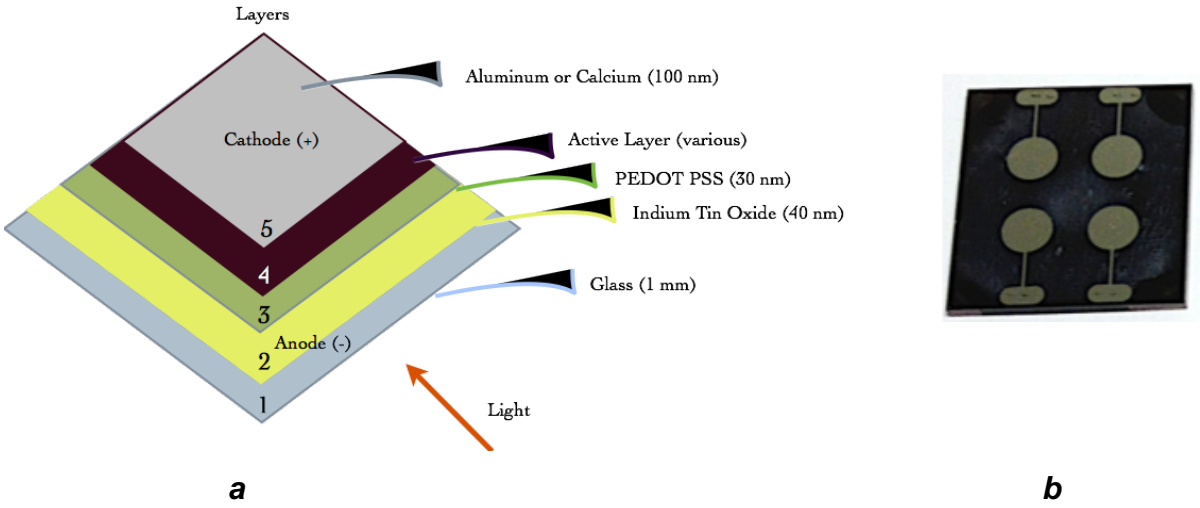

Figure S3.1. (a) Schematic representation of the architecture of OPVs used in the present study. (b) Photograph of four-cell substrate with circular Al back electrodes.

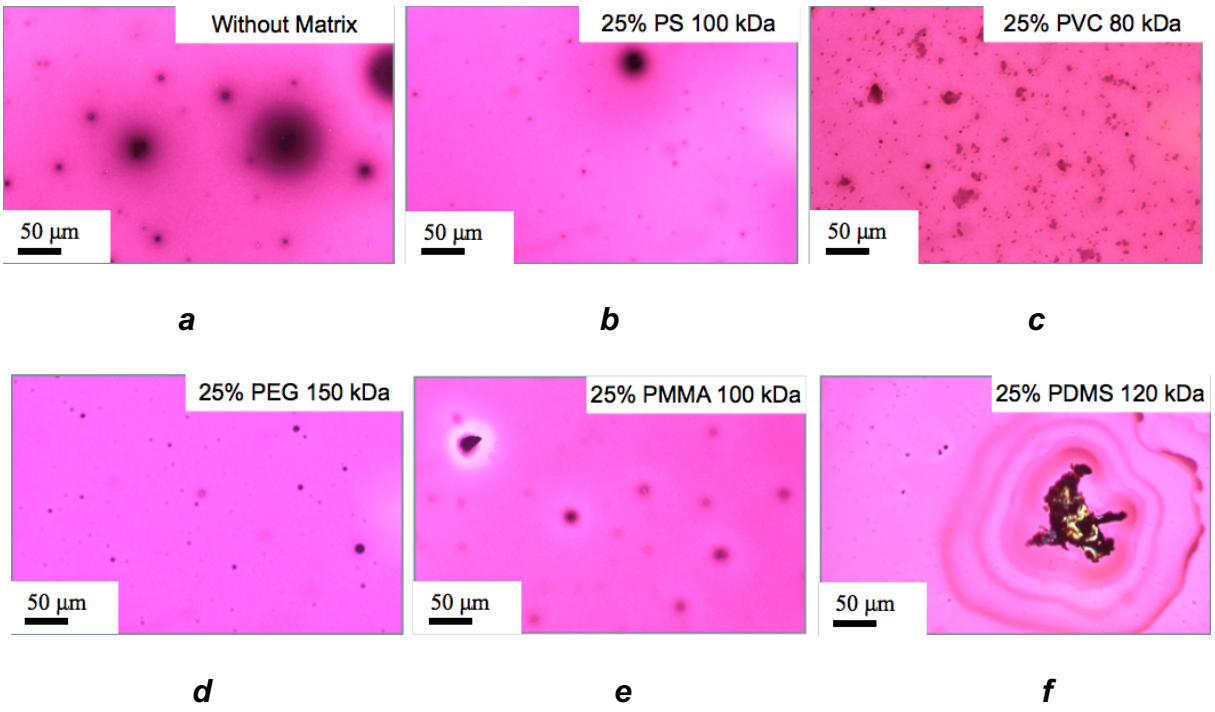

Figure S3.2. Optical micrographs under polarized light, showing thin films of ID(BTC)$_2$:PC$_{71}$BM with or without matrices, after annealing at 165 °C. (a) Without matrix. (b) 25% by weight PS100 (100 kDa). (c) 25% PVC80 (80 kDa). (d) 25% PEG150 (150 kDa). (e) 25% PMMA100 (100 kDa). (f) 25% PDMS120 (120 kDa).

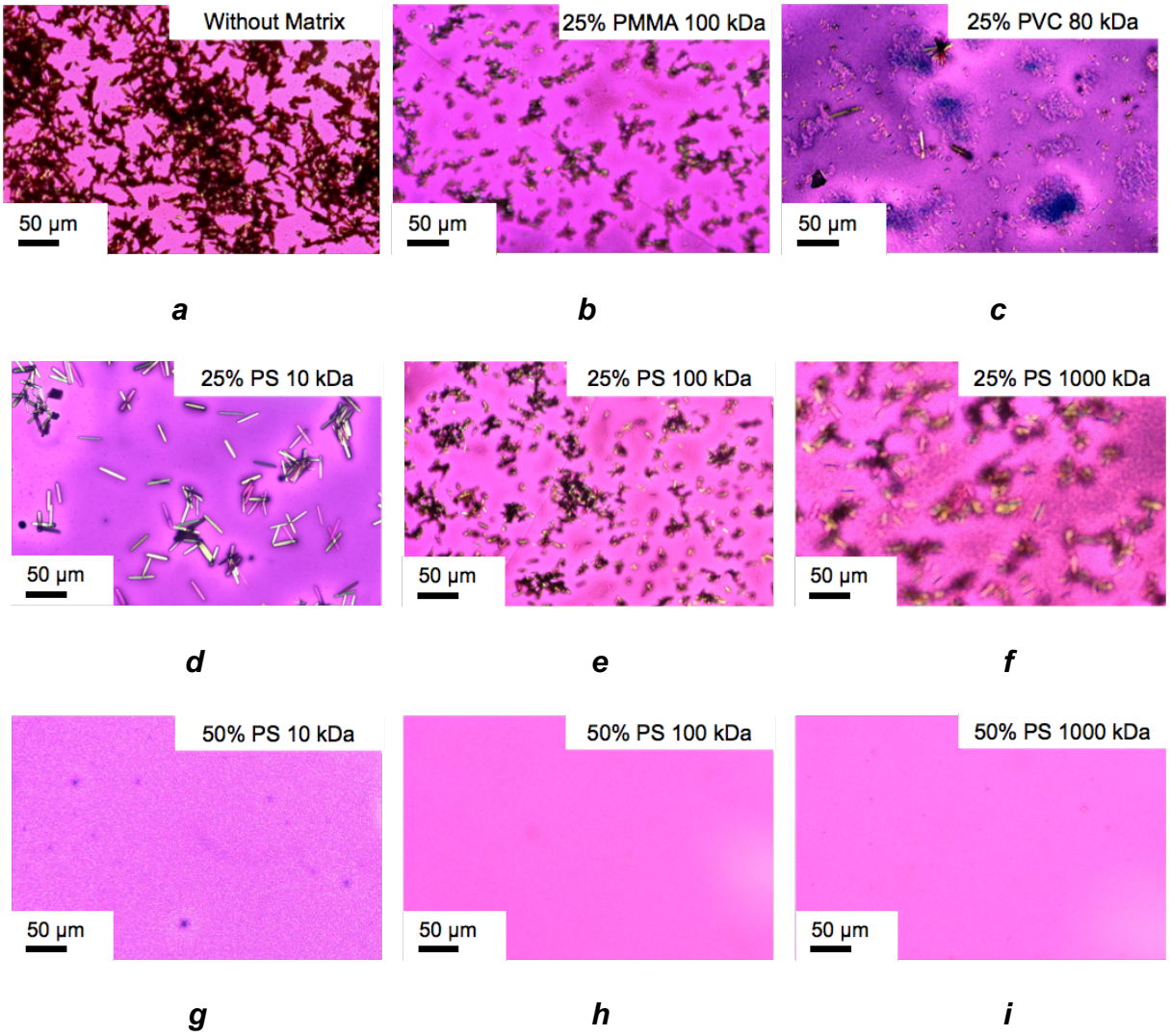

Figure S3.3. Optical micrographs under polarized light, showing thin films of F-DTS:$PC_{71}BM$ with or without matrices. The thin films were created by spin coating at 30 °C, followed by annealing at 165 °C. (a) Without matrix. (b) 25% by weight PMMA100 (100 kDa). (c) 25% PVC80 (80 kDa). (d) 25% PS10 (10 kDa). (e) 25% PS100 (100 kDa). (f) 25% PS1000 (1000 kDa). (g) 50% PS10 (10 kDa). (h) 50% PS100 (100 kDa). (i) 50% PS1000 (1000 kDa).

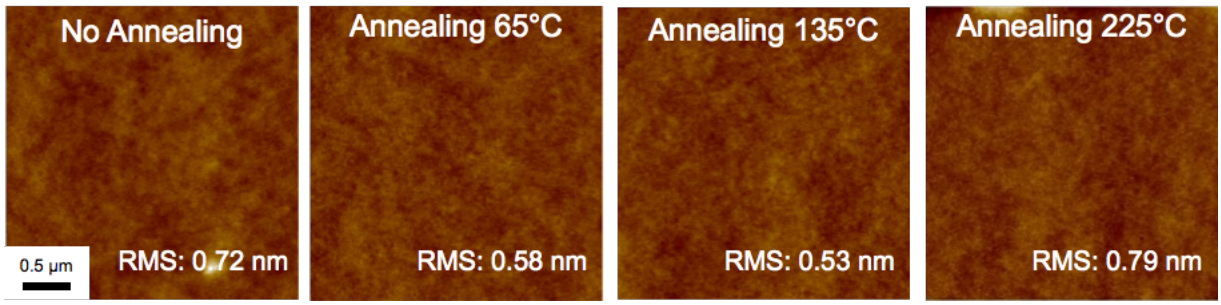

a

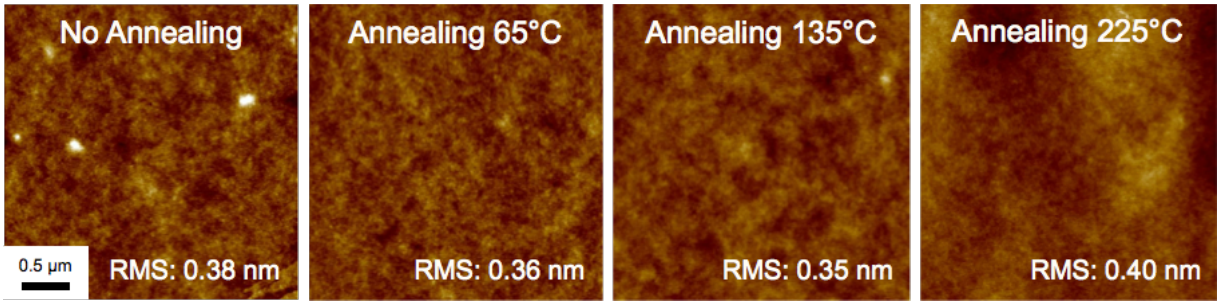

b

Figure S3.4. AFM images of thin films of pure samples of polymers created by spin coating and annealed at 25, 65, 135, and 225 °C for 10 min. (a) PS100. (b) PVC80.

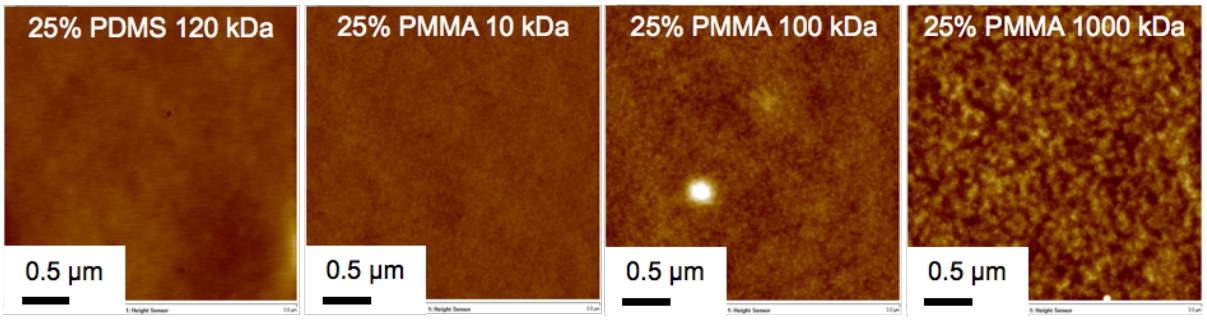

a *b* *c* *d*

Figure S3.5. AFM images showing the topography of unannealed thin films of ID(BTC)$_2$:PC$_{71}$BM containing 25% by weight of selected polymers. (a) PDMS120 (120 kDa). (b) PMMA10 (10 kDa). (c) PMMA100 (100 kDa). (d) PMMA1000 (1000 kDa).

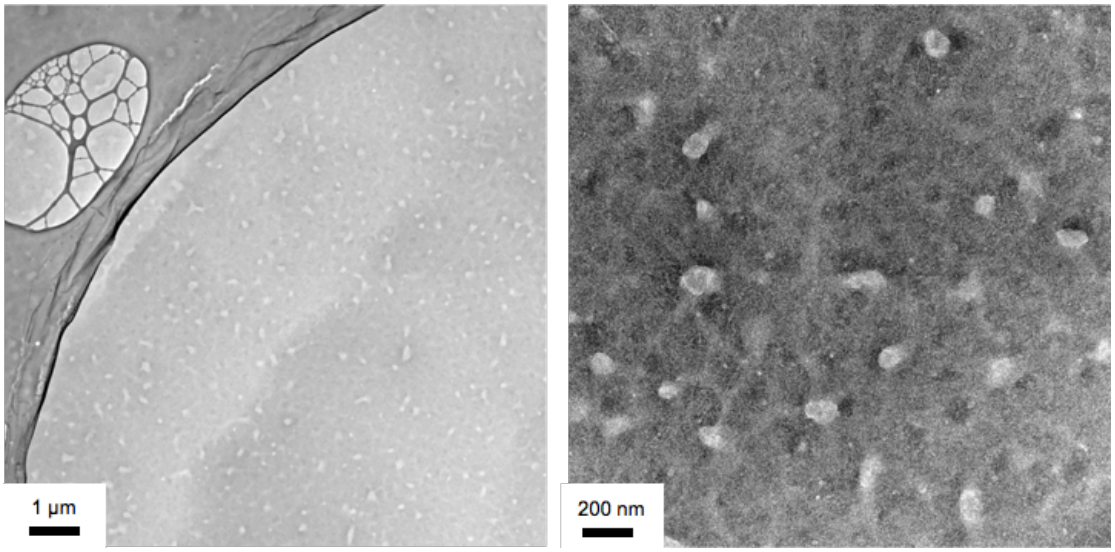

Figure S3.6. TEM images obtained on a support of holey carbon, showing an unannealed thin film containing F-DTS, $PC_{71}BM$, and 15% by weight PEG150. (a) Scale 10 × 10 μm^2. (b) Scale 2 × 2 μm^2.

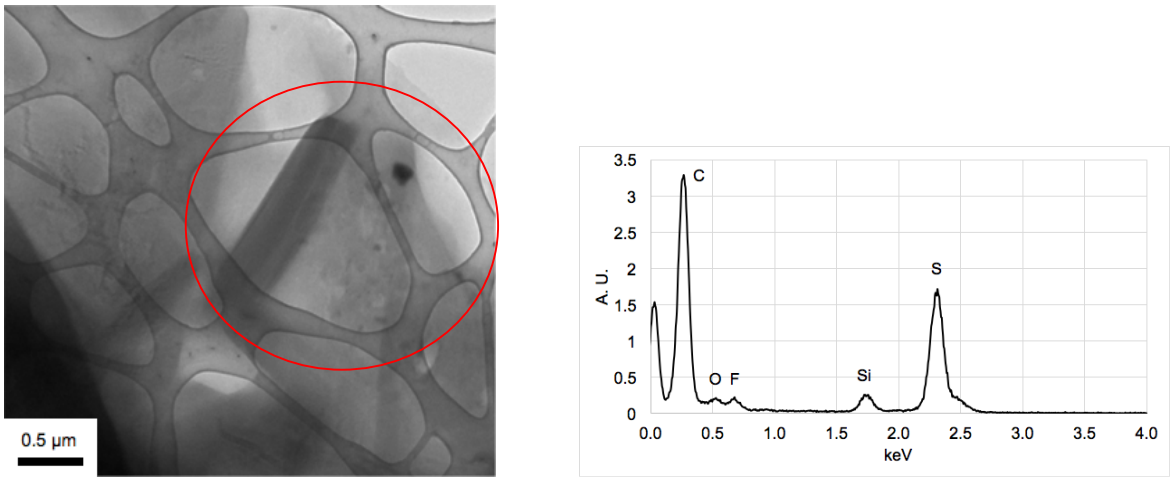

Figure S3.7. (a) TEM image obtained on a support of holey carbon, showing an un-annealed matrix-free thin film of F-DTS and $PC_{71}BM$ created by spin coating at 25 °C. (b) Analysis by EDXS of a dark region (circled in red) identified as a crystallite of F-DTS imbedded in the film.

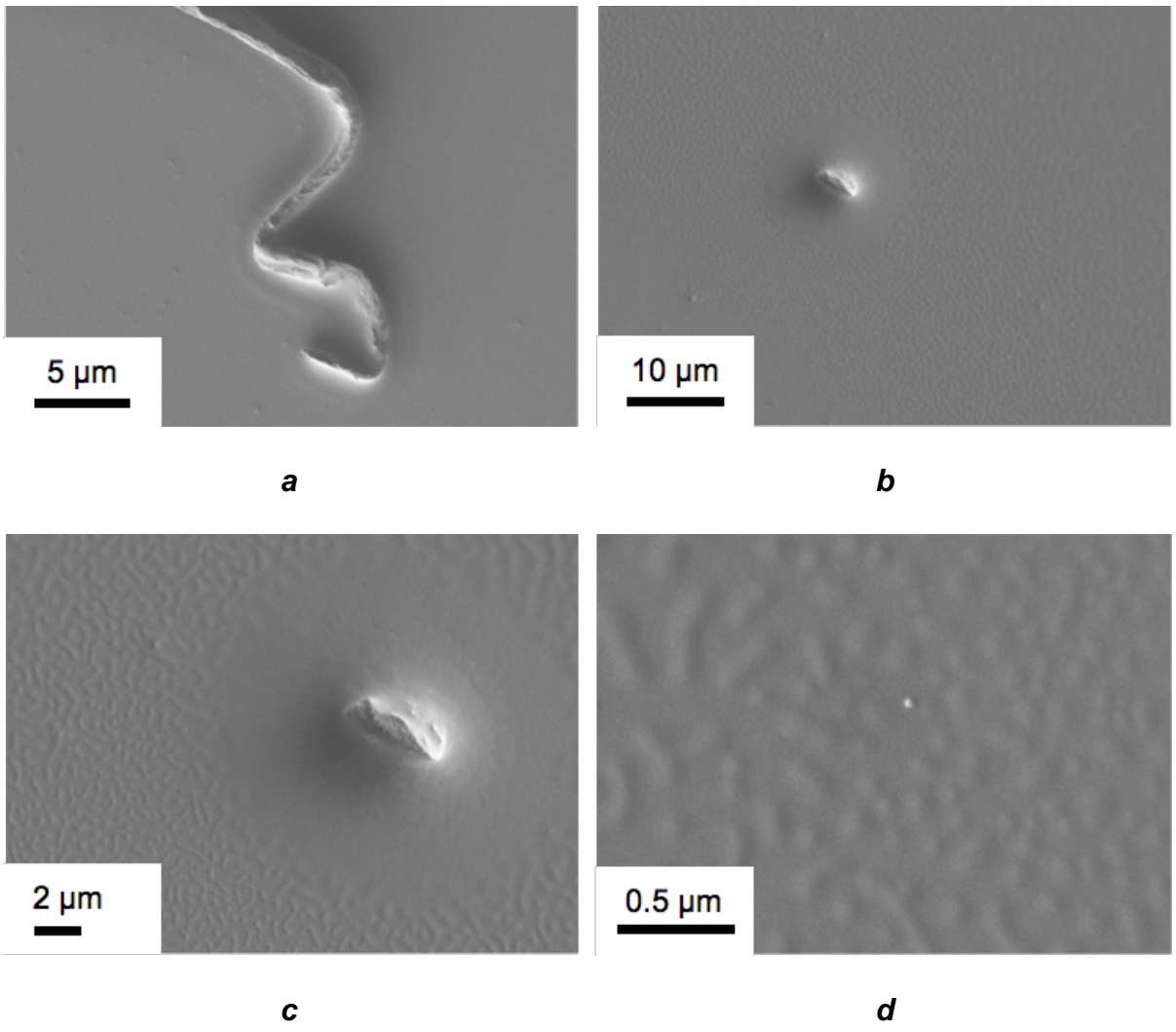

Figure S3.8. SEM images of thin films containing $ID(BTC)_2$, $PC_{71}BM$, and 25% by weight PS100, after annealing at 165 °C (a) Image showing large crystal of $ID(BTC)_2$. (b-d) Images at various scales showing smaller crystals of $ID(BTC)_2$, together with the surrounding depleted regions.

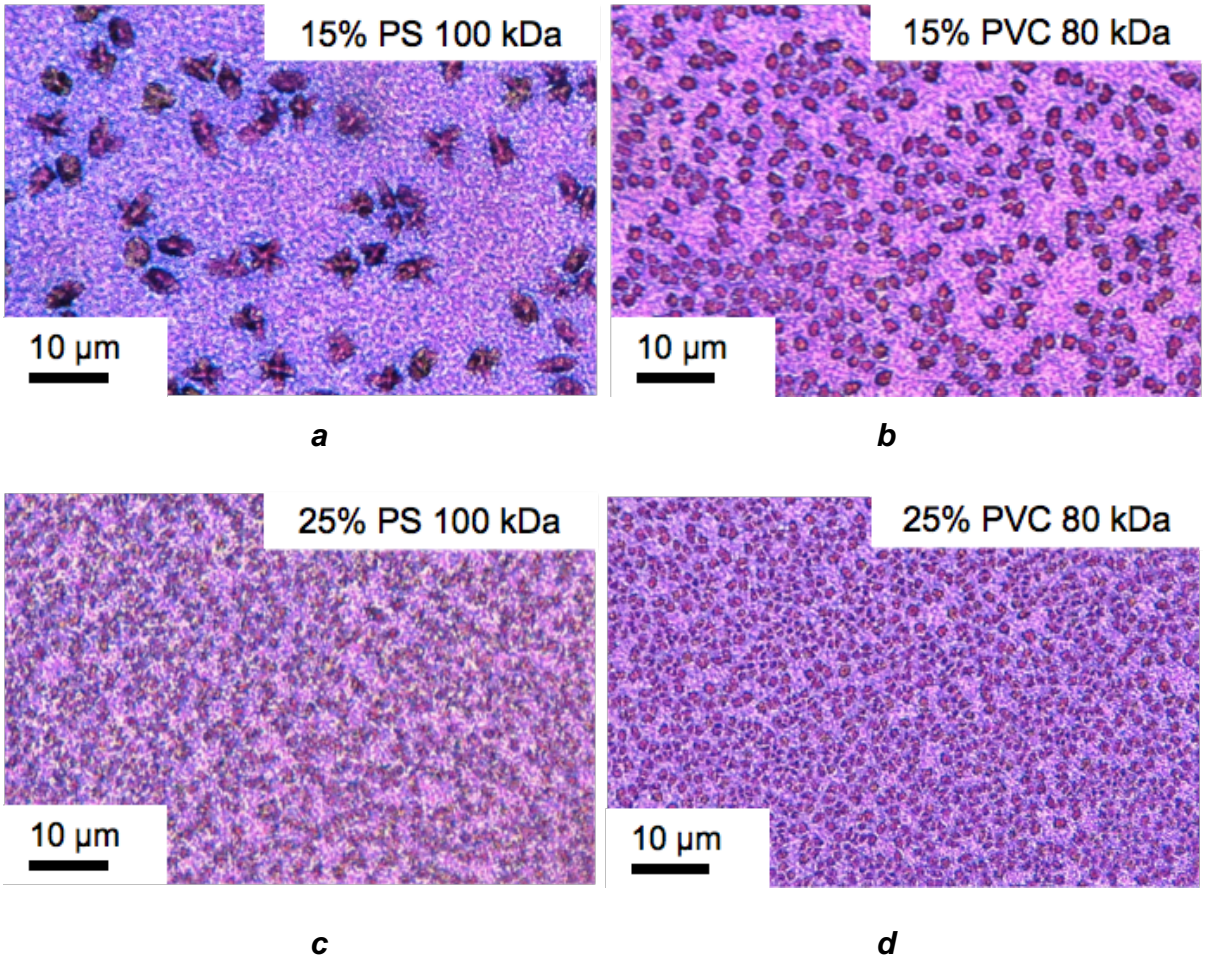

Figure S3.9. Optical micrographs under polarized light showing crystals present in thin films containing F-DTS, $PC_{71}BM$, and various polymeric matrices, deposited by spin coating at 80 °C and subsequently annealed at 195 °C. (a) 15% PS100 (100 kDa). (b) 15% PVC80 (80 kDa). (c) 25% PS100 (100 kDa). (d) 25% PVC80 (80 kDa).

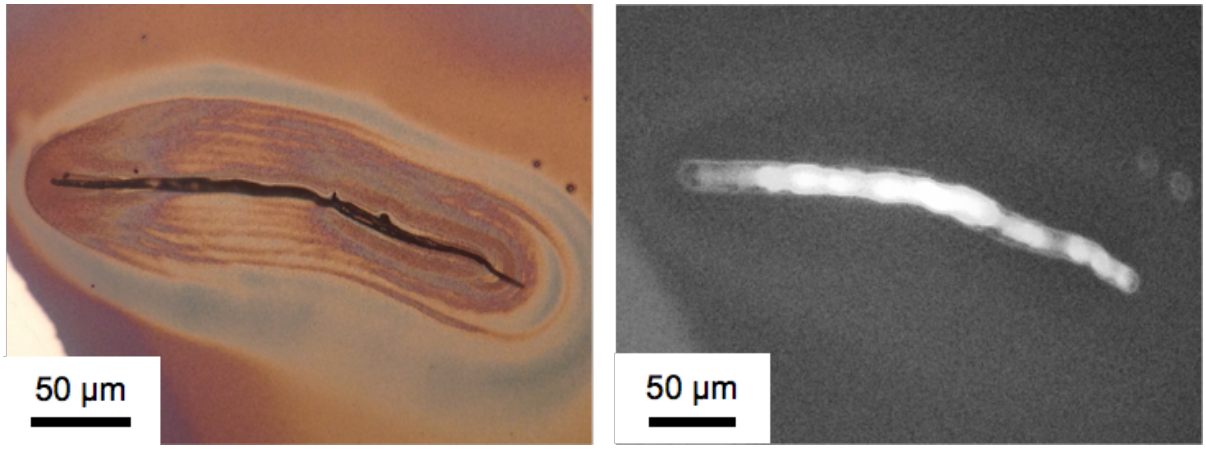

Figure S3.10. Optical micrographs showing a large crystallite of F-DTS in a thin film of F-DTS:$PC_{71}BM$ without a polymer matrix. (a) Under polarized light showing the surrounding depletion zone. (b) Under illumination, using a Zeiss DAPI filter.

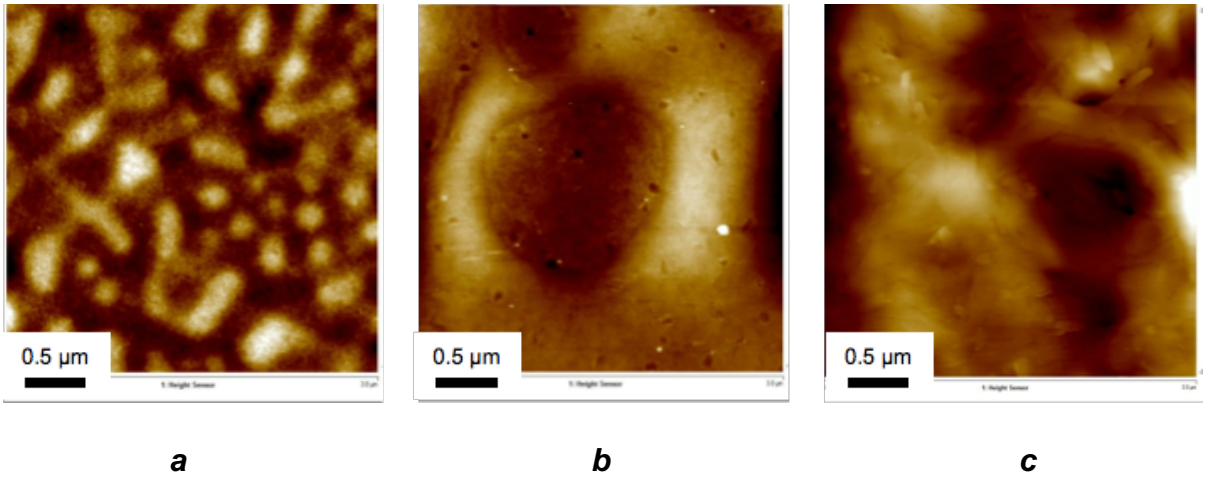

Figure S3.11. AFM images showing the topography of unannealed thin films containing F-DTS, $PC_{71}BM$, and 25% by weight of PS with different values of M_W. (a) 10 kDa. (b) 100 kDa. (c) 1000 kDa.

3.2.8.1 Characterization of polymeric matrices by gel-permeation chromatography (GPC)

Samples of P3HT and PCDTBT were characterized by GPC according to the following protocol. The polymers were dissolved in THF (2 mg/mL), and the solutions were filtered through a 0.45 μ membrane. GPC analyses were carried out using a Waters 1525 binary pump system, a Waters 717 Plus autosampler, and a Waters 2414 refractive index detector. The flow was set at 1 mL/min and was passed through a Waters column heater at 35 °C, then into a Waters Styragel pre-column (50 mm × 7.8 mm), and finally into a series of three Phenomenex columns: Phenogel 500 Å (300 mm × 7.8 mm), Phenogel 10^4 Å (300 mm × 7.8 mm), and Phenogel 10^5 Å (300 mm × 7.8 mm). Analyte (100 μL) was injected after 2 h of system equilibration. Nine narrow polystyrene standards in three THF solutions were used to plot a calibration curve and allow calculation of the number-average molar mass (M_N), the weight-average molar mass (M_W), and the polydispersity (PDI) of analytes, using the Waters software system Breeze.

3.2.8.2 Cyclic voltammetry

Cyclic voltammetry (CV) was carried out using a BASi C3 cell stand with a glassy carbon working electrode, an Ag/Ag^+ ($AgNO_3$) reference electrode, and a platinum counter electrode. Tetrabutylammonium hexafluorophosphate (99.0%, Aldrich), recrystallized from deionized water and vacuum dried, was used as the supporting salt. Analytes were dissolved in THF (30 mg mL^{-1}), coated on the carbon glassy working electrode by dipping, and allowed to dry for 5 min under N_2. Scans were taken at the rate of 25 mVs^{-1} using ferrocene as the internal reference. The standard reduction potential of ferrocene ($E^o_{Fc+/Fc}$ = 0.64 V vs the standard hydrogen electrode (SHE))[49] was measured at +0.09 V versus an Ag/Ag^+ reference electrode ($E^o_{Ag/Ag+}$ = 0.23 V vs SHE)[50] with a SHE absolute potential, $E^o_{(H+/H2)}$ ^{H_2O} (abs) = 4.44 ± 0.02 eV),[51] using a glassy carbon working electrode. The HOMO and LUMO energy levels were calculated from the oxidation and reduction onset values of the first scan.

3.2.9 References

[1] Conti, J. J.; Holtberg, P. D.; Beamon, J. A.; Napolitano, S. A.; Schaal, M. A.; Turnure, J. T.; Westfall, L. D. International Energy Outlook 2013. *U. S. Energy Information Administration* **2013**.

[2] Dudley, B. BP Statistical Review of World Energy June 2014. *BP Statistical Review of World Energy* **2014,** *63* (63rd Edition), 1-48.

[3] Tang, C. W. Two-layer organic photovoltaic cell. *Appl. Phys. Lett.* **1986,** *48* (2), 183-185.

[4] Heliatek. Heliatek sets new Organic Photovoltaic world record efficiency of 13.2%. http://www.heliatek.com/en/press/press-releases/details/heliatek-sets-new-organic-photovoltaic-world-record-efficiency-of-13-2 (accessed February 2016).

[5] Kim, J.; Cho, N.; Ko, H. M.; Kim, C.; Lee, J. K.; Ko, J. Push-pull organic semiconductors comprising of bis-dimethylfluorenyl amino benzo[b]thiophene donor and various acceptors for solution processed small molecule organic solar cells. *Sol. Energ. Mat. Sol. Cells* **2012,** *102*, 159–166.

[6] Ko, H. M.; Choi, H.; Paek, S.; Kim, K.; Song, K.; Lee, J. K.; Ko, J. Molecular engineering of push-pull chromophore for efficient bulkheterojunction morphology in solution processed small molecule organic photovoltaics. *J. Mater. Chem.* **2011,** *21*, 7248-7253.

[7] Liu, Y.; Chen, C.-C.; Hong, Z.; Gao, J.; Yang, Y. M.; Zhou, H.; Dou, L.; Li, G.; Yang, Y. Solution-processed small-molecule solar cells: breaking the 10% power conversion efficiency. *Sci. Rep.* **2013,** *3* (3356), 1-8.

[8] Mikroyannidis, J. A.; Tsagkournos, D. V.; Sharma, S. S.; Vijay, Y. K.; Sharma, G. D. Low band gap conjugated small molecules containing benzobisthiadiazole and thienothiadiazole central units: synthesis and application for bulk heterojunction solar cells. *J. Mater. Chem.* **2011,** *21*, 4679-4688.

[9] Zhang, L.; Pei, K.; Zhao, H.; Wu, S.; Wang, Y.; Gao, J. Rational design of novel A-A-D-A-A type electron donors for small molecule organic solar cells. *Chem. Phys. Lett.* **2012,** *543*, 199–204.

[10] Cheng, Y.-J.; Yang, S.-H.; Hsu, C.-S. Synthesis of Conjugated Polymers for Organic Solar Cell Applications. *Chem. Rev.* **2009,** *109*, 5868–5923.

[11] Brunner, P.-L. M.; Beaudoin, D.; Heskia, A.; Maris, T.; Dubois, M.-A.; Wuest, J. D. Low-Bandgap Push-Pull Molecules in Polymer Matrices for Use in Thin-Film Organic Photovoltaic Devices. **2015**, submitted for publication.

[12] Liua, Y.; Du, X.; Xiao, Z.; Cao, J.; Tan, S.; Zuo, Q.; Ding, L. Solution processable low bandgap small molecule donors with naphthalene end-groups for organic solar cells. *Synth. Met.* **2012,** *162*, 1665–1671.

[13] Kaura, N.; Singh, M.; Pathak, D.; Wagner, T.; Nunzi, J. M. Organic materials for photovoltaic applications: Review and mechanism. *Synth. Met.* **2014,** *190*, 20-26.

[14] Pauszek, R. F.; Kodali, G.; Caldwell, S. T.; Fitzpatrick, B.; Zainalabdeen, N. Y.; Cooke, G.; Rotello, V. M.; Stanley, R. J. Excited State Charge Redistribution and Dynamics in the Donor-π-Acceptor Flavin Derivative ABFL. *J. Phys. Chem. B* **2012,** *117* (49), 15684–15694.

[15] Yan, L.; Chen, X.; He, Q.; Wang, Y.; Wang, X.; Guo, Q.; Bai, F.; Xia, A.; Aumiler, D.; Vdović, S. Localized Emitting State and Energy Transfer Properties of Quadrupolar Chromophores and (Multi)Branched Derivatives. *J. Phys. Chem. A* **2012,** *116* (34), 8693–8705.

[16] Lin, Y.; Lia, Y.; Zhan, X. Small molecule semiconductors for high-efficiency organic photovoltaics. *Chem. Soc. Rev.* **2012,** *41*, 4245–4272.

[17] Liu, H. Q.; Xiang, L. H. Recent progress of bulk heterojunction solar cells based on small-molecular donors. *Chin. Sci. Bull.* **2013,** *58*, 2677-2685.

[18] Roncali, J.; Leriche, P.; Blanchard, P. Molecular Materials for Organic Photovoltaics: Small is Beautiful. *Adv. Mater.* **2014,** *26*, 3821–3838.

[19] Walker, B.; Kim, C.; Nguyen, T.-Q. Small Molecule Solution-Processed Bulk Heterojunction Solar Cells. *Chem. Mater.* **2011,** *23* (3), 470–482.

[20] Yu, G.; Gao, J.; Hummelen, J. C.; Wudl, F.; Heeger, A. J. Polymer Photovoltaic Cells: Enhanced Efficiencies via a Network of Internal Donor-Acceptor Heterojunctions. *Science* **1995,** *270* (5243), 1789-1791.

[21] Van der Poll, T. S.; Love, J. A.; Nguyen, T.-Q.; Bazan, G. C. Non-Basic High-Performance Molecules for Solution- Processed Organic Solar Cells. *Adv. Mater.* **2012,** *24* (27), 3646–3649.

[22] Sun, Z.; Xiao, K.; Keum, J. K.; Yu, X.; Hong, K.; Browning, J.; Ivanov, I. N.; Chen, J.; Alonzo, J.; Li, D.; Sumpter, B. G.; Payzant, E. A.; Rouleau, C. M.; Geohegan, D. B. PS-b-P3HT Copolymers as P3HT/PCBM Interfacial Compatibilizers for High Efficiency Photovoltaics. *Adv. Mater.* **2011,** *23* (46), 5529-5535.

[23] Wu, M.-C.; Liao, H.-C.; Lo, H.-H.; Chen, S.; Lin, Y.-Y.; Yen, W.-C.; Zeng, T.-W.; Chen, C.-W.; Chen, Y.-F.; Su, W.-F. Nanostructured polymer blends (P3HT/PMMA): Inorganic titania hybrid photovoltaic devices. *Sol. Energ. Mat. Sol. Cells* **2009,** *93*, 961-965.

[24] Wong, H. C.; Li, Z.; Tan, C. H.; Zhong, H.; Huang, Z.; Bronstein, H.; McCulloch, I.; Cabral, J. T.; Durrant, J. R. Morphological Stability and Performance of Polymer-Fullerene Solar Cells under Thermal Stress: The Impact of Photoinduced PC60BM Oligomerization. *ACS Nano* **2014,** *8* (2), 1297–1308.

[25] Segui, J. A.; Black, C. T.; Satija, S. In *Self Assembled Heterojunction Solar Cell Active Layers*, Adv. Ener. 2010, New York, USA, November; New York, USA, **2010**.

[26] Botiz, I.; Freyberg, P.; Leordean, C.; Gabudean, A.-M.; Astileana, S.; Yang, A. C.-M.; Stingelin, N. Emission properties of MEH-PPV in thin films simultaneously illuminated and annealed at different temperatures. *Synt. Met.* **2015,** *199*, 33-36.

[27] Vacha, M.; Habuchi, S. Conformation and physics of polymer chains: a single-molecule perspective. *NPG Asia Mater.* **2010,** *2* (4), 134-142.

[28] Dou, L.; You, J.; Yang, J.; Chen, C.-C.; He, Y.; Murase, S.; Moriarty, T.; Emery, K.; Li, G.; Yang, Y. Tandem polymer solar cells featuring a spectrally matched low-bandgap polymer. *Nature Photon.* **2012,** *6*, 180-185.

[29] Scharber, M. C.; Móhlbacher, D.; Koppe, M.; Denk, P.; Waldauf, C.; Heeger, A. J.; Brabec, C. J. Design Rules for Donors in Bulk-Heterojunction Solar Cells - Towards 10 % Energy-Conversion Efficiency. *Adv. Mater.* **2006,** *18* (6), 789-794.

[30] Koster, L. J. A.; Mihailetchi, V. D.; Xie, H.; Blom, P. W. M. Origin of the light intensity dependence of the short-circuit current of polymer/fullerene solar cells. *Appl. Phys. Lett.* **2005,** *87* (20), 203502-3.

[31] Rotha, C. B.; Pound, A.; Kamp, S. W.; Murray, C. A.; Dutcherb, J. R. Molecular-weight dependence of the glass transition temperature of freely-standing poly(methyl methacrylate) films. *Eur. Phys. J. E* **2006,** *20*, 441–448.

[32] Mark, J. E. *Polymer Data Handbook*. Oxford University Press: New York, USA, **1999**.

[33] Reding, F. P.; Walter, E. R.; Welch, F. J. Glass Transition and Melting Point of Poly (vinyl Chloride). *J. Polym. Sci.* **1962,** *56*, 225-231.

[34] Brabec, C. J.; Cravino, A.; Meissner, D.; Sariciftci, N. S.; Fromherz, T.; Rispens, M. T.; Sanchez, L.; Hummelen, J. C. Origin of the Open Circuit Voltage of Plastic Solar Cells. *Adv. Funct. Mater.* **2001,** *11* (5), 374-380.

[35] Williams, G.; Aziz, H. Implications of the device structure on the photo-stability of organic solar cells. *Sol. Energ. Mat. Sol. Cells* **2014,** *128*, 320-329.

[36] *See the supporting information for details.*

[37] Friend, R. H.; Denton, G. J.; Halls, J. J. M.; Harrison, N. T.; Holmes, A. B.; Köhler, A.; Lux, A.; Moratti, S. C.; Pichler, K.; Tessler, N.; Towns, K. Electronic Processes of Conjugated Polymers in Semiconductor Device Structures. *Synth. Met.* **1997,** *84* (1-3), 463-470.

[38] Haugeneder, A.; Neges, M.; Kallinger, C.; Spirkl, W.; Lemmer, U.; Feldmann, J.; Scherf, U.; Harth, E.; Gügel, A.; Müllen, K. Exciton diffusion and dissociation in conjugated polymer/fullerene blends and heterostructures. *Phys. Rev. B* **1999,** *59* (23), 15346.

[39] Shaw, P. E.; Ruseckas, A.; Samuel, D. W. Exciton Diffusion Measurements in Poly(3-hexylthiophene). *Adv. Mater.* **2008,** *20* (18), 3516-3520.

[40] Yi, Z.; Ni, W.; Zhang, Q.; Li, M.; Kan, B.; Wan, X.; Chen, Y. Effect of thermal annealing on active layer morphology and performance for small molecule bulk heterojunction organic solar cells. *J. Mater. Chem. C* **2014,** *2*, 7247-7255.

[41] Yang, X.; Uddin, A.; Wright, M. Effects of Annealing on Bulk-heterojunction Organic Solar Cells. *Adv. Sci. Eng. Med.* **2012,** *4* (1), 19-25.

[42] Tamayo, J.; García, R. Deformation, Contact Time, and Phase Contrast in Tapping Mode Scanning Force Microscopy. *Langmuir* **1996,** *12*, 4430-4435.

[43] Sariciftci, N. S.; Smilowitz, L.; Heeger, A. J.; Wudl, F. Photoinduced Electron Transfer from a Conducting Polymer to Buckminsterfullerene. *Science* **1992,** *258*, 1474.

[44] Haugeneder, A.; Neges, M.; Kallinger, C.; Spirkl, W.; Lemmer, U.; Feldmann, J. Exciton diffusion and dissociation in conjugated polymer/fullerene blends and heterostructures. *Phys. Rev. B* **1999,** *59* (23), 15346-15351.

[45] Park, S. H.; Roy, A.; Beaupré, S.; Cho, S.; Coates, N.; Moon, J. S.; Moses, D.; Leclerc, M.; Lee, K.; Heeger, A. J. Bulk heterojunction solar cells with internal quantum efficiency approaching 100%. *Nature Photon.* **2009,** *3* (5), 297-302.

[46] Cravino, A.; Schilinsky, P.; Brabec, C. J. Characterization of organic solar cells: The importance of device layout. *Adv. Funct. Mater.* **2007,** *17* (18), 3906-3910.

[47] Kim, M.-S.; Kang, M.-G.; Guo, L. J.; Kim, J. Choice of electrode geometry for accurate measurement of organic photovoltaic cell performance. *Appl. Phys. Lett.* **2008,** *92* (13), 133301-133303.

[48] Brunner, P.-L. M.; Masse, J.-P.; L'Espérance, G.; Wuest, J. D. Imaging Layers in Thin-Film Molecular Devices by Transmission Electron Microscopy, Using Milling by Focused Ion Beams and Deposition on NaCl and Si. **2015**, submitted for publication.

[49] Connelly, N. G.; Geiger, W. E. Chemical Redox Agents for Organometallic Chemistry. *Chem. Rev.* **1996,** *96*, 877-910.

[50] Bates, R. G.; MacAskill, J. B. Standard Potential of the Silver-Silver Chloride Electrode. *Pure Appl. Chem.* **1978,** *50*, 1701-1706.

[51] Trasatti, S. The absolute electrode potential: An explanatory note. *Pure Appl. Chem.* **1986,** *58* (7), 955-966.

Chapitre 4

Dépendance de performance de diodes organiques luminescentes en fonction de la masse moléculaire de polymères électroluminescents

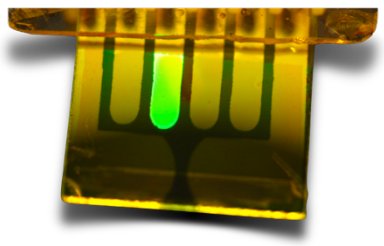

« Fiat Lux», Diode organique en opération

4.1 Introduction Article 3

Si le type de polymère utilisé dans les matrices passives polymériques fait varier grandement la morphologie des films actifs minces, tel que vu au chapitre 3, la variation de leurs masses molaires est également importante dans le contrôle de celle-ci. Il est raisonnable de penser que la variation de la masse molaire d'un polymère semi-conducteur aura également un effet sur les propriétés morphologiques et électroniques du film actif mince constitué de celui-ci. Si la synthèse des petites molécules assure des structures définies et reproductibles des matériaux, la synthèse de polymères donne souvent des produits ayant des masses molaires et des index de polydispersité variables, résultant en des mélanges moléculaires plus ou moins homogènes. Cet article tente d'élucider comment ce mélange d'une même espèce polymérique peut affecter les propriétés de dispositifs électroniques organiques.

La synthèse du poly[(9,9-dioctyl-2,7-divinylène-fluorènylène)-alt-co-(2-méthoxy-5-(2-éthylhéxyloxy)-1,4-phénylène)] (PFO-MEH-PPV) via un couplage de Wittig est connue,[73-76] mais le contrôle de la masse molaire est problématique. Cette synthèse a donc été explorée et perfectionnée pour obtenir des polymères aux masses molaires souhaitées. Une gamme de polymères a ainsi été produite pour permettre cette étude sur les performances de dispositifs électroniques organiques en fonction de la masse molaire des ces constituants actifs. Le choix d'une étude de dispositifs OLED plutôt que photovoltaïques fut guidé par deux critères. Premièrement, nous étions attirés par la possibilité d'obtenir un polymère semi-conducteur soluble sur une vaste gamme de masses molaires. Secondement, ce type de dispositif, contrairement aux cellules photovoltaïques, ne requière pas dans son mode de fonctionnement l'ajout d'un accepteur d'électrons de type n pour bien performer éliminant ainsi une variable.

Ces dispositifs promettent également un futur "brilliant" dans le domaine de l'éclairage[77-79], des lasers organiques[80-81] et de l'affichage électroluminescent large, à bas prix, consommant peu d'énergie et possiblement flexible.[82-85]

4.2 Article 3

Dependence of the Performance of Light-Emitting Diodes on the Molecular Weight of Electroluminescent Polymers

Pierre-Louis M. Brunner [1]*, Dominic Laliberté [2], Minh Trung Dang [1], Guillaume Wantz [3,4]*, and James D. Wuest [1]*

[1] *Département de Chimie, Université de Montréal, Montréal, Québec H3C 3J7, Canada*

[2] *Solaris Chem Inc, 5155 Decelles Avenue, Montréal, Québec H3T 2B1, Canda*

[3] *CNRS, IMS, UMR 5218, F-33400, Talence, France*

[4] *Bordeaux INP, IMS, UMR 5218, F-33400, Talence, France*

Organic Electronics, **2016**, soumis pour publication.

4.2.1 Keywords

Keywords: Organic light-emitting diodes (OLEDs), electroluminescent polymers, molecular weight, photoluminescence quantum yield

4.2.2 Abstract

Controlled synthesis of the electroluminescent polymer PFO-MEH-PPV (poly[(9,9-dioctyl-2,7-divinylenefluorenylene)-*alt*-*co*-(2-methoxy-5-(2-ethylhexyloxy)-1,4-phenylene)]) provided samples of varying molecular weight in the range 20-360 kDa, which were characterized by gel-permeation chromatography and light scattering. By incorporating the samples as the active layers in polymer-based organic light-emitting diodes (OLEDs), we were able to study how the performance of the devices depends on M_W. Turn-on voltages fell in the range 1.92-2.78 V, luminances varied from 231 to 5826 cd/m^2, and luminous efficacies ranged from 0.06 to 0.90 lm/W. The emitted color was found to vary from green to yellow as M_W increases. Optimal performance was attained by using PFO-MEH-PPV with M_W = 100 kDa. To help reveal how M_W determines the performance of OLEDs, relative quantum yields of photoluminescence in solutions and films were measured, and films were characterized by atomic force microscopy and transmission electron microscopy.

4.2.3 Introduction

The world needs renewable sources of energy to reduce dependency on fossil fuels, and efforts must also be made to moderate the increasing global demand for energy. At present, 11% of electricity consumed in the U. S. is used to power residential and commercial lighting.[1-2] Replacing conventional incandescent and fluorescent lights by light-emitting diodes (LEDs) would provide an annual savings of 300 billion kWh worldwide, or the equivalent of over 30 billion liters of gasoline in the U. S. alone. New devices for producing light more economically are organic light-emitting diodes (OLEDs), which are thin-film electroluminescent devices constructed by sandwiching suitable molecular semiconductors between electrodes. Applying a potential across the electrodes generates electron-hole pairs within the molecular film, which combine to release energy in the form of light. Because the films have molecular components and do not typically need to be thicker than 100 nm, OLEDs can be used to make lightweight flexible displays, and they can be produced by inexpensive methods of large-scale manufacturing such as roll-to-roll printing.[3-5]

In 1987, Tang and VanSlyke reported the first OLED, which was made from tris(8-hydroxyquinolinato)aluminum.[6] In 1990, Burroughes and coworkers described new polymer-based OLEDs made from poly(*p*-phenylenevinylene), a solution-processable π-conjugated polymer.[7] Since then, the technology has advanced rapidly, and OLEDS are now found in many commercial devices, including television screens and displays for cell phones. OLEDs are likely to find other important uses in the future, including white glare-free light sources,[8-10] organic lasers,[11-12] and large, flexible, low-cost displays that require little energy to operate.[13-16]

Unlike simple small molecules, polymers do not have uniform, well-defined structures and compositions, and their molecular weight (M_W) and dispersity can vary from batch to batch. These variations can be expected to affect the properties of polymer-based OLEDs, leading to uneven performance. In the present study, we have investigated the effect of M_W over a wide range on the performance of OLEDs in which the active layer is composed of

PFO-MEH-PPV (poly[(9,9-dioctyl-2,7-divinylene-9*H*-fluorenylene)-*alt*-*co*-(2-methoxy-5-(2-ethylhexyloxy)-1,4-phenylene)]), end-capped with 3,5-dimethylphenyl groups.[17] We have found that M_W has an important effect on luminance, efficacy, and the output color of devices based on PFO-MEH-PPV.

4.2.4 Experimental

4.2.4.1 Active materials

PFO-MEH-PPV was synthesized by the route shown in Scheme 4.1. 2-Methoxy-5-(2-ethylhexyloxy)-1,4-bis(diethoxyphosphonomethyl)benzene (**1**) and 9,9-dioctyl-9*H*-fluorene-2,7-dicarbaldehyde (**2**) were prepared by published methods.[18-20] General experimental procedures are summarized in the Supporting Information. PEDOT:PSS was purchased from Heraeus-Clevios (Clevios™ P VP *AI* 4083).

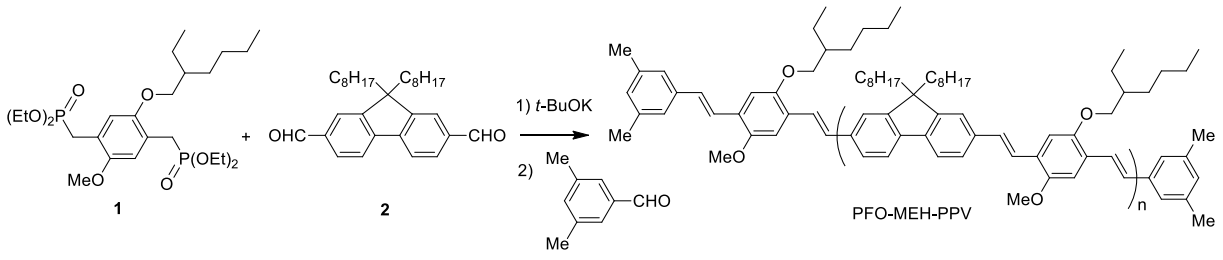

Scheme 4.1. Synthesis of PFO-MEH-PPV end-capped by 3,5-dimethylphenyl groups. C_8H_{17} denotes straight alkyl chains.

Poly[(9,9-dioctyl-2,7-divinylene-9*H*-fluorenylene)-*alt*-*co*-(2-methoxy-5-(2-ethylhexyloxy)-1,4-phenylene)] (PFO-MEH-PPV). A solution of 2-methoxy-5-(2-ethylhexyloxy)-1,4-bis(diethoxyphosphonomethyl)benzene (**1**) (9.01 g, 16.8 mmol) and 9,9-dioctyl-9*H*-fluorene-2,7-dicarbaldehyde (**2**) (7.50 g, 16.8 mmol) in dry THF (500 mL) was sparged with N_2 for 30 min. A solution of potassium *tert*-butoxide (7.60 g, 67.7 mmol) in THF (100 mL) was sparged

with N_2 for 30 min and added dropwise to the solution of monomers. The resulting mixture was stirred at 25 °C for 4 h to allow polymerization to occur. A small extra portion of 2-methoxy-5-(2-ethylhexyloxy)-1,4-bis(diethoxyphosphonomethyl)benzene (0.100 g, 0.186 mmol) in THF (25 mL) was added, and the mixture was stirred at 25 °C for 30 min to ensure homogeneity of the terminal groups of the polymer. 3,5-Dimethylbenzaldehyde (0.10 g, 0.75 mmol) in THF (25 mL) was then added as end-capping agent, and the solution was stirred at 25 °C for 1 h. The mixture was then added dropwise to stirred methanol, and the precipitated yellow fibers were separated by filtration on a Büchner funnel and washed twice with methanol. The isolated polymer was subjected to Soxhlet extraction with methanol, and the insoluble portion was dissolved in THF. The THF solution was then added dropwise to stirred methanol, and the precipitated yellow fibers were separated again by filtration on a Büchner funnel and washed twice with methanol. Drying under vacuum yielded PFO-MEH-PPV as bright yellow fibers (9.38 g, 13.9 mmol, 82.7%).

4.2.4.2 Fabrication and characterization of OLEDs

Glass substrates coated with indium tin oxide (ITO), with a sheet resistance of 30-60 Ω/square, were washed successively with acetone, ethanol, and isopropanol in an ultrasonic bath and were then exposed to UV-ozone for 20 min. A layer of poly(3,4-ethylenedioxythiophene):polystyrenesulfonate (PEDOT:PSS, Clevios™ P VP *AI* 4083) was deposited on the substrates by spin coating in air at a rate of 4000 rpm for 60 s, and the added layer was baked under vacuum at 110 °C for 30 min. PFO-MEH-PPV was stirred in cyclohexanone at 50 °C for 2 h to produce a solution (10-20 mg/mL), which was then deposited on top of the layer of PEDOT:PSS by spin coating at a rate of 1000 rpm for 60 s (spreading) increased subsequently to 2000 rpm for 60 s (drying). The resulting assemblies were transferred to a chamber for further deposition under vacuum. A 300 nm-thick cathode of calcium (Sigma-Aldrich) was then thermally evaporated onto the active layer under secondary vacuum (10^{-6} mbar) through a shadow mask at a rate of 1-2 Å/sec. All thicknesses and deposition rates were monitored by a quartz crystal microbalance. The active area of the OLEDs was determined to be 7.5 mm^2. The devices were thermally annealed at 140 °C for 10

min under N_2 in a glove box. Current density-voltage-luminescence (J-V-L) curves were measured with a Keithley 4200 Source-Measure Unit coupled with a Hamamatsu light sensor calibrated with a Minolta CS-100 luminance meter. Electroluminescence (EL) spectra were recorded with an Ocean Optics HR2000 spectrometer. Chromatic coordinates were calculated from the EL spectra and reported according to the CIE-1964 chromaticity diagram. The device structure, as well as a photograph and video of a four-cell device in operation, can be found in the Supporting Information.

4.2.4.3 Imaging by atomic force microscopy (AFM)

AFM images were acquired in air at 25 °C using a Digital Instruments EnviroScope (Santa Barbara, California) and a Nanoscope IIIa controller (Veeco/Bruker). Imaging in tapping mode was performed at a scan rate of 1 Hz using etched Si cantilevers (ACTA, Applied NanoStructures Inc.) with a resonant frequency of about 300 kHz, a spring constant of approximately 42 N/m, and a tip radius of <10 nm. All AFM images were acquired with medium damping of tip oscillation (20-30%).

4.2.4.4 Imaging by transmission electron microscopy (TEM)

TEM imaging was carried out using a JEOL JEM-2100F instrument operated at 200 keV in bright-field mode. Samples of thin films were prepared by a new method,[21] in which materials of interest are first deposited by spin coating on Si wafers. Subsequent shattering of the wafers yields small fragments (approximately 1 mm^2), with portions of the film overhanging the broken edges. The fragments were mounted on standard 50-mesh Cu grids in order to image the overhanging films. Annealing could be carried out directly on the Cu grids, under the conditions described for the fabrication of completed OLEDs.

4.2.5 Results and Discussion

4.2.5.1 Synthesis of PFO-MEH-PPV

Samples of PFO-MEH-PPV with varying M_W were obtained by highly controlled Wittig condensations of 2-methoxy-5-(2-ethylhexyloxy)-1,4-bis(diethoxyphosphonomethyl) benzene (**1**) with 9,9-dioctyl-9*H*-fluorene-2,7-dicarbaldehyde (**2**), as depicted in Scheme 4.1. Termination of polymerization by adding excess diphosphonate **1** and end-capping with 3,5-dimethylbenzaldehyde was carried out to eliminate the presence of potentially reactive aldehyde or phosphonate terminal groups, which may alter the performance of the resulting polymer.

Slight variations in the ratio of monomers **1** and **2** determined M_W of the resulting polymer. To attain a high value of M_W, the ratio of **1**:**2** must be as close to 1:1 as possible. Great care was taken to obtain pure bifunctional monomers and to thereby avoid chain termination caused by reactions with monofunctionalized monomers. Thermogravimetric analysis (TGA) was used to estimate the content of residual volatile impurities in the monomers, and the results were taken into account in adjusting the ratio **1**:**2**. The evolution of M_W during polymerization was monitored by gel-permeation chromatography (GPC) to further control the final value. The 2-ethylhexyloxy group of diphosphonate **1** incorporates a stereogenic center, so the resulting polymers are presumably complex mixtures of diastereomers.

4.2.5.2 Physicochemical properties of PFO-MEH-PPV

Full understanding of the properties of a polymer and its performance in a device requires accurate measurement of M_W and related parameters. PFO-MEH-PPV is highly soluble in THF, so analyses by GPC were carried out using THF as the mobile phase. Narrow polystyrene standards (PS) were used to produce a calibration curve with a coefficient of

determination (R^2) of 0.9995. Values of M_W for various samples of PFO-MEH-PPV are summarized in Table 4.1.

Table 4.1. Properties of PFO-MEH-PPV

Sample[a]	$M_{w/GPC}$ (kDa)[b]	$M_{n/GPC}$ (kDa)[b]	PDI_{GPC}[c]	$M_{w/LS}$ (kDa)[d]	T_g (°C)[e]
P20	20	10	2.0	9.5	65.2
P40	37	18	2.1	18	70.6
P70	71	30	2.4	34	79.7
P100	98	45	2.2	48	81.7
P200	196	93	2.1	89	82.8
P360	362	157	2.3	162	83.1

[a] Name of polymer sample derived from the approximate value of $M_{W/GPC}$
[b] Molecular weight (M_W = weight average molecular weight and M_N = number average molecular weight) determined by GPC using PS standards
[c] Polydispersity index calculated as M_W/M_N
[d] Molecular weight determined by light scattering (LS), using a measured value of *dn/dc* (0.285 ± 0.004 mL/g)
[e] Glass-transition temperature measured under N_2 by differential scanning calorimetry (DSC), using heating and cooling rates of 10 °C/min

Values of M_W estimated by GPC for samples of PFO-MEH-PPV are relative to PS, which does not have the same intrinsic properties in THF, so values of M_W were also independently measured by light scattering (LS) in THF. The differential index of refraction, *dn/dc*, which reflects the variation of the refractive index of the medium as a function of changes in the concentration of the analyte, was determined at 25 °C using ten solutions of known concentration in the range 0.200-2.000 mg/mL. The value of *dn/dc* measured for PFO-MEH-PPV in THF was 0.285 ± 0.004 mL/g. Table 1 shows that the values of M_N determined by GPC are closely similar to values of M_W measured by LS. The glass transition temperatures (T_g) of the various samples of PFO-MEH-PPV were measured by differential scanning calorimetry (DSC) and are reported in Table 4.1. The values of T_g increase in tandem with

M_W, as expected for longer polymer chains with decreasing degrees of freedom due to higher entanglement.

4.2.5.3 OLEDs incorporating PFO-MEH-PPV

Samples of PFO-MEH-PPV with values of $M_{W/GPC}$ in the range 20-362 kDa were tested as the active emitting layer in OLEDs. The devices featured a standard architecture (glass/ITO/PEDOT:PSS/PFO-MEH-PPV/Ca) and were fabricated using conventional methods under N_2, unless specified. The performance of the devices was assessed as a function of M_W of the polymers, with the thickness of the active layer kept constant at 110 ± 10 nm and with uniform post-production thermal annealing at 140 °C for 10 min. The results are reported in Table 4.2. PFO-MEH-PPV with $M_{W/GPC}$ = 362 kDa (P360) was found to have the highest luminance, which was determined to be 5826 cd/m^2 at an applied bias of 5.7 V. However, a sample with $M_{W/GPC}$ = 98 kDa (P100) gave the best overall performance, with a luminous efficacy of 0.90 lm/W (compared to 0.67 lm/W for P360), a turn-on voltage below 2.0 V, and an optimal working voltage below 4.0 V.

As shown in Table 4.2, Figure 4.1, and Figure S4.2,[22] samples of PFO-MEH-PPV with the lowest values of M_W (P20 and P40) gave OLEDs that showed poor performance, as measured by luminances of only 231 and 935 cd/m^2, luminous efficacies of 0.06 and 0.20 lm/W, and turn-on voltages above 2.0 V. However, performance was markedly improved by increasing M_W above 70 kDa, which yielded devices with luminances above 4000 cd/m^2 (Figure 4.1a). The luminous efficacy of the devices also increased with rising M_W until a maximum of about 0.90 lm/W was reached when sample P100 (98 kDa) was used (Figure 4.1b). A further increase in M_W to 196 kDa (sample P200) led to lowered efficacy, but a modest rise was observed at still higher values of M_W (sample P360). This trend, which may result from subtle differences in the polydispersity index, is further examined below in the discussion of fluorescence quantum yields.

Table 4.2. Properties related to the performance of OLEDs incorporating PFO-MEH-PPV

Sample	$M_{w/GPC}$ (kDa)[a]	Film Thick. (nm)[b]	RMS R_q (nm)[c]	Turn-on Voltage (V)[d]	Optimal Voltage (V)[e]	Luminance at 5.7 V (cd/m^2)[f]	Efficacy (lm/W)[g]	Emission λ_{max} (nm)[h]
P20	20	108 ± 8	5.31	2.78	6.30	231	0.06	543.5
P40	37	113 ± 6	3.13	2.20	5.00	935	0.20	546.7
P70	71	116 ± 9	4.28	2.14	4.60	4415	0.48	548.1
P100	98	110 ± 9	4.56	1.98	3.94	5561	0.90	549.4
P200	196	108 ± 9	6.07	1.92	4.62	5671	0.48	547.2
P360	362	114 ± 6	6.31	1.96	4.64	5826	0.67	548.5

[a] Molecular weight of PFO-MEH-PPV determined by GPC using PS standards
[b] Determined by profilometry
[c] Root-mean-square (RMS) roughness (R_q) of films of PFO-MEH-PPV after annealing at 140 °C for 10 min, as measured by AFM
[d] Lowest voltage at which electroluminescence was detectable
[e] Voltage at which the greatest luminous efficacy was measured
[f] Maximal luminance at an applied bias of 5.7 V
[g] Maximal luminous efficacy
[h] Wavelength of light emitted by electroluminescence

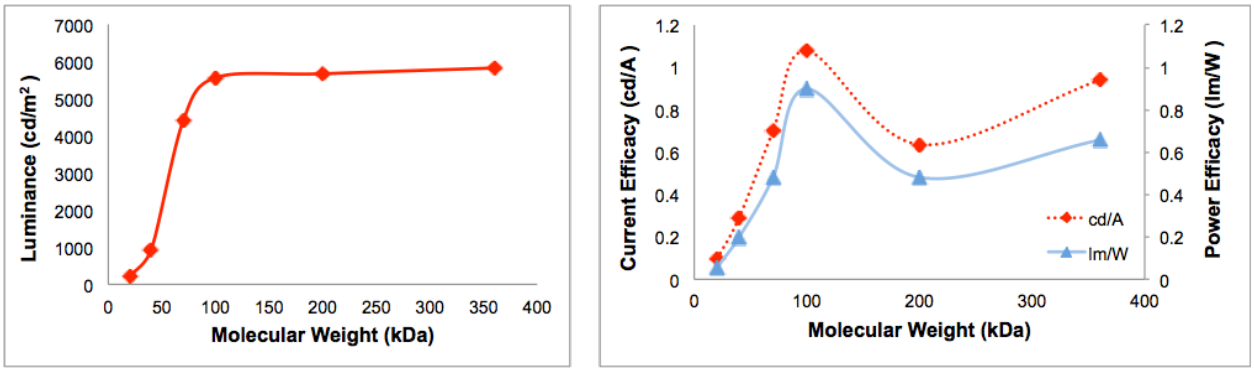

a ***b***

Figure 4.1. Performance of OLEDs containing PFO-MEH-PPV as a function of $M_{W/GPC}$. (a) Luminance at a bias of 5.7 V. (b) Luminous efficacy.

The color of electroluminescence produced by OLEDs containing PFO-MEH-PPV was found to shift almost linearly from green (higher energy) to yellow (lower energy) as M_w increased from 20 to 360 kDa (Figure 4.2). Figure S4.4a depicts the λ_{max} of emission from PFO-MEH-PPV as a function of M_w. The relationship is similar to the one shown in Figure 4.1b, which reveals how efficacy depends on M_w. The value of λ_{max} increases from sample P20 (543.5 nm) to P100 (549.4 nm), and then drops slightly for P200 (547.2 nm) and P360 (548.5 nm). This suggests that the color emitted by OLEDs can be modulated to obtain a particular desired output by adjusting the molecular weight used.

The color of electroluminescence produced by OLEDs containing PFO-MEH-PPV was found to shift almost linearly from green (higher energy) to yellow (lower energy) as M_W increased from 20 to 360 kDa (Figure 4.2). Figure S4.4a depicts the λ_{max} of emission from PFO-MEH-PPV as a function of M_W.[22] The relationship is similar to the one shown in Figure 4.1b, which reveals how efficacy depends on M_W. The value of λ_{max} increases from sample

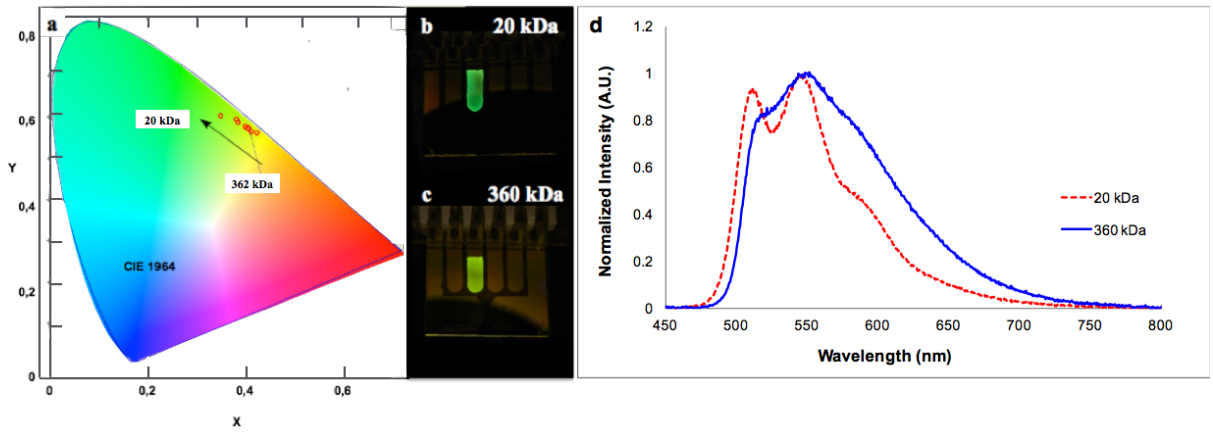

Figure 4.2. Electroluminescence of OLEDs containing PFO-MEH-PPV. (a) Color mapping of the output as a function of $M_{W/GPC}$, using the 1964 coordinates of the Commission Internationale d'Eclairage (CIE). (b) Photograph showing the output color of a device containing P20. (c) Photograph showing the output color of a device containing P360. (d) Corresponding electroluminescence spectra for devices containing P20 (red dashed line) and P360 (blue solid line).

P20 (543.5 nm) to P100 (549.4 nm), and then drops slightly for P200 (547.2 nm) and P360 (548.5 nm). This suggests that the color emitted by OLEDs can be modulated to obtain a particular desired output by adjusting the molecular weight used.

The electroluminescence (EL) spectra (Figure 4.2d) and photoluminescence (PL) spectra (Figure S4.3) show a loss of vibronic structure, broadening, and a bathochromic shift of emission as M_W increases. Conjugated polymers can be described as conformationally dynamic entities composed of multiple shortened chromophores that interact strongly through the connecting π-system.[23] The extent to which the overall π-conjugation is interrupted by chain torsion or kinks depends on the conformation of the individual polymer chains, which in turn depends on molecular packing within films. Longer effective π-conjugation leads to polymers with smaller bandgaps and absorption at longer wavelengths. EL and PL spectra for samples P20, P100, and P360 are collected in Figure S4.3 to facilitate comparison.[22] Appearance of underlying vibronic structure in the spectra of the low M_W polymer can be attributed to a more ordered structure, as it has been observed for similar polymers.[24-28]

In EL spectra, emission arises from radiative recombination of excess carriers produced by charge injection, whereas in PL spectra, emission results from radiative recombination of photoexcited electron or hole carriers (S_1-S_0 transition). Comparing EL and PL spectra can shed light on the conformation of polymers and the presence of excited aggregates such as dimers (eximers).[29-30] EL spectra of samples of PFO-MEH-PPV were found to exhibit more intense and broad vibronic bands near 550 nm and 590 nm, compared with the corresponding PL spectra. The EL spectra appear to reflect the generation of excited aggregates by charge injection, followed by the cascade of energy from neighboring emissive excitons down to more weakly emissive lower-energy aggregates. We attribute the loss of spectral resolution and the global bathochromic shifts to recombinations and self-quenching of emission caused by the close proximity of chains within the aggregates.[23, 31]

It is well known that the performance of thin-film OLEDs can depend on the morphology of the active layer,[32-35] and post-production annealing above the glass-transition

temperature (T_g) is widely used to alter molecular organization in polymer-based active layers and thereby maximize performance. These treatments can improve the long-term stability of OLEDs and cause a shift in the λ_{max} of emission. For example, the emission of OLEDs containing polyfluorenes was reported to shift from blue (435 nm) to green (525 nm) upon annealing above T_g, due to changes in the aggregation of chains and induced crystallization, as indicated by an increase in the roughness of films.[32] In addition, the λ_{max} of emission from MEH-PPV polymers is known to depend on the configuration of the side chain and on M_W,[36] possibly because the formation of normal helical supramolecular aggregates is inhibited when the polymers are enantiomerically pure and have low values of M_W.

In the case of PFO-MEH-PPV, layers of samples P20 to P360 were annealed above T_g at 140 °C for 10 min, and all produced very smooth thin films. Only a slight increase in film roughness was measured by AFM as M_W of the polymers increased, and all recorded values of R_q (RMS) lay in the range 3.13-6.31 nm (Table 4.2 and Figure S4.5). However, examination of the films by transmission electron microscopy (TEM) revealed coarser features in samples with low values of M_W (Figure 4.3). In particular, sample P20 has a granular surface and darker spots with diameters of about 20 nm (Figure 4.3a), whereas sample P100 (Figure 4.3b)

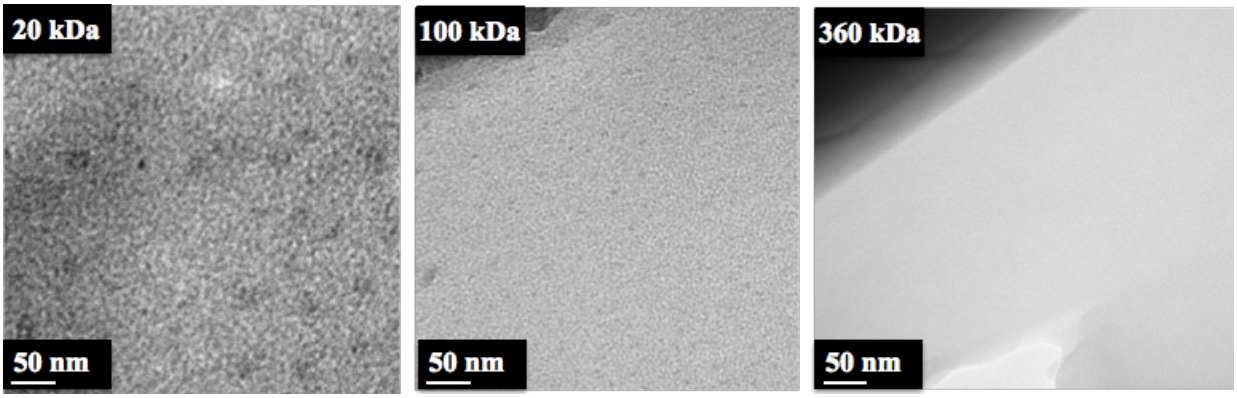

Figure 4.3. TEM images of annealed films of PFO-MEH-PPV as a function of $M_{W/GPC}$. (a) Sample P20 (M_W = 20 kDa). (b) Sample P100 (M_W = 100 kDa). (c) Sample P360 (M_W = 360 kDa).

shows a more subtle granularity with features that are more fine-grained (around 3 nm). In the case of sample P360, the film is homogenous and shows no traces of aggregates or patterns on the same scale (Figure 4.3c).

As revealed by luminescence spectra and other data, aromatic interactions between chains of PFO-MEH-PPV in thin films can lead to the formation of π-stacked aggregates that affect the emissive properties of the polymer, including self-quenching of excimers during radiative decay and the formation of weakly emissive associated species. To investigate these phenomena in greater detail, we measured relative quantum yields (RQY) for the fluorescence of samples of PFO-MEH-PPV, both as dilute solutions in THF and as thin films. Equation 4.1 expresses the relationship between the photoluminescence quantum yields (Φ_f) of two materials, where the superscripts *s* and *r* denote sample and reference, *F* is the integrated intensity of emission, *n* is the refractive index of the medium, and *A* is the absorption.[37] Instead of using a reference material of known photoluminescence quantum yield, we compared different samples of PFO-MEH-PPV with one another (set as *s* and *r*) to determine the values of RQY. Comparing samples of closely similar materials minimizes errors resulting from unmatched absorption spectra or the use of solvents with different refractive indexes.

$$\Phi_f^s = \Phi_f^r \frac{F^s(1-10^{-A_r})n_s^2}{F^r(1-10^{-A_s})n_r^2} \qquad \text{Equation 4.1}$$

The highest values of integrated intensity (*F*) in solution were measured for sample P20, and its photoluminescence quantum yield was arbitrarily set to 100% and used as the reference value. The values of RQY for samples of PFO-MEH-PPV of higher M_W (P40-P360) were calculated using the integrated intensities of their photoluminescence (F^s). The results, presented in Figure 4.4a, show a steady loss in efficiency as M_W increases in the series P20-P100, with little subsequent change at still higher values of M_W. Measurements of RQY in thin films used samples of constant thickness (110 ± 10 nm), and the highest integrated intensity of photoluminescence was observed in sample P100. In unannealed films, the values of RQY

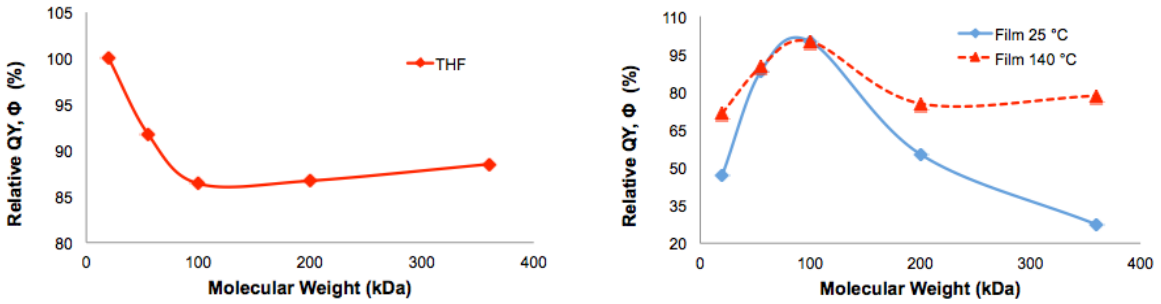

Figure 4.4. Relative quantum yields (RQY) of photoluminescence of PFO-MEH-PPV as a function of $M_{W/GPC}$. (a) Solutions in THF. (b) Thin films on glass.

increased significantly with rising M_W in samples P20-P100, and then dropped in samples with still higher values of M_W (Figure 4.4b). Films annealed at 140 °C for 10 min showed similar emissive behavior, but the effects of M_W were moderated (Figure 4.4b).

These data show that samples with the lowest value of M_W give the highest quantum yields of emission in dilute solution, where the relatively short chains can adopt conformations with an extended length of effective conjugation, and where aggregation is negligible. In contrast, samples with higher values of M_W have an increasing propensity to adopt coiled molecular structures that favor greater self-quenching of fluorescence by intracoil electronic energy transfer,[38] also known as homo-Förster resonance energy transfer.[39-40] Samples with lower values of M_W are likely to adopt rod-shape conformations, thereby limiting intramolecular self-quenching.

The behavior of PFO-MEH-PPV in thin films is more complex, and the highest values of RQY were found in samples with intermediate values of M_W. Figure 4.4b shows that annealing films of PFO-MEH-PPV greatly increased the RQY of samples with high values of M_W. Previous work has suggested that enhanced quantum yield and efficacy can arise in annealed films of fluorene-based polymers through the creation of domains of crystalline order

that serve as efficient self-dopants.[41-43] Self-doping arises when the crystallites are small, whereas larger crystallites behave as the bulk material.[44] Examining films of PFO-MEH-PPV by TEM revealed granular nanostructures in samples of low M_W (Figures 4.3a-b), whereas no similar features were observed in samples of high M_W (Figure 4.3c). It is possible that the observed granularity reflects organization of PFO-MEH-PPV in ordered domains, which are too large to enhance efficacy by self-doping in the case of sample P20, whereas the domains in P100 are of optimal size and number. The increased RQY in samples with higher values of M_W suggests that the crystalline domains increase in size when the films are heated. In all cases, annealing was carried out above T_g. DSC data (Table 4.1) confirmed that T_g increases with M_W, so that samples with low values of M_W have higher chain mobilities at the temperature of annealing, thereby favoring a degree of crystallization. It is worth noting that the curved plot of RQY as a function of M_W in thin films, which is shown in Figure 4.4b, closely resembles the dependency of luminous efficacy on M_W (Figure 4.1b). This similarity highlights how the efficiency of OLEDs, exemplified by devices incorporating PFO-MEH-PPV, depends strongly on the morphology of thin films and on M_W of the active polymeric component.

4.2.6 Conclusions

Samples of PFO-MEH-PPV with closely controlled values of M_W were synthesized to reveal how the performance of thin-film polymer-based OLEDs depends on molecular weight. Samples with M_W in the range 20-362 kDa were prepared, characterized by GPC and LS, and used to fabricate thin-film OLEDS with standard architectures. Properties of these devices, including luminous efficacies, λ_{max} of emission, and relative quantum yields of photoluminescence, were measured and found to show a significant dependence on M_W. A sample of PFO-MEH-PPV with M_W = 100 kDa proved to yield the best-performing OLED, which showed an efficacy of 0.90 lm/W, a low turn-on voltage of 1.98 V, and a low optimal working voltage of 3.94 V. Our observations underscore the importance of developing synthetic methods that reproducibly yield polymers with closely controlled values of M_W for

use in thin-film devices such as OLEDs. Our work also suggests that attaining optimal performance requires preparing samples with specific molecular weights that yield thin films with nanoscale ordered domains of a size that allows self-doping of the active layer. In addition, by measuring relative quantum yields of emission from thin films made using samples of polymers with controlled values of M_W, it may be possible to assess performance without making full devices, thereby accelerating the screening of materials and the optimization of devices for production.

4.2.7 Associate Content

Supporting Information Available: Schematic representation of the architecture of OLEDs, photograph of a representative OLED, video of a working OLED, L-V characteristics (including luminance, luminous efficacy, photoluminescence, and electroluminescence as a function of M_W), AFM images of thin films, general procedures related to the synthesis of PFO-MEH-PPV, and characterization of samples of the polymer by GPC and LS. This material is available free of charge via the Internet at http://pubs.acs.org.

4.2.8 Acknowledgments

We are grateful to the Natural Sciences and Engineering Research Council of Canada, the Ministère de l'Éducation du Québec, the Canada Foundation for Innovation, the Canada Research Chairs Program, NanoQuébec, and the Université de Montréal for financial support. We acknowledge with gratitude the fruitful advice of Patricia Moraille and Pierre Ménard-Tremblay (Laboratoire de caractérisation des matériaux, Département de chimie, Université de Montréal). In addition, we thank Jean-Philippe Masse (Centre de Caractérisation Microscopique des Matériaux $(CM)^2$, École Polytechnique de Montréal).

4.2.9 Supporting Information

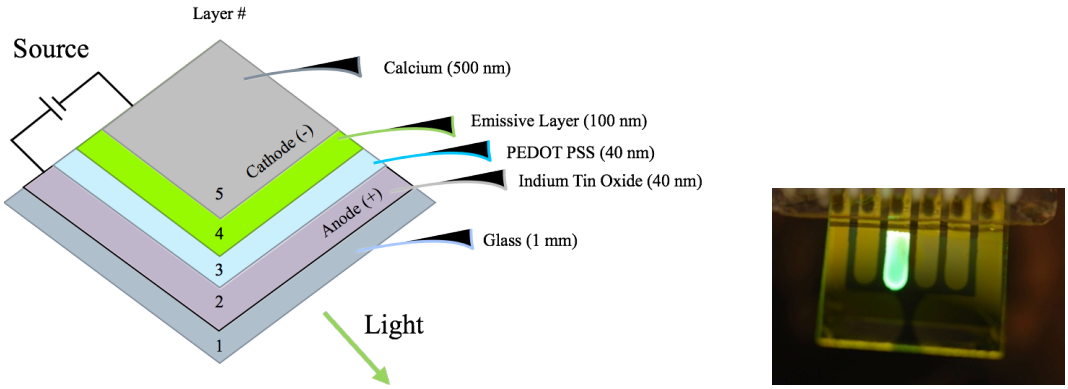

a b

Figure S4.1. (a) Schematic representation of the architecture of OLEDs used in the present study. (b) Photograph of a four-cell substrate using cylindrical calcium electrodes, with one device operating.

Video S4.1. Video of a working OLED containing sample P100 of PFO-MEH-PPV, with biases in the range 0-8 V applied.

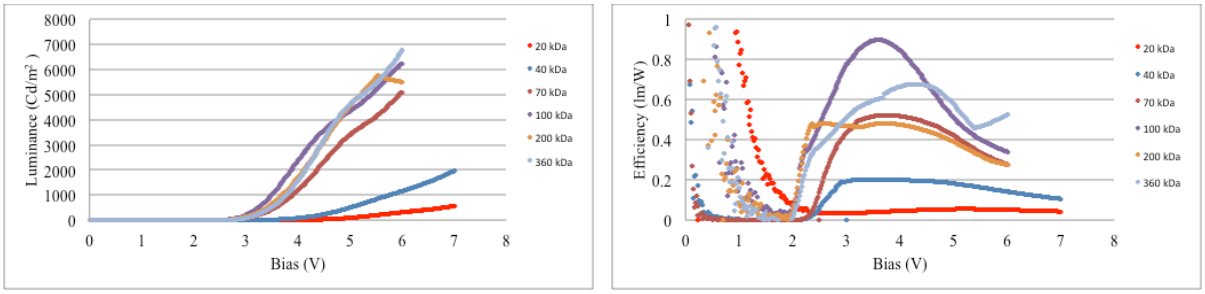

a b

Figure S4.2. L–V characteristics of OLEDs based on PFO-MEH-PPV of various molecular weights ($M_{W/GPC}$). (a) Luminance (L_v) in cd/m^2. (b) Luminous efficacy (η) in lm/W.

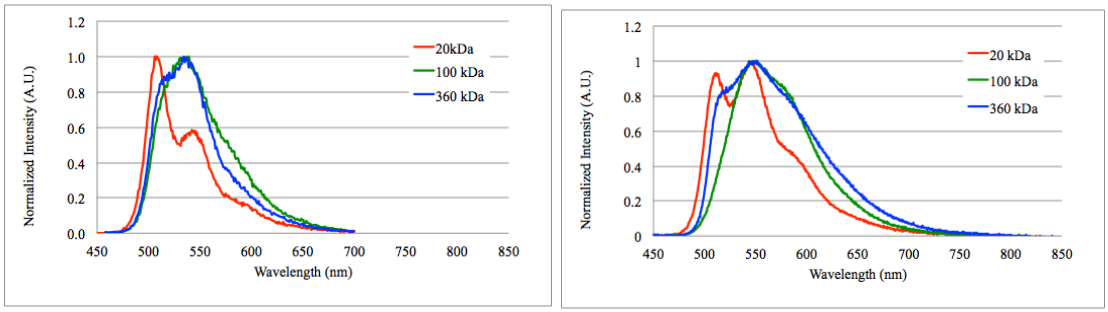

a b

Figure S4.3. Normalized emission of films of PFO-MEH-PPV with M_w of 20 kDa, 100 kDa and 360 kDa, annealed at 140 °C for 10 min. (a) Photoluminescence. (b) Electroluminescence.

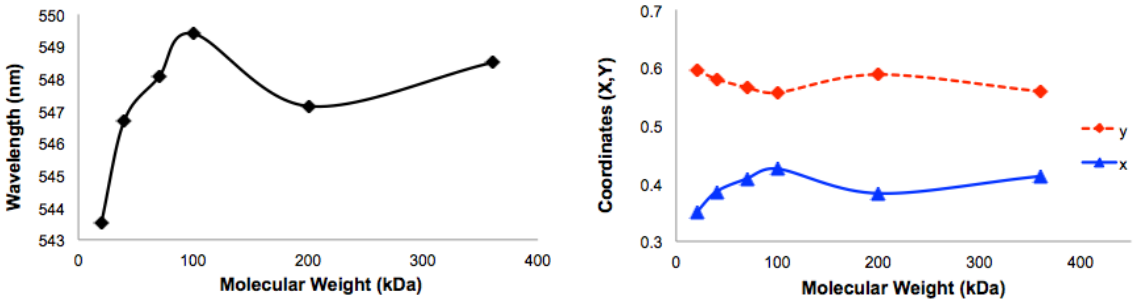

Figure S4.4. Electroluminescence of films of PFO-MEH-PPV annealed at 140 °C for 10 min. (a) Values of λ_{max} as a function of $M_{W/GPC}$. (b) CIE 1964 coordinates of OLED emission as a function of $M_{W/GPC}$.

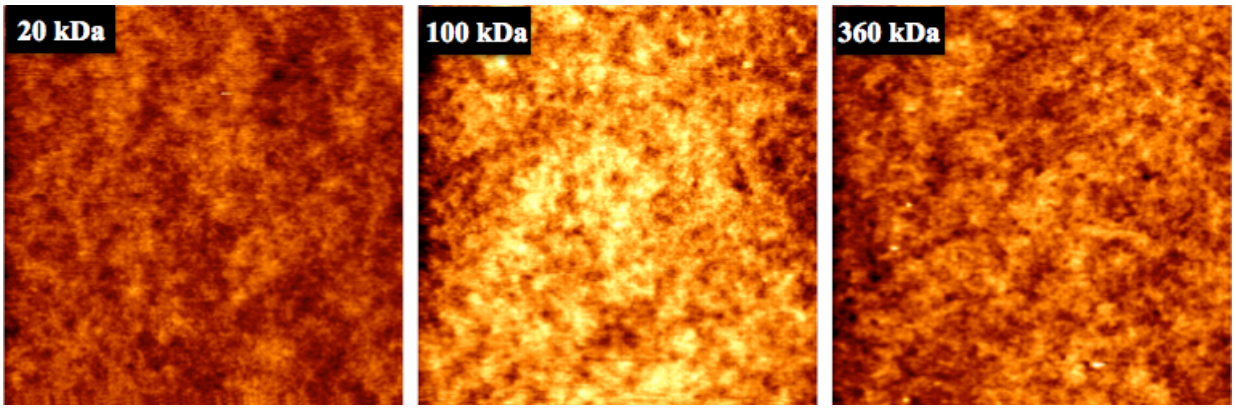

Figure S4.5. AFM images of films of PFO-MEH-PPV as a function of $M_{W/GPC}$ annealed at 140 °C for 10 min. (a) Sample P20 (20 kDa). (b) Sample P100 (100 kDa). (c) Sample P360 (360 kDa). Scan size: 10 µm × 10 µm.

4.2.9.1 Synthesis and characterisation

4.2.9.1.1 General procedures

Unless stated otherwise, commercially available reagents were used without further purification. Dry oxygen-free tetrahydrofuran was prepared by passage through columns packed with activated alumina and supported copper catalyst (Glass Contour, Irvine, CA). 2-Methoxy-5-(2-ethylhexyloxy)-1,4-bis(diethoxyphosphonomethyl)benzene and 9,9-dioctylfluorene-1,4-dicarboxaldehyde were prepared according to reported procedures.[18-20, 45] Unless indicated otherwise, reactions were carried out under an atmosphere of dry N_2 with rigid exclusion of moisture, using standard techniques for manipulating air-sensitive compounds.

Analytical thin-layer chromatography was performed using silica gel precoated on glass slides. Developed chromatograms were visualized by exposure to UV or vapors of iodine. Flash column chromatography was carried out using 230-400 mesh silica. Thermogravimetric analysis (TGA) was performed on a TA Instruments Thermogravimetric Analyzer (TGA Q500) at a heating rate of 10 °C /min under N_2 using a platinum pan. ^{1}H and ^{13}C NMR spectra of intermediates and monomers were recorded on a Bruker Avance 400 spectrometer (400 MHz for ^{1}H NMR spectra and 100 MHz for ^{13}C NMR spectra) and were found to match published data. UV-Vis measurements were done using a Cary 500 spectrophotometer.

4.2.9.2 Characterization of the polymers by gel-permeation chromatography (GPC)

Samples of PFO-MEH-PPV were dissolved in THF (2 mg/mL), and the solutions were filtered through a 0.45 μ membrane. GPC analyses were carried out using a Waters 1525 binary pump system, a Waters 717 Plus autosampler, and a Waters 2414 refractive index detector. The flow was set at 1 mL/min and was passed through a Waters column heater at 35 °C, then into a Waters Styragel pre-column (50 mm × 7.8 mm), and finally through a series of

three Phenomenex columns: Phenogel 500 Å (300 mm × 7.8 mm), Phenogel 10^4 Å (300 mm × 7.8 mm), and Phenogel 10^5 ÅÅ (300 mm × 7.8 mm). Analyte (100 μL) was injected after 2 h of system equilibration. Nine narrow polystyrene standards in three THF solutions were used to plot a calibration curve and allow calculation of the number-average molar mass (M_N), the weight-average molar mass (M_W), and the polydispersity (PDI) of analytes, using the Waters software system Breeze.

4.2.9.3 Characterization of the polymers by light scattering (LS)

Samples of PFO-MEH-PPV were dissolved in THF to produce ten solutions of with various precise concentrations in the range 0.200-2.000 mg/mL with increments of 0.200 mg/mL). The solutions were filtered through a 0.45 μ membrane and then used to determine the proper *dn/dc* value for PFO-MEH-PPV using a Wyatt Optilab rEX refractive index detector. LS analyses were carried out using a Waters 600 controller pump, a Waters 717 Plus autosampler, and a Wyatt Dawn EOS fixed 18 multi-angle LS detector with a 690 nm laser as the incident light source. The flow was set at 1 mL/min, and the analytes (100 μL) were passed at 25 °C through a series of two columns: a PLgel 5 μm 10^3 Å (300 mm × 7.8 mm), and a PLgel 5 μm 10^5 Å (300 mm × 7.8 mm). Analyses were performed after 2 h of system equilibration. The absolute molecular weight was obtained using the previously determined specific *dn/dc* and Wyatt Technology ASTRA 5.3.4 software.

4.2.10 References

[1] Hong, L. C. E.; Conroy, L. A.; Scholand, M. J. U.S. Lighting Market Characterization - Energy Efficient Lighting Technology Options. *U.S. Department of Energy* **2005,** *2*, 1-286.

[2] Conti, J. J.; Holtberg, P. D.; Beamon, J. A.; Napolitano, S. A.; Schaal, M. A.; Turnure, J. T.; Westfall, L. D. International Energy Outlook 2013. *U. S. Energy Information Administration* **2013**.

[3] Mogck, S.; Wanski, T.; Lehmann, C.; May, C. Present Status of Roll-to-Roll OLED Fabrication and Encapsulation. *J. Jpn. Soc. Colour Mater.* **2013,** *86* (12), 461-465.

[4] Choi, H. W.; Zhou, T.; Singh, M.; Jabbour, G. E. Recent developments and directions in printed nanomaterials. *Nanoscale* **2015,** *7*, 3338-3355.

[5] Patchett, E. R.; Williams, A.; Ding, Z.; Abbas, G.; Assender, H. E.; Morrison, J. J.; Yeates, S. G.; Taylor, D. M. A high-yield vacuum-evaporation-based R2R-compatible fabrication route for organic electronic circuits. *Organic Electronics* **2014,** *15*, 1493–1502.

[6] Tang, C. W.; VanSlyke, S. A. Organic electroluminescent diodes. *Appl. Phys. Lett.* **1987,** *51* (12), 913-915.

[7] Burroughes, J. H.; Bradley, D. D. C.; Brown, A. R.; Marks, R. N.; Mackay, K.; Friend, R. H.; Burns, P. L.; Holmes, A. B. Light-emitting diodes based on conjugated polymers. *Nature* **1990,** *347* (6293), 539-541.

[8] D'Andrade, B. W.; Forrest, S. R. White Organic Light-Emitting Devices for Solid-State Lighting. *Adv. Mater.* **2004,** *16* (18), 1585-1595.

[9] Farinola, G. M.; Ragni, R. Electroluminescent materials for white organic light emitting diodes. *Chem. Soc. Rev.* **2011,** *40*, 3467–3482.

[10] Reineke, S.; Thomschke, M.; Lüssem, B.; Leo, K. White organic light-emitting diodes: Status and perspective. *Rev. Mod. Phys.* **2013,** *85*, 1285-1293.

[11] Tessler, N.; Denton, G. J.; Friend, R. H. Lasing from conjugated-polymer microcavities. *Nature* **1996,** *382*, 695-697.

[12] Chénais, S.; Forget, S. Recent advances in solid-state organic lasers. *Polym. Int.* **2012,** *61* (3), 390–406.

[13] Forrest, S. R. The path to ubiquitous and low-cost organic electronic appliances on plastic. *Nature* **2004,** *428*, 911-918.

[14] Arias, A. C.; MacKenzie, J. D.; McCulloch, I.; Rivnay, J.; Salleo, A. Materials and Applications for Large Area Electronics: Solution-Based Approaches. *Chem. Rev.* **2010,** *110*, 3–24.

[15] Søndergaard, R. R.; Hösel, M.; Krebs, F. C. Roll-to-Roll fabrication of large area functional organic materials. *J. Polym. Sci. Part B Polym. Phys.* **2013,** *51* (1), 16–34.

[16] Sekine, C.; Tsubata, Y.; Yamada, T.; Kitano, M.; Doi, S. Recent progress of high performance polymer OLED and OPV materials for organic printed electronics. *Sci. Technol. Adv. Mater.* **2014,** *15*, 1-15.

[17] Kalifha, M. B.; Wantz, G.; Parneix, J. P.; Hirsch, L. Multilayer fluorescent polymer light emitting diode with low voltage and high efficiency. *European Physics Journal: Applied Physics* **2008,** *41*, 29-32.

[18] Burn, P. L.; Holmes, A. B.; Kraft, A.; Baigent, D. R.; Bradley, D. D. C.; Brown, A. B.; Friend, R. H. Chemical Tuning of the Electronic Properties of poly(p-phenylenevinylene)-Based Copolymers. *J. Am. Chem. Soc.* **1993,** *115*, 10117-10124.

[19] Pei, J.; Wen, S.; Zhou, Y.; Dong, Q.; Liu, Z.; Zhang, J.; Tian, W. A low band gap donor–acceptor copolymer containing fluorene and benzothiadiazole units: synthesis and photovoltaic properties. *New J. Chem.* **2011,** *35*, 385–393.

[20] Tan, T. A. T.; Clarke, T. M.; James, D.; Durrant, J. R.; White, J. M.; Ghiggino, K. P. Synthesis and photo-induced charge separation of confined conjugation length phenylene vinylene-based polymers. *Polym. Chem.* **2013,** *4*, 5305-5309.

[21] Brunner, P.-L. M.; Masse, J.-P.; L'Espérance, G.; Wuest, J. D. Imaging Layers in Thin-Film Molecular Devices by Transmission Electron Microscopy, Using Milling by Focused Ion Beams and Deposition on NaCl and Si. **2015**, submitted for publication.

[22] *See the supporting information for details.*

[23] Schwartz, B. J. Conjugated Polymers as Molecular Materials: How Chain Conformation and Film Morphology Influence Energy Transfer and Interchain Interactions. *Annu. Rev. Phys. Chem.* **2003,** *54*, 141–172.

[24] Hagler, T. W.; Pakbaz, K.; Voss, K. F.; Heeger, A. J. Enhanced order and electronic delocalization in conjugated polymers oriented by gel processing in polyethylene. *Phys. Rev. B* **1991,** *44* (16), 8652-8666.

[25] Jui-Hung Hsu; Wunshain Fann; Pei-Hsi Tsao; Kuen-Ru Chuang; Chen, S.-A. Fluorescence from Conjugated Polymer Aggregates in Dilute Poor Solution. *J. Phys. Chem. A* **1999,** *103*, 2375-2380.

[26] Scholes, G. D.; Larsen, D. S.; Fleming, G. R. Origin of line broadening in the electronic absorption spectra of conjugated polymers: Three-pulse-echo studies of MEH-PPV in toluene. *Phys. Rev. B* **2000,** *61* (20), 13670.

[27] Koren, A. B.; Curtis, M. D.; Francis, A. H.; Kampf, J. W. Intermolecular Interactions in π-Stacked Conjugated Molecules. Synthesis, Structure, and Spectral Characterization of Alkyl Bithiazole Oligomers. *J. Am. Chem. Soc.* **2003,** *125*, 5040-5050.

[28] Huber, J.; Mullen, K.; Salbeck, J.; Schenk, H.; Scherf, U.; Stehlin, T.; Stern, R. Blue Light-emitting Diodes Based on Ladder Polymers of the PPPType. *Acta Polymer* **1994,** *45*, 244-247.

[29] Xu, H.; Lv, Y.; Zhu, W.; Xu, F.; Long, L.; Yu, F.; Wang, Z.; Wei, B. Difference between photoluminescence and electroluminescence of excimer-based platinum [1, 3-difluoro-4,6-di(2-pyridinyl) benzene]chloride. *J. Phys. D: Appl. Phys.* **2011,** *44*, 415102-415105.

[30] Setayesh, S.; Grimsdale, A. C.; Weil, T.; Enkelmann, V.; Mullen, K.; Meghdadi, F.; List, E. J. W.; Leising, G. Polyfluorenes with Polyphenylene Dendron Side Chains: Toward Non-Aggregating, Light-Emitting Polymers. *J. Am. Chem. Soc.* **2001,** *123*, 946-953.

[31] Lemmer, U.; Heun, S.; Mahrt, R. F.; Scherf, U.; Hopmeier, M.; Siegner, U.; Göbel, E. O.; Müllen, K.; Bassler, H. Aggregate fluorescence in conjugated polymers. *Chem. Phys. Lett.* **1995,** *240* (4), 373–378.

[32] Gong, S. C.; Chang, H. J. Low Temperature Annealing Effect of PFO-Poss Emission Layer on the Properties of Polymer Light Emitting Diodes. *Kor. J. Mater. Res.* **2009,** *19* (6), 313-318.

[33] Tu, M.-L.; Su, Y.-K.; Lu, W.-C. Postdeposition Annealing Effect on Redshift Behavior of Electroluminescence for Polymer Light-Emitting Diodes. *Jpn. J. Appl. Phys.* **2006,** *45* (10A), 7737–7740.

[34] Kim, J.; Lee, J.; Han, C. W.; Lee, N. Y.; Chung, I.-J. Effect of thermal annealing on the lifetime of polymer light-emitting diodes. *Appl. Phys. Lett.* **2003,** *82* (24), 4238-4240.

[35] Wantz, G.; Dautel, O. J.; Hirsch, L.; Vignau, L.; Lère-Porte, J. P.; Moreau, J. J. E.; Parneix, J. P.; Serein-Spirau, F.; Almairac, R. Layered molecular film growth by substrate temperature tuning for efficiency-enhanced OLED. *Organic Electronics* **2006,** *7* (1), 38-44.

[36] Resta, C.; DiPietro, S.; Elenkov, M. M.; Hamersăk, Z.; Pescitelli, G.; Bari, L. D. Consequences of Chirality on the Aggregation Behavior of Poly[2- methoxy-5-(2′-ethylhexyloxy)- p-phenylenevinylene] (MEH-PPV). *Macromolecules* **2014,** *47*, 4847−4850.

[37] Brouwer, A. M. Standards for photoluminescence quantum yield measurements in solution. *Pure Appl. Chem.* **2011,** *83* (12), 2213–2228.

[38] Webber, S. E. Photon-Harvesting Polymers. *Chem. Rev.* **1990,** *90*, 1490.

[39] Förster, T. *In modern quantum chemistry: istanbul lectures.part III, Action of light and organic crystals*. Academic Press: New York, **1965**.

[40] Luchowski, R.; Matveeva, E. G.; Gryczynski, I.; Terpetschnig, E. A.; Patsenker, L.; Laczko, G.; Borejdo, J.; Gryczynski, Z. Single Molecule Studies of Multiple-Fluorophore Labeled Antibodies. Effect of Homo-FRET on the Number of Photons Available Before Photobleaching. *Curr Pharm Biotechnol.* **2008,** *9* (5), 411.

[41] Zhang, B.; Qin, C.; Ding, J.; Chen, L.; Xie, Z.; Cheng, Y.; Wang, L. High-Performance All-Polymer White-Light-Emitting Diodes Using Polyfluorene Containing Phosphonate Groups as an Efficient Electron-Injection Layer. *Adv. Funct. Mater.* **2010,** *20*, 2951–2957.

[42] Lu, H.-H.; Liu, C.-Y.; Chang, C.-H.; Chen, S.-A. Self-Dopant Formation in Poly(9,9-di-n-octylfluorene) Via a Dipping Method for Efficient and Stable Pure-Blue Electroluminescence. *Adv. Mater.* **2007,** *19*, 2574.

[43] Ariu, M.; Lidzey, D. G.; Sims, M.; Cadby, A. G.; Lane, P. A.; Bradley, D. D. C. The effect of morphology on the temperature-dependent photoluminescence quantum efficiency of the conjugated polymer poly(9, 9-dioctylfluorene). *J. Phys.: Condens. Matter* **2002,** *14*, 9975.

[44] Chen, X.; Wan, H.; Li, H.; Cheng, F.; Ding, J.; Yao, B.; Xie, Z.; Wang, L.; Zhang, J. Influence of thermal annealing temperature on electro-optical properties of

polyoctylfluorene thin film: Enhancement of luminescence by self-doping effect of low-content a phase crystallites. *Polymer* **2012,** *53*, 3827.

[45] Rosa, A. L.; Gillemot, K.; Leary, E.; Evangeli, C.; Gonzaĺez, M. a. T.; Filippone, S.; Rubio-Bollinger, G.; Agrait, N.; Lambert, C. J.; Martín, N. Does a Cyclopropane Ring Enhance the Electronic Communication in Dumbbell-Type C60 Dimers? *J. Org. Chem.* **2014,** *79*, 4871-4877.

Chapitre 5

Imagerie par microscopie électronique à transmission de dispositifs à films minces, découpés par faiceaux d'ions focusés ou déposés sur substrats de NaCl et Si

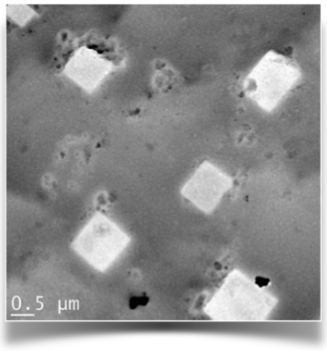

« Hip to be square », Image MET d'un polymère à trous carrés

5.1 Introduction Article 4

Les efforts récents focalisés sur la mise à niveau des technologies de l'électronique organique face aux dispositifs homologues basés sur des matériaux inorganiques, ont multipliés la production de nouveaux composés organiques simples ou polymériques pouvant prendre forme en films minces. Leurs performances en diodes organique électroluminescentes, en cellules photovoltaïques organiques, ou en transistors à films organiques minces, sont reliées de très près aux morphologies adoptées par ceux-ci sous forme de films. Plusieurs stratégies incluant la variation des techniques d'applications des solutions, les recuits thermiques, ou les traitements sous solvants, sont souvent utilisés pour modifier la morphologie des films et optimiser les performances des dispositifs. Pour comprendre et suivre les variations des arrangements moléculaires produits, l'imagerie par microscopie électronique à transmission (MET) est souvent utilisée conjointement avec la microscopie électronique à balayage (MEB) et la microscopie à force atomique (AFM). Le présent travail est focalisé sur la préparation pour le MET des échantillons de matériaux organiques actifs. Une nouvelle méthode basée sur l'imagerie des films à partir de gaufres de silicium est présentée et comparée à d'autres méthodes d'extraction des films.

5.2 Article 4

Imaging Layers in Thin-Film Molecular Devices by Transmission Electron Microscopy, Using Milling by Focused Ion Beams and Deposition on NaCl and Si Substrates

Pierre-Louis M. Brunner,[1*] Jean-Philippe Masse,[2*] Gilles L'Espérance,[2] and James D. Wuest[1*]

[1]*Département de Chimie, Université de Montréal, Montréal, Québec H3C 3J7, Canada*

[2]*Centre de Caractérisation Microscopique des Matériaux (CM)², École Polytechnique de Montréal, Montréal, Québec H3C 3A7, Canada*

Applied Materials & Interfaces, **2015**, Soumis pour publication

5.2.1 Keywords

Keywords: Transmission electron microscopy (TEM), Molecular materials, Thin-film devices, Focused ion beams (FIB), Si wafer substrates, NaCl substrates, Nanopatterning

5.2.2 Abstract

The performance of molecule-based thin-film devices such as organic light-emitting diodes, photovoltaic cells, and thin-film transistors depends on the electronic properties of the individual molecular components, as well as on their association to form complex morphologies. Transmission electron microscopy (TEM) can be used to image the morphologies and help reveal how the devices work. We have examined new ways to prepare samples of thin molecular films for imaging by TEM. Specifically, we report the use of focused ion beams to mill cross sections of complete devices that have been glued together with epoxy adhesives. In addition, we show that thin layers can be deposited on disks of NaCl, which can then be dissolved in water to release free-standing films that can be imaged by TEM. Finally, we also demonstrate that films can be deposited on Si wafers, which can then be fractured to expose sections of film that overhang edges of fragments and can be imaged conveniently by TEM.

5.2.3 Introduction

Historically, basic electronic devices such as light-emitting diodes, photovoltaic cells, and field-effect transistors have been made primarily from inorganic materials. More recently, however, a new generation of analogous devices has begun to emerge, in which active inorganic components are replaced by carbon-based molecular materials. These new materials are exciting because they may ultimately yield flexible, light-weight, high-performance optoelectronic devices that can be produced inexpensively from renewable sources by large-scale methods such as roll-to-roll printing. The accelerating international effort to develop such devices has led to the design and synthesis of a wide range of new materials composed of polymers and small molecules, which have been converted into active thin films for use in organic light-emitting diodes (OLEDs),[1-3] photovoltaic cells (OPVs),[4-6] thin-film transistors (OTFTs), and other devices.[7-10]

The performance of these devices depends not only on the properties of the individual molecular components, but also on collective behavior, including molecular association and the creation of films with complex nanomorphologies.[11-13] Various strategies have been devised to alter the morphology of molecular thin films and to thereby optimize the performance of devices, such as by varying the method of depositing films[14-19] or by modifying films after their initial formation, using subsequent exposure to heat (thermal annealing) or selected solvents (solvent annealing).[15, 20-29] Transmission electron microscopy (TEM) is one of the primary techniques for characterizing the morphology of molecular materials and for following its evolution. In our on-going work with thin-layer devices and active molecular components, we encountered shortcomings in existing techniques used to prepare samples for analysis by TEM. In response, we developed fast, simple new procedures that are particularly suitable for imaging thin molecular films created by methods such as spin coating. We believe that our techniques will also be useful in other areas of imaging.

Many methods are already used to prepare related samples for analysis by TEM, including sectioning by ultramicrotomy at various temperatures,[30-31] milling by focused ion beams

(FIB),[32-33] small-angle cleavage of Si wafers and other hard substrates,[34-38] direct dipping of TEM support grids in solutions containing compounds of interest,[39-40] and casting films from solutions[13, 29, 41-45]. Shortcomings of these approaches are summarized below:

- **Ultramicrotomy.** Ultramicrotomy is widely used to slice bulk samples, but it is not well-suited for studying thin layers such as those created by spin coating,[31] and it is impossible to use when thin films are deposited on hard substrates in working devices such as OLEDs, OPVs, and OTFTs. Thin films of molecular materials can be cast onto epoxy resins or other solids, which can then be cut into sections by ultramicrotomy, but subsequent treatments of the films by annealing or other methods may no longer be possible. Moreover, ultramicrotomy can also modify the morphology of materials by causing plastic deformations.[46]
- **FIB milling**. FIB milling can be used in analyses of a very wide range of materials, and it is well suited for preparing samples of thin films already incorporated in electronic devices. Milling can be used to reveal how methods of layer-by-layer deposition affect the morphology of existing layers. Although FIB milling is frequently used to prepare cross sections of materials for analysis by TEM, it is much less suitable for exposing the surface of layers in thin-film devices. Furthermore, samples prepared by FIB milling are known to suffer damage, even when the process is carried out at glancing angles.[33] This may lead to partial thermal amorphization of surfaces and ion implantation.[47] These effects can be minimized by using the shadow-FIB method,[32] but they cannot be totally avoided, particularly for sensitive molecular materials.
- **Small-angle cleavage**. This technique requires deposition of samples on hard substrates with appropriate planes of cleavage. It is faster than ion milling, but it requires manipulations that are not compatible with most molecular thin films. Samples must be immobilized with glue or high-melting waxes, then detached after grinding, polishing, scribing, and exposure to organic solvents or high temperatures. These steps would compromise integrity of molecular films, but the technique has been used successfully with inorganic materials deposited by different techniques on

various hard substrates, including Si, sapphire, quartz, glass, GaAs, and silicon carbide.[36]

- **Dipping and casting**. Casting thin molecular layers from solution is widely used to prepare samples for analysis by TEM.[13, 29, 41-45] Dissolved material can be coated directly onto soluble substrates or onto existing soluble layers such as PEDOT:PSS, and the newly created films can be subsequently lifted off by dissolution of the underlying material. NaCl disks[29, 43] or Si wafers coated with soluble photoresists have been employed,[41-42] with water or acetone used as typical solvents. However, the process of detaching the layers may affect their morphology. It is also possible to cast solutions directly onto TEM grids coated with holey or lacey carbon.[39-40] In addition, mechanical detachment of molecular thin layers has been reported with no experimental details.[44]

The present work examines different ways to prepare samples of thin molecular films so that their morphology can be examined by TEM. In particular, we report FIB milling to produce samples from a complete OLED device, analyses of spin-coated thin films lifted from NaCl disks, and the examination of thin layers on the edges of fractured Si wafers.

5.2.4 Experimental Section

5.2.4.1 Active materials

Thin layers suitable for analysis by TEM were prepared from a series of polymers and well-defined molecular compounds that have found use in existing thin-film devices. The materials were prepared according to published methods or were obtained from commercial sources. The compound known as IF(BTC)$_2$ (which is 2,2'-[[5',5'''-(6,6,12,12-tetraoctyl-6,12-dihydroindeno[1,2-*b*]fluorene-2,8-diyl)bis[(2'',2'''-bithiophene)-5'',5'-diyl]]bis(methanyl-ylidene))dimalononitrile) was synthesized according to a reported method.[48] Known compounds P3HT (poly(3-hexylthiophene-2,5-diyl)), PTB7 (poly[[4,8-bis[(2-ethylhexyl)oxy]benzo[1,2-*b*:4,5-*b'*]dithiophene-2,6-diyl][3-fluoro-2-[(2-

ethylhexyl)carbonyl]thieno[3,4-*b*]thiophenediyl]]), $PC_{61}BM$ ([6,6]-phenyl-C_{61}-butyric acid methyl ester), Si-PCPDTBT (poly[2,6-(4,4-bis(2-ethylhexyl)dithieno[3,2-*b*:2,3-*d*]silole)-*alt*-4,7-(2,1,3-benzothiadiazole)]) and PFO-MEH-PPV (poly[(9,9-dioctyl-9*H*-fluorene-2,7-diyl)-1,2-ethenediyl[2-methoxy-5-(2-ethylhexyloxy)-1,4-phenylene]-1,2-ethenediyl]) were provided by Solaris Chem Inc. The corresponding structures are shown in Figure S5.1 (see Supporting Information).

5.2.4.2 Sample preparation: Generalities

To make our work directly relevant to the study of molecular devices, films for analysis by TEM were prepared under conditions closely similar to those used in the fabrication of working devices. Films on NaCl disks or Si wafers were deposited by spin coating and were annealed when needed by using a hotplate in an N_2-filled glove box. Sections made by FIB milling were cut from standard working OLEDs glued together in a face-to-face arrangement, as described below.

5.2.4.3 Sample preparation: FIB milling by the in situ lift-out "sandwich" method

Milling of samples by FIB was performed using a Hitachi FB-2000A focused ion beam system operating at 30 keV. This system produces an intense beam of Ga ions using a high-brightness liquid-metal ion source and a double lens focusing system. The resulting FIB can mill various materials with a spatial resolution of 50-100 nm. A gun to deposit tungsten was used to cover and protect areas selected for characterization. An in situ lift-out FIB technique was used to prepare TEM samples from OLEDs containing a 100 nm-thick layer of PFO-MEH-PPV placed between a layer of PEDOT/PSS and a Ca cathode. A schematic representation of the architecture of the devices can be found in Figure S5.2 of the Supporting Information, along with a photograph of a representative OLED. The OLEDs and their fabrication have been described in detail elsewhere.[49] A similar representation of OPVs appears in Figure S5.3 of the Supporting Information, along with a photograph of a typical

device. To avoid FIB-induced damage of the surface of the active molecular material during deposition of the sacrificial layer of tungsten, a sandwich was prepared by using an epoxy adhesive to glue two 2 × 4 mm^2 pieces of the OLED face-to-face. To limit the thickness of the layer of epoxy to a few micrometers, mechanical pressure was applied during curing. The sandwich was then polished in cross section using silicon carbide papers of different grits, followed by polishing by diamond and colloidal suspensions of alumina to reach a final surface finish of 0.05 micrometer. A sacrificial layer of tungsten about 0.5-1 μm in thickness was deposited on the polished cross section of the sandwich. The lift-out method was used to extract a thin lamella, which was then fixed to a Cu half-disk TEM support using tungsten deposition/welding.

5.2.4.4 Sample preparation: Spin coating on NaCl disks

Spin coating was used to deposit thin films of PFO-MEH-PPV, Si-PCPDTBT, PTB7, and a mixture of P3HT and $PC_{61}BM$ (1:1 w/w) on water-polished disks made of single-crystalline NaCl (25 mm in diameter and 5 mm in thickness). Spin coating employed solutions in cyclohexanone for PFO-MEH-PPV (15 mg/mL) or chlorobenzene for the other materials (10 mg/mL) and was performed at a speed of 1000 rpm for 90 sec to give deposited films with a thickness of about 100 nm, as measured by profilometry using a Dektak 3030ST stylus profilometer. Films of PFO-MEH-PPV and P3HT:$PC_{61}BM$ were subjected to thermal annealing at 140 °C for 10 min and at 150 °C for 20 min, respectively. The films were then lifted off by immersing the NaCl disks in deionized water (Figure S5.4, Video S5.1). Before release from the surface, the films could also be scored with a razor blade to create small squares (3 × 3 mm^2) to facilitate lifting, as shown by the optical micrograph in Figure 1a. Double folding Cu grids (50-mesh) were then used to scoop up pieces of film floating on the surface (Figure 5.1b).

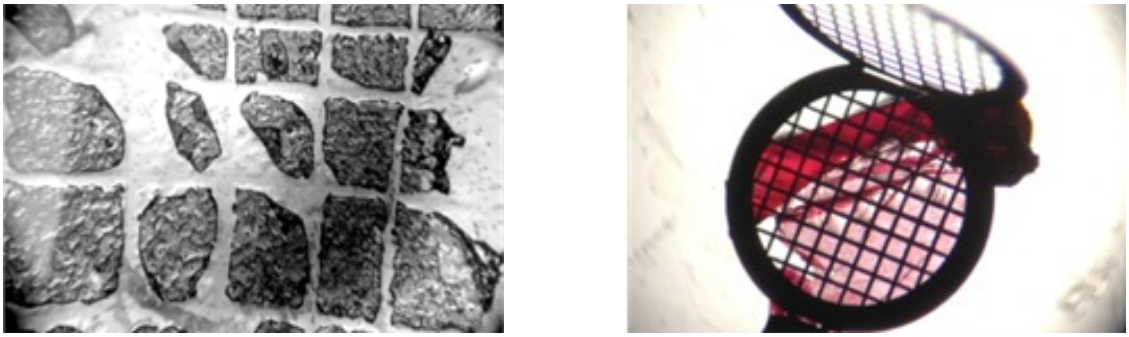

a *b*

Figure 5.1. (a) Optical micrograph showing a film of PTB7 deposited on an NaCl disk and scored into pieces approximately 3 × 3 mm^2 in size. (b) Films of blended P3HT:$PC_{61}BM$, detached from the surface of NaCl disks by exposure to water and scooped from the surface using a 50-mesh double folding Cu grid.

5.2.4.5 Sample preparation: Spin coating on Si wafers

Spin coating was used to deposit thin films of PFO-MEH-PPV and blended P3HT:$PC_{61}BM$ on square wafers of single-crystalline Si (25 mm on each edge and 700 μm in thickness). Spin coating used solutions in cyclohexanone and chlorobenzene respectively (15 mg/mL), and was performed at a speed of 1000 rpm for 90 sec to give films about 100 nm in thickness as measured by profilometry. Subsequent thermal annealing was carried out at 140 °C for 10 min and at 150 °C for 20 min, respectively. Treatment of the wafers with hexamethyldisilazane (HMDS) before spin coating was found to enhance the wettability of the surface by various organic solvents. Coated wafers were then shattered into small pieces with a mortar and pestle. Fragments with adhering film were different in color from pristine pieces of wafer and could be selected by optical microscopy for mounting on 50-mesh double folding Cu grids (Figure 5.2).

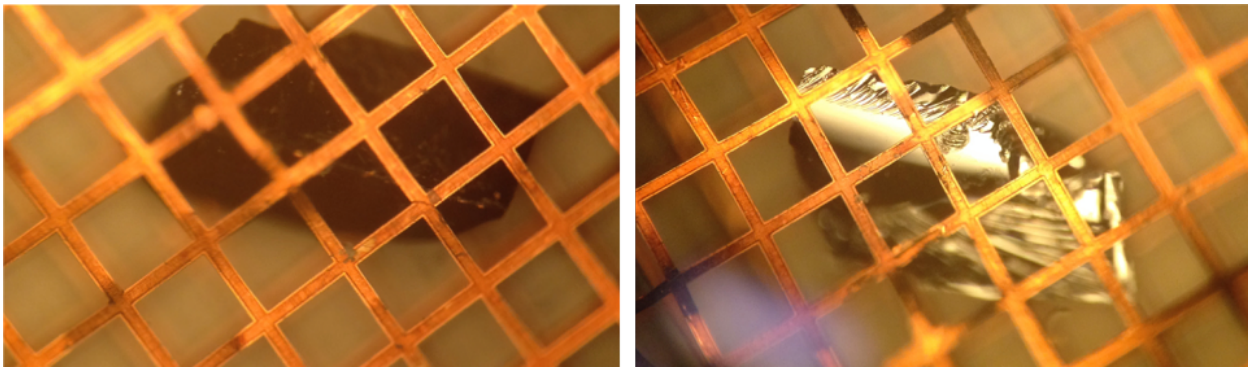

a *b*

Figure 5.2. Optical micrographs showing both sides of a fragment of coated Si wafer, mounted on a 50-mesh Cu grid for imaging by TEM. (a) Side coated with a blend of P3HT:$PC_{61}BM$. (b) Uncoated side showing the pristine surface of the wafer.

5.2.4.6 Characterization by TEM

TEM was performed using a JEOL JEM-2100F instrument equipped with a Schottky field-emission electron source, which was operated at 200 keV in bright-field mode for all samples analyzed. The use of low doses and a high voltage minimized damage to samples. Digital images were acquired using a Gatan UltraScan 1000 high-speed digital camera and Gatan digital micrographic software. Samples lifted from solid substrates were observed perpendicular to the plane of the films, and samples prepared by FIB milling were observed in cross section. All samples were examined at 25 °C with a defocus between 0 and -5 μm.

5.2.5 Results and Discussion

When individual layers in thin-film electronic devices need to be examined by TEM, they can in principle be freed from adjacent layers by exploiting differences in solubility or chemical reactivity.[13] This requires that the layer of interest be more resistant to selected agents than the materials next to it. In addition, the agents must be able to diffuse efficiently around the layer of interest so that they can act on the neighboring layers. This process of

selective penetration is expected to become slower as the surface area of the thin-film device becomes larger. Using an ultrasonic bath can accelerate the process but may alter the morphology of the film of interest. Ideally, individual films should be imaged directly in working devices without additional manipulation.

Imaging films in working devices allows direct examination of the complex relationship between the morphology of films and their performance. As a first step in characterizing complete devices and their constituent layers by TEM, we cut devices into cross sections by FIB milling. The schematic representation in Figure 5.3a shows how two OLEDs were first glued together symmetrically with an epoxy adhesive. The active layer to be examined is generally near the top of the device, so the epoxy acts as a thick protective layer to ensure the integrity of the edge of the film. Sectioning by milling is laborious, and the strategy of gluing allows two samples to be prepared at the same time. Furthermore, the two samples can be compared directly because they were handled under identical conditions. The resulting sandwiches were sliced by milling to give cross sections approximately 100 nm in thickness, which were imaged by TEM (Figure 5.3b). Figures 5.3c-d provide increasingly detailed views of the cross section of one of the glued OLEDs, and the active layer of PFO-MEH-PPV in the device is easily discerned. The sputtered ITO anode appears as discontinuous, but it is rectified and smoothed by the adlayer of PEDOT:PSS. In contrast, the layer of PFO-MEH-PPV is uniform and consistently about 105 nm in thickness. The lack of internal nanoscale organization in the active layer may mean that it had no conspicuous morphological features when created, or that its original morphology was altered by amorphization during milling. Despite this uncertainty, milling allows characterization of the gross features of the device in cross section; however, the technique is not suitable for obtaining detailed views of the surface of individual layers, which must be acquired by complementary methods.

To obtain complementary images of the surfaces of active layers, spin coating was used to deposit various samples onto NaCl disks of the type frequently used for recording IR spectra of films. The surfaces of the NaCl substrates were first polished with deionized water

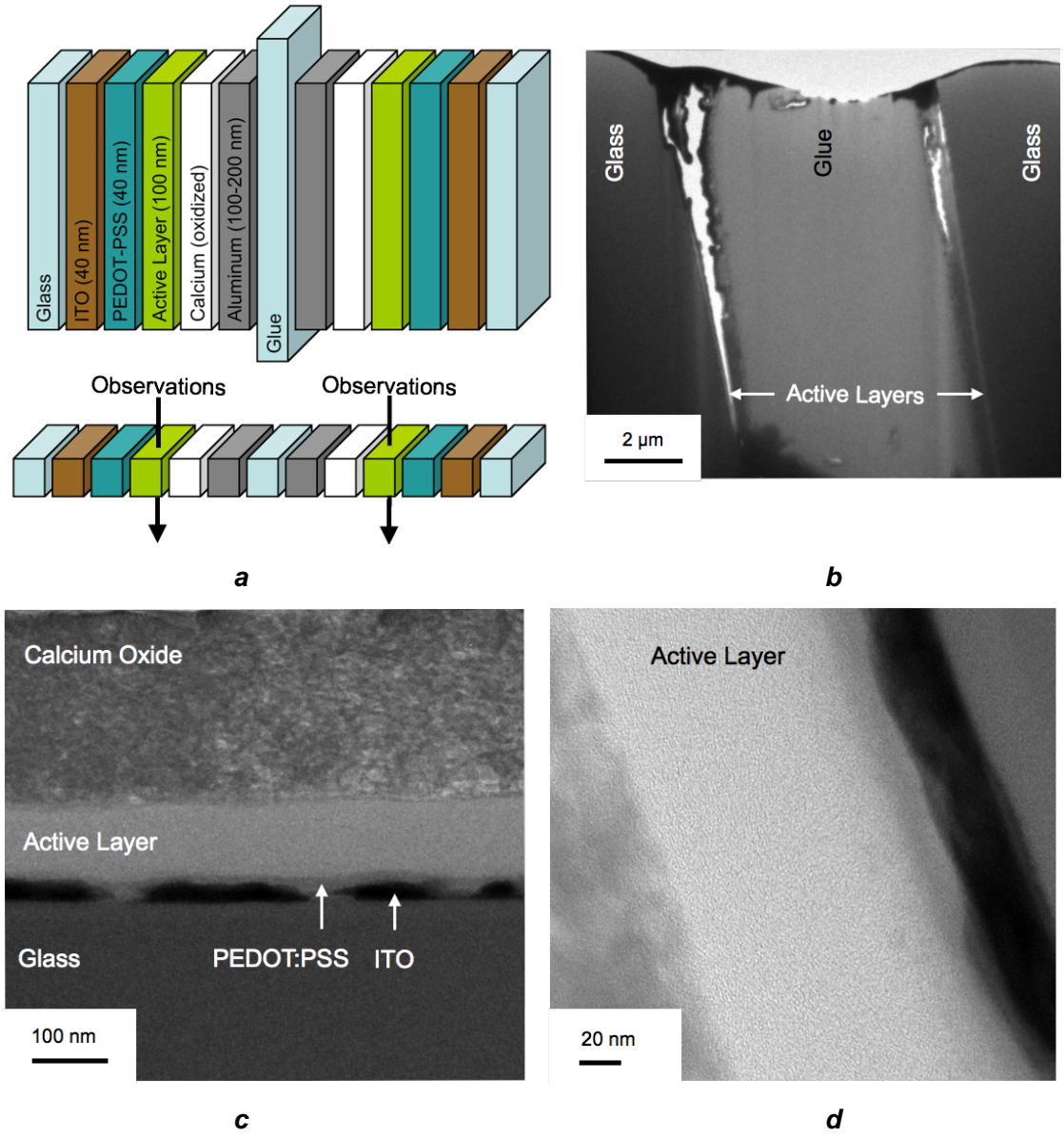

Figure 5.3. (a) Schematic representation of two complete OLEDs glued together face-to-face, as well as the cross section cut by FIB milling for characterization by TEM. (b) Bright-field TEM image of the complete cross section, showing voids created by milling. (c) Detailed image of the cross section of one device. (d) Enlarged view of the active layer between the calcium cathode and the PEDOT:PSS/ITO anode.

to remove nanocrystals of NaCl resulting from extended exposure to moist air. If this is not done, films lifted from the surface by exposing the disks to water typically show intact imprints of nanocrystals (Figures 5.4a-b). This observation suggests that customizable nanoimpressions can be cast with high fidelity in thin molecular films of the type used in optoelectronic devices or in other applications. In principle, these empty impressions can then be filled with other materials to create more complex hybrid structures, such as multiple ordered p-n junctions or more effective interfaces between electrodes and active layers.

Spin coating on water-polished NaCl disks yielded regular films similar to those deposited on normal ITO/PEDOT:PSS substrates. The films could then be lifted off by dissolving the disks in water, as described in the Experimental Section. The process of deposition on NaCl disks and subsequent detachment did not appear to induce changes in the gross morphology of the films, as long as the disks were polished to remove adhering nanocrystals (Figures 5.4a-c). This method of liberating free-standing films is very convenient, and thermal annealing can be performed directly on the disks, just as it is done during the fabrication of complete devices. Figures 5.4d-e show how thermal annealing on NaCl disks can induce normal phase separation in blends frequently used in OPVs.

It is important to note that this method allows many prospective blends to be deposited as films on NaCl, annealed, and analyzed by TEM in a short time, thereby allowing phase separation to be assessed quickly without actually making full devices. As a result, the method promises to accelerate the development of new high-performance devices. The method also allows rapid analysis by TEM to be carried out during the synthesis and processing of promising molecular materials as a way to identify residual impurities such as catalysts. For example, Figure 5.4f shows a TEM image of a detached film of PTB7 that reveals the presence of an additional phase, presumably catalytic nanoparticles of $Pd/Sn/SiO_2$ derived from the final step in the synthesis, as determined by energy-dispersive X-ray spectroscopy (Figure S5.5). These particles must be removed to produce material suitable for manufacturing optimized electronic devices, so the use of TEM to monitor films deposited on NaCl and then detached is a potentially important analytical tool.

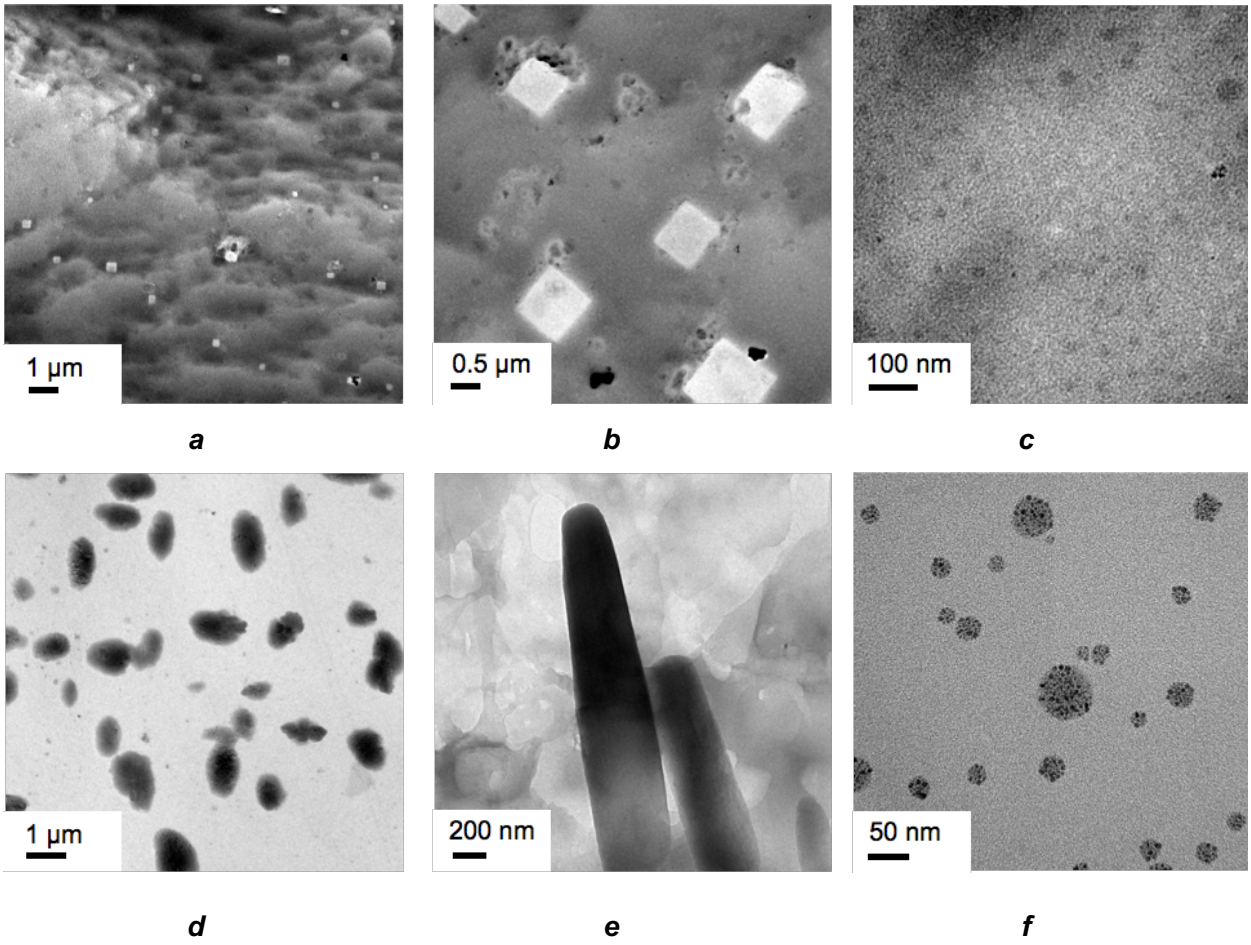

Figure 5.4. TEM images of thin molecular films lifted from the surface of NaCl disks and mounted on 50-mesh Cu grids. (a) Film of PFO-MEH-PPV with irregularities caused by using an unpolished NaCl disk. (b) Detailed view of nanoimpressions left in film of PFO-MEH-PPV by nanocrystals of NaCl not removed by preliminary polishing. (c) Nanostructure of a thin film of PFO-MEH-PPV deposited on polished NaCl. (d) Phase-separated particles of $PC_{61}BM$ (dark objects) produced by thermally annealing a film of admixed P3HT and $PC_{61}BM$ deposited on NaCl. (e) Crystals of $IF(BTC)_2$ separated from a matrix of P3HT by thermal annealing of a mixed film deposited on NaCl. (f) Nanoparticles of $Pd/Sn/SiO_2$ present in an impure sample of PTB7, as revealed by using TEM (EDS) to image a thin film detached from NaCl.

Using spin coating to deposit layers of molecular materials on disks of NaCl, followed by dissolving the disks in water, is a powerful way to produce free-standing films for various purposes, including imaging by TEM. Obviously, this technique is limited to preparing films of materials that are not themselves soluble in water, and it can produce ghost morphologies when the surface of NaCl is not properly cleaned. To allow a wider range of layers to be analyzed by TEM, we developed a new technique using spin coating on wafers of single-crystalline Si. This substrate cleaves sharply along crystallographically determined planes, and many broken edges are overhung by the adhering amorphous film, which can then be imaged conveniently by TEM. Again, this technique allows films to be annealed by exposure to heat or solvents to mimic steps in the fabrication of complete devices. If desired, the surface of Si wafers can be pretreated with HMDS to facilitate wetting by certain solvents used in spin coating, but this step was not generally needed in our studies, and no significant differences between films deposited on normal Si and HMDS-treated Si were noted.

Once layers were deposited and then annealed if necessary, coated Si wafers were shattered in a mortar by pressing them with a pestle. Colored fragments were rapidly identified by optical microscopy and mounted in standard 50-mesh double folding Cu grids. When stressed, Si wafers crack easily, and fractures propagate along atomic planes to form sharp edges of various thicknesses depending on the angle of rupture at the edge.[50-51] In contrast, the adhering films are not typically ordered or epitaxially deposited on the underlying surface of Si, so fractures of the molecular material do not follow breakage of the wafers, and parts of the deposited films invariably overhang edges of the fragments. Overhanging portions of film are typically large enough (100 nm to 5 μm) to allow informative TEM images to be recorded, as shown in Figure 5.5. In this way, the inherent morphology of films can be observed without interference from the substrate, whereas in adjacent areas interference fringes characteristic of thin fractured edges of Si wafers are also visible (Figures 5.5b-c). This method of imaging molecular thin films is faster and more reliable than the alternative of using NaCl, which requires the additional step of detachment using water and may thereby alter the morphology of certain films. The TEM image in Figure 5.5c closely resembles the result of analyzing the cross section of a complete OLED prepared by FIB milling (Figure 5.3d), suggesting that the

absence of a complex morphology is characteristic of the material, not a result of amorphization during milling.

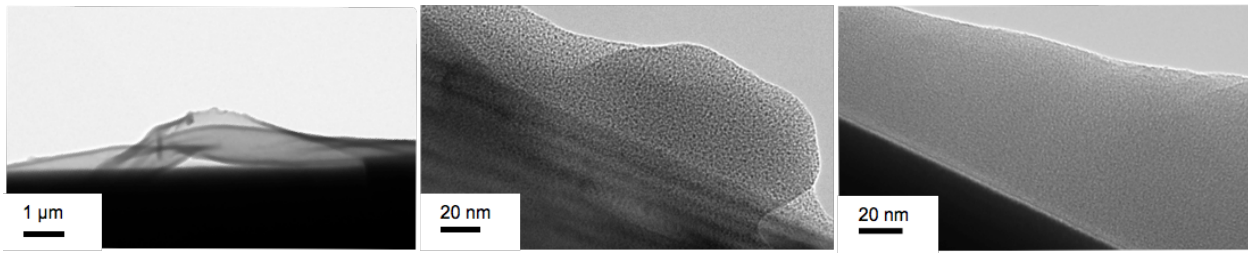

Figure 5.5. Bright-field TEM images of molecular films deposited on fractured pieces of Si wafers mounted in 50-mesh double folding Cu grids. (a) Film composed of a blend of P3HT:$PC_{61}BM$ slightly overhanging the edge of a fragment. (b) Thin film of PFO-MEH-PPV overhanging the edge of a thin fragment of Si wafer, which gives rise to interference fringes (banded region of image). (c) Thin film of PFO-MEH-PPV overhanging the edge of a thick layer of Si (dark region of image).

5.2.6 Conclusions

The performance of thin-layer devices that incorporate molecular materials depends not only on the identity of the individual components, but also on nanostructures resulting from processes of self-association and phase separation that take place within the materials. Learning how to assess and control the internal nanomorphology of complex molecular materials is a prerequisite for making rational advances in many areas of science and technology, including the development of improved thin-film optoelectronic devices. TEM is a powerful tool for revealing morphological details, but our initial efforts to use it to image molecule-based thin-film devices uncovered various shortcomings, including a lack of convenient methods for preparing samples by methods that avoid introducing artifacts and resemble steps used in fabricating working devices. We have summarized three techniques that we have found to be particularly suitable for imaging both the surface and cross section of

thin molecular films produced by spin coating for use in devices. These techniques feature the use of FIB milling to cut devices into sections for imaging, as well as the deposition of thin films on solid substrates under conditions that allow the films to be annealed if necessary, then imaged directly or detached before imaging. In addition, we have reported evidence suggesting that these techniques may have ancillary benefits of broad potential in the field of molecular materials. In particular, our method of spin coating on NaCl disks and subsequent detachment allows the preparation of thin free-standing molecular films that preserve nanostructural details imprinted by the underlying solid surface. Moreover, our method of spin coating on Si wafers and shattering the solid substrate to expose overhanging areas of pristine thin films allows convenient real-time screening of samples by TEM. In such ways, TEM can be used to monitor the purification of molecular materials containing undesired contaminants such as nanoparticulate catalysts, thereby avoiding the need for time- and material-consuming analytical methods such as atomic absorption spectroscopy.

5.2.7 Associated Content

Supporting Information Available : Structures of the molecular components of thin films imaged by TEM, schematic representations and photographs of typical thin-layer devices, photographs and videos showing how films can be lifted from substrates of NaCl, and analysis of detached films by energy-dispersive X-ray spectroscopy. This material is available free of charge via the Internet at http://pubs.acs.org.

5.2.8 Acknowledgments

The authors are grateful to the Natural Sciences and Engineering Research Council of Canada, the Ministère de l'Éducation du Québec, the Canada Foundation for Innovation, the Canada Research Chairs Program, NanoQuébec, and the Université de Montréal for financial support.

5.2.9 Supplemental Information

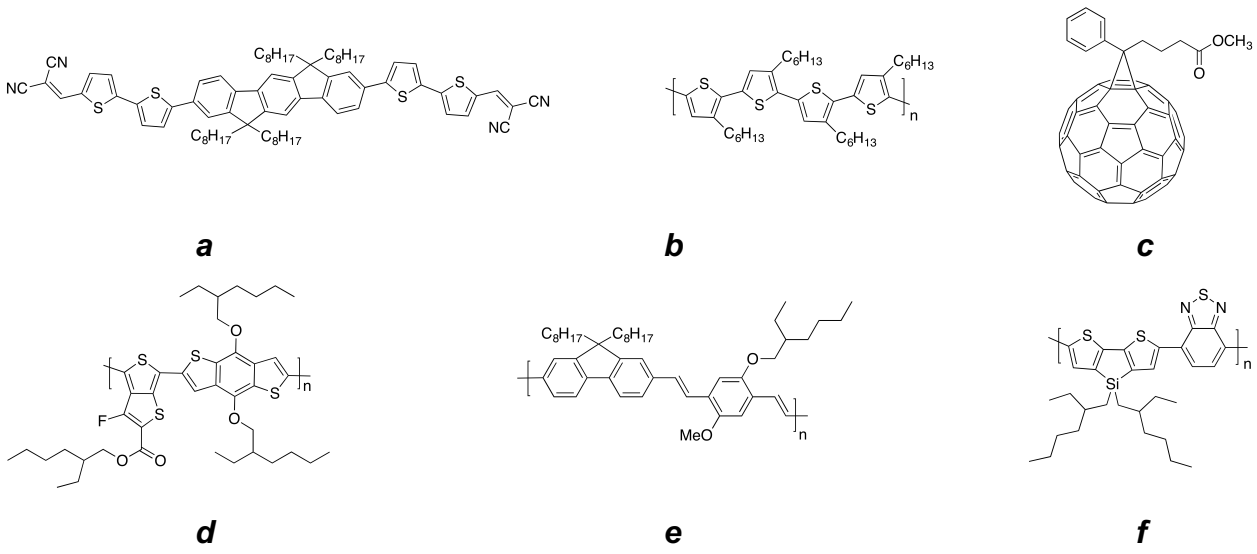

Figure S5.1. Active materials used in thin-film compositions. (a) 2,2'-[[5',5'''-(6,6,12,12-Tetraoctyl-6,12-dihydroindeno[1,2-*b*]fluorene-2,8-diyl)bis[(2'',2'''-bithiophene)-5'',5'-diyl]]bis(methanylylidene)dimalononitrile ($IF(BTC)_2$). (b) Poly(3-hexylthiophene-2,5-diyl) (P3HT). (c) [6,6]-Phenyl-C_{61}-butyric acid methyl ester ($PC_{61}BM$). (d) Poly[[4,8-bis[(2-ethylhexyl)oxy]benzo[1,2-*b*:4,5-*b'*]dithiophene-2,6-diyl][3-fluoro-2-[(2-ethylhexyl)carbonyl]thieno[3,4-*b*]thiophenediyl] (PTB7). (e) Poly[(9,9-dioctyl-9*H*-fluorene-2,7-diyl)-1,2-ethenediyl[2-methoxy-5-(2-ethylhexyloxy)-1,4-phenylene]-1,2-ethenediyl] (PFO-MEH-PPV). (f) Poly[2,6-[4,4-bis(2-ethylhexyl)dithieno[3,2-*b*:2,3-*d*]silole]-*alt*-4,7-(2,1,3-benzothiadiazole)] (Si-PCPDTBT).

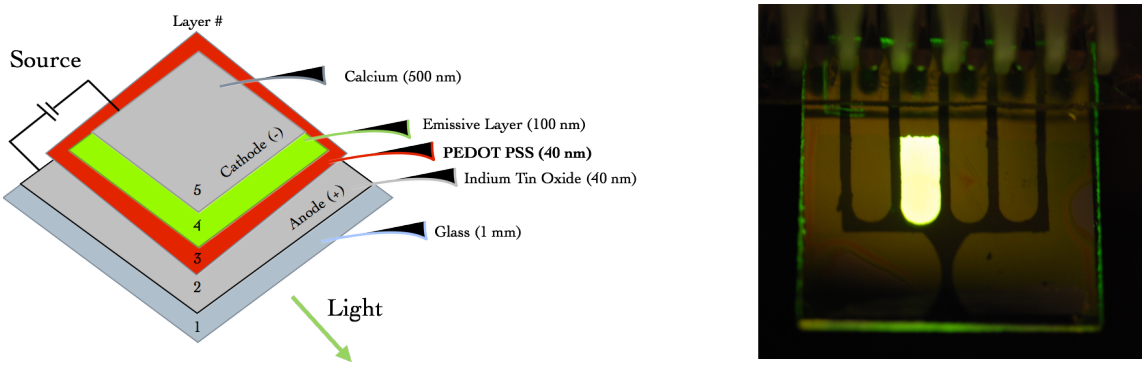

Figure S5.2. (a) Schematic representation of the architecture of an OLED, with the removable PEDOT:PSS layer shown in red. (b) Photograph of representative OLED operating under bias.

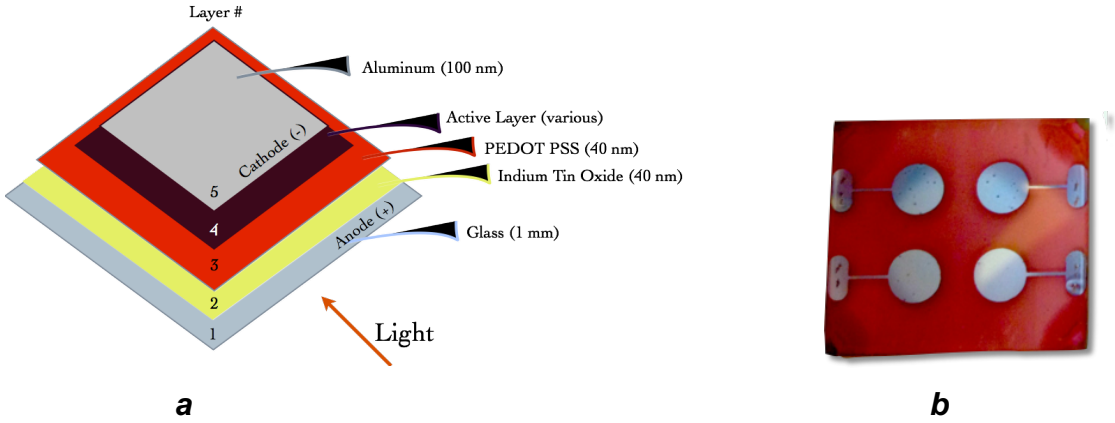

Figure S5.3. (a) Schematic representation of the architecture of an OPV, with the removable PEDOT:PSS layer shown in red. (b) Photograph of four OPVs on a 10 × 18 mm^2 glass substrate.

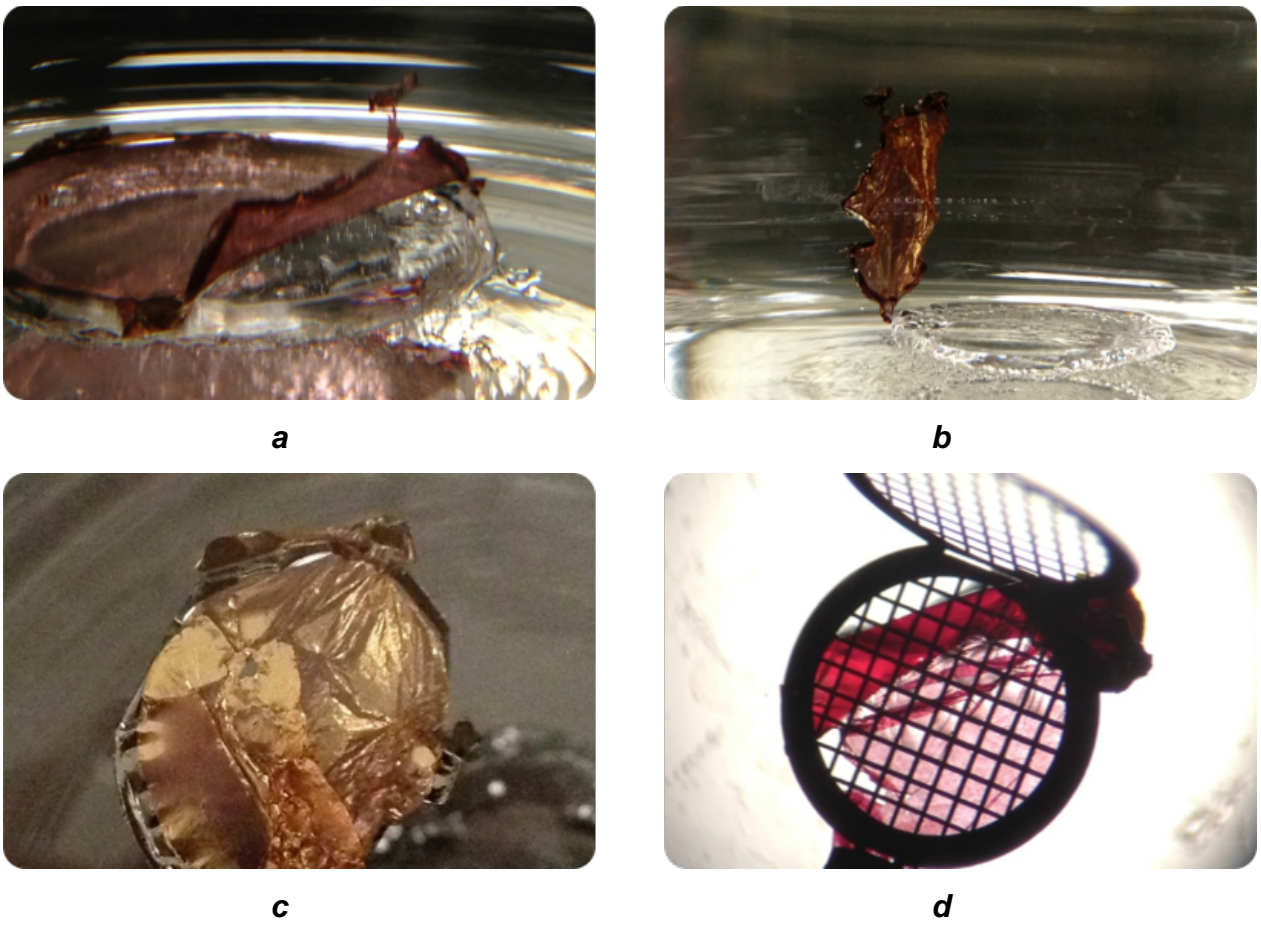

Figure S5.4. Lifting a film of P3HT:$PC_{61}BM$ by exposing the underlying substrate of NaCl to deionized water. (a) First stage, showing the film starting to lift from the substrate. (b) Freed film. (c) Film floating on water. (d) Film scooped onto a double folding 50-mesh Cu TEM grid.

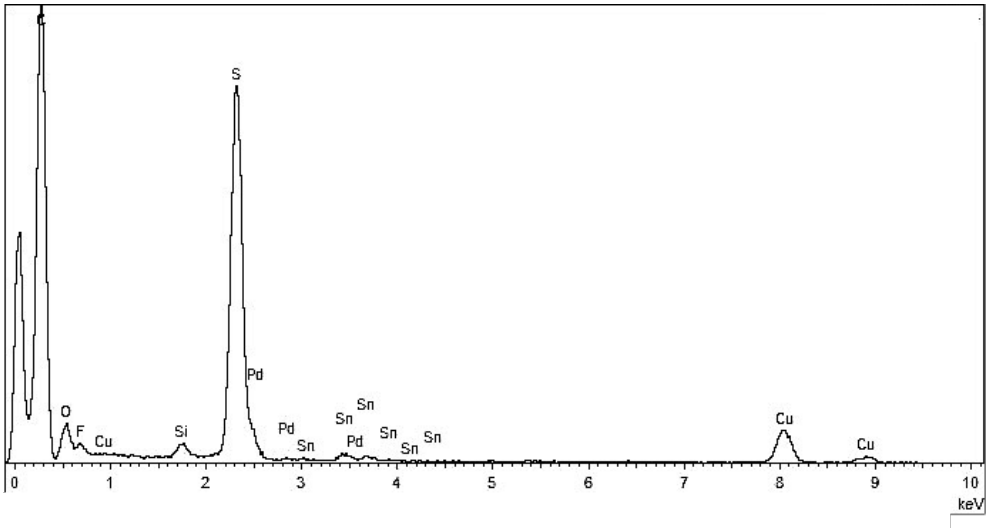

Figure S5.5. Energy-dispersive X-ray spectroscopy (EDS) performed on particles present in a thin film of PTB7 lifted by exposing a substrate of NaCl to deionized water.

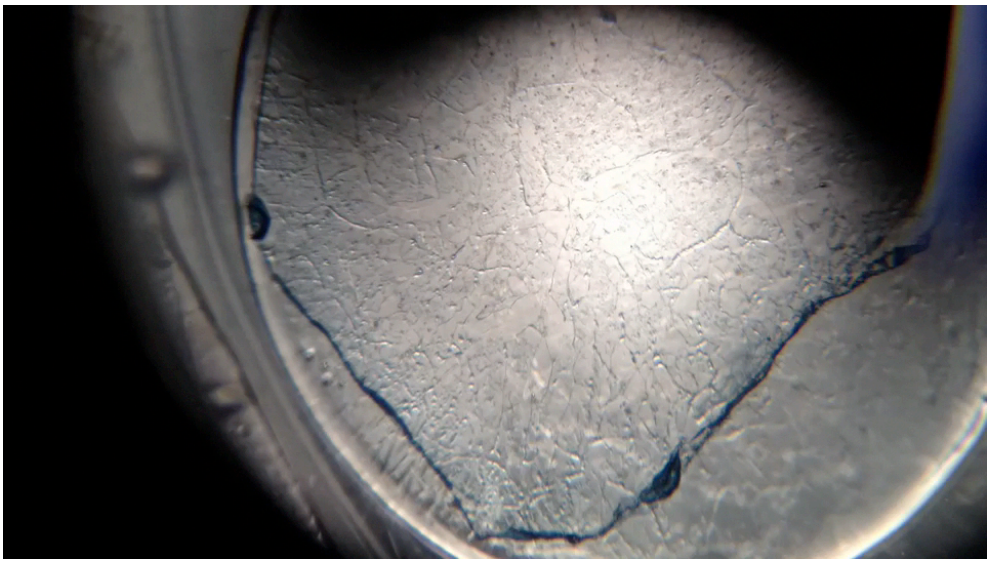

Video S5.1. Lifting a thin film of Si-PCPDTBT by exposing a substrate of NaCl to deionized water.

5.2.10 References

[1] Wu, Q.-H. Progress in Modification of Indium-Tin Oxide/Organic Interfaces for Organic Light-Emitting Diodes. *Crit. Rev. Solid State Mater. Sci.* **2013,** *38*, 318-352.

[2] Tsutsui, T.; Takada, N. Progress in Emission Efficiency of Organic Light-Emitting Diodes: Basic Understanding and Its Technical Application. *Jpn. J. Appl. Phys.* **2013,** *52*, 110001.

[3] Geffroy, B.; le Roy, P.; Prat, C. Organic light-emitting diode (OLED) technology: materials, devices and display technologies. *Polym. Int.* **2006,** *55* (6), 10.

[4] Li, G.; Zhu, R.; Yang, Y. Polymer solar cells. *Nature Photon.* **2012,** *6* (3), 153-161.

[5] Brabec, C. J.; Gowrisanker, S.; Halls, J. J. M.; Laird, D.; Jia, S.; Williams, S. P. Polymer–Fullerene Bulk-Heterojunction Solar Cells. *Adv. Mater.* **2010,** *22* (34), 3839–3856.

[6] Liu, Y.; Chen, C.-C.; Hong, Z.; Gao, J.; Yang, Y. M.; Zhou, H.; Dou, L.; Li, G.; Yang, Y. Solution-processed small-molecule solar cells: breaking the 10% power conversion efficiency. *Sci. Rep.* **2013,** *3* (3356), 1-8.

[7] Orgiu, E.; Masillamani, A. M.; Vogel, J.-O.; Treossi, E.; Kiersnowski, A.; Kastler, M.; Pisula, W.; Dotz, F.; Palermo, V.; Samorí, P. Enhanced mobility in P3HT-based OTFTs upon blending with a phenylene–thiophene–thiophene–phenylene small molecule. *Chem. Commun.* **2012,** *48*, 1562–1564.

[8] Yang, Y.; Wudl, F. Organic electronics: From materials to devices. *Adv. Mater.* **2009,** *21* (14-15), 1401-1403.

[9] de Leeuw, D. M.; Cantatore, E. Organic electronics: Materials, technology and circuit design developments enabling new applications. *Mat. Sci. Semi. Proc.* **2008,** *11* (5-6), 199-204.

[10] Dimitrakopoulos, C. D.; Malenfant, P. R. L. Organic Thin Film Transistors for Large Area Electronics. *Adv. Mater.* **2002,** *14* (2), 99-117.

[11] Yi, Z.; Ni, W.; Zhang, Q.; Li, M.; Kan, B.; Wan, X.; Chen, Y. Effect of thermal annealing on active layer morphology and performance for small molecule bulk heterojunction organic solar cells. *J. Mater. Chem. C* **2014,** *2*, 7247-7255.

[12] Dang, M. T.; Hirsch, L.; Wantz, G.; Wuest, J. D. Controlling the Morphology and Performance of Bulk Heterojunctions in Solar Cells. Lessons Learned from the Benchmark Poly(3-hexylthiophene):[6,6]-Phenyl-C61-butyric Acid Methyl Ester System. *Chem. Rev.* **2013,** *113* (5), 3734-3765.

[13] Sun, Y.; Welch, G. C.; Leong, W. L.; Takacs, C. J.; Bazan, G. C.; Heeger, A. J. Solution-processed small-molecule solar cells with 6.7% efficiency. *Nat. Mater.* **2012,** *11* (1), 44-48.

[14] Motaung, D.; Malgas, G.; Arendse, C. Correlation between the morphology and photo-physical properties of P3HT:fullerene blends. *J. Mater. Sci.* **2010,** *45* (12), 3276-3283.

[15] Kim, Y. S.; Lee, Y.; Kim, J. K.; Seo, E.-O.; Lee, E.-W.; Lee, W.; Han, S.-H.; Lee, S.-H. Effect of solvents on the performance and morphology of polymer photovoltaic devices. *Curr. Appl. Phys.* **2010,** *10* (4), 985-989.

[16] Kim, S.; Yim, J.; Wang, X.; Bradley, D. D. C.; Lee, S.; deMello, J. C. Spin- and Spray-Deposited Single-Walled Carbon-Nanotube Electrodes for Organic Solar Cells. *Adv. Funct. Mater.* **2010,** *20* (14), 2310-2316.

[17] Tremolet de Villers, B.; Tassone, C. J.; Tolbert, S. H.; Schwartz, B. J. Improving the Reproducibility of P3HT:PCBM Solar Cells by Controlling the PCBM/Cathode Interface. *J. Phys. Chem. C* **2009,** *113* (44), 18978-18982.

[18] Krebs, F. C.; Gevorgyan, S. A.; Alstrup, J. A roll-to-roll process to flexible polymer solar cells: model studies, manufacture and operational stability studies. *J. Mater. Chem.* **2009,** *19* (30), 5442-5451.

[19] Chang, Y.-H.; Tseng, S.-R.; Chen, C.-Y.; Meng, H.-F.; Chen, E.-C.; Horng, S.-F.; Hsu, C.-S. Polymer solar cell by blade coating. *Org. Electron.* **2009,** *10* (5), 741-746.

[20] Xin, H.; Reid, O. G.; Ren, G.; Kim, F. S.; Ginger, D. S.; Jenekhe, S. A. Polymer Nanowire/Fullerene Bulk Heterojunction Solar Cells: How Nanostructure Determines Photovoltaic Properties. *ACS Nano* **2010,** *4* (4), 1861-1872.

[21] Wu, P.-T.; Ren, G.; Kim, F. S.; Li, C.; Mezzenga, R.; Jenekhe, S. A. Poly(3-hexylthiophene)-poly(3-cyclohexylthiophene): Synthesis, microphase separation, thin film transistors, and photovoltaic applications. *J. Polym. Sci. A Polym. Chem.* **2010,** *48* (3), 614-626.

[22] Sharma, G. D.; Suresh, P.; Sharma, S. S.; Vijay, Y. K.; Mikroyannidis, J. A. Effect of Solvent and Subsequent Thermal Annealing on the Performance of Phenylenevinylene Copolymer:PCBM Solar Cells. *ACS Appl. Mater. Interfaces* **2010,** *2*, 504-510.

[23] Keawprajak, A.; Piyakulawat, P.; Klamchuen, A.; Iamraksa, P.; Asawapirom, U. Influence of crystallizable solvent on the morphology and performance of P3HT:PCBM bulk-heterojunction solar cells. *Sol. Energ. Mat. Sol. Cells* **2010,** *94* (3), 531-536.

[24] Zhao, Y.; Guo, X.; Xie, Z.; Qu, Y.; Geng, Y.; Wang, L. Solvent vapor-induced self assembly and its influence on optoelectronic conversion of poly(3-hexylthiophene): Methanofullerene bulk heterojunction photovoltaic cells. *J. Appl. Polym. Sci.* **2009,** *111* (4), 1799-1804.

[25] Zhao, J.; Swinnen, A.; Van Assche, G.; Manca, J.; Vanderzande, D.; Van Mele, B. Phase diagram of P3HT/PCBM blends and its implication for the stability of morphology. *J. Phys. Chem. B* **2009,** *113* (6), 1587-1591.

[26] Park, J. H.; Kim, J. S.; Lee, J. H.; Lee, W. H.; Cho, K. Effect of Annealing Solvent Solubility on the Performance of Poly(3-hexylthiophene)/Methanofullerene Solar Cells. *J. Phys. Chem. C* **2009,** *113* (40), 17579-17584.

[27] Guo, T.-F.; Wen, T.-C.; L'vovich Pakhomov, G.; Chin, X.-G.; Liou, S.-H.; Yeh, P.-H.; Yang, C. H. Effects of film treatment on the performance of poly(3-hexylthiophene)/soluble fullerene-based organic solar cells. *Thin Solid Films* **2008,** *516* (10), 3138-3142.

[28] Campoy-Quiles, M.; Ferenczi, T.; Agostinelli, T.; Etchegoin, P. G.; Kim, Y.; Anthopoulos, T. D.; Stavrinou, P. N.; Bradley, D. D. C.; Nelson, J. Morphology evolution via self-organization and lateral and vertical diffusion in polymer:fullerene solar cell blends. *Nat. Mater.* **2008**.

[29] Kim, G.; Libera, M. Morphological Development in Solvent-Cast Polystyrene-Polybutadiene-Polystyrene (SBS) Triblock Copolymer Thin Films. *Macromolecules* **1998,** *31*, 2569-2577.

[30] Akcora, P.; Briber, R. M.; Kofinas, P. TEM characterization of diblock copolymer templated iron oxide nanoparticles: Bulk solution and thin film surface doping approach. *Polymer* **2006,** *47*, 2018–2022.

[31] Michler, G. H. *Electron Microscopy of Polymers*. Springer-Verlag: Berlin: **2008**; p 473.

[32] Kim, S.; Liu, G.; Minor, A. M. FIB Sample Preparation of Polymer Thin Films on Hard Substrates Using the Shadow-FIB Method. *Micros. Today* **2009,** *17* (6), 20-23.

[33] Mayer, J.; Giannuzzi, L. A.; Kamino, T.; Michael, J. TEM Sample Preparation and FIB-Induced Damage. *MRS Bull.* **2007,** *32*, 400.

[34] McCaffrey, J. P. Small-angle cleavage of semiconductors for transmission electron microscopy. *Ultramicroscopy* **1991,** *38* (2), 149-157.

[35] McCaffrey, J. P. Improved TEM samples of semiconductors prepared by a small-angle cleavage technique. *Microsc. Res. Tech.* **1993,** *24*, 180-184.

[36] Walck, S. D.; McCaffrey, J. P. The small angle cleavage technique applied to coatings and thin films. *Thin Solid Films* **1997,** *308-309*, 399-405.

[37] Suder, S.; Faunce, C. A.; Donnelly, S. E. Thin solid film sample preparation by a small-angle cleavage for transmission electron microscopy. *Thin Solid Films* **1997,** *304* (1-2), 157-159.

[38] Teodorescu, V. S.; Blanchin, M.-G. Fast and Simple Specimen Preparation for TEM Studies of Oxide Films Deposited on Silicon Wafers. *Microsc. Microanal.* **2009,** *15*, 15-19.

[39] Alam, M. M.; Jenekhe, S. A. Binary Blends of Polymer Semiconductors: Nanocrystalline Morphology Retards Energy Transfer and Facilitates Efficient White Electroluminescence. *Macromol. Rapid Commun.* **2006,** *27*, 2053–2059.

[40] van de Ruit, K.; Cohen, R. I.; Bollen, D.; van Mol, T.; Yerushalmi-Rozen, R.; Janssen, R. A. J.; Kemerink, M. Quasi-One Dimensional in-Plane Conductivity in Filamentary Films of PEDOT:PSS. *Adv. Funct. Mater.* **2013,** *23*, 5778–5786.

[41] Zhou, J.; Anjum, D. H.; Chen, L.; Xu, X.; Ventura, I. A.; Jiang, L.; Lubineau, G. The temperature-dependent microstructure of PEDOT/PSS films: insights from morphological, mechanical and electrical analyses. *J. Mater. Chem. C* **2014,** *2*, 9903-9910.

[42] Lang, U.; Müller, E.; Naujoks, N.; Dual, J. Microscopical Investigations of PEDOT:PSS Thin Films. *Adv. Funct. Mater.* **2009,** *19*, 1215–1220.

[43] Greenham, N. C.; Peng, X.; Alivisatos, A. P. Charge separation and transport in conjugated-polymer/semiconductor-nanocrystal composites studied by photoluminescence quenching and photoconductivity. *Phys. Rev. B* **1996,** *54* (24), 17628.

[44] Martens, T.; D'Haen, J.; Munters, T.; Beelen, Z.; Goris, L.; Manca, J.; D'Olieslaeger, M.; Vanderzande, D.; De Schepper, L.; Andriessen, R. Disclosure of the nanostructure of MDMO-PPV:PCBM bulk hetero-junction organic solar cells by a combination of SPM and TEM. *Synt. Met.* **2003,** *138*, 243–247.

[45] Yang, C. Y.; Heeger, A. J. Morphology of composites of semiconducting polymers mixed with C60. *Synt. Met.* **1996,** *83*, 85-88.

[46] Sleytr, U. B.; Robards, A. W. Plastic deformation during freeze-cleavage: a review. *J. Microsc.* **1977,** *110* (1), 1-25.

[47] Meyerhofer, D. Characteristics of resist films produced by spinning. *J. Appl. Phys.* **1978,** *49* (7), 3993-3997.

[48] Brunner, P.-L. M.; Beaudoin, D.; Heskia, A.; Maris, T.; Dubois, M.-A.; Wuest, J. D. Low-Bandgap Push-Pull Molecules in Polymer Matrices for Use in Thin-Film Organic Photovoltaic Devices. **2015**, submitted for publication.

[49] Brunner, P.-L. M.; Laliberté, D.; Dang, M. T.; Wantz, G.; Wuest, J. D. Effect of the Molecular Weight on the Performance of Organic Light Emitting Diodes based on poly[(9,9-dioctyl-2,7-divinylene-fluorenylene)-alt- co-(2-methoxy-5-(2-ethylhexyloxy)-1,4-phenylene)]. submitted for publication.

[50] Danilewsky, A.; Wittge, J.; Kiefl, K.; Allen, D.; McNally, P.; Garagorri, J.; Elizalde, M. R.; Baumbach, T.; Tanner, B. K. Crack propagation and fracture in silicon wafers under thermal stress. *J. Appl. Cryst.* **2013,** *46*, 849-855.

[51] Brun, X. F.; Melkote, S. N. Analysis of stresses and breakage of crystalline silicon wafers during handling and transport. *Sol. Energ. Mat. Sol. Cells* **2009,** *93*, 1238–1247.

Chapitre 6

Une approche verte appliquée aux dispositifs électroniques organiques à films minces : Le recyclage des électrodes composées d'oxydes d'indium et d'étain (ITO)

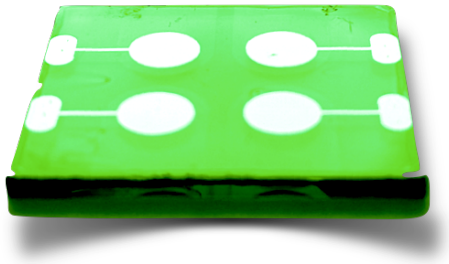

« Vert sur Verre » ; Cellules photovoltaïques

6.1 Introduction Article 5

Tous les dispositifs réalisés au cours des recherches présentées aux chapitres précédants ont été réalisés sur des substrats de verre supportant une électrode d'oxydes d'indium et d'étain (ITO) déposé par pulvérisation en couches minces d'environ 40 nm. Une fois caractérisés, la plupart de ceux-ci ce retrouveront éliminés parmi les déchets dangereux. Si l'ITO est très utilisé comme électrode, c'est qu'il est conducteur, incolore et transparent en couches minces. Que ce soit en technologie OLED[86-88], en photovoltaïque organique[89-90] ou en transistors organiques à films minces,[91-95] il est de loin le matériel le plus utilisé comme électrode transparente en électronique organique.

Bien que l'ITO soit populaire, la rareté de l'indium, l'incertitude de sa disponibilité dans le futur et le prix de ce matériau ont généré beaucoup de recherches pour trouver des alternatives à son usage.[96-97] Une étude récente attribue 31 à 51% des coûts de fabrication des cellules au substrat d'ITO.[98] Parmi les alternatives proposées, les nanotubes de carbone,[99-103] le graphène[103-105] et les polymères conducteurs, comme le polyaniline[106-108] ou le PEDOT:PSS,[109-110] peuvent remplacer l'ITO pour certaines applications. Bien que plus faciles à produire, moins chers et plus flexibles, ces alternatives ont généralement des conductivités plus faibles. Alternativement, des oxydes d'aluminium, de gallium ou de zinc (AZO, GZO, or IZO)[111-114] peuvent aussi être utilisés, mais leur résistance à l'hydrolyse est moins bonne.[115]

Malgré les recherches soutenues pour son remplacement, l'ITO demeure un chef de fil pour les recherches sur les matériaux organiques en cellules photovoltaïques, produisant déjà des résultats de rendements supérieurs à 10%.[38, 72, 116-120] La multitude de substrats utilisés permet de pensé que la possibilité de les recycler permettrait de diminuer les coûts de la recherche, tout en revalorisant le matériel.

Une méthode efficace de recyclage des substrats d'ITO a donc été mise au point, permettant la réutilisation de ceux-ci sans compromettre l'efficacité des dispositifs. De plus, la séquence de lavage à l'eau ne nécessite pas de solvants organiques, limitant ainsi les déchets

supplémentaires. Bien que les substrats recyclés fussent testés en cellules photovoltaïques, il est raisonnable de penser que le procédé peut s'appliquer à d'autres types de dispositifs.

6.2 Article 5

A Green Approach to Organic Thin-Film Electronic Devices: Recycling Electrodes Composed of Indium Tin Oxide (ITO)

Minh Trung Dang, Pierre-Louis M. Brunner, and James D. Wuest

ACS Sustainable Chem. Eng., **2014**, *2* (12), 2715–2721

6.2.1 Keywords

Keywords: Recycling, Tin-doped indium oxide (ITO), Thin-film devices, Solar cells

6.2.2 Abstract

Organic thin-film optoelectronic devices, unlike inorganic analogues, offer the attractive prospect of large, flexible, and inexpensive arrays made by simple procedures such as roll-to-roll printing. In current organic thin-film devices, layers of tin-doped indium oxide (ITO) are widely used as electrodes. Motivated by the increasing price of indium and the high cost of ITO-coated substrates, we have examined ways to recover and recycle ITO substrates in typical devices by environmentally benign methods. A process using only water yields recovered ITO substrates that can be reused at least 10 times to prepare new devices without loss of efficiency.

6.2.3 Introduction

Tin-doped indium oxide (ITO) is a conductive solid solution of tin(IV) oxide (SnO_2) in indium(III) oxide (In_2O_3). It is essentially transparent and colorless in thin layers. Its electrical conductivity, optical transparency, and well-established methods of deposition make it widely used as an electrode in organic thin-film devices such as light-emitting diodes (OLEDs),[1-3] photovoltaic devices (OPVs),[4] and field-effect transistors (OFETs).[5-9] At present, ITO films supported on transparent insulators such as glass are the most frequently encountered electrodes in organic optoelectronic devices.

Despite the popularity of ITO, efforts to develop alternatives are under investigation for multiple reasons.[10] In particular, the growing cost of ITO reflects limited supplies of indium and uncertainty about its availability in the future.[11] Economic analyses have considered the energy required to produce devices, as well as the cost of the basic components. For example, a recent study by Azzopardi et al. attributed 31–51% of the total cost of a standard flexible OPV device to the ITO electrode.[12] In addition, the properties of ITO are not ideal. It can be deposited on flexible substrates such as poly(ethylene terephthalate),[13-15] but layers of ITO crack readily when the underlying substrate is bent, leading to defects in the device.[16, 17] Moreover, the preparation of thin layers of ITO requires advanced technology for depositing and doping under vacuum.

Among the potential substitutes are carbon-based alternatives such as nanotubes[18-22] and graphene,[22-24] which have been shown to give flexible layers with 90% transparency and an electrical resistance lower than that of standard ITO.[24, 25] Conductive polymers such as poly(aniline)[26-28] and poly(3,4-ethylenedioxythiophene) : poly(styrenesulfonate) (PEDOT:PSS)[29, 30] may also be able to replace ITO in certain applications. Their conductivity is typically lower, but they are more flexible, cheaper, and more easily manufactured and processed by methods that are environmentally benign. Potential inorganic alternatives to ITO include aluminum-, gallium-, or indium-doped zinc oxide (AZO, GZO, or IZO),[31-34] although ITO shows higher resistance to hydrolysis when exposed to water.[35]

Despite the ongoing search for substitutes, most laboratory-scale thin-film organic optoelectronic devices continue to incorporate ITO electrodes, and their performance is increasingly impressive. For example, efficiencies have now reached 10% in photovoltaic devices containing ITO electrodes.[36-42] This has contributed to an international surge of research covering topics such as new photoactive materials, nanomorphology of active layers, and underlying photophysical aspects, all requiring extensive use of glass-coated ITO electrodes. As a result, it has become important to examine the ability to recycle ITO and recover intact working electrodes by suitable treatment of devices no longer needed.

In earlier work related to green thin-film devices, Zhou and co-workers built polymer-based solar cells on free-standing transparent substrates of nanocrystalline cellulose.[43] A degree of recycling was achieved by simply immersing spent cells in water at room temperature, which led to redispersal of the nanocrystalline cellulose and separation of membranes consisting of the photoactive polymeric layer and adhering electrodes. The membranes were be removed by filtration, and their various components were then separated by extracting the photoactive polymeric layer into organic solvents, leaving behind the components of the electrodes, which were recovered by filtration.

In the present study, we have taken a significant further step forward by developing a method to recover ITO electrodes from representative organic thin-film devices in a way that allows repeated reuse of the electrodes without loss of efficiency. The process is performed in water without using organic solvents. Although our initial study has focused on the use of recycled ITO electrodes in thin-film solar cells, we believe that our method will be effective for recycling ITO electrodes in other types of devices as well.

6.2.4 Experimental Section

6.2.4.1 Fabrication of thin-film photovoltaic devices

Thin-film devices were fabricated by a standard protocol. ITO-coated glass slides (12 mm × 18 mm, with a standard resistivity of about 20 Ω/square) were purchased from Colorado

Concept Coatings, Limited, and used as substrates for the construction of devices. The glass/ITO substrates were cleaned in an ultrasonic bath using deionized water, acetone, ethanol, and isopropanol in sequence. The cleaned substrates were then exposed to UV/ozone for 15 min to destroy any residual contaminants.[44] An aqueous dispersion of PEDOT:PSS (PH1000, Clevios) was initially filtered using a PTFE filter (0.45 μm) and was then deposited on the cleaned substrate by spin coating in air at 25 °C, using a speed of 4000 rpm during 1 min. The samples then were heated in air at 110 °C for 30 min. The thickness of the resulting film of PEDOT:PSS was determined by profilometry to be 30 ± 4 nm.

All subsequent manipulations and characterizations were carried out in a glovebox under N_2 with residual concentrations of O_2 and H_2O below 0.1 ppm. Poly(3-hexylthiophene) (P3HT; Rieke, Inc. and Solaris Chem, Inc.) and phenyl-C_{61}-butyric acid methyl ester (PCBM; Solaris Chem, Inc.) were used as received. Blends of P3HT and PCBM have been extensively used as the active layer in molecular photovoltaic devices.[45, 46] P3HT, which acts as an electron donor, exhibits good solubility in standard organic solvents, suitable chemical stability, relatively low band gap (~2 eV), and high mobility of holes.[46] PCBM, which acts as an electron acceptor, also has adequate solubility and complementary electronic properties.[46] A mixture of P3HT and PCBM (1:0.8 by weight) was stirred at 45 °C overnight in chlorobenzene to give a solution containing 10 mg of P3HT per mL. The solution was then deposited on the underlying PEDOT:PSS layer by spin coating at 1000 rpm for 90 s. The thickness of the resulting active layer was measured to be 100 ± 5 nm. Finally, a top electrode of Al (100 nm) was thermally deposited on the P3HT:PCBM layer under vacuum (2×10^{-6} Torr). This resulted in thin-film devices with the following sequence of layers: glass/ITO/PEDOT:PSS/P3HT:PCBM/Al (Figure 6.1). To increase the photovoltaic performance of the resulting devices, improved organization of P3HT and PCBM in the active layer was achieved by thermal annealing in a glovebox at 160 °C for 30 min.[46]

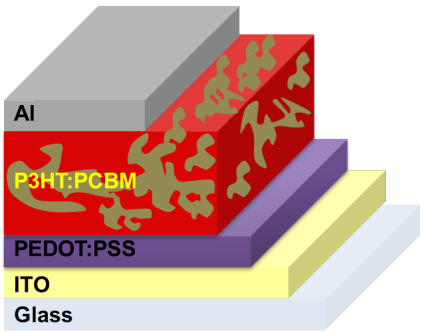

Figure 6.1. Schematic representation of thin-film photovoltaic devices subjected to recycling.

6.2.4.2 Assessment of the performance of thin-film photovoltaic devices

Current density–voltage (*J-V*) curves were measured using a Keithley 2400 Source Measure Unit. The photocurrent was measured under standard illumination (AM1.5G, 100 mW/cm^2) using a 150 W Oriel solar simulator. The intensity of light was determined using a monosilicon detector calibrated by the National Renewable Energy Laboratory. The reported measures of photovoltaic performance (current density, open-circuit voltage, fill factor, and power conversion efficiency) were taken as the average of the values determined for all devices. It should be noted that our devices were built with a cross bar configuration, and photovoltaic performances were measured using a shadow mask with an aperture that determined the active area of the devices (12.6 mm^2). In this way, overestimations of performance were avoided.[47-50]

6.2.4.3 Recycling by recovering glass/ITO substrates and reusing them to fabricate new thin-film devices

Devices prepared with pristine ITO substrates are considered to be reference cells and are labeled C_0, whereas cells derived from recycled ITO substrates are labeled as C_n, where *n* is the number of previous uses of the substrate. After measurements of performance were

completed, reference cells were immersed in water in a Branson 3510 ultrasonic cleaner and sonicated at 45 °C. After 15 min, ITO substrates were freed of supernatant layers of Al, P3HT:PCBM, and PEDOT:PSS. Substrates could also be cleaned by sonication at 25 °C, but the process was slower (>60 min). Cleaned substrates were then used to prepare new thin-film devices according to the protocol described above, starting with the same ultrasonic washings with solvents and exposure to UV/ozone, followed by deposition of PEDOT:PSS, P3HT:PCBM, and the top electrode of Al. The resulting cells, containing ITO recycled once, are labeled C_1. These cycles were repeated to demonstrate the ability to create new devices incorporating ITO recycled multiple times. In each cycle, we simultaneously fabricated devices using pristine ITO substrates, and we used these devices as benchmarks to allow their photovoltaic performance to be compared with that of recycled cells obtained in the same cycle. Sets of at least 16–20 devices of each type (pristine and recycled ITO) were prepared and characterized to assess the reproducibility of our methods. In standard testing, the PEDOT:PSS layer remained in contact with the underlying ITO substrate for approximately 48 h, which is the normal interval between the deposition of PEDOT:PSS and the steps of recycling. However, we also tested ITO substrates recovered from devices of the same type after extended storage in ambient light for periods of over one year.

6.2.4.4 Characterization of the morphology of ITO by atomic force microscopy (AFM)

AFM images were acquired in air at 25 °C using a Digital Instruments MultiMode microscope and extended Nanoscope IIIa controller (Bruker, Santa Barbara, CA). Intermittent contact imaging ("tapping mode") was performed at a scan rate of 1 Hz using Al-coated etched silicon cantilevers (ACTA probes from Applied NanoSystems, Inc.) with a resonant frequency around 300 kHz, spring constant of ~42 N/m, and tip radius of <10 nm. All images were acquired with medium tip oscillation damping (20–30%).

6.2.4.5 Characterization of the surface of ITO by X-ray photoelectron spectroscopy (XPS)

XPS studies were conducted using a VG ESCALAB 3 MKII spectrometer at a base pressure below 1×10^{-10} Torr with nonmonochromated Mg Kα radiation ($h\nu$ = 1256.4 eV). For all data collected, the size of the spot analyzed was 2 mm × 3 mm, and the electrons were detected at a takeoff angle of 90°. The power of the X-ray source was 300 W (15 kV and 20 mA). For survey scans, the pass energy was set to 100 eV, with an energy step size of 1 eV. For high-resolution scans, the pass energy was set to 20 eV, with an energy step size of 0.05 eV. Spectra were analyzed with VG Avantage software v. 4.12; high-resolution spectra were fitted using symmetrical Gaussian–Lorentzian curves, keeping the FWHM of component peaks for each element fixed and allowing the binding energy and intensity of peaks to vary. Charge correction was performed with respect to C_{1s} of adventitious carbon at a binding energy of 285 eV.

6.2.4.6 Measurements of resistance using the 4-point probe method

The sheet resistance of glass/ITO substrates was measured using a 4-point probe system (Microworld S302 K-Standard). Measurements were performed on 8–12 substrates.

6.2.4.7 Measurements of the thickness of layers

The sheet resistance of glass/ITO substrates was measured using a 4-point probe system (Microworld S302 K-Standard). Measurements were performed on 8–12 substrates.

6.2.5 Results and Discussion

6.2.5.1 Overview of procedure for recycling ITO electrodes

The feasibility of recycling ITO electrodes was tested by using thin-film photovoltaic cells as representative devices. The devices were fabricated with a standard architecture (Figure 6.1) according to the protocol set out in the Experimental Section. Subsequent sonication of the devices in water removed upper layers and freed the underlying glass/ITO substrates, which could be recovered, examined by various analytical methods, and reused to produce new devices. Water is presumably effective because it can penetrate and solubilize the adjacent ionic layer of PEDOT:PSS.

6.2.5.2 Surface properties of recycled ITO substrates

Analysis by AFM confirmed that the surfaces of commercial thin films of ITO are textured, and it suggests that grains are formed during the process of sputtering under vacuum, with an overall roughness that can vary somewhat even within a single batch of ITO. However, Figure 6.2 shows that the morphology of ITO changes little as a result of recycling. Pristine ITO shows clusters with diameters of 100–200 nm, which can be resolved into individual grains with diameters of 20–40 nm (Figure 6.2a). It should be noted that the surfaces of at least two samples were analyzed by AFM, and both individual and average values of root-mean-squared roughness (R_{RMS}) are shown in Figure 6.2.

Both pristine and recycled ITO (Figure 6.2a) show cornflake-like clusters of small grains, although the clusters are slightly larger after recycling and the surface is somewhat smoother. These small changes may result from contact with PEDOT:PSS. The dispersions of PEDOT:PSS used for spin coating have a pH of ~2 and may initially etch the underlayer of ITO,[51] but subsequent recycling does not appear to lead to further changes of morphology.

Analysis of the surfaces of pristine and recycled ITO by XPS showed no contamination by sulfur derived from PEDOT:PSS or other sources.[52] Table 6.1 summarizes relative atomic

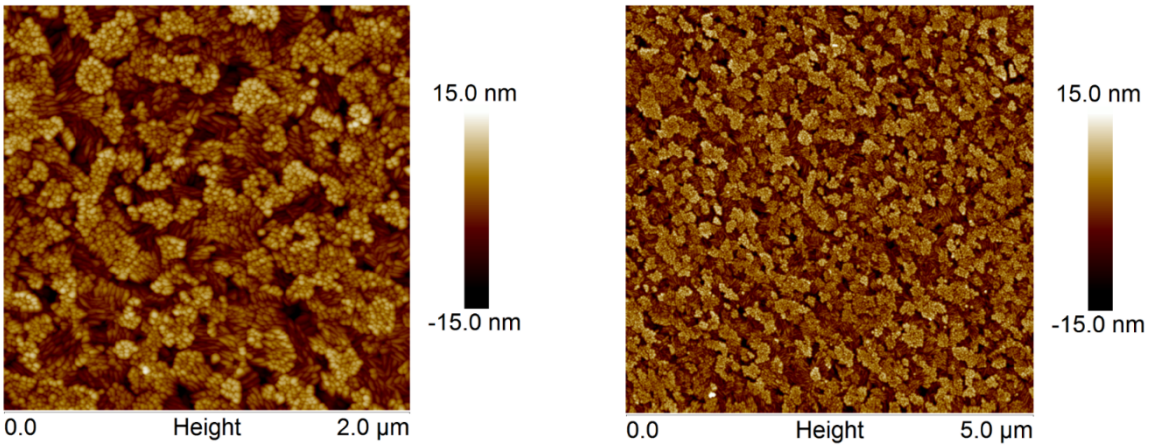
15.0 nm
-15.0 nm
0.0
Height
2.0 µm
15.0 nm
-15.0 nm
0.0
Height
5.0 µm

a

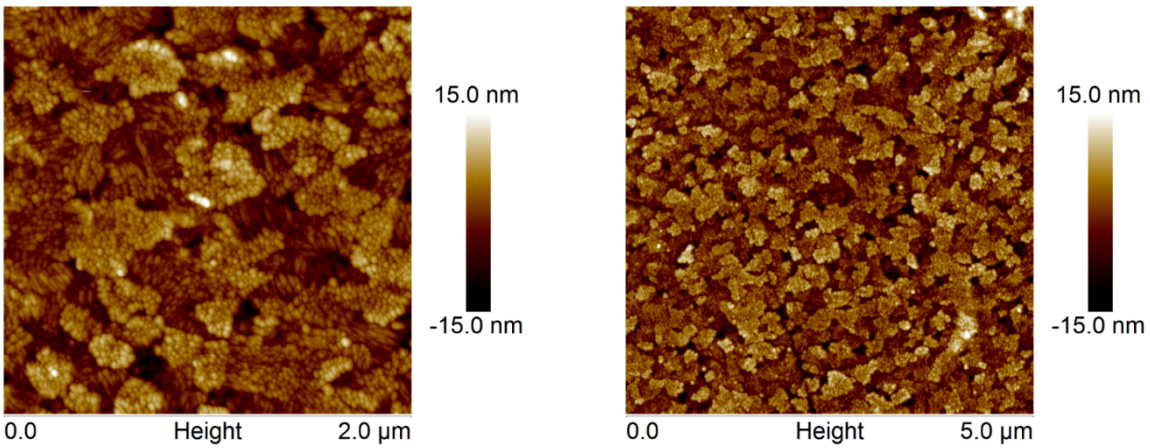
15.0 nm
-15.0 nm
0.0
Height
2.0 µm
15.0 nm
-15.0 nm
0.0
Height
5.0 µm

b

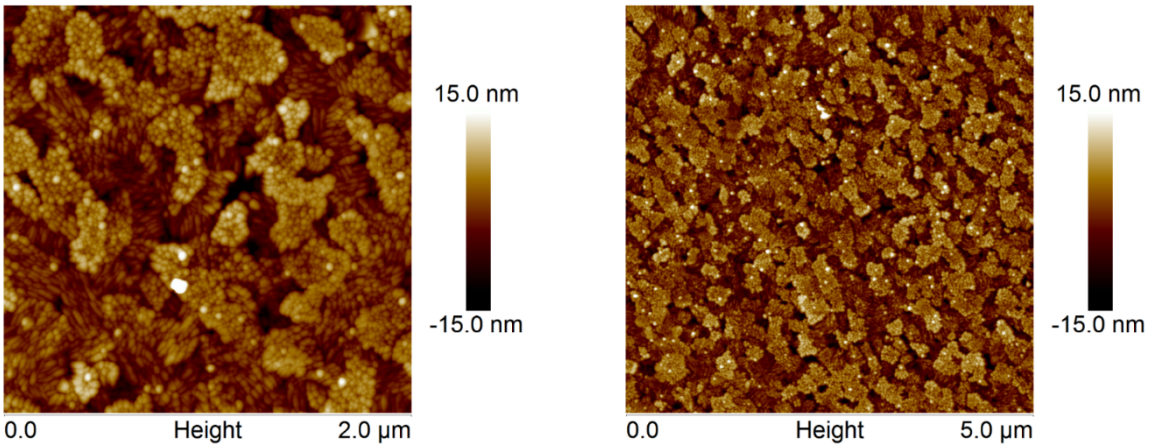
15.0 nm
-15.0 nm
0.0
Height
2.0 µm
15.0 nm
-15.0 nm
0.0
Height
5.0 µm

c

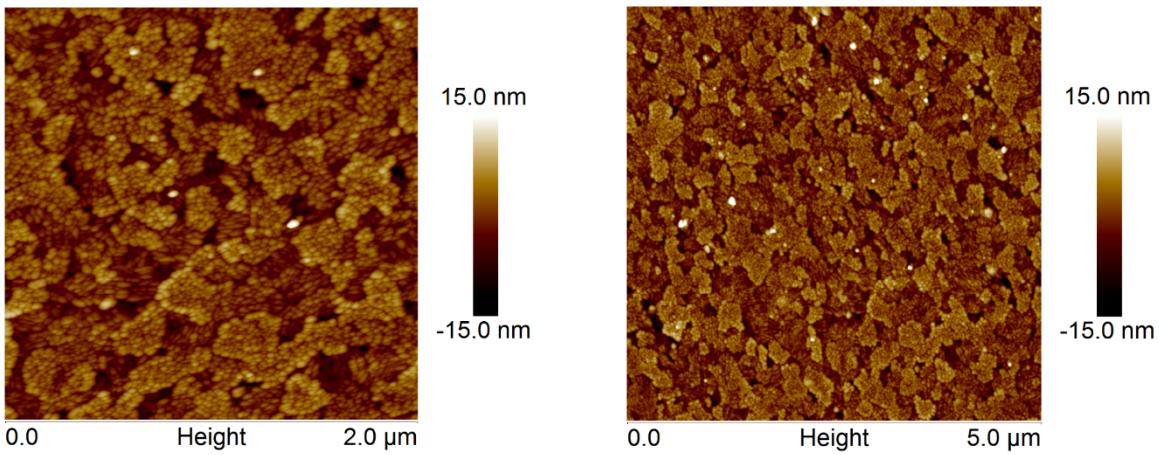

Figure 6.2. Topographic AFM images of the surfaces of pristine and recycled films of ITO. (a) Reference C_0 (R_{RMS} = 4.17 nm for sample shown; average R_{RMS} = 4.13 ± 0.10 nm). (b) C_1 (R_{RMS} = 3.85 nm for sample shown; average R_{RMS} = 3.78 ± 0.09 nm). (c) C_3 (R_{RMS} = 3.97 nm for sample shown; average R_{RMS} = 4.18 ± 0.09 nm). (d) C_8 (R_{RMS} = 3.25 nm for sample shown; average R_{RMS} = 3.32 ± 0.09 nm).

concentrations measured on the surface of pristine ITO (C_0) and recycled ITO (C_1). It should be noted that these samples were cleaned ultrasonically with solvents and exposed to UV/ozone before analysis, as in the protocol used to fabricate photovoltaic devices. Ex situ analysis by XPS could not distinguish between carbon remaining on the samples due to insufficient cleaning and carbon derived from atmospheric recontamination. Differences observed in the composition of pristine ITO (C_0) and recycled ITO (C_1) are small, which is consistent with the close similarity of the AFM images.

Measurements using a 4-point probe showed that the sheet resistance of ITO substrates remains essentially constant, even after recycling 10 times (Figure 6.3). This observation confirms observations by AFM that surface morphology is virtually unchanged and supports the conclusion that layers of ITO are not significantly altered by the fabrication of cells and subsequent recycling. In particular, the thickness of the layers was found to remain essentially constant at ~120 nm (Figure 6.3).

Table 6.1. Relative atomic concentrations for pristine ITO (C_0) and recycled ITO (C_1) as measured by XPS (atomic %), along with corresponding In/Sn and O/In ratios.

	C1s	O1s	$In3d_{5/2}$	$Sn3d_{5/2}$	In/Sn	O/In
C_0	11.0	58.3	26.7	4.6	5.8	2.18
C_1	13.7	57.8	24.2	4.3	5.6	2.39

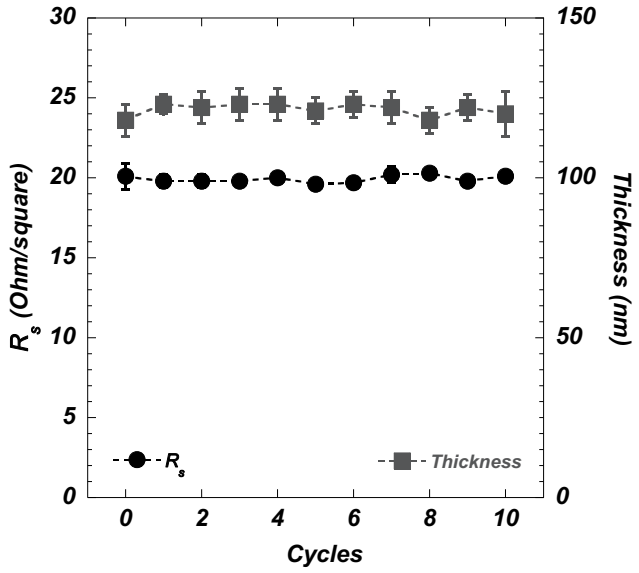

Figure 6.3. Sheet resistance and thickness of layers of ITO on glass substrates before and after recycling (C_0–C_{10}).

6.2.5.3 Performance of photovoltaic devices prepared with pristine ITO (reference cells)

Photovoltaic devices prepared using pristine ITO substrates according to the protocol set out in the Experimental Section showed efficiencies of about 2.5%, which is standard for cells incorporating active layers of P3HT:PCBM.[45] It should be noted that our devices have the simplest possible architecture (glass/ITO/PEDOT:PSS/P3HT:PCBM/Al), were produced

without incorporating buffer layers such as LiF or other metal oxides, and were characterized using a mask with the same area as the Al electrode, so their performance was not overestimated.[47, 48]

6.2.5.4 Performance of photovoltaic devices prepared with recycled ITO

Characteristics of devices incorporating recycled ITO (C_1–C_{10}) are summarized in Figure 6.4 and compared with those of cells containing pristine ITO (C_0). Values of open-circuit voltage (V_{oc}), current density (J_{sc}), fill factor, and power conversion efficiency (PCE) showed no major changes. In our protocol for assessing the effects of using recovered ITO, each cycle of fabrication included devices made using pristine ITO substrates. This allowed us to compare the performance of new and recycled cells obtained in the same cycle of fabrication, thereby permitting the calculation of normalized values of PCE that take into account minor variations between batches of cells. When this is done, no significant variation in the normalized values of PCE can be seen.[52] Similar results were obtained when ITO-coated glass substrates obtained from other suppliers were recycled.[52] Together, these data thereby establish the feasibility of reusing ITO electrodes many times.

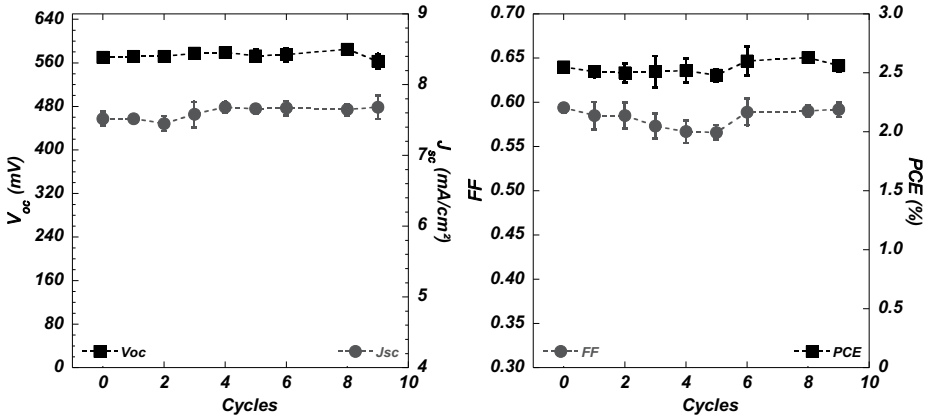

Figure 6.4. Performance of photovoltaic devices incorporating pristine (C_0) and recycled ITO-coated glass substrates (C_1–C_9).

The essentially unaltered performance reflects the fact that the morphology and composition of the layer of ITO remain substantially unchanged, despite direct contact with the adjacent conductive layer of PEDOT:PSS, which ensures the transport and collection of holes.[53-56] Our study has focused primarily on recycling ITO substrates in prototypical laboratory-scale devices that have been used for relatively short periods of time. However, we have also tested ITO substrates recovered from devices of the same type after exposure to ambient light for over one year. Again, devices made with the recycled substrates show no significant variation in the values of V_{oc}, J_{sc}, fill factor, and PCE.[52] These observations indicate that our protocol for recycling ITO substrates is likely to be broadly effective even after extended use.

6.2.6 Conclusions

Our work has established a reliable process for recovering and recycling ITO electrodes used as an underlying substrate for fabricating representative organic thin-film optoelectronic devices. In our process, sonication in water is used to remove the upper layers of the devices, including the top Al electrode, P3HT:PCBM active layer, and adjacent thin film of PEDOT:PSS. Minor morphological and compositional changes in the ITO underlayer are observed but do not appear to alter the performance of photovoltaic devices made using recycled ITO.

Even after extended use in working devices, ITO electrodes can be recycled by our process at least 10 times without losing their ability to be incorporated in photovoltaic devices that meet normal standards of efficiency. Recycling the components of photovoltaic devices with alternative architectures and compositions is currently under investigation. In addition, our method promises to be useful for recovering and recycling ITO electrodes in other thin-film devices such as OLEDs and OFETs. Furthermore, our method is expected to preserve layers of ITO with complex patterns created by techniques such as photolithography and wet chemical etching, thereby allowing more sophisticated and costly devices to be reused.

6.2.7 Acknowledgments

The authors are grateful to the Natural Sciences and Engineering Research Council of Canada, Ministère de l'Éducation du Québec, Canada Foundation for Innovation, Canada Research Chairs Program, and Université de Montréal for financial support. The authors acknowledge with gratitude the fruitful advice of Patricia Moraille (Laboratoire de caractérisation des matériaux, Department of Chemistry, Université de Montréal) and Dr. Josianne Lefebvre (GCM Lab, École Polytechnique de Montréal). In addition, the authors thank the reviewers of the manuscript for their constructive suggestions.

6.2.8 Supplemental Information

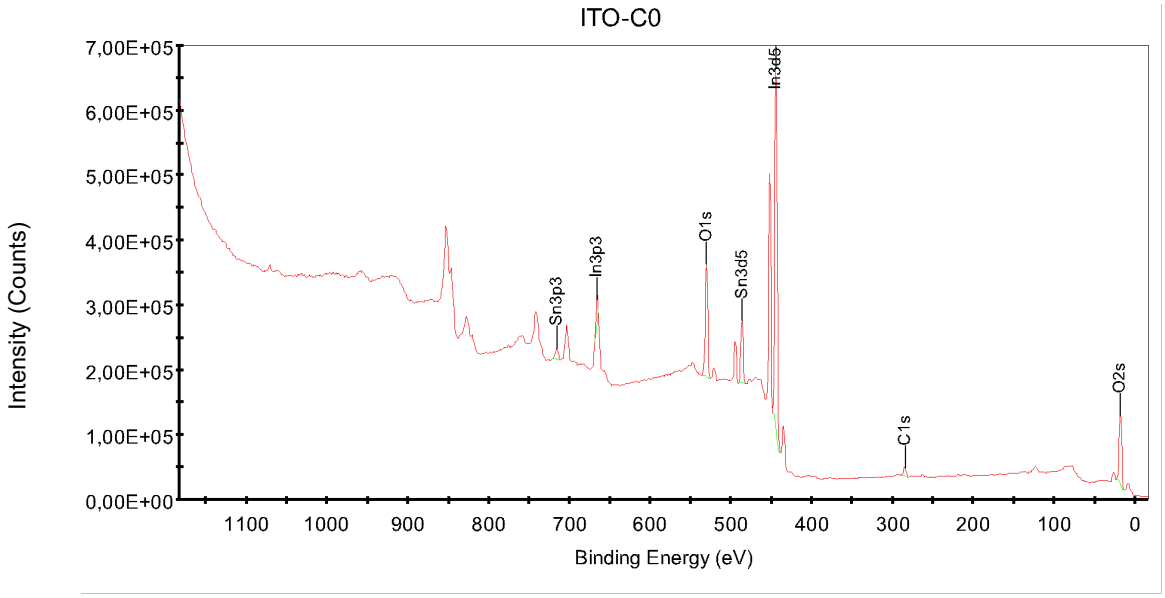

a

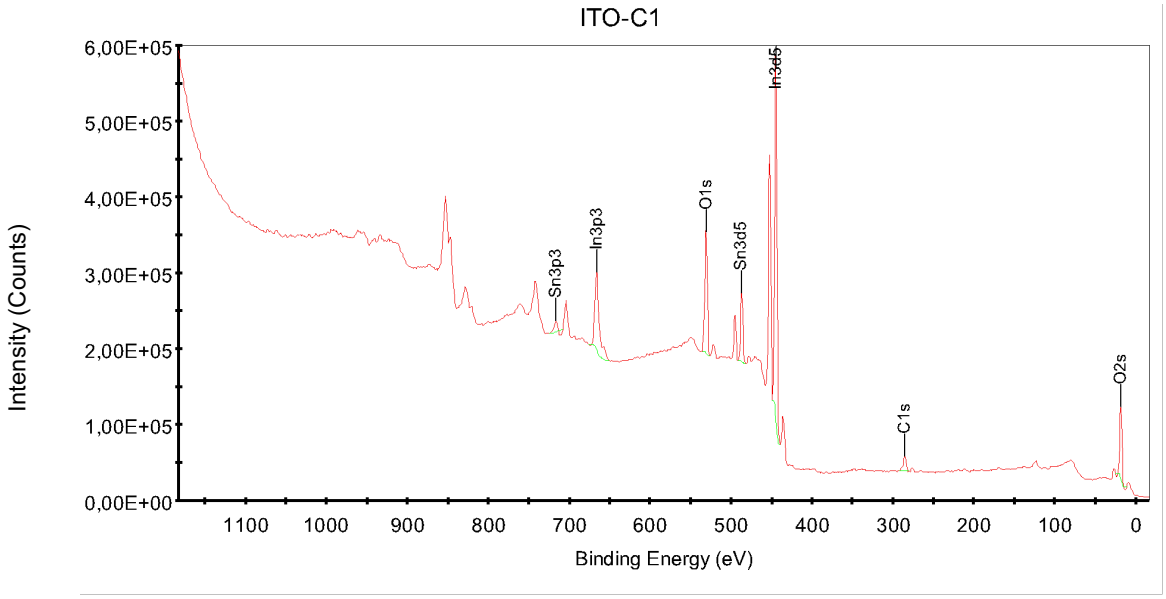

b

Figure S6.1. Survey scans analyzing the surface of ITO by XPS. (a) Pristine ITO (C_0). (b) Recycled ITO (C_1).

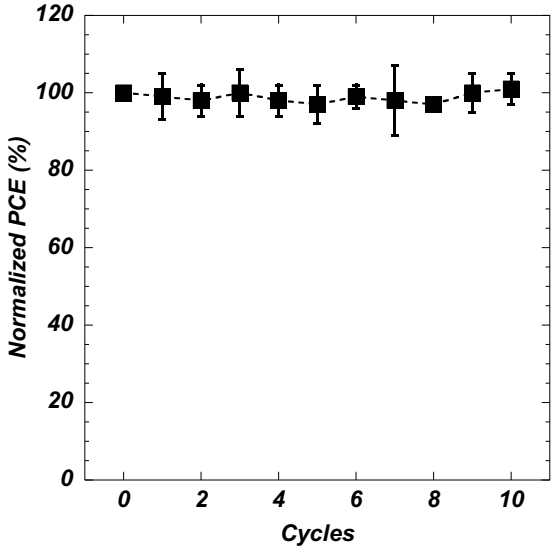

Figure S6.2. Normalized values of PCE for photovoltaic devices incorporating pristine ITO (C_0) and recycled ITO (C_1-C_{10}).

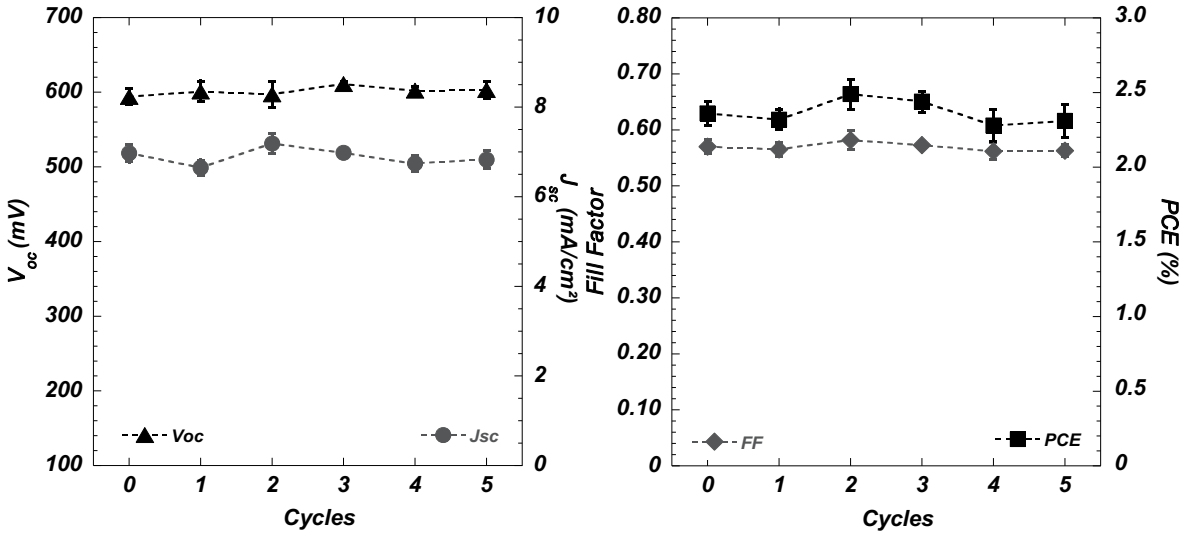

Figure S6.3. Performance of photovoltaic devices incorporating pristine ITO (C_0) and recycled ITO (C_1-C_5). The ITO-coated glass slides were purchased from Kintec (Hong Kong).

Table S6.1. Performance of photovoltaic devices incorporating ITO substrates recycled after extended exposure.

Storage conditions	V_{oc} (mV)	J_{sc} (mA/cm^2)	FF	PCE (%)
Pristine (C_0) [a]	615 ± 5	6.09 ± 0.09	0.634 ± 0.020	2.38 ± 0.10
12 months in glove box + 2 months in air (C_1) [a]	615 ± 12	6.09 ± 0.20	0.636 ± 0.017	2.36 ± 0.16
Pristine (C_0) [b]	610 ± 6	5.97 ± 0.10	0.644 ± 0.017	2.35 ± 0.09
16 months in glove box (C_1) [b]	610 ± 4	5.97 ± 0.27	0.655 ± 0.016	2.39 ± 0.14
12 months in glove box + 2 months in air (C_1) [b]	612 ± 4	6.17 ± 0.15	0.650 ± 0.019	2.46 ± 0.11
38 months in glove box + 11 months in air (C_1) [b]	608 ± 5	6.09 ± 0.15	0.651 ± 0.013	2.40 ± 0.12

[a] Supplier: Colorado Concept Coatings
[b] Supplier: Kintec

6.2.9 References

[1] Cui, J.; Wang, A.; Edleman, N. L.; Ni, J.; Lee, P.; Armstrong, N. R.; Marks, T. J. Indium Tin Oxide Alternatives-High Work Function Transparent Conducting Oxides as Anodes for Organic Light-Emitting Diodes. *Adv. Mater.* **2001**, *13*, 1476-1480.

[2] Wu, Q.-H. Progress in Modification of Indium-Tin Oxide/Organic Interfaces for Organic Light-Emitting Diodes. *Crit. Rev. Solid State Mater. Sci.* **2013**, *38*, 318-352.

[3] Kim, H.; Gilmore, C. M.; Piqué, A.; Horwitz, J. S.; Mattoussi, H.; Murata, H.; Kafafi, Z. H.; Chrisey, D. B. Electrical, optical, and structural properties of indium-tin-oxide thin films for organic light-emitting devices. *J. Appl. Phys.* **1999**, *86*, 6451-6461.

[4] Armstrong, N. R.; Veneman, P. A.; Ratcliff, E.; Placencia, D.; Brumbach, M. Oxide Contacts in Organic Photovoltaics Characterization and Control of Near-Surface Composition in Indium-Tin Oxide [ITO] Electrodes. *Acc. Chem. Res.* **2009**, *42*, 1748-1757.

[5] Yang, C.-M.; Wang, I.-S.; Lin, Y.-T.; Huang, C.-H.; Lu, T.-F.; Lue, C.-E.; Pijanowska, D. G.; Hua, M.-Y.; Lai, C.-S. Low cost and flexible electrodes with NH_3 plasma treatments in extended gate field effect transistors for urea detection. *Sens. Actuators B-Chem.* **2013**, *187*, 274-279.

[6] Lee, H. S.; Cho, J. H.; Kim, W.-K.; Lee, J.-L.; Cho, K. Effects of Physical Treatment of ITO Electrodes on the Electrical Properties of Pentacene Thin-Film Transistors. *Electrochem. Solid-State Lett.* **2007**, *10*, H239-H242.

[7] Cho, J. H.; Lee, H. S.; Hwang, M.; Choi, H. H.; Kim, W.-K.; Lee, J.-L.; Cho, K. Enhancement of Hole Injection in Organic TFTs by Ozone Treatment of Indium Tin Oxide Electrodes. *Electrochem. Solid-State Lett.* **2007**, *10*, H156-H159.

[8] Nguyen, T. N. T.; Seol, Y. G.; Lee, N.-E. Organic field-effect transistor with extended indium tin oxide gate structure for selective pH sensing. *Org. Electron.* **2011**, *12*, 1815-1821.

[9] Palai, A. K.; Lee, J.; Shin, T. J.; Kumar, A.; Park, S.-U.; Pyo, S. Solution-grown single-crystalline microwires of a molecular semiconductor with improved charge transport properties. *Chem. Commun.* **2014**, *50*, 8845-8848

[10] Emmott, C. J. M.; Urbina, A.; Nelson, J. Environmental and economic assessment of ITO-free electrodes for organic solar cells. *Sol. Energy Mater. Sol. Cells* **2012**, *97*, 14-21.

[11] Candelise, C.; Speirs, J. F.; Gross, R. J. K. Materials availability for thin film [TF] PV technologies development A real concern? *Renew. Sust. Energ. Rev.* **2011**, *15*, 4972-4981.

[12] Azzopardi, B.; Emmott, C. J. M.; Urbina, A.; Krebs, F. C.; Mutale, J.; Nelson, J. Economic assessment of solar electricity production from organic-based photovoltaic modules in a domestic environment. *Energy Environ. Sci.* **2011**, *4*, 3741-3753.

[13] Gu, G.; Burrows, P. E.; Venkatesh, S.; Forrest, S. R.; Thompson, M. E. Vacuum-deposited, nonpolymeric flexible organic light-emitting devices. *Opt. Lett.* **1997**, *22*, 172-174.

[14] Choi, K.-H.; Jeong, J.-A.; Kang, J.-W.; Kim, D.-G.; Kim, J. K.; Na, S.-I.; Kim, D.-Y.; Kim, S.-S.; Kim, H.-K. Characteristics of flexible indium tin oxide electrode grown by continuous roll-to-roll sputtering process for flexible organic solar cells. *Sol. Energy Mater. Sol. Cells* **2009**, *93*, 1248-1255.

[15] Steim, R.; Schilinsky, P.; Choulis, S. A.; Brabec, C. J. Flexible polymer photovoltaic modules with incorporated organic bypass diodes to address module shading effects. *Sol. Energy Mater. Sol. Cells* **2009**, *93*, 1963-1967.

[16] Paetzold, R.; Heuser, K.; Henseler, D.; Roeger, S.; Wittmann, G.; Winnacker, A. Performance of flexible polymeric light-emitting diodes under bending conditions. *Appl. Phys. Lett.* **2003**, *82*, 3342-3344.

[17] Chen, Z.; Cotterell, B.; Wang, W.; Guenther, E.; Chua, S.-J. A mechanical assessment of flexible optoelectronic devices. *Thin Solid Films* **2001**, *394*, 201-205.

[18] Du Pasquier, A.; Unalan, H. E.; Kanwal, A.; Miller, S.; Chhowalla, M. Conducting and transparent single-wall carbon nanotube electrodes for polymer-fullerene solar cells. *Appl. Phys. Lett.* **2005**, *87*, 203511-203513.

[19] van de Lagemaat, J.; Barnes, T. M.; Rumbles, G.; Shaheen, S. E.; Coutts, T. J.; Weeks, C.; Levitsky, I.; Peltola, J.; Glatkowski, P. Organic solar cells with carbon nanotubes replacing In_2O_3:Sn as the transparent electrode. *Appl. Phys. Lett.* **2006**, *88*, 233503-233505.

[20] Su, C.-Y.; Lu, A.-Y.; Chen, Y.-L.; Wei, C.-Y.; Wang, P.-C.; Tsai, C.-H. Chemically-treated single-walled carbon nanotubes as digitated penetrating electrodes in organic solar cells. *J. Mater. Chem.* **2010**, *20*, 7034-7042.

[21] Hecht, D. S.; Hu, L.; Irvin, G. Emerging Transparent Electrodes Based on Thin Films of Carbon Nanotubes, Graphene, and Metallic Nanostructures. *Adv. Mater.* **2011**, *23*, 1482-1513.

[22] Wassei, J. K.; Kaner, R. B. Graphene, a promising transparent conductor. *Mater. Today* **2010**, *13*, 52-59.

[23] Iwan, A.; Chuchmała, A. Perspectives of applied graphene: Polymer solar cells. *Prog. Polym. Sci.* **2012**, *37*, 1805-1828.

[24] Wan, X.; Huang, Y.; Chen, Y. Focusing on Energy and Optoelectronic Applications: A Journey for Graphene and Graphene Oxide at Large Scale. *Acc. Chem. Res.* **2012**, *45*, 598-607.

[25] Li, J.; Liu, Y.; Chen, D.; Zhang, H. Graphene and Its Derivatives for the Development of Photoelectrochemical Solar Cells and Photocatalysis. *Energy Environ. Sci.* **2013**, 6, 1362-1387.

[26] Bejbouji, H.; Vignau, L.; Miane, J.-L.; Dang, M. T.; Oualim, E. M.; Harmouchi, M.; Mouhsen, A. Polyaniline as a hole injection layer on organic photovoltaic cells. *Sol. Energy Mater. Sol. Cells* **2010**, *94*, 176-181.

[27] Ke, W.-J.; Lin, G.-H.; Hsu, C.-P.; Chen, C.-M.; Cheng, Y.-S.; Jen, T.-H.; Chen, S.-A. Solution processable self-doped polyaniline as hole transport layer for inverted polymer solar cells. *J. Mater. Chem.* **2011**, *21*, 13483-13489.

[28] Fan, B.; Araujo de Castro, F.; Chu, B. T.-T.; Heier, J.; Opris, D.; Hany, R.; Nuesch, F. Improved performance of cyanine solar cells with polyaniline anodes. *J. Mater. Chem.* **2010**, *20*, 2952-2955.

[29] Elschner, A.; Lövenich, W. Solution-deposited PEDOT for transparent conductive applications. *MRS Bull.* **2011**, *36*, 794-798.

[30] Ouyang, J. "Secondary doping" methods to significantly enhance the conductivity of PEDOT:PSS for its application as transparent electrode of optoelectronic devices. *Displays* **2013**, *34*, 423-436.

[31] Cho, S.-W.; Kim, Y. T.; Shim, W. H.; Park, S.-Y.; Kim, K.-D.; Seo, H. O.; Dey, N. K.; Lim, J.-H.; Jeong, Y.; Lee, K. H.; Kim, Y. D.; Lim, D. C. Influence of surface roughness of aluminum-doped zinc oxide buffer layers on the performance of inverted organic solar cells. *Appl. Phys. Lett.* **2011**, *98*, 023102-023104.

[32] Lee, J.; Lim, D.; Yang, K.; Choi, W. Influence of different plasma treatments on electrical and optical properties on sputtered AZO and ITO films. *J. Cryst. Growth* **2011**, *326*, 50-57.

[33] Oh, H.; Krantz, J.; Litzov, I.; Stubhan, T.; Pinna, L.; Brabec, C. J. Comparison of various sol–gel derived metal oxide layers for inverted organic solar cells. *Sol. Energy Mater. Sol. Cells* **2011**, *95*, 2194-2199.

[34] Minami, T. Present status of transparent conducting oxide thin-film development for Indium-Tin-Oxide [ITO] substitutes. *Thin Solid Films* **2008**, *516*, 5822-5828.

[35] Pern, F. J.; Glick, S. H.; Li, X.; DeHart, C.; Gennett, T.; Contreras, M.; Gessert, T. Stability of TCO window layers for thin-film CIGS solar cells upon damp heat exposures. part III. **2009**, Proc. SPIE 7412, Reliability of Photovoltaic Cells, Modules, Components, and Systems II, 74120K.

[36] Li, G.; Zhu, R.; Yang, Y. Polymer solar cells. *Nature Photon.* **2012**, *6*, 153-161.

[37] Dou, L.; You, J.; Yang, J.; Chen, C.-C.; He, Y.; Murase, S.; Moriarty, T.; Emery, K.; Li, G.; Yang, Y. Tandem polymer solar cells featuring a spectrally matched low-bandgap polymer. *Nature Photon.* **2012**, *6*, 180-185.

[38] He, Z.; Zhong, C.; Su, S.; Xu, M.; Wu, H.; Cao, Y. Enhanced power-conversion efficiency in polymer solar cells using an inverted device structure. *Nature Photon.* **2012**, *6*, 591-595.

[39] Duan, C.; Zhang, K.; Guan, X.; Zhong, C.; Xie, H.; Huang, F.; Chen, J.; Peng, J.; Cao, Y. Conjugated zwitterionic polyelectrolyte-based interface modification materials for high performance polymer optoelectronic devices. *Chem. Sci.* **2013**, *4*, 1298-1307.

[40] Sun, Y.; Welch, G. C.; Leong, W. L.; Takacs, C. J.; Bazan, G. C.; Heeger, A. J. Solution-processed small-molecule solar cells with 6.7% efficiency. *Nat. Mater.* **2012**, *11*, 44-48.

[41] Van der Poll, T. S.; Love, J. A.; Nguyen, T.-Q.; Bazan, G. C. Non-Basic High-Performance Molecules for Solution-Processed Organic Solar Cells. *Adv. Mater.* **2012**, *24*, 3646-3649.

[42] Cnops, K.; Rand, B. P.; Cheyns, D.; Verreet, B.; Empl, M. A.; Heremans, P. 8.4% efficient fullerene-free organic solar cells exploiting long-range exciton energy transfer. *Nat. Commun.* **2014**, *5*, 1-6.

[43] Zhou, Y.; Fuentes-Hernandez, C.; Khan, T. M.; Liu, J.-C.; Hsu, J.; Shim, J. W.; Dindar, A.; Youngblood, J. P.; Moon, R. J.; Kippelen, B. Recyclable organic solar cells on cellulose nanocrystal substrates. *Sci. Rep.* **2013**, *3*, 1536.

[44] Sugiyama, K.; Ishii, H.; Ouchi, Y.; Seki, K. Dependence of indium-tin-oxide work function on surface cleaning method as studied by ultraviolet and x-ray photoemission spectroscopies. *J. Appl. Phys.* **2000**, *87*, 295-298.

[45] Dang, M. T.; Hirsch, L.; Wantz, G. P3HT:PCBM, Best Seller in Polymer Photovoltaic Research. *Adv. Mater.* **2011**, *23*, 3597-3602.

[46] Dang, M. T.; Hirsch, L.; Wantz, G.; Wuest, J. D. Controlling the Morphology and Performance of Bulk Heterojunctions in Solar Cells. Lessons Learned from the Benchmark Poly[3-hexylthiophene]:[6,6]-Phenyl-C_{61}-butyric Acid Methyl Ester System. *Chem. Rev.* **2013**, *113*, 3734-3765.

[47] Cravino, A.; Schilinsky, P.; Brabec, C. J. Characterization of Organic Solar Cells: the Importance of Device Layout. *Adv. Funct. Mater.* **2007**, *17*, 3906-3910.

[48] Kim, M.-S.; Kang, M.-G.; Guo, L. J.; Kim, J. Choice of electrode geometry for accurate measurement of organic photovoltaic cell performance. *Appl. Phys. Lett.* **2008**, *92*, 133301-133303.

[49] Muhsin, B.; Renz, J.; Drüe, K.-H.; Gobsch, G.; Hoppe, H. Influence of polymer solar cell geometry on series resistance and device efficiency. *Phys. Status Solidi [a]* **2009**, *206*, 2771-2774.

[50] Mallajosyula, A. T.; Srivastava, N.; Iyer, S. S. K.; Mazhari, B. Characterization of matrix and isolated organic solar cells. *Sol. Energy Mater. Sol. Cells* **2010**, *94*, 1319-1323.

[51] de Jong, M. P.; van Ijzendoorn, L. J.; de Voigt, M. J. A. Stability of the interface between indium-tin-oxide and poly[3,4-ethylenedioxythiophene]/poly[styrenesulfonate] in polymer light-emitting diodes. *Appl. Phys. Lett.* **2000**, *77*, 2255-2257.

[52] See the Supporting Information for details.

[53] Frohne, H.; Shaheen, S. E.; Brabec, C. J.; Müller, D. C.; Sariciftci, N. S.; Meerholz, K. Influence of the Anodic Work Function on the Performance of Organic Solar Cells. *ChemPhysChem* **2002**, *3*, 795-799.

[54] Zhang, F. L.; Gadisa, A.; Inganäs, O.; Svensson, M.; Andersson, M. R. Influence of buffer layers on the performance of polymer solar cells. *Appl. Phys. Lett.* **2004**, *84*, 3906-3908.

[55] Yoo, I.; Lee, M.; Lee, C.; Kim, D. W.; Moon, I. S.; Hwang, D. H. The effect of a buffer layer on the photovoltaic properties of solar cells with P3OT:fullerene composites. *Synth. Met.* **2005**, *153*, 97-100.

[56] Ramuz, M.; Bürgi, L.; Winnewisser, C.; Seitz, P. High sensitivity organic photodiodes with low dark currents and increased lifetimes. *Org. Electron.* **2008**, *9*, 369-376

Chapitre 7

Conclusions et Perspectives

"The illusion of purpose and design is perhaps the most pervasive illusion about nature that science has to confront on a daily basis."

- Lawrence M. Krauss

7.1 Conclusions

Le premier objectif de ce travail était de pouvoir réaliser des dispositifs organiques fonctionnels à partir de matériaux semi-conducteurs efficaces connus. Grâce au développement d'outils et de techniques de manufacture, une ligne de production de dispositifs a pu être mise en place et les résultats obtenus validés par rapport à des dispositifs référentiels.

Au deuxième chapitre, deux nouvelles petites molécules à bandes interdites étroites de type semi-conducteur p ont été synthétisées et testées comme matériaux actifs dans les dispositifs solaires. Leur mise en forme en films minces étant compromise par une tendance à cristalliser facilement lors de leur dépôt, des polymères semi-conducteurs ont été utilisés comme matrices actives, rectifiant ainsi la formation des films. Des rendements supérieurs de plus de 30% ont été enregistrés dans le cas du PCDTBT, et l'ajout de seulement 25% du polymère a permis de faire fonctionner décemment des dispositifs à partir de ces petites molécules.

Suite à ces résultats, des polymères isolants ont été utilisés pour remplir le rôle de rectifieurs de films, sans contribuer cette fois-ci aux rendements des dispositifs de manière active électroniquement. Ces matrices passives, présentées au chapitre 3, permirent d'augmenter les rendements des dispositifs à base d'ID$(BTC)_2$ ou de F-DTS de manière substantielle. Les variations de la nature du polymère isolant, de sa masse molaire et de la concentration de celui-ci à l'intérieur de la couche active ont permis d'identifier certains modes de dispersion et de cristallisation présents dans ces systèmes. La création de pochettes de polymères permet une ségrégation pseudo contrôlée des matériaux donneurs et accepteurs tout en rectifiant la propension des petites molécules actives à cristalliser facilement, et ce, même dans des conditions de mises en formes à température pièce. Ces matrices étant très peu

couteuses, une opportunité d'économie de matériaux de haute technologie a également été soulignée.

Au chapitre 4, une librairie de masse molaire du PFO-MEH-PPV a été produite grâce à un contrôle pointu de la polymérisation de monomères purs par réaction de Wittig contrôlée. Il a été validé que les performances des dispositifs organiques électroniques dépendent grandement de la masse molaire du polymère utilisé. Si les basses masses forment des régions plus cristallines à partir de l'agrégation de chaines polymériques linéaires, les polymères de fortes masses forment des films plus réguliers qui produise des dispositifs ayant de meilleurs rendements. Par contre, les rendements quantiques en solution sont inférieurs pour les polymères de fortes masses.

Les dispositifs fabriqués ont été caractérisés par différentes méthodes dont le MET, le MEB et le AFM. La morphologie des films actifs jouant un rôle déterminant sur les performances des dispositifs, une étude approfondie utilisant les films actifs ou reproduits dans des conditions similaires aux traitements infligés aux dispositifs, a été entreprise. Si le MEB et le AFM sont des techniques de surface, le MET requière des films minces et transparents électroniquement. Au chapitre 5, trois différentes techniques de préparation ont été exploitées, dont une nouvelle méthode permettant de rapidement former des films dénudés de tout contaminant par suspension dans le vide sur un substrat de silicium. L'utilisation de substrats de sel (NaCl monocristallin) permis également d'obtenir des films actifs minces libres et la possibilité d'appliquer des motifs nanométriques aux couches actives.

Par souci du cout et de la disponibilité limitée des substrats d'ITO sur verre, les dispositifs ayant terminé leur vie utile ont été recyclés efficacement par une nouvelle méthode qui a été présentée au chapitre 6. Les différentes méthodes de caractérisation n'ont pas permis de découvrir de contaminants résiduels après nettoyage. Les performances des dispositifs sont restées constantes même après dix cycles de nettoyage et de traitement. Cette approche permet d'utiliser des matériaux performants à des couts très minimisés, ce qui favorise un échantillonnage plus large et plus rigoureux pour un même budget.

7.2 Perspectives

Si la présente étude sur les matériaux oligomériques et polymériques π-conjugués a permis de mieux comprendre le rôle et les arrangements possibles des différentes composantes organiques actives des dispositifs électroniques organiques, plusieurs questions et pistes sont maintenant ouvertes et demandent à être explorées. Plusieurs méthodes de synthèse, de fabrication de dispositifs et d'analyse ont été présentées, permettant d'assoir les futures recherches sur des bases solides. Les infrastructures incluant un laboratoire permettant la fabrication séquentielle de ces dispositifs et les appareils nécessaires à leur caractérisation ont été montées avec le souci de permettre des études complètes et flexibles sur les cellules photovoltaïques et les diodes luminescentes organiques à films minces.

7.2.1 Petites molécules actives

De nouvelles petites molécules de type "push-pull" à bandes interdites étroites ont été présentées. Leur mise en forme en films minces homogènes, grâce à l'ajout de matrices polymériques conductrices, ont permis de construire des cellules hybrides à trois composantes de type donneur-accepteur. Ce concept ayant fait ces preuves, une première voie d'exploration fut de remplacer les matrices semi-conductrices par des polymères communs de type isolant. Cette nouvelle avenue permet maintenant de concevoir des petites molécules conjuguées à bandes interdites étroites pour leurs caractéristiques électroniques, en laissant les fonctions de mises en forme en films minces à une matrice polymère. Il est à noter que les petites molécules pourraient également être utilisées comme additifs (moins de 50%) aux polymères actifs tels le PCDTBT et le P3HT en cellules solaires organiques, pour augmenter leurs rendements.

Il est important de réaliser que la partie électroniquement active de ces matériaux semi-conducteurs réside à travers leurs systèmes π-conjugués, et que les chaines alkyles ajoutées servent principalement à les rendre solubles et transformables ou de contrôler leur degré d'agrégation.[121] En minimisant le nombre de chaines non-actives ou leurs longueurs, la densité de chromophores actifs par unité de volume du film sera ainsi augmentée, augmentant le coefficient d'absorptivité massique des matériaux et possiblement les rendements des dispositifs électroniques organiques en permettant l'utilisation de films plus minces, limitant la distance à parcourir par les transporteurs de charges vers les électrodes.

Les deux nouvelles molécules présentées étant très solubles dans les solvants des systèmes utilisés, une première modification pourrait être faite sur les longues chaines alkyles linéaires adjacentes qui, à l'étape de conception des molécules, devaient leur assurer une grande solubilité. Il est très possible que des chaines plus courtes de quatre ou six carbones seraient largement suffisantes pour assurer leur mise en forme. Des chaines à branches pourraient également permettre de limiter leur agrégation en limitant la possibilité d'empilement π des cycles aromatiques par augmentation de l'encombrement stérique autour des chromophores.

Nous avons également pu constater que la minimisation des atomes pouvant altérer la planéité du système π permettait d'obtenir des composés à bandes interdites très étroites en modifiant légèrement la structure. L'augmentation du nombre de cycles aromatiques fusionnés et la substitution des cycles benzéniques par des cycles hétérogènes contenant des atomes ayant une électronégativité plus élevée que celle du carbone permet également d'étendre la conjugaison à travers le système et d'ajuster la position des niveaux énergétiques HOMO et LUMO de ces matériaux actifs. L'élongation des corps des petites molécules synthétisées par un ou deux cycles aromatiques permettrait de prolonger cette série vers des bandes interdites encore plus étroites.

L'utilisation de cycles fusionnés pour remplacer les groupements thiophène périphériques par des groupements thiénothiophène ou benzothiadiazole, par exemple, permettrait d'étendre le plan de conjugaison. Comme pour le F-DTS présenté plus tôt, l'ajout de groupements électro-attracteurs comme le fluor permet également de modifier la structure électronique de ces matériaux ou d'augmenter leur stabilité (en substituant, dans le cas du F-DTS, un groupement de type pyridinium pouvant réagir avec le PEDOT:PSS acide).[72, 122]

Si les recuits thermiques permettent d'obtenir des morphologies plus optimales grâce aux mouvements des différentes molécules et polymères actifs par séparation de phases, il n'est pas garanti que ces morphologies soient stables et fixes dans le temps. La possibilité de figer une morphologie optimale, une fois celle-ci obtenue, permettrait d'augmenter le temps de vie utile des dispositifs. Une stratégie envisageable est l'ajout de chaines réactionnelles en périphérie des chromophores, permettant de réticuler les composantes une fois celle-ci en place. Les petites molécules seraient ainsi beaucoup moins mobiles et une séparation de phase optimale pourrait ainsi être conservée. Par exemple, l'ajout de groupements vinyles[123] ou acrylates[124] en bouts des chaines alkyles du polyfluorène a été étudiés pour obtenir cet effet, sans affecter les propriétés électroniques des chromophores.

7.2.2 Matrices polymériques

Plusieurs matrices polymères permettant de limiter la cristallisation des petites molécules actives et d'appliquer un certain contrôle sur la morphologie des films actifs ont été présentées. Par contre, cette approche représente seulement un échantillonnage très restreint de la multitude de polymères disponibles commercialement pouvant possiblement être utilisés comme matrices. Pour un même type de polymère, la variation de ces caractéristiques intrinsèques telles le M_w et la polydispersité joueront un rôle déterminant dans la mobilité des chaines, les interactions avec les autres composantes et les caractéristiques des films minces résultants.

Si la grande majorité des recherches en dispositifs électroniques organiques se consacrent à obtenir les matériaux ou les dispositifs les plus performants possibles, très peu de recherches se penchent sur leur temps de vie utile. Ceci s'explique possiblement par une tendance de la littérature actuelle à favoriser les plus hauts rendements ponctuels sans se soucier nécessairement de leur continuité temporelle. L'industrie favorisera, par exemple, des rendements plus faibles sur une plus longue période.

Des rendements décents ont été présenté plus tôt pour des cellules photovoltaïques à base de matrices de PVC après des recuits à hautes températures (225 °C). Il est possible que l'utilisation de matrices polymériques adaptées puisse également servir de barrière face à différents éléments externes responsables de la dégradation des matériaux actifs tel l'oxygène et l'eau. Il est possible également que ces barrières soient efficaces contre la dérive interne de certains éléments tels les métaux provenant des électrodes par électro-migration.[125-126]

Les résultats démontrent également que l'ajout de 15 à 25% de matrices polymériques peu dispendieuses et largement disponibles, permet de garder un niveau de performance acceptable pour les dispositifs qui ont été étudiés. En considérant les couts élevés de la plupart des matériaux actifs ou leur disponibilité parfois restreinte, la possibilité d'inclure de larges proportions de matrices polymériques communes procurera également un avantage distinct.

7.2.3 Impressions de motifs nanométriques

L'étude de la morphologie des films par microscopie électronique à transmission a permit de découvrir que les films formés sur des substrats de NaCl reproduisaient fidèlement les nano-impressions présentes sur les substrats. Il a été démontré qu'un appareil destiné à la microscopie à force atomique (AFM) peut être utilisé pour créer des motifs nanométriques sur différents substrats.[127-128] Il est donc envisageable de former des moules nanométriques en sel (NaCl ou autre) qui pourront par la suite être complètement détachés par lavage à l'eau,

laissant un motif à haute résolution sur la surface d'un film actif mince. Ces motifs pourraient par la suite être remplis ou recouvert par d'autres matériaux pour former différentes interfaces ou jonctions p-n contrôlées.

Bibliographie

[1] Conti, J. J.; Holtberg, P. D.; Beamon, J. A.; Napolitano, S. A.; Schaal, M. A.; Turnure, J. T.; Westfall, L. D. International Energy Outlook 2013. *U. S. Energy Information Administration* **2013**.

[2] Gerland, P.; Raftery, A. E.; Ševčíková, H.; Li, N.; Gu, D.; Spoorenberg, T.; Alkema, L.; Fosdick, B. K.; Chunn, J.; Lalic, N.; Bay, G.; Buettner, T.; Heilig, G. K.; Wilmoth, J. World population stabilization unlikely this century. *Science* **2014,** *346* (6206), 234-237.

[3] Dudley, B. BP Statistical Review of World Energy June 2014. *BP Statistical Review of World Energy* **2014,** *63* (63rd Edition), 1-48.

[4] Qian, Z.; Zhang, J. J.; Korn, L. R.; Wei, F.; Chapman, R. S. Exposure–response relationships between lifetime exposure to residential coal smoke and respiratory symptoms and illnesses in Chinese children. *J. Expo. Sci. Environ. Epidemiol.* **2004,** *14*, S78-84.

[5] Hong, L. C. E.; Conroy, L. A.; Scholand, M. J. U.S. Lighting Market Characterization - Energy Efficient Lighting Technology Options. *U.S. Department of Energy* **2005,** *2*, 1-286.

[6] Sharkawi, M. A. *Electric energy : an introduction*. CRC Press: Boca Raton, Florida, **2005**; p 472.

[7] Becquerel, A. E. Memoire sur les effets electriques produit sous l'influence des rayons solaires. *C. R. Acad. Sci.* **1839,** *9*, 561-567.

[8] Einstein, A. On a Heuristic Point of View about the Creation and Conversion of Light. *Ann. Phys.* **1905,** *17* (6), 132-148.

[9] Smith, Z. A.; Taylor, K. D. *Renewable and Alternative Energy Resources: A Reference Handbook*. ABC-CLIO: Santa-Barbara, California, **2008**.

[10] Fagen, M. D.; Joel, A. E. *A history of engineering and science in the Bell system. Physical sciences (1925-1980)*. New York, **1983**; Vol. 1.

[11] Chiang, C. K.; Fincher, C. R.; Park, Y. W.; Heeger, A. J.; Shirakawa, H.; Louis, E. J.; Gau, S. C.; MacDiarmid, A. G. Electrical Conductivity in Doped Polyacetylene. *Phys. Rev. Lett.* **1977,** *39* (17), 1098-1101.

[12] Heeger, A. J. Nobel Lecture: Semiconducting and metallic polymers: The fourth generation of polymeric materials. *Rev. Mod. Phys.* **2001,** *73* (3), 681-701.

[13] Shirakawa, H. Nobel Lecture: The discovery of polyacetylene film—the dawning of an era of conducting polymers. *Rev. Mod. Phys.* **2001,** *73* (3), 713-718.

[14] MacDiarmid, A. G. Nobel Lecture: "Synthetic metals": A novel role for organic polymers. *Rev. Mod. Phys.* **2001,** *73* (3), 701-712.

[15] Tang, C. W. Two-layer organic photovoltaic cell. *Appl. Phys. Lett.* **1986,** *48* (2), 183-185.

[16] Tang, C. W.; VanSlyke, S. A. Organic electroluminescent diodes. *Appl. Phys. Lett.* **1987,** *51* (12), 913-915.

[17] NREL. http://www.nrel.gov/ (accessed May 2015).

[18] Heliatek. Heliatek sets new Organic Photovoltaic world record efficiency of 13.2%. http://www.heliatek.com/en/press/press-releases/details/heliatek-sets-new-organic-photovoltaic-world-record-efficiency-of-13-2 (accessed February 2016).

[19] Flowers, E. C.; McCormick, R. A.; Kurfis, K. R. Atmospheric Turbidity over the United States, 1961-1966. *J. Appl. Meteorol.* **1969,** *8*, 955-962.

[20] Ångström, A. On the atmospheric transmission of Sun radiation and on dust in the air. *Geograph. Ann.* **1929,** *11*, 156-166.

[21] Peierls, R. Zur Theorie der elektrischen und thermischen Leitfähigkeit von Metallen. *Ann. Phys.* **1930,** *396* (2), 121-148.

[22] Friend, R. H.; Denton, G. J.; Halls, J. J. M.; Harrison, N. T.; Holmes, A. B.; Köhler, A.; Lux, A.; Moratti, S. C.; Pichler, K.; Tessler, N.; Towns, K. Electronic Processes of Conjugated Polymers in Semiconductor Device Structures. *Synth. Met.* **1997,** *84* (1-3), 463-470.

[23] Shaw, P. E.; Ruseckas, A.; Samuel, D. W. Exciton Diffusion Measurements in Poly(3-hexylthiophene). *Adv. Mater.* **2008,** *20* (18), 3516-3520.

[24] Yu, G.; Gao, J.; Hummelen, J. C.; Wudl, F.; Heeger, A. J. Polymer Photovoltaic Cells: Enhanced Efficiencies via a Network of Internal Donor-Acceptor Heterojunctions. *Science* **1995,** *270* (5243), 1789-1791.

[25] Ma, W.; Yang, C.; Gong, X.; Lee, K.; Heeger, A. J. Thermally Stable, Efficient Polymer Solar Cells with Nanoscale Control of the Interpenetrating Network Morphology. *Adv. Funct. Mater.* **2005,** *15* (10), 1617-1622.

[26] Walker, B.; Kim, C.; Nguyen, T.-Q. Small Molecule Solution-Processed Bulk Heterojunction Solar Cells. *Chem. Mater.* **2011,** *23* (3), 470–482.

[27] Kietzke, T. Recent Advances in Organic Solar Cells. *Adv. Optoelectron.* **2007,** *2007*, 1-15.

[28] Blouin, N.; Michaud, A.; Gendron, D.; Wakim, S.; Blair, E.; Neagu-Plesu, R.; Belletête, M.; Durocher, G.; Tao, Y.; Leclerc, M. Toward a Rational Design of Poly(2,7-Carbazole) Derivatives for Solar Cells. *J. Am. Chem. Soc.* **2008,** *130* (2), 732-742.

[29] Coughlin, J. E.; Henson, Z. B.; Welch, G. C.; Bazan, G. C. Design and Synthesis of Molecular Donors for Solution-Processed High-Efficiency Organic Solar Cells. *Acc. Chem. Res.* **2014,** *47* (1), 257-270.

[30] Leclerc, M.; Gauvin, R. *Functional Materials: For Energy, Sustainable Development and Biomedical Sciences*. Walter de Gruyter GmbH & Co KG: Berlin, **2014**; p 493.

[31] Scharber, M. C.; Muhlbacher, D.; Koppe, M.; Denk, P.; Waldauf, C.; Heeger, A. J.; Brabec, C. J. Design Rules for Donors in Bulk-Heterojunction Solar Cells - Towards 10 % Energy-Conversion Efficiency. *Adv. Mater.* **2006,** *18* (6), 789-794.

[32] Li, Y. Molecular Design of Photovoltaic Materials for Polymer Solar Cells: Toward Suitable Electronic Energy Levels and Broad Absorption. *Acc. Chem. Res.* **2012,** *45* (5), 723-733.

[33] knupfer, M. Exciton binding energies in organic semiconductors. *Applied Physics A* **2003,** *77*, 623–626.

[34] Brabec, C. J.; Cravino, A.; Meissner, D.; Sariciftci, N. S.; Fromherz, T.; Rispens, M. T.; Sanchez, L.; Hummelen, J. C. Origin of the Open Circuit Voltage of Plastic Solar Cells. *Adv. Funct. Mater.* **2001,** *11* (5), 374-380.

[35] Lin, Y.; Lia, Y.; Zhan, X. Small molecule semiconductors for high-efficiency organic photovoltaics. *Chem. Soc. Rev.* **2012,** *41*, 4245–4272.

[36] Liu, H. Q.; Xiang, L. H. Recent progress of bulk heterojunction solar cells based on small-molecular donors. *Chin. Sci. Bull.* **2013,** *58*, 2677-2685.

[37] Liu, Y.; Chen, C.-C.; Hong, Z.; Gao, J.; Yang, Y. M.; Zhou, H.; Dou, L.; Li, G.; Yang, Y. Solution-processed small-molecule solar cells: breaking the 10% power conversion efficiency. *Sci. Rep.* **2013,** *3* (3356), 1-8.

[38] Dou, L.; You, J.; Yang, J.; Chen, C.-C.; He, Y.; Murase, S.; Moriarty, T.; Emery, K.; Li, G.; Yang, Y. Tandem polymer solar cells featuring a spectrally matched low-bandgap polymer. *Nature Photon.* **2012,** *6* (3), 180-185.

[39] Leeuw, D. M. d.; Simenon, M. M. J.; Brown, A. R.; Einerhand, R. E. F. Stability of n-type doped conducting polymers and consequences for polymeric microelectronic devices. *Synt. Met.* **1997,** *87* (1), 53-59.

[40] Coropceanu, V.; Cornil, J.; Filho, D. A. d. S.; Olivier, Y.; Silbey, R.; Brédas, J.-L. Charge Transport in Organic Semiconductors. *Chem. Rev.* **2007,** *107*, 926-952.

[41] Lombeck, F.; Komber, H.; Sepe, A.; Friend, R. H.; Sommer, M. Enhancing Phase Separation and Photovoltaic Performance of All- Conjugated Donor−Acceptor Block Copolymers with Semifluorinated Alkyl Side Chains. *Macromolecules* **2015,** *48*, 7851-7860.

[42] Morse, G. E.; Tournebize, A.; Rivaton, A.; Chassé, T.; Taviot-Gueho, C.; Blouin, N.; Lozman, O. R.; Tierney, S. The effect of polymer solubilizing side-chains on solar cell stability. *Phys. Chem. Chem. Phys.* **2015,** *7*, 11884-11897.

[43] Partridge, R. H. Electroluminescence from polyvinylcarbazole films: 2. Polyvinylcarbazole films containing antimony pentachloride. *Polymers* **1981,** *24* (6), 739-747.

[44] Burroughes, J. H.; Bradley, D. D. C.; Brown, A. R.; Marks, R. N.; Mackay, K.; Friend, R. H.; Burns, P. L.; Holmes, A. B. Light-emitting diodes based on conjugated polymers. *Nature* **1990,** *347* (6293), 539-541.

[45] Mi, B.-X.; Wang, P.-F.; Liu, M.-W.; Kwong, H.-L.; Wong, N.-B.; Lee, C.-S.; Lee, S.-T. Thermally Stable Hole-Transporting Material for Organic Light-Emitting Diode: an Isoindole Derivative. *Chem. Mater.* **2003,** *15*, 3148-3151.

[46] Huang, Q.; Evmenenko, G. A.; Dutta, P.; Lee, P.; Armstrong, N. R.; Marks, T. J. Covalently Bound Hole-Injecting Nanostructures. Systematics of Molecular Architecture, Thickness, Saturation, and Electron-Blocking Characteristics on Organic Light-Emitting Diode Luminance, Turn-on Voltage, and Quantum Efficiency. *J. Am. Chem. Soc.* **2005,** *127*, 10227-10242.

[47] Kulkarni, A. P.; Tonzola, C. J.; Babel, A.; Jenekhe, S. A. Electron Transport Materials for Organic Light-Emitting Diodes. *Chem. Mater.* **2004,** *16*, 4556-4573.

[48] Greenham, N. C.; Moratti, S. C.; Bradley, D. D. C.; Friend, R. H.; Holmes, A. B. Efficient light-emitting diodes based on polymers with high electron affinities. *Nature* **1993,** *365* (6447), 628-630.

[49] Inbasekaran, M.; Woo, E.; Wu, W.; Bernius, M.; Wujkowski, L. Fluorene homopolymers and copolymers. *Synt. Met.* **2000,** *111–112*, 397-401.

[50] Braun, D.; Heeger, A. J. Visible light emission from semiconducting polymer diodes. *Appl. Phys. Lett.* **1991,** *58* (18), 1982-1984.

[51] Gustafsson, G.; Cao, Y.; Treacy, G. M.; Klavetter, F.; Colaneri, N.; Heeger, A. J. Flexible light-emitting diodes made from soluble conducting polymers. *Nature* **1992,** *357* (6378), 477-479.

[52] McGoldrick, K. In *Mobile Friendly Rollable Displays*, 2006 Proceedings of the 32nd European Solid-State Circuits Conference, Montreux, Switzerland, Montreux, Switzerland, **2006**.

[53] Krebs, F. C. Roll-to-roll fabrication of monolithic large-area polymer solar cells free from indium-tin-oxide. *Sol. Energ. Mat. Sol. Cells* **2009,** *93* (9), 1636-1641.

[54] Krebs, F. C. All solution roll-to-roll processed polymer solar cells free from indium-tin-oxide and vacuum coating steps. *Org. Electron.* **2009,** *10* (5), 761-768.

[55] Krebs, F. C. Fabrication and processing of polymer solar cells: A review of printing and coating techniques. *Sol. Energ. Mat. Sol. Cells* **2009,** *93* (4), 394-412.

[56] Kim, J.; Cho, N.; Ko, H. M.; Kim, C.; Lee, J. K.; Ko, J. Push-pull organic semiconductors comprising of bis-dimethylfluorenyl amino benzo[b]thiophene donor and various acceptors for solution processed small molecule organic solar cells. *Sol. Energ. Mat. Sol. Cells* **2012,** *102*, 159–166.

[57] Ko, H. M.; Choi, H.; Paek, S.; Kim, K.; Song, K.; Lee, J. K.; Ko, J. Molecular engineering of push-pull chromophore for efficient bulkheterojunction morphology in solution processed small molecule organic photovoltaics. *J. Mater. Chem.* **2011,** *21*, 7248-7253.

[58] Mikroyannidis, J. A.; Tsagkournos, D. V.; Sharma, S. S.; Vijay, Y. K.; Sharma, G. D. Low band gap conjugated small molecules containing benzobisthiadiazole and thienothiadiazole central units: synthesis and application for bulk heterojunction solar cells. *J. Mater. Chem.* **2011,** *21*, 4679-4688.

[59] Zhang, L.; Pei, K.; Zhao, H.; Wu, S.; Wang, Y.; Gao, J. Rational design of novel A-A-D-A-A type electron donors for small molecule organic solar cells. *Chem. Phys. Lett.* **2012,** *543*, 199–204.

[60] Kroto, H. W.; Heath, J. R.; O'Brien, S. C.; Curl, R. F.; Smalley, R. E. C60: Buckminsterfullerene. *Nature* **1985,** *318* (6042), 162-163.

[61] Cheng, Y.-J.; Yang, S.-H.; Hsu, C.-S. Synthesis of Conjugated Polymers for Organic Solar Cell Applications. *Chem. Rev.* **2009,** *109*, 5868–5923.

[62] Chen, T. A.; Rieke, R. D. The first regioregular head-to-tail poly(3-hexylthiophene-2,5-diyl) and a regiorandom isopolymer: nickel versus palladium catalysis of 2(5)-bromo-5(2)-(bromozincio)-3-hexylthiophene polymerization. *Journal of the American Chemical Society* **1992,** *114* (25), 10087-10088.

[63] Blouin, N.; Michaud, A.; Leclerc, M. A Low-Bandgap Poly(2,7-Carbazole) Derivative for Usein High-Performance Solar Cells. *Adv. Mater.* **2007,** *19*, 2295-2300

[64] Lee, H. K. H.; Chan, K. K. H.; So, S. K. Charge transport studies of polymeric photovoltaic thin films with an electron blocking and trapping layer. *Org. Photon. V* **2012,** *8435*, 84351U.

[65] Orgiu, E.; Masillamani, A. M.; Vogel, J.-O.; Treossi, E.; Kiersnowski, A.; Kastler, M.; Pisula, W.; Dotz, F.; Palermo, V.; Samorí, P. Enhanced mobility in P3HT-based OTFTs upon blending with a phenylene–thiophene–thiophene–phenylene small molecule. *Chem. Commun.* **2012,** *48*, 1562–1564.

[66] Wu, M.-C.; Liao, H.-C.; Lo, H.-H.; Chen, S.; Lin, Y.-Y.; Yen, W.-C.; Zeng, T.-W.; Chen, C.-W.; Chen, Y.-F.; Su, W.-F. Nanostructured polymer blends (P3HT/PMMA):

Inorganic titania hybrid photovoltaic devices. *Sol. Energ. Mat. Sol. Cells* **2009,** *93*, 961-965.

[67] Wong, H. C.; Li, Z.; Tan, C. H.; Zhong, H.; Huang, Z.; Bronstein, H.; McCulloch, I.; Cabral, J. T.; Durrant, J. R. Morphological Stability and Performance of Polymer-Fullerene Solar Cells under Thermal Stress: The Impact of Photoinduced PC60BM Oligomerization. *ACS Nano* **2014,** *8* (2), 1297–1308.

[68] Segui, J. A.; Black, C. T.; Satija, S. In *Self Assembled Heterojunction Solar Cell Active Layers*, Adv. Ener. 2010, New York, USA, November; New York, USA, **2010**.

[69] Sun, Z.; Xiao, K.; Keum, J. K.; Yu, X.; Hong, K.; Browning, J.; Ivanov, I. N.; Chen, J.; Alonzo, J.; Li, D.; Sumpter, B. G.; Payzant, E. A.; Rouleau, C. M.; Geohegan, D. B. PS-b-P3HT Copolymers as P3HT/PCBM Interfacial Compatibilizers for High Efficiency Photovoltaics. *Adv. Mater.* **2011,** *23* (46), 5529-5535.

[70] Botiz, I.; Freyberg, P.; Leordean, C.; Gabudean, A.-M.; Astileana, S.; Yang, A. C.-M.; Stingelin, N. Emission properties of MEH-PPV in thin films simultaneously illuminated and annealed at different temperatures. *Synt. Met.* **2015,** *199*, 33-36.

[71] Vacha, M.; Habuchi, S. Conformation and physics of polymer chains: a single-molecule perspective. *NPG Asia Mater.* **2010,** *2* (4), 134-142.

[72] Van der Poll, T. S.; Love, J. A.; Nguyen, T.-Q.; Bazan, G. C. Non-Basic High-Performance Molecules for Solution-Processed Organic Solar Cells. *Adv. Mater.* **2012,** *24* (27), 3646-3649.

[73] Burn, P. L.; Holmes, A. B.; Kraft, A.; Baigent, D. R.; Bradley, D. D. C.; Brown, A. B.; Friend, R. H. Chemical Tuning of the Electronic Properties of poly(p-phenylenevinylene)-Based Copolymers. *J. Am. Chem. Soc.* **1993,** *115*, 10117-10124.

[74] Pei, J.; Wen, S.; Zhou, Y.; Dong, Q.; Liu, Z.; Zhang, J.; Tian, W. A low band gap donor–acceptor copolymer containing fluorene and benzothiadiazole units: synthesis and photovoltaic properties. *New J. Chem.* **2011,** *35*, 385–393.

[75] Tan, T. A. T.; Clarke, T. M.; James, D.; Durrant, J. R.; White, J. M.; Ghiggino, K. P. Synthesis and photo-induced charge separation of confined conjugation length phenylene vinylene-based polymers. *Polym. Chem.* **2013,** *4*, 5305-5309.

[76] Rosa, A. L.; Gillemot, K.; Leary, E.; Evangeli, C.; Gonzaĺez, M. a. T.; Filippone, S.; Rubio-Bollinger, G.; Agrait, N.; Lambert, C. J.; Martín, N. Does a Cyclopropane Ring

Enhance the Electronic Communication in Dumbbell-Type C60 Dimers? *J. Org. Chem.* **2014,** *79*, 4871-4877.

[77] D'Andrade, B. W.; Forrest, S. R. White Organic Light-Emitting Devices for Solid-State Lighting. *Adv. Mater.* **2004,** *16* (18), 1585-1595.

[78] Farinola, G. M.; Ragni, R. Electroluminescent materials for white organic light emitting diodes. *Chem. Soc. Rev.* **2011,** *40*, 3467–3482.

[79] Reineke, S.; Thomschke, M.; Lüssem, B.; Leo, K. White organic light-emitting diodes: Status and perspective. *Rev. Mod. Phys.* **2013,** *85*, 1285-1293.

[80] Tessler, N.; Denton, G. J.; Friend, R. H. Lasing from conjugated-polymer microcavities. *Nature* **1996,** *382*, 695-697.

[81] Chénais, S.; Forget, S. Recent advances in solid-state organic lasers. *Polym. Int.* **2012,** *61* (3), 390–406.

[82] Forrest, S. R. The path to ubiquitous and low-cost organic electronic appliances on plastic. *Nature* **2004,** *428*, 911-918.

[83] Arias, A. C.; MacKenzie, J. D.; McCulloch, I.; Rivnay, J.; Salleo, A. Materials and Applications for Large Area Electronics: Solution-Based Approaches. *Chem. Rev.* **2010,** *110*, 3–24.

[84] Søndergaard, R. R.; Hösel, M.; Krebs, F. C. Roll-to-Roll fabrication of large area functional organic materials. *J. Polym. Sci. Part B Polym. Phys.* **2013,** *51* (1), 16–34.

[85] Sekine, C.; Tsubata, Y.; Yamada, T.; Kitano, M.; Doi, S. Recent progress of high performance polymer OLED and OPV materials for organic printed electronics. *Sci. Technol. Adv. Mater.* **2014,** *15*, 1-15.

[86] Cui, J.; Wang, A.; Edleman, N. L.; Ni, J.; Lee, P.; Armstrong, N. R.; Marks, T. J. Tin Oxide Alternatives-High Work Function Transparent Conducting Oxides as Anodes for Organic Light-Emitting Diodes. *Adv. Mater.* **2001,** *13*, 1476-1480.

[87] Wu, Q.-H. Progress in Modification of Indium-Tin Oxide/Organic Interfaces for Organic Light-Emitting Diodes. *Crit. Rev. Solid State Mater. Sci.* **2013,** *38*, 318-352.

[88] Kim, H.; Gilmore, C. M.; Piqué, A.; Horwitz, J. S.; Mattoussi, H.; Murata, H.; Kafafi, Z. H.; Chrisey, D. B. Electrical, optical, and structural properties of indium-tin-oxide thin films for organic light-emitting devices. *J. Appl. Phys.* **1999,** *86*, 6451-6461.

[89] Armstrong, N. R.; Carter, C.; Donley, C.; Simmonds, A.; Lee, P.; Brumbach, M.; Kippelen, B.; Domercq, B.; Yoo, S. Interface modification of ITO thin films: organic photovoltaic cells. *Thin Solid Films* **2003,** *445* (2), 342-352.

[90] Armstrong, N. R.; Veneman, P. A.; Ratcliff, E.; Placencia, D.; Brumbach, M. Oxide Contacts in Organic Photovoltaics Characterization and Control of Near-Surface Composition in Indium-Tin Oxide (ITO) Electrodes. *Acc. Chem. Res.* **2009,** *42*, 1748-1757.

[91] Lee, H. S.; Cho, J. H.; Kim, W.-K.; Lee, J.-L.; Cho, K. Effects of Physical Treatment of ITO Electrodes on the Electrical Properties of Pentacene Thin-Film Transistors. *Electrochem. Solid State Lett.* **2007,** *10* (8), H239-H242.

[92] Yang, C.-M.; Wang, I.-S.; Lin, Y.-T.; Huang, C.-H.; Lu, T.-F.; Lue, C.-E.; Pijanowska, D. G.; Hua, M.-Y.; Lai, C.-S. Low cost and flexible electrodes with NH3 plasma treatments in extended gate field effect transistors for urea detection. *Sens. Actuator B-Chem.* **2013,** *187* (0), 274-279.

[93] Cho, J. H.; Lee, H. S.; Hwang, M.; Choi, H. H.; Kim, W.-K.; Lee, J.-L.; Cho, K. Enhancement of Hole Injection in Organic TFTs by Ozone Treatment of Indium Tin Oxide Electrodes. *Electrochem. Solid State Lett.* **2007,** *10* (5), H156-H159.

[94] Nguyen, T. N. T.; Seol, Y. G.; Lee, N.-E. Organic field-effect transistor with extended indium tin oxide gate structure for selective pH sensing. *Org. Electron.* **2011,** *12* (11), 1815-1821.

[95] Palai, A. K.; Lee, J.; Shin, T. J.; Kumar, A.; Park, S.-U.; Pyo, S. Solution-grown single-crystalline microwires of a molecular semiconductor with improved charge transport properties. *Chem. Commun.* **2014,** *50*, 8845-8848.

[96] Emmott, C. J. M.; Urbina, A.; Nelson, J. Environmental and economic assessment of ITO-free electrodes for organic solar cells. *Sol. Energ. Mat. Sol. Cells* **2012,** *97* (0), 14-21.

[97] Candelise, C.; Speirs, J. F.; Gross, R. J. K. Materials availability for thin film (TF) PV technologies development: A real concern? *Renew. Sust. Energ. Rev.* **2011,** *15* (9), 4972-4981.

[98] Azzopardi, B.; Emmott, C. J. M.; Urbina, A.; Krebs, F. C.; Mutale, J.; Nelson, J. Economic assessment of solar electricity production from organic-based photovoltaic modules in a domestic environment. *Energy Environ. Sci.* **2011,** *4* (10), 3741-3753.

[99] Du Pasquier, A.; Unalan, H. E.; Kanwal, A.; Miller, S.; Chhowalla, M. Conducting and transparent single-wall carbon nanotube electrodes for polymer-fullerene solar cells. *Appl. Phys. Lett.* **2005,** *87* (20), 203511-203513.

[100] van de Lagemaat, J.; Barnes, T. M.; Rumbles, G.; Shaheen, S. E.; Coutts, T. J.; Weeks, C.; Levitsky, I.; Peltola, J.; Glatkowski, P. Organic solar cells with carbon nanotubes replacing In_2O_3:Sn as the transparent electrode. *Appl. Phys. Lett.* **2006,** *88* (23), 233503–233513.

[101] Su, C.-Y.; Lu, A.-Y.; Chen, Y.-L.; Wei, C.-Y.; Wang, P.-C.; Tsai, C.-H. Chemically-treated single-walled carbon nanotubes as digitated penetrating electrodes in organic solar cells. *J. Mater. Chem.* **2010,** *20* (33), 7034-7042.

[102] Hecht, D. S.; Hu, L.; Irvin, G. Emerging Transparent Electrodes Based on Thin Films of Carbon Nanotubes, Graphene, and Metallic Nanostructures. *Adv. Mater.* **2011,** *23* (13), 1482-1513.

[103] Wassei, J. K.; Kaner, R. B. Graphene, a promising transparent conductor. *Mater. Today* **2010,** *13* (3), 52-59.

[104] Iwan, A.; Chuchmała, A. Perspectives of applied graphene: Polymer solar cells. *Prog. Polym. Sci.* **2012,** *37* (12), 1805-1828.

[105] Wan, X.; Huang, Y.; Chen, Y. Focusing on Energy and Optoelectronic Applications: A Journey for Graphene and Graphene Oxide at Large Scale. *Acc. Chem. Res.* **2012,** *45* (4), 598-607.

[106] Bejbouji, H.; Vignau, L.; Miane, J. L.; Dang, M.-T.; Oualim, E. M.; Harmouchi, M.; Mouhsen, A. Polyaniline as a hole injection layer on organic photovoltaic cells. *Sol. Energ. Mat. Sol. Cells* **2010,** *94* (2), 176-181.

[107] Ke, W.-J.; Lin, G.-H.; Hsu, C.-P.; Chen, C.-M.; Cheng, Y.-S.; Jen, T.-H.; Chen, S.-A. Solution processable self-doped polyaniline as hole transport layer for inverted polymer solar cells. *J. Mater. Chem.* **2011,** *21* (35), 13483-13489.

[108] Fan, B.; Araujo de Castro, F.; Chu, B. T.-T.; Heier, J.; Opris, D.; Hany, R.; Nüesch, F. Improved performance of cyanine solar cells with polyaniline anodes. *J. Mater. Chem.* **2010,** *20* (15), 2952-2955.

[109] Elschner, A.; Lövenich, W. Solution-deposited PEDOT for transparent conductive applications. *MRS Bull.* **2011,** *36* (10), 794-798.

[110] Ouyang, J. "Secondary doping" methods to significantly enhance the conductivity of PEDOT:PSS for its application as transparent electrode of optoelectronic devices. *Displays* **2013,** *34*, 423-436.

[111] Cho, S.-W.; Kim, Y. T.; Shim, W. H.; Park, S.-Y.; Kim, K.-D.; Seo, H. O.; Dey, N. K.; Lim, J.-H.; Jeong, Y.; Lee, K. H.; Kim, Y. D.; Lim, D. C. Influence of surface roughness of aluminum-doped zinc oxide buffer layers on the performance of inverted organic solar cells. *Appl. Phys. Lett.* **2011,** *98* (2), 023102-023104.

[112] Lee, J.; Lim, D.; Yang, K.; Choi, W. Influence of different plasma treatments on electrical and optical properties on sputtered AZO and ITO films. *J. Cryst. Growth* **2011,** *326* (1), 50-57.

[113] Oh, H.; Krantz, J.; Litzov, I.; Stubhan, T.; Pinna, L.; Brabec, C. J. Comparison of various sol–gel derived metal oxide layers for inverted organic solar cells. *Sol. Energ. Mat. Sol. Cells* **2011,** *95* (8), 2194-2199.

[114] Minami, T. Present status of transparent conducting oxide thin-film development for Indium-Tin-Oxide (ITO) substitutes. *Thin Solid Films* **2008,** *516* (17), 5822-5828.

[115] Pern, F. J.; Glick, S. H.; Li, X.; DeHart, C.; Gennett, T.; Contreras, M.; Gessert, T. 35th IEEE Photovoltaic Specialists Conference, Honolulu, USA, Honolulu, USA, **2010**.

[116] Li, G.; Zhu, R.; Yang, Y. Polymer solar cells. *Nature Photon.* **2012,** *6* (3), 153-161.

[117] He, Z.; Zhong, C.; Su, S.; Xu, M.; Wu, H.; Cao, Y. Enhanced power-conversion efficiency in polymer solar cells using an inverted device structure. *Nature Photon.* **2012,** *6* (9), 591-595.

[118] Duan, C.; Zhang, K.; Guan, X.; Zhong, C.; Xie, H.; Huang, F.; Chen, J.; Peng, J.; Cao, Y. Conjugated zwitterionic polyelectrolyte-based interface modification materials for high performance polymer optoelectronic devices. *Chem. Sci.* **2013,** *4* (3), 1298-1307.

[119] Sun, Y.; Welch, G. C.; Leong, W. L.; Takacs, C. J.; Bazan, G. C.; Heeger, A. J. Solution-processed small-molecule solar cells with 6.7% efficiency. *Nat. Mater.* **2012,** *11* (1), 44-48.

[120] Cnops, K.; Rand, B. P.; Cheyns, D.; Verreet, B.; Empl, M. A.; Heremans, P. 8.4% efficient fullerene-free organic solar cells exploiting long-range exciton energy transfer. *Nat Commun* **2014,** *5*, 1-6.

[121] Setayesh, S.; Grimsdale, A. C.; Weil, T.; Enkelmann, V.; Mullen, K.; Meghdadi, F.; List, E. J. W.; Leising, G. Polyfluorenes with Polyphenylene Dendron Side Chains: Toward Non-Aggregating, Light-Emitting Polymers. *J. Am. Chem. Soc.* **2001,** *123*, 946-953.

[122] Welch, G. C.; Perez, L. A.; Hoven, C. V.; Zhang, Y.; Dang, X.-D.; Sharenko, A.; Toney, M. F.; Kramer, E. J.; Nguyen, T.-Q.; Bazan, G. C. A modular molecular framework for utility in small-molecule solution-processed organic photovoltaic devices. *J. Mater. Chem.* **2011,** *21*, 12700-12709.

[123] Davis, A. R.; Carter, K. R. Controlling Optoelectronic Behavior in Poly(fluorene) Networks Using Thiol−Ene Photo-Click Chemistry. *Macromolecules* **2015,** *48*, 1711-1722.

[124] Scheler, E.; Strohriegl, P. Tailoring fluorene-based oligomers for fast photopatterning. *J. Mater. Chem.* **2009,** *19*, 3207–3212.

[125] Cumpston, B. H.; Jensen, K. F. Electromigration of aluminum cathodes in polymer-based electroluminescent devices. *Appl. Phys. Lett.* **1996,** *69* (25), 3941-3943.

[126] Cumpston, B. H.; Parker, I. D.; Jensen, K. F. In situ characterization of the oxidative degradation of a polymeric light emitting device. *J. Appl. Phys.* **1997,** *81* (8), 3716-3720.

[127] Lieber, C. M.; Kim, Y. Nanomachining and manipulation with the atomic force microscope. *Adv. Mater.* **1993,** *5* (5), 392-394.

[128] Liu, W.; Yan, Y.; Hu, Z.; Zhao, X.; Yan, J.; Dong, S. Study on the nano machining process with a vibrating AFM tip on the polymer surface. *Appl. Surf. Sci.* **2012,** *258*, 2620–2626.

[129] Kaltenbrunner, M.; White, M. S.; Głowacki, E. D.; Sekitani, T.; Someya, T.; Sariciftci, N. S.; Bauer, S. Ultrathin and lightweight organic solar cells with high flexibility. *Nat. Commun.* **2012,** *3* (770), 1-7.

[130] Cravino, A.; Schilinsky, P.; Brabec, C. J. Characterization of organic solar cells: The importance of device layout. *Adv. Funct. Mater.* **2007,** *17* (18), 3906-3910.

[131] Kim, M.-S.; Kang, M.-G.; Guo, L. J.; Kim, J. Choice of electrode geometry for accurate measurement of organic photovoltaic cell performance. *Appl. Phys. Lett.* **2008,** *92* (13), 133301-133303.

Annexe 1 : Laboratoire pour l'organique électronique

1.1 Architecture des dispositifs

Le choix de la direction de construction des dispositifs à base de films minces dicte la séquence à suivre pour compléter le dispositif. Il faut déterminer également le type d'électrodes qui seront utilisées, en prenant soin de déterminer quelle électrode sera transparente, bien qu'il soit possible de réaliser des dispositifs organiques où l'anode et la cathode sont toutes deux transparentes. Si le verre est couramment utilisé comme support de base pour les dispositifs, il est également possible de réaliser des dispositifs sur substrats flexibles tel le polyéthylène téréphtalate (PET).[129] L'architecture de base la plus répandue dans le domaine consiste à construire les dispositifs sur des substrats de verre, recouverts d'oxydes d'indium et d'étain servant d'anode. À partir de ces substrats, les différentes couches organiques sont appliquées et, finalement, une électrode métallique déposée par évaporation vient compléter le dispositif OPV ou OLED (Figure A1.1).

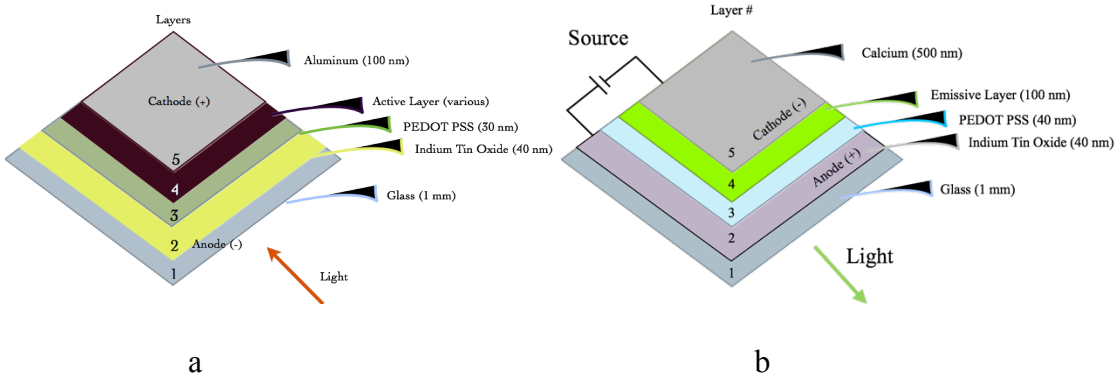

Figure A1.1. Représentations schématisées des dispositifs organiques. (a) Cellule photovoltaïque. (b) Diode électroluminescente.

1.2 Les substrats

Le choix des matériaux constituant les anodes et cathodes se fait en fonction des matériaux utilisés dans la couche active et leurs niveaux énergétiques HOMO-LUMO pour ainsi permettre une collection efficace des trous à l'anode et des électrons à la cathode. L'utilisation du calcium comme cathode peut impliquer une double évaporation de métaux puisque celui-ci devrait être recouvert d'aluminium pour limiter son oxydation. Le choix de manipuler et caractériser les dispositifs sous atmosphère inerte en boite à gants permet de limiter également cette oxydation des électrodes de calcium qui n'exigera plus nécessairement de recouvrement à l'aluminium. Pour l'anode, une solution solide d'oxydes d'indium et d'étain permet d'obtenir une transparence de 85 à 95 % selon l'épaisseur et une faible résistance dans le plan entre 10 et 20 Ω/carré.

L'ITO est déposé par pulvérisation en couches minces d'environ 40 nm. Pour s'assurer qu'aucun court-circuit ne sera créé lors de la connexion des électrodes, une déposition selon un diagramme précis permettra de définir en partie les dimensions des dispositifs ainsi que les zones de contact souhaitées. Pour ce faire, un masque de pulvérisation a été conçu selon le plan présenté à la Figure A1.2.

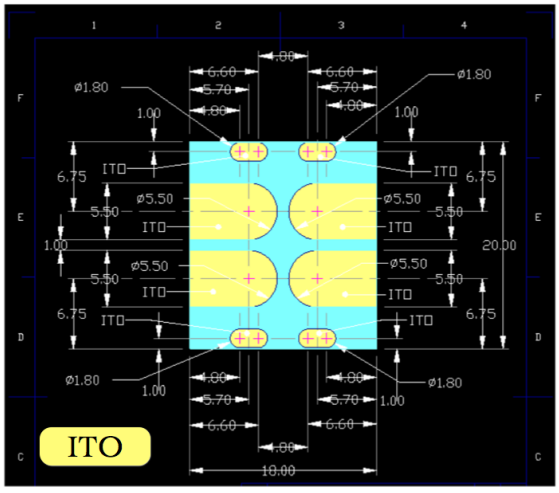

Figure A1.2. Plan des substrats d'ITO sur verre réalisés par pulvérisation.

Les quatre plus petites zones d'ITO présentes sur le substrat permettent un court-circuit contrôlé favorisant une connectivité accrue entre l'aiguille de connexion et la cathode. Il est à noter que ces zones d'ITO devront être dénudées du film actif avant l'évaporation pour permettre un bon contact entre l'ITO et la cathode. Ceci permet une plus grande stabilité des mesures répétitives sur le même substrat, lors, par exemple, de recuits additifs.

Les substrats d'ITO sont par la suite identifiés par gravure à l'aide d'une pointe au diamant. Les débris de verre générés ainsi que les contaminants présents sur la surface des substrats sont nettoyés dans des bains subséquents d'eau déionisée, d'acétone et d'isopropanol pendant 15 min. Les substrats sont passés par la suite à un traitement à l'UV-ozone. Des supports en Téflon ont été conçus à cet effet, permettant d'exposer les deux faces des substrats aux lavages qui se font dans un bain ultrasonique.

1.3 Les couches organiques

Une fois les substrats d'ITO traités, une couche mince de 30 à 40 nm de poly(3,4-éthylènedioxythiophène):polystyrène sulfonate) (PEDOT:PSS, Clevios PH1000) est par la suite appliquée par "spin coating" pour rectifier les inégalités du films d'ITO et produire une surface lisse et semi-conductrice de type p. Ce matériel étant soluble dans l'eau, une couche subséquente à base de solvant organique pourra être appliquée sans le dissoudre. Une vitesse de déposition et d'étalage de 4000 tours/min permet d'obtenir l'épaisseur voulue. La filtration de la solution de PEDOT:PSS à travers une membrane de Téflon de 0.45 μm permet de limiter la présence de granulats. Les substrats sont par la suite séchés à 110 °C sur une plaque chauffante à l'air pendant 20 minutes. Ils pourront au besoin, être conservés dans une boite-à-gants pendant quelques jours. Les films actifs sont par la suite appliqués sur les substrats par "spin coating" sous atmosphère inerte dans une boite-à-gants. Des traitements thermiques ou par vapeur de solvants avant la déposition des électrodes métalliques peuvent être effectués à ce moment.

1.4 Électrodes métalliques

Les substrats couverts de film actif sont transférés dans l'évaporateur pour le dépôt de la cathode d'aluminium ou de calcium sous pression réduite (10^{-6} mbar) à travers un masque de dépôt à un taux de 1-2 Å s^{-1}. Le masque de dépôt a été conçu sur mesure et détermine la surface finale (12.6 mm^2) des dispositifs (Figure A1.3). Les points de contact se retrouvent à 90° par rapport aux points de contact avec l'ITO présent sous le film actif (Figure A1.3c).

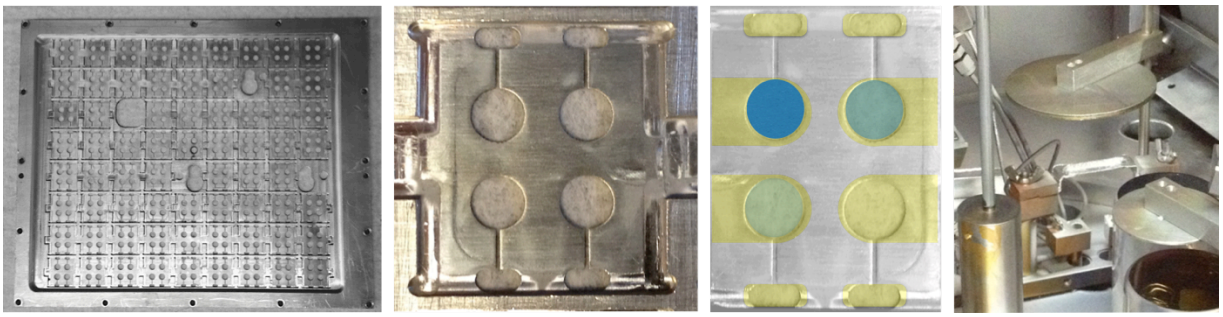

a b c d

Figure A1.3. Équipement pour le dépôt des électrodes métalliques. (a) Masque complet d'évaporation en aluminium. (b) Puit pour un substrat permettant la formation de quatre électrodes. (c) Juxtaposition des électrodes métalliques et de l'ITO sous-jacent (jaune) montrant leurs positions relatives et les superficies des cellules résultantes (bleus). (d) Bateau de tungstène pour l'évaporation de l'électrode métallique à l'intérieur de l'évaporateur.

1.5 Caractérisation des cellules photovoltaïques

Les cellules complétées sont par la suite caractérisées sous illumination d'un simulateur solaire à lampe de xénon calibré à 100 $mWcm^{-2}$ à l'aide d'une cellule de référence de silicium monocristallin, elle-même calibrée et certifiée par NREL. Pour éviter une

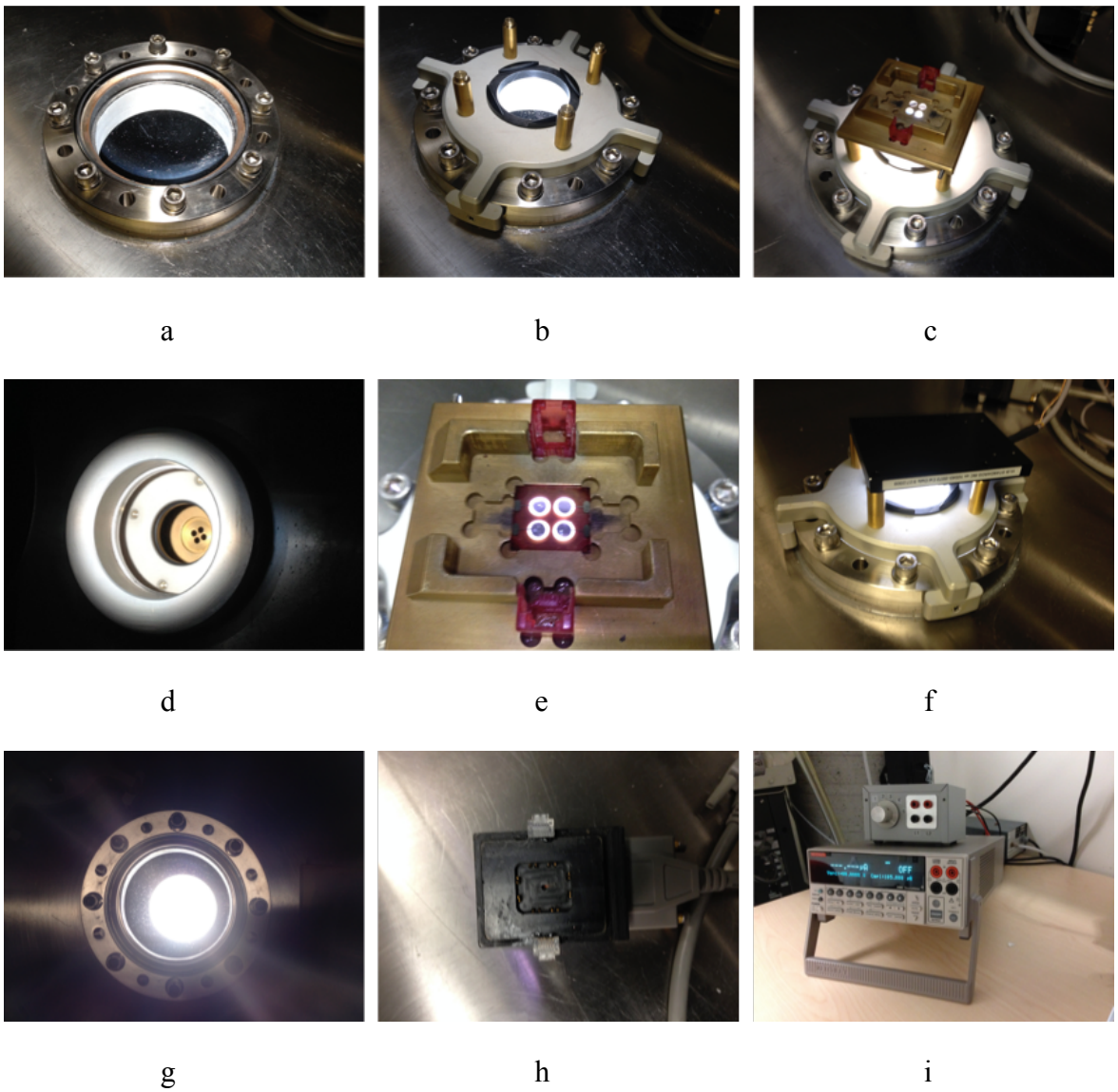

a b c

d e f

g h i

Figure A1.4. Pièces conçues sur mesure pour l'exposition et l'analyse des dispositifs photovoltaïques. (a) Port de quartz dans le planché de la boite à gants. (b) Support pour la cellule de référence ou la tête de contact des substrats. (c) Support et filtre d'exposition pour le substrat. (d) Vue du dessous du port de quartz et du faisceau provenant du simulateur solaire collimaté sur le support à substrat. (e) Support contenant un substrat. (f) Cellule de référence Si-monocristallin calibrée à 100 $mWcm^{-2}$ sur le support. (g) Vue aérienne du faisceau collimaté à travers le port de quartz. (h) Tête de contacts à électrodes plates de type poussoirs. (i) Sélecteur manuel du dispositif à mesurer à partir de la tête de contact, connecté à un instrument Keithley Model 236.

surestimation des performances photovoltaïques,[130-131] les cellules circulaires sont mesurées à travers un masque quasi correspondant à leur surface. La Figure A1.4 présente les différentes composantes qui ont dû être fabriquées sur mesure pour accueillir les substrats et caractériser les cellules photovoltaïques. Le système de mesure est doté d'un simulateur solaire Oriel SOL3A 2x2 de 450 W (Newport Corporation) placé à l'extérieur sous la boite à gants. Le plancher de la boite à gants a été percé pour pouvoir ajouter un port de quartz, permettant au faisceau de lumière provenant du simulateur d'illuminer l'échantillon sous atmosphère inerte. Le port de quartz est constitué d'une fenêtre de quartz de 9.86 cm de diamètre et 6.35 mm d'épaisseur (Kurt J. Lesker), retenue et scellée par des brides de 15.24 cm (Figure A1.4a). Un support à par la suite été conçu pour s'ajuster sur la bride intérieure du port de quartz et recevoir tant le support à substrat (Figure A1.4c) que la cellule de référence (Figure A1.4f) se retrouvant ainsi à la même distance du faisceau incident. Une fois le substrat positionné dans le support, la tête de contacts à électrodes doubles plates de type poussoirs (Figure A1.4h) est apposée et les contacts créés. Le sélecteur ajouté avant la source et instrument de mesure Keithley Model 236 permet de sélectionner la cellule à mesurer. Les courbes I-V sont enregistrées une à une pour les quatre cellules à l'aide du logiciel de chez PV Measurements Inc. Les différents traitements thermiques sont également faits sous atmosphère inerte sur une plaque chauffante (Electronic Micro Systems Ltd, EMS Precision Electronic Hot Plate model 1000-1).

Les diodes organiques électroluminescentes ont été complétés de la même manière que pour les cellules photovoltaïques. Suite aux dépôts des électrodes et après les traitements thermiques, les dispositifs ont été caractérisés sous atmosphère inerte en boite à gants. Les performances des diodes ont été mesurées à l'aide d'un spectrophotomètre HR2000 de chez Ocean Optics, à l'intérieur d'une boite noire en même temps que la mesure de la courbe I-V. Les coordonnées chromatiques ont été calculées à partir des données d'électroluminescence et rapportées selon le diagramme de la Commission Internationale de l'Éclairage (CIE) 1964.

"*Always look on the bright side of life.*"

- Eric Idle, Monty Python